



UNIL | Université de Lausanne

Unicentre

CH-1015 Lausanne

<http://serval.unil.ch>

Year : 2022

Hijacked NAD⁺ metabolism during axon degeneration in *Drosophila*

Llobet Rosell Arnau

Llobet Rosell Arnau, 2022, Hijacked NAD⁺ metabolism during axon degeneration in *Drosophila*

Originally published at : Thesis, University of Lausanne

Posted at the University of Lausanne Open Archive <http://serval.unil.ch>

Document URN : urn:nbn:ch:serval-BIB_1BF79C6CF1514

Droits d'auteur

L'Université de Lausanne attire expressément l'attention des utilisateurs sur le fait que tous les documents publiés dans l'Archive SERVAL sont protégés par le droit d'auteur, conformément à la loi fédérale sur le droit d'auteur et les droits voisins (LDA). A ce titre, il est indispensable d'obtenir le consentement préalable de l'auteur et/ou de l'éditeur avant toute utilisation d'une oeuvre ou d'une partie d'une oeuvre ne relevant pas d'une utilisation à des fins personnelles au sens de la LDA (art. 19, al. 1 lettre a). A défaut, tout contrevenant s'expose aux sanctions prévues par cette loi. Nous déclinons toute responsabilité en la matière.

Copyright

The University of Lausanne expressly draws the attention of users to the fact that all documents published in the SERVAL Archive are protected by copyright in accordance with federal law on copyright and similar rights (LDA). Accordingly it is indispensable to obtain prior consent from the author and/or publisher before any use of a work or part of a work for purposes other than personal use within the meaning of LDA (art. 19, para. 1 letter a). Failure to do so will expose offenders to the sanctions laid down by this law. We accept no liability in this respect.



UNIL | Université de Lausanne

Faculté de biologie
et de médecine

Département des Neurosciences Fondamentales

Hijacked NAD⁺ metabolism during axon degeneration in *Drosophila*

Thèse de doctorat en Neurosciences

présentée à la

Faculté de biologie et de médecine
de l'Université de Lausanne

par

Arnau LLOBET ROSELL

Master en Neurosciences de l'Université de Barcelone

Jury

Prof. Nicolas Toni, Président
Prof. Lukas Neukomm, Directeur de thèse
Prof. Micah Murray, Co-directeur de thèse
Dre. MER Julijana Ivanisevic, Experte
Prof. Thomas Wishart, Expert
Prof. Emi Nagoshi, Experte

Thèse n° 353

Lausanne
2022

***Programme doctoral interuniversitaire en
Neurosciences***

des Universités de Lausanne et Genève



Imprimatur

Vu le rapport présenté par le jury d'examen, composé de

Président·e	Monsieur	Prof.	Nicolas Toni
Directeur·trice de thèse	Monsieur	Prof.	Lukas Neukomm
Co-directeur·trice de thèse	Monsieur	Prof.	Micah Murray
Expert·e·s	Madame	Dre	Julijana Ivanisevic
	Madame	Prof.	Emi Nagoshi
	Monsieur	Prof.	Thomas Wishart

le Conseil de Faculté autorise l'impression de la thèse de

Monsieur Arnau Llobet Rosell

Titulaire d'un Master en neurosciences
de l'Université de Barcelone, Espagne

intitulée

**Hijacked NAD⁺ metabolism during axon
degeneration in *Drosophila***

Lausanne, le 7 décembre 2022

pour Le Doyen
de la Faculté de Biologie et de Médecine

Prof.  Nicolas Toni

Best moments in science are these small events of discovery when you finally get the answer to your question and when what you are doing suddenly makes perfect sense. It's like a mind fusion with the world you are trying to understand.

– Dan Hartl

TABLE OF CONTENTS

TABLE OF CONTENTS.....	5
ACKNOWLEDGEMENTS	7
ABSTRACT.....	9
RESUMÉ.....	10
LIST OF ABBREVIATIONS.....	11
CHAPTER 1 Introduction.....	13
I. History.....	15
II. Background	16
III. Phases of Wallerian degeneration.....	17
IV. The discovery and implications of Wld ^S	18
V. Axon death mediators	19
VI. Advantages of different animal models	27
VII. Commonalities and differences across species	28
VIII. Axon death signalling in disease.....	30
SUMMARY OF AIMS AND GENERAL SCOPE OF THE THESIS.....	33
CHAPTER 2 Observation and analysis of axon death in injured neurons of <i>Drosophila melanogaster</i>	35
1.1 Summary of the results	37
1.2 Personal contribution.....	37
CHAPTER 3 The NAD ⁺ precursor NMN activates dSarm to trigger axon degeneration in <i>Drosophila</i>	51
2.1 Summary of the results	53
2.2 Personal contribution.....	53
CHAPTER 4 Additional experiments to chapter 3	111
3.1 Summary of the results	113
3.2 Methods.....	113
3.3 Results	113
CHAPTER 5 Divergent signaling requirements of dSarm in injury-induced degeneration and developmental glial phagocytosis.....	117
4.1 Summary of the results	119
4.2 Personal contribution.....	119

CHAPTER 6 Adaptive optics in single objective inclined light sheet microscopy enables three-dimensional localization microscopy in whole adult <i>Drosophila</i> brains	149
5.1 Summary of the results	151
5.2 Personal contribution.....	151
CHAPTER 7 Identification of Axed-interacting proteins	183
6.1 Summary of the results	185
6.2 Personal contribution.....	185
6.3 Results	185
CHAPTER 8 Discussion and perspectives.....	189
<i>Drosophila</i> as a tool to study axon degeneration	191
The expression of NMN-Deamidase	191
NMN levels after injury	192
NMN to NAD ⁺ ratio.....	193
SARM1/dSarm as a central executioner of axon degeneration	194
CRISPR/Cas9 mediated KO	195
The function of Axed	196
FINAL REMARKS.....	197
REFERENCES	199
ANNEX 1 Review: Axon death signalling in Wallerian degeneration among species and in disease	215
ANNEX 2 DALI search for Axed 3D structure	229

ACKNOWLEDGEMENTS

These are the most important pages of the whole thesis. There are so many people that helped me during these years, and that I will be forever grateful to. The thesis is signed under my name, but without all of them, it wouldn't have been possible. I will try to be as honest as I can, hoping to not leave anyone behind.

To Lukas Neukomm, my PI and mentor: I enjoyed our relationship since the first day we skyped, back on August 18'. Since then, you've taught me the wonderful world of *Drosophila*, genetics and neuroscience with great passion. I honestly couldn't have hoped for more. I've always felt taken care of by you, supported in all the aspects possible—I never had a negative comment even when I would order the wrong primers for the millionth time—, and motivated to continue the project—you will remember how I told you that I still believed in the project the month before submitting the thesis—; I've learnt a handful of techniques, concepts, and pieces of advice that I will never forget. Most importantly, the art of making great presentations (idiot proof as someone says). We make a great team and we've come a long way. Academia needs more PIs like you. Thank you!

To Maria: we've built an entire lab from literally zero. From a set of Gilson to a fully equipped wet lab with all the facilities. Only you and I know how hard and rewarding at the same time it has been. Looking backwards I think it's safe to say that our ride has been like a rollercoaster, full of emotions, shared and opposite opinions, complete opposite scientific backgrounds, fun but also challenging moments... but we share a passion, the most important of them all: science. In a way, we always understood and took care of each other, our differences only made us better scientists and the different approaches to the problems made us grow a better laboratory. Thank you!

To the rest of the Neukomm lab: Magda, you were the third one to arrive in the lab. I imagine at the beginning it was challenging to fit in between Maria and me, but you soon managed to make your own space. Thanks for all the moments shared, for all the beers (and vodka) drunk, for the gossiping in the fly room, for the science we've learnt, and for supporting each other every day since day 1. I'm glad I made a polish friend; we've got a pending trip to Warsaw! Christel, I still remember how I thought you how to hold a pipette and calculate molarity before the start of your PhD. You've come a long way and you should be proud of yourself. Cathy, you've been the last one to arrive, but it's been a fabulous journey. It has been great to see you finish your thesis successfully after so many challenges; you deserve every piece of it! Thank you!

To the working engine of the department: the secretary office (Lise, Katharine, Alexandra, Katerina) the concierge (Eric) and the laverie (Andreia, Ana). There's so much work going on behind our backs and we are not aware of it. Thank you for making our everyday work much easier and smoother.

To my friend Laura: you've become one of my greatest supports, not only in the department but in my life. Meeting you at the department has been one of the greatest gifts of the PhD. We've found support in each other every time we've needed it. Sharing the window spots of the office has been one of the best things that could have happened to me in that office. Thank you for always being there.

To the friends that I made at the department, but that I hope to keep as friends for life: cheers to the lunches, dinners, beers, gintonics, parties, swims in the lake, trips to the mountain and sails with the boat. And cheers to many more! I'm so grateful to have met you and have you in my life. I can only hope to have you as friends for the rest of my life despite the distance.

To the friends that I made outside the department: thanks to all the Catalans that helped me feel a bit closer to home, to the skimo group for sharing the same passion, and to les loups du TC la Sallaz for all the tennis matches played. Thank you for letting me into your life.

To the friends from my hometown (la Bisbal) and my friends from the university of Barcelona: it's not easy to keep in contact with everyone when you are abroad, and I'm sure I could have done better. Thank you for always finding the time to see me every time I would come back home, whether it was for a day or two or for a week, whether it was for a 30-minute visit or for a whole day activity. It meant the world to me. A special mention goes to those who will come (or came or had the will to come) to my public defence, we'll have fun!

To my grandparents: thanks for giving me all the love of your lives, for waiting impatiently for me when I come back home. I know that you miss me (probably more than I do) but at the same time, I know that you understand how doing a PhD in Switzerland was the best for my future.

To my parents: Do you remember when we came to Switzerland for the first time? I was probably 13 or 14. Who would have said that some years later I would end up living in this country! And do you remember the second time? You came two weeks after I moved to Lausanne when I was living in that 18 m² apartment (if you can call it apartment) and you brought all the essentials for me - yes, I had been sleeping in a sleeping bag until then -. We will agree that my life has changed quite a bit since then. Thank you for our every day "bon dia" (and when I say every day, I mean it literally). Two words were sufficient to start the day by reassuring each other that everything was in order. Thank you for the weekly "dinner video call" although you would have the news in the background, it would make me feel as if we were eating all together at the same table. Thank you for supporting me in every decision I've made, and for all the given advice. One can't have better advice than his parents', and I am forever grateful. Thank you for coming once, twice, three or four times a year; and cooking for me, and cleaning for me even if I would say no 20 times. I know that I don't say it enough; I miss you and I love you. I wouldn't be myself if it wasn't for you.

And finally, to Júlia: I never thought I would find the love of my life in Lausanne, and I never thought she'd be Catalan and from l'Empordà. You've been my greatest support over these last years, you've gotten to understand me better than anyone else—and I know it's not the easiest job—, you've accepted me the way that I am and you've never let me down; you've taken care of me when I've been sick, you've always listened to me—even when I would repeat the same complaint over and over—, you've been (very) patient while I was immersed in the lab writing the thesis AND doing revisions for the article. I cannot wait to start a new chapter of my life next to you because everything is much better at your side. I love you.

ABSTRACT

Axon loss is the earliest shared and detectable feature of nervous systems being challenged in degenerative disorders, by chemotherapy or mechanical forces. Yet intrinsic molecular mechanisms that execute axon degeneration remain largely unknown, making the development of therapeutics to attenuate axon degeneration challenging.

Injury-induced axon degeneration (Wallerian degeneration) is a simple and well-established system to study how axons execute their destruction (axon death). After injury, in the axon separated from the soma, a temporal rise of the metabolite NMN occurs, followed by rapid depletion of NAD^+ , a metabolite crucial for axonal survival. To date, four essential and evolutionary conserved axon death genes dictate levels of NMN and NAD^+ in *Drosophila*: Highwire regulating levels of the NMN-consuming and NAD^+ -synthesising dNmnat upstream, the NAD^+ hydrolase dSarm in the centre, and Axed downstream in this signalling cascade. My Ph.D. thesis aims to gain further insights into i) how NAD^+ metabolites modulate dSarm activity and ii) the precise function of Axed during axon death signalling in *Drosophila*.

I could demonstrate in the fly that lowering NMN levels through the expression of a newly generated prokaryotic NMN-Deamidase (NMN-D) preserves severed axons for months and keeps them circuit-integrated for weeks. In contrast, elevated NMN levels, through the expression of mouse nicotinamide phosphoribosyltransferase (mNAMPT), lead to faster axon degeneration after injury. I also show that dSarm mediates axon degeneration through NMN-induced activation, which is regulated by the NMN/ NAD^+ ratio *in vivo*. Finally, NM-D delays neurodegeneration caused by the loss of the sole NMN-consuming and NAD^+ -synthesising enzyme dNmnat.

Axed is the most downstream candidate of the signalling pathway. I performed *in vivo* pulldowns using endogenously tagged Axed (Axed^{eGFP::3xFLAG}) to identify Axed-interacting proteins. They were classified by DAVID analyses in GO terms for biological processes, cellular compartments, and molecular function. The predicted 3D structure of Axed was modelled by implementing several described structural homologues. It will help to decipher the precise mechanistic role of Axed or at least identify additional proteins required for the axon death signalling cascade.

Axon death signalling is also activated in the absence of injury, such as in diseased and challenged nervous systems. Thus, understanding the mechanisms underlying axon death signalling could help define therapeutic targets to block axon loss.

RESUMÉ

La perte d'axones est la première caractéristique partagée et détectable des systèmes nerveux mis à l'épreuve dans les troubles dégénératifs, par la chimiothérapie ou les forces mécaniques. Pourtant, les mécanismes moléculaires intrinsèques qui exécutent la dégénérescence des axones restent largement inconnus, ce qui rend difficile le développement de thérapies pour atténuer la dégénérescence des axones.

La dégénérescence des axones induite par une blessure (Wallerian degeneration) est un système simple et bien établi pour étudier comment les axones exécutent leur destruction (mort des axones). Après blessure, dans l'axone séparé du soma, une élévation temporelle du métabolite NMN se produit, suivie d'une déplétion rapide du NAD^+ , un métabolite crucial pour la survie axonale. À ce jour, quatre gènes essentiels et évolutifs conservés de la mort des axones dictent les niveaux de NMN et de NAD^+ chez la *Drosophila* : les niveaux de régulation élevés du dNmnat consommant du NMN et synthétisant du NAD^+ en amont, le dSarm hydrolase de NAD^+ au centre et Axed en aval dans cette cascade de signalisation. Ma thèse de doctorat vise à mieux comprendre i) comment les métabolites NAD^+ modulent l'activité de dSarm et ii) la fonction précise d'Axed lors de la signalisation de la mort des axones chez la drosophile.

J'ai pu démontrer chez la mouche que l'abaissement des niveaux de NMN par l'expression d'une NMN-Deamidase procaryote nouvellement générée (NMN-D) préserve les axones coupés pendant des mois et les maintient intégrés au circuit pendant des semaines. En revanche, des niveaux élevés de NMN, grâce à l'expression de la nicotinamide phosphoribosyltransférase de souris (mNAMPT), conduisent à une dégénérescence axonale plus rapide après une blessure. Je montre également que dSarm intervient dans la dégénérescence des axones par l'activation induite par le NMN, qui est régulée par le rapport NMN/ NAD^+ *in vivo*. Enfin, NMN-D retarde la neurodégénérescence causée par la perte de la seule enzyme dNmnat consommatrice de NMN et synthétisant NAD^+ .

Axed est le candidat le plus en aval de la voie de signalisation. J'ai effectué des immunoprécipitations *in vivo* à l'aide d'Axed marqué de manière endogène (Axed^{eGFP::3xFLAG}) pour identifier les protéines interagissant avec Axed. Ils ont été classés par des analyses DAVID en termes GO pour les processus biologiques, les compartiments cellulaires et la fonction moléculaire. La structure 3D prédite d'Axed a été modélisée en mettant en œuvre plusieurs homologues structurels décrits. Cela aidera à déchiffrer le rôle mécaniste précis d'Axed ou au moins à identifier les protéines supplémentaires nécessaires à la cascade de signalisation de la mort des axones.

La signalisation de mort axonale est également activée en l'absence de blessure, comme dans les systèmes nerveux malades et en difficulté. Ainsi, comprendre les mécanismes sous-jacents à la signalisation de la mort des axones pourrait aider à définir des cibles thérapeutiques pour bloquer la perte d'axones.

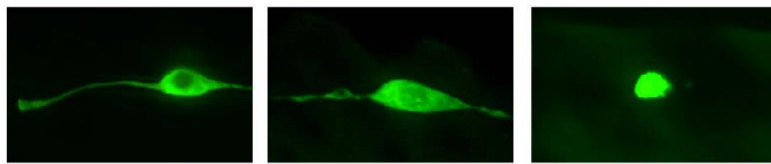
LIST OF ABBREVIATIONS

WD	Wallerian Degeneration	Hiw	Highwire
Wld ^s	Wallerian degeneration Slow	PHR1	PAM/Highwire/RPM-1
AD	Alzheimer's disease	SCF	Skp/Cullin/F-box
ALS	Amyotrophic lateral sclerosis	SKIP1A	S-phase kinase-associated protein 1A
MS	Multiple sclerosis	FBXO45	F-box protein 45
PD	Parkinson's disease	MAPK	Mitogen-activated protein kinase
TBI	Traumatic brain injury	JNK	c-Jun N-terminal kinases
CIPN	Chemotherapy-induced peripheral neuropathy	SARM	Sterile alpha and armadillo motif
Ca ²⁺	Calcium	ARM	Armadillo/HEAT
NAD ⁺	Nicotinamide adenine dinucleotide	SAM	Sterile alpha motif
ATP	Adenosine triphosphate	TIR	Toll/interleukin-1 receptor homology
ROS	Reactive oxygen species	ADPR	ADP-ribose
CNS	Central nervous system	cADPR	Cyclic ADP-ribose
PNS	Peripheral Nervous System	Axed	Axundead
UBE4B	ubiquitination factor E4B	TAI	Traumatic axonal injury
NMNAT	Nicotinamide mononucleotide adenylyltransferase	SCG	Superior cell ganglia
NMN	Nicotinamide mononucleotide	RGC	Retinal ganglion cells
NaMN	Nicotinic acid mononucleotide	FADS	Foetal akinesia deformation sequence
DRG	dorsal root ganglia	ORN	Olfactory receptor neurons
JO	Johnston òrgan	NaDS	NAD ⁺ synthase
NAM	Nicotinamide	dNaam	<i>Drosophila</i> nicotinamidase
NAMPT	Nicotinamide phosphoribosyltransferase	TLR	Toll-like receptor
NR	Nicotinamide riboside	Ask1	Apoptosis signal-regulated kinase 1
NRK	Nicotinamide riboside kinase	AO	Adaptive optics
NMN-D	NMN-Deamidase	PSF	Point spread function
UPS	Ubiquitin-proteasome System	SOLEIL	Single-objective lens-inclined light

IP	Immunoprecipitation	AB	Antibody
DAVID	Database for annotation, visualization and integrated discovery	LC-MS/MS	Liquid chromatography-tandem mass spectrometry
DALI	Distance matrix alignment	GO	Gene ontology
WB	Western blot	PDB	Protein data bank
		VNC	Ventral nerve cord

CHAPTER 1

Introduction



Course of a degenerating neuron.

I. History

Axon degeneration was first described by Augustus Waller in 1849. He observed that after cutting a nerve fibre from the tongue of a frog, the distal stump located in the tongue itself, separated from the cell bodies located in the spinal marrow, would appear unchanged for a few days until it rapidly disintegrated into fragments or, in Waller's words, a "curdling of the medulla into separate particles of various sizes" (Waller, 1850)¹. This phenomenon has been named after Augustus Waller, e.g., Wallerian degeneration (WD). WD is a two-step process: the degeneration of the injured axon is followed by an immune response to clear all the cellular debris within 3 to 5 days (Figure 1). The common assumption was that WD happened due to separating the axonal distal segments from the neuronal cell bodies, which contain the source of protein synthesis and other necessary supportive elements (Perry et al., 1987).

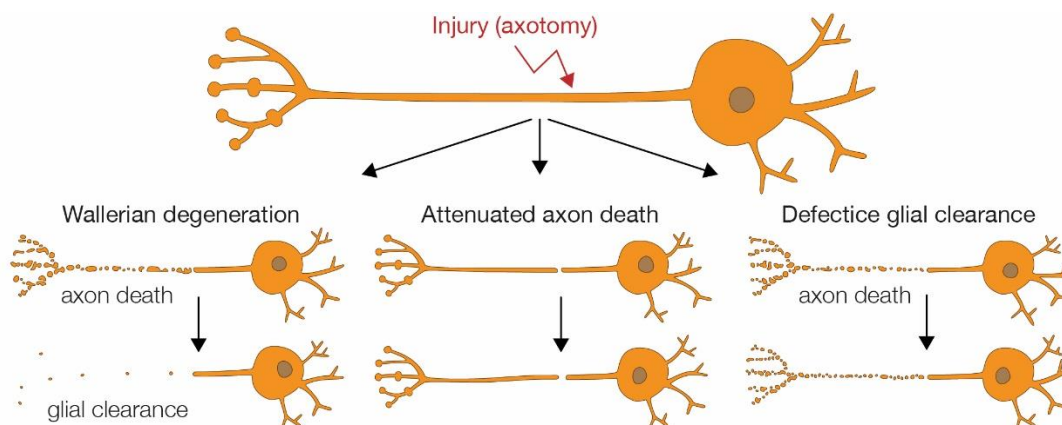


Figure 1. Wallerian degeneration consists of two molecularly distinct programs. Upon axotomy, the axon separated from the soma actively executes its fragmentation (axon death), which is mediated by an evolutionarily conserved axon death signalling cascade. The severed axon undergoes axon death within 1 day. Surrounding glial cells will then engage and clear the resulting axonal debris within 3–5 days (left side). Attenuated axon death results in severed axons which remain morphologically preserved and circuit integrated for weeks to months (middle). Defective glial clearance culminates in axonal debris which persists for a similar time *in vivo* (right side). Adapted from (Llobet Rosell & Neukomm, 2019).

140 years after Waller's experiments, the accidental discovery of a mutant mouse changed the perception of WD forever. A spontaneously generated mutant mouse exhibited morphologically preserved and circuit-integrated distal axonal segments for several weeks after transection (Figure 1) (Lunn et al., 1989). Remarkably, injured axons were able to conduct evoked action potentials for several weeks after injury, suggesting that they remain circuit integrated (Lunn et al., 1989). The mutant mouse line was named Wallerian degeneration Slow (Wld^s) and made everyone aware that WD—rather than a passive process—is an active axonal dismantling program that can be genetically perturbed (Perry et al., 1991). Delaying axon degeneration prevents the progression of the subsequent immune response, suggesting that the physical breakdown of the axonal cytoskeleton is required to trigger surrounding glial activation during WD (R. George & Griffin, 1994; Lunn et al., 1989) Similarly, defective glial clearance culminates in axonal

¹ Interestingly enough, the tongue has two main nerve fibres. Waller would only injure one fibre, leaving the other one intact, so that he could compare the injured fibre side by side with the uninjured control one. This is basically the same concept that we try to apply to our experiments as you'll see later with the wing injury and the antennal ablation. It's fascinating to see that two centuries ago, the principle was already the same.

debris which persists for weeks *in vivo* (Figure 1) (MacDonald et al., 2006; Neukomm et al., 2014). See also (Llobet Rosell & Neukomm, 2019 added in annex 1). This discovery opened the way to study and treat neurodegenerative human diseases as we know them today, as I will discuss in the following chapters.

II. Background

Neurons use their axons to communicate with remote cells. These axons can be extremely long, ranging from millimetres to centimetres to metres depending on the host, the type of neuron and the target cell (Matsuda et al., 2009; Wedel, 2012). The estimated cumulative length of axons in human brain white matter at the age of 20 is 149.000 to 176.000 km, about four times the Earth's circumference (Marner et al., 2003). In other words, axons can take up more than 99.9% of the neuronal volume. Axons also harbour a remarkably elaborate axonal cytoskeleton (axoskeleton) (Xu et al., 2013), which allows them to withstand stretch, compression, tension and torsion (Fournier et al., 2015; Hammarlund et al., 2007; Krieg et al., 2017; D. H. Smith, 2009; D. H. Smith et al., 2001). To ensure continued circuit function, the nervous system established soma-independent, local axonal-intrinsic and glial-extrinsic mechanisms to support lifelong axon survival (Mariano et al., 2018). If these survival mechanisms are impaired, axons will undergo axon degeneration (Burgess & Crish, 2018; Neukomm & Freeman, 2014).

Axonopathies are increasingly recognized as major contributors to neurological conditions, such as Alzheimer's disease (AD), amyotrophic lateral sclerosis (ALS) and multiple sclerosis (MS) (Vickers et al., 2009), Parkinson's disease (PD) (Burke & O'Malley, 2013), traumatic brain injury (TBI) (Hill et al., 2016), and chemotherapy-induced peripheral neuropathy (CIPN) (Flatters et al., 2017). Axon degeneration occurs before neuronal loss in a broad range of injured and diseased nervous systems. Indeed, axon death signalling is activated not only when the axon is cut, crushed or stretched (Bridge et al., 1994; Maxwell et al., 2015), but it also seems to be a major contributor in different animal models of neurological conditions, e.g., where axons degenerate in the absence of injury (Conforti et al., 2014). Targeting the signalling pathway by therapeutics could serve as a promising opportunity to ameliorate neurological disorders (Coleman & Perry, 2002; Simon & Watkins, 2018) beyond a simple injury model or, as August Waller wrote (Waller, 1850), "*It is impossible not to anticipate important results from the application of this inquiry to the different nerves of the animal system. But it is particularly with reference to nervous diseases that it will be most desirable to extend these research*". Gaining insights into underlying mechanisms executing axon degeneration will help define targets for developing efficacious drugs for therapeutic intervention. However, most of the developing therapeutics have proved inefficacious due to the poor understanding of the molecular and cellular processes that drive axonal degeneration.

Over recent years, significant advancements broadened our understanding of axon death signalling in WD. While these discoveries shed light on distinct mediators of axon death, they also led to more unanswered questions. First, how complete is our understanding of axon death signalling? Second, what differences or commonalities have been observed across species? And third, how do these findings bring us closer to defining new pharmacological targets that could prevent axon degeneration in the diseased and injured nervous system?

III. Phases of Wallerian degeneration

Immediately after axotomy, the axon separated from the soma goes through a lag phase where its overall morphology remains unchanged for 6–24 h depending on several factors, such as *in vitro*, *in vivo* models, and animal models (Figure 2A). While the lag phase lasts, the ability to conduct action potentials is preserved (Moldovan et al., 2009) and both anterograde and retrograde transport activities continue to happen in the distal axon (R. S. Smith & Bisby, 1993). The earliest feature observed immediately after injury is a rapid, short-term increase of axonal calcium (Ca^{2+}) levels in both the proximal and distal axon stump (Figure 2B). This is primarily due to extracellular Ca^{2+} influx at the lesion site, and to a lesser extent from axon internal Ca^{2+} stores (Adalbert et al., 2012; Avery et al., 2012; B. George et al., 1995; Villegas et al., 2014). After the first, rapid short-term Ca^{2+} wave, nicotinamide adenine dinucleotide (NAD^+) and adenosine triphosphate (ATP) are rapidly depleted, thus impairing axonal energy homeostasis (Park et al., 2013; Shen et al., 2013; Q. Zhai et al., 2003). Mitochondria lose their membrane potential and begin to swell, thereby increasing the generation of reactive oxygen species (ROS). Ultimately, they release their internal Ca^{2+} stores, which culminates in a second, long-term Ca^{2+} wave (Barrientos et al., 2011; Bernardi et al., 2006; Martin et al., 2010; Park et al., 2013). At this point, the gross axonal morphology remains unchanged, despite the already initiated destabilization of microtubules (Park et al., 2013; Q. Zhai et al., 2003).

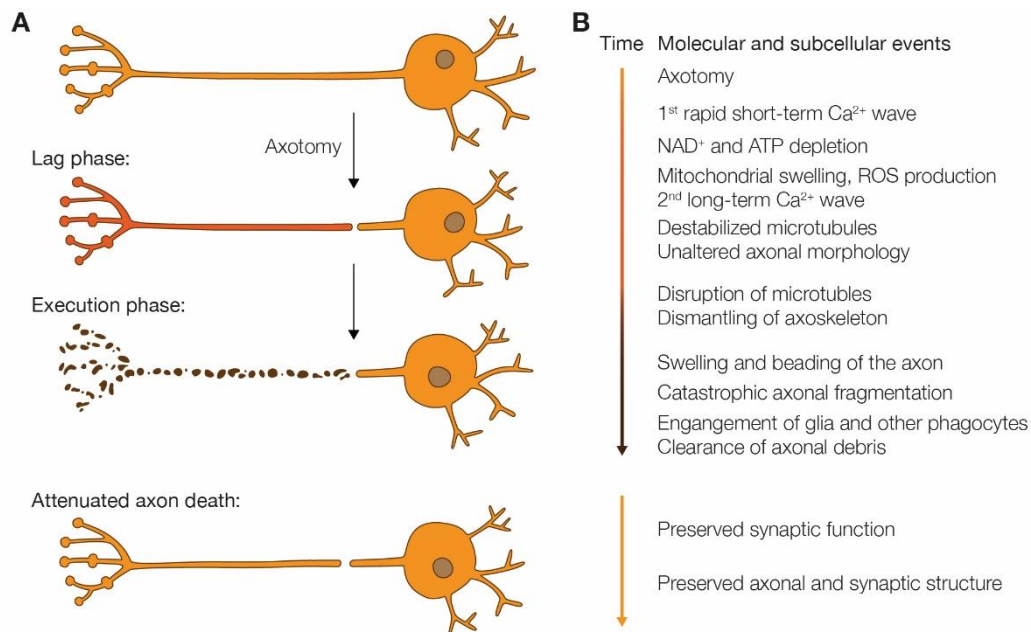


Figure 2. Phases and events during Wallerian degeneration. **A** Morphological phases of WD. After axotomy, the axon separated from the soma goes through a lag phase (red), where its morphology remains grossly intact. During the execution phase (brown), the axon undergoes catastrophic axon fragmentation (axon death). Surrounding glia engage and clear the resulting axonal debris. The attenuation of axon death signalling results in morphologically and functionally preserved axons and synapses. **B** Molecular and subcellular events during WD. Axotomy, lag and execution phase (orange, red and brown, respectively). The precise onset and duration of each event depends on the model system used. Attenuated axon death signalling preserves axons' structure and function and synapses. Adapted from (Llobet Rosell & Neukomm, 2019).

Suddenly, the execution phase starts: the axon begins to disassemble. Catastrophic granular fragmentation is observed at the molecular, ultrastructural and morphological levels (Park et al., 2013). Microtubules start to disrupt, alongside the dismantling of the axoskeleton. The axon

starts “beading” or swelling, culminating in catastrophic axonal fragmentation (Shen et al., 2013; Villegas et al., 2012; Yang et al., 2013) which can be completed along the length of the axolemma as fast as 1-2h from the onset, with a rate of up to 24 mm/h *in vivo* and 0.4 mm/h in cultured cells (Beirowski et al., 2005; Sievers et al., 2003).

During the execution phase, surrounding glial cells and specialized phagocytes not only clear the resulting axonal debris by activating multiple signalling pathways (T.-Y. Lu et al., 2017; MacDonald et al., 2006; Perry et al., 1987; Purice et al., 2016; R. G. Zhai et al., 2006) but also actively enhance axonal fragmentation (Vaquié et al., 2019). Several key questions remain unresolved, such as what kind of axonal ‘eat me’ signals are presented to surrounding glia (Shacham-Silverberg et al., 2018), and where glial cells are located within the execution phase engage in clearing axonal debris.

Once the execution phase is over, e.g., when the injured axon is disassembled and the resulting debris cleared by surrounding glia, WD is also over. While WD occurs in both the central and peripheral nervous system (CNS and PNS, respectively), it is of particular importance in the PNS to pave the way for the proximal axon still attached to the neuronal soma, which ultimately activates its regenerative programme, to regrow and thereby to re-establish circuit function (Martin et al., 2010).

IV. The discovery and implications of *Wld^S*

Axon death within WD was long thought to be a simple passive wasting away of severed axons (Waller, 1850). In 1989, the serendipitous discovery of the ‘Wallerian degeneration slow’ (*Wld^S*) mouse challenged this idea. Severed *Wld^S* axons remained preserved for weeks rather than undergoing axon death within a day (Figure 2) (Lunn et al., 1989). Two opposing explanations for this remarkable phenotype were proposed: some believed that *WLD^S* would exclude from the axon a signal necessary to trigger WD; others thought that *WLD^S* would provide an axon maintenance factor that needed to be continuously delivered (J. T. Wang et al., 2012). Subsequently, the molecular change in *Wld^S* mice was identified as a tandem triplication of two neighbouring genes: the N-terminal 70 amino acid fragment of the ubiquitination factor E4B (UBE4B) fused to full-length nicotinamide mononucleotide adenylyltransferase 1 (NMNAT1) (Mack et al., 2001). This fusion results in a translocation of nuclear NMNAT1 to the axon, where it exerts axon death attenuation (this will be discussed further below). The *Wld^S* neomorph provided the first evidence that axon death is an active self-destruction programme to eliminate damaged axons because sole overexpression of *WLD^S* profoundly attenuates this programme. Following the identification of *WLD^S*, several important discoveries were made, which are summarized below.

- First, *WLD^S* harbours an evolutionarily conserved function. While it was first found to delay axon death in mice (Lunn et al., 1989; Mack et al., 2001), the mouse chimeric protein performs its function equally well in rats (Adalbert et al., 2005), fruit flies (MacDonald et al., 2006) and zebrafish (Feng et al., 2010; Martin et al., 2010). *WLD^S* is therefore capable of delaying axon death across multiple species.

- Second, WLD^S acts autonomously in neurons and is dosage-dependent. The *Wld^S* mouse harbours a tandem triplication that results in over-expressed WLD^S (Mack et al., 2001). The higher the levels, the better its capability to preserve severed axons (Mack et al., 2001).
- Third, WLD^S acts locally within axons. While abundant in both nuclei and axons, WLD^S confers potent attenuation of axon death signalling specifically in axons (Beirowski et al., 2009). Viral transduction of multiple modified versions of WLD^S into severed axons up to 4 h after axotomy (e.g., early within the lag phase) is sufficient to attenuate axon death signalling (Sasaki & Milbrandt, 2010).
- Fourth, WLD^S is specific for axon death. Its expression blocks axon death and seems to have largely no effect on developmental pruning (Hoopfer et al., 2006), or other types of neuronal death such as apoptosis (Finn et al., 2000),
- And fifth, WLD^S is beneficial in many models of neurodegenerative conditions. Since its discovery, the *Wld^S* mouse has been crossed into many different neurological models to assess its protective ability in the injured and diseased nervous system (Conforti et al., 2014). These findings support the idea that axon death is shared in injury and disease, and, more importantly, that axon degeneration is a significant driver in different neurological conditions.

WLD^S provided the first evidence that, at the molecular level, axon death can be attenuated by overexpression of a single protein. Its discovery and characterization raised two key questions: first, how is WLD^S able to attenuate an axonal-intrinsic axon death signalling pathway actively executing the degeneration of severed axons; and second, what are the mediators of axon death signalling? The following will summarise our current knowledge related to these two questions.

V. Axon death mediators

To date, axon death in WD has been observed in several species such as mice, rats, flies and fish (Figure 3). Each animal model has contributed to the discovery of important axon death mediators and also offered distinct insights into axon death signalling. Notably, the modification of each mediator of the pathway can attenuate axon death comparable to the effects of WLD^S—in the range of days to weeks—.

1) Ca²⁺

As mentioned above, an initial local influx of Ca²⁺ right after axotomy from the site of injury is observed in both invertebrate and vertebrate models *in vivo* and *in vitro* (Adalbert et al., 2012; very et al., 2012; Mishra et al., 2013a; Vargas et al., 2015). The first, rapid short-term Ca²⁺ wave precedes the lag phase (Figure 2). High extra-axonal Ca²⁺ concentrations initiate the disassembly of severed axons: if the extracellular environment is devoid of Ca²⁺ (by adding EGTA or in a medium lacking Ca²⁺), or when voltage-gated Ca²⁺ channels are inhibited, the fragmentation of severed axons is significantly delayed, whereas adding Ca²⁺ ionophores is sufficient to revert the protective phenotype and induce degeneration in uninjured neurites (Figure 3A) (B. George et al., 1995; Kerchensteiner et al., 2005; Knöferle et al., 2010; Mishra et al., 2013; Schlaepfer, 1974).

The second, long-term Ca^{2+} wave is present solely in the separated axon. It appears before axonal fragmentation and is believed to be a critical instructive component for the execution phase (Loreto et al., 2015; Vargas et al., 2015). Because the exposed axonal membrane of the injured ends is quickly sealed by Ca^{2+} -dependent fusion vesicles (Eddleman et al., 1998) and because the highest axonal Ca^{2+} levels occur at significant distances away from the injury site (Ziv & Spira, 1993), during the second wave, Ca^{2+} is released primarily from intra-axonal stores (e.g. mainly from mitochondria, and to a lesser extent from the endoplasmic reticulum), and the inhibition thereof can significantly delay the disassembly of the axon (Villegas et al., 2014).

The expression of WLD^{S} in zebrafish and rodent neuronal cultures largely suppresses the second, but not the first Ca^{2+} wave, suggesting that the second wave is responsible for triggering axon fragmentation (Adalbert et al., 2012; Vargas et al., 2015). In *Drosophila* larvae, WLD^{S} also suppresses the first Ca^{2+} wave, reflecting minor differences between the experimental systems (Avery et al., 2012). On the other hand, the exogenous addition of Ca^{2+} is sufficient to abolish WLD^{S} -mediated axonal protection (Glass et al., 1994) suggesting that Ca^{2+} could be an effector of other upstream signalling events rather than an early trigger to activate the axon death pathway after injury.

The rise in intra-axonal Ca^{2+} , both during the immediate first short-term and during the slower and delayed second long-term Ca^{2+} wave, is a crucial instructive signal to trigger axon death signalling. However, how transient high Ca^{2+} levels are linked to the initiation of axon death signalling remains completely unknown.

2) NMNAT2/dNmnat

WLD^{S} is an over-expressed version of NMNAT1 translocated from the nucleus to the axon (Conforti et al., 2000; Mack et al., 2001). NMNAT proteins are essential for ATP-dependent NAD^+ synthesis from either nicotinamide mononucleotide (NMN) or nicotinic acid mononucleotide (NaMN) (Sasaki, 2018). Mammals and zebrafish harbour three different *Nmnat* genes (*Nmnat1–3*) with other subcellular locations and kinetic properties (Berger et al., 2005). In contrast, *Drosophila* relies on a single *nmnat* gene (*dnmnat*) (R. G. Zhai et al., 2006), which is alternatively spliced to generate variants localized to the nucleus and the cytoplasm (Ruan et al., 2015). The discovery of Wld^{S} , and subsequently the extensive research on NMNAT proteins and their biosynthetic NAD^+ activity, provided the following four major insights: levels and localization of NMNAT proteins, as well as levels of NAD^+ and its precursor NMN, are all crucial for the execution of axon death signalling.

- **NMNAT2/dNmnat levels**

Among the three mammalian *Nmnat* isoforms, NMNAT2 is the gatekeeper of axon death: it is a limiting, labile axon survival factor (Gilley & Coleman, 2010). Synthesized in the soma and transported into the axon, NMNAT2 must be constantly replenished in axons due to its rapid turnover (Figure 3A): NMNAT2 is the most labile member of its family with a half-life of less than 4 h, despite being the most highly expressed isoform in the brain (Yan et al., 2010) and an essential NAD^+ biosynthesis enzyme for the peripheral nervous system homeostasis (Hicks et al., 2012).

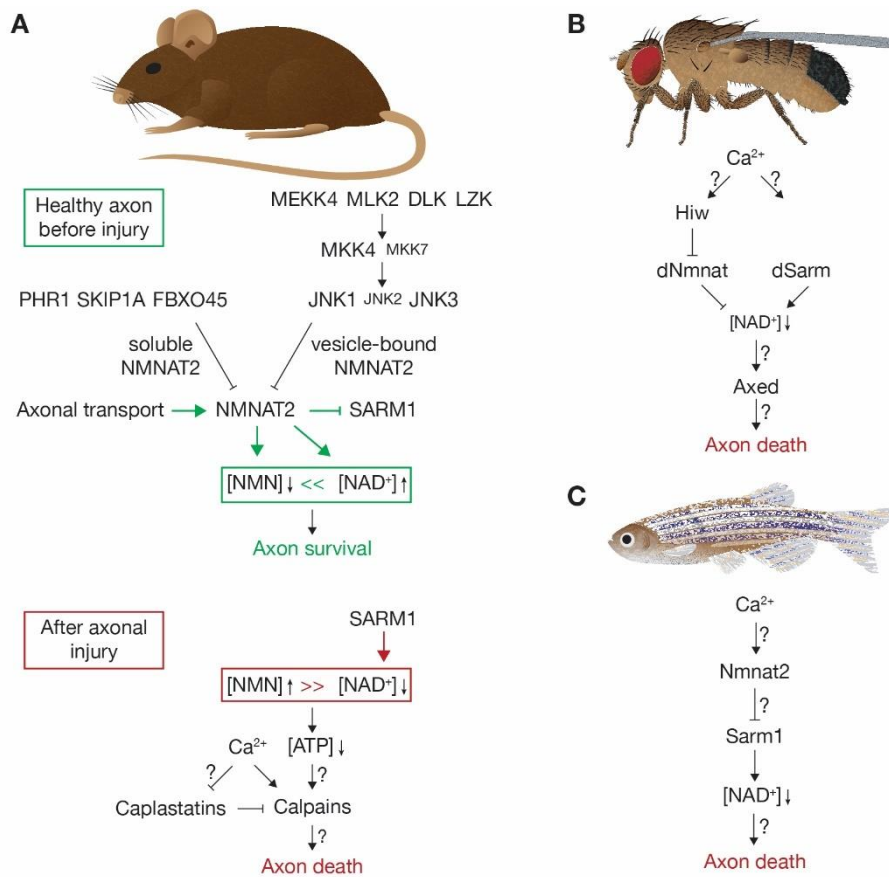


Figure 3. Axon death signalling across species. **A** In mouse axons, axonal survival is ensured by above-threshold levels of NMNAT2. NMNAT2 is constantly replenished by axonal transport, while the atypical ubiquitin ligase complex and the MAPK pathway rapidly degrade soluble and vesicle-bound NMNAT2, respectively. NMNAT2 keeps NMN levels low, and NAD⁺ levels constant. NMNAT2 also blocks SARM1 through an unknown mechanism. Upon axotomy, NMNAT2 drops below threshold levels, which induces axon death. NMN levels rise, and the SARM1 NADase activity rapidly depletes NAD⁺ levels. **B** Axon death signalling in flies. See text for details. **C** Axon death signalling in fish. The genetic interactions of Ca²⁺, NMNAT2 and SARM1 remain to be determined. See text for details. Adapted from (Llobet Rosell & Neukomm, 2019).

Upon axotomy, NMNAT2 cannot be transported to the axon; thus, NMNAT2 levels drop rapidly in severed axons, and axon death is initiated (Gilley & Coleman, 2010). *Vice versa*, depletion of NMNAT2 in neurons is sufficient to induce axon degeneration in the absence of injury: axons undergo Wallerian-like degeneration—because they can be attenuated by WLD^S—while the soma remains unaffected (Gilley & Coleman, 2010; Milde, Gilley, et al., 2013). Similarly, *Nmnat2*^{-/-} mice harbour perinatal lethality due to limited axon extensions, and their isolated neuronal cultures from both PNS and CNS contain neurite outgrowth consistently stalling at 1–2 mm (Gilley et al., 2013). Likewise, in *Drosophila*, RNAi-mediated knockdown, or a lack of *dnmnat* in knockouts, leads to spontaneous axon degeneration before cell body degeneration (Y. Fang et al., 2012; Neukomm et al., 2017). In zebrafish, overexpression of either WLD^S or *Nmnat2* results in a potent attenuation of axon death *in vivo* (Feng et al., 2010; Martin et al., 2010). Whether knockdown of *Nmnat2* also results in Wallerian-like degeneration remains to be determined. Taken together, levels of mammalian, fish and fly NMNAT2/*dNmnat* are crucial for axonal survival (Figure 3). It is important to note that any engineered version of stabilized NMNAT protein is capable of attenuating axon death in a variety of different models, e.g. WLD^S as non-nuclear NMNAT1, NMNAT1 that fails to localize to nuclei (e.g. cytosolic and axonal NMNAT1, cyt-NMNAT1 and ax-NMNAT1, respectively), NMNAT2 able to persist longer in axons,

Drosophila dnmnat over-expressed in cultured mouse dorsal root ganglia (DRG) or fly Johnston Organ (JO) neurons or mouse *Nmnat1* in *Drosophila* olfactory receptor neurons (ORNs) (Avery et al., 2009; Babetto et al., 2010; Feng et al., 2010; Milde, Gilley, et al., 2013; Paglione et al., 2020; Sasaki et al., 2009; Yan et al., 2010). Therefore, above-threshold levels of NMNAT2 or modified versions thereof ensure the survival of the axon, while sub-threshold levels trigger axon death.

- **NMNAT2/dNmnat localization**

NMNAT2 is predominantly found in the cytoplasm and axoplasm and is associated with membranes of Golgi-derived transport vesicles undergoing fast axonal transport (Gilley et al., 2013). Both the removal of the vesicle-association domain in NMNAT2 (Milde, Gilley, et al., 2013) and the modification of its residues required for palmitoylation (Summers et al., 2018) lead to increased NMNAT2 half-lives. Moreover, in mammals or flies, the overexpression of NMNAT3, predominantly found in mitochondria in mammals, potentially attenuates axon death (Avery et al., 2009; Sasaki et al., 2006). Therefore, the subcellular localization dictates the turnover of NMNAT proteins. By targeting them to different axonal compartments relative to endogenously localized NMNAT2, their turnover is reduced, which results in increased NMNAT protein half-lives, and ultimately in attenuated axon death.

- **NMNAT substrate: nicotinamide mononucleotide (NMN)**

Though NMN is naturally found in small amounts in fruits and vegetables such as broccoli, avocados, edamame, and cucumbers (Revollo et al., 2004), most of the NMN in mammals is synthesized from vitamin B3 in the form of nicotinamide (NAM) through nicotinamide phosphoribosyltransferase (NAMPT), an essential rate-limiting enzyme that catalyses the conversion from NAM to NMN (Mills et al., 2016). Another way of synthesising NMN—the only one in the case of *Drosophila* as they lack the NAMPT enzyme—is through nicotinamide riboside (NR) (Figure 4): NMN is cell-impermeable, thus, it needs to be converted extracellularly to NR first (Shade, 2020a). NR enters cells and is converted back to NMN by nicotinamide riboside kinase (NRK) (Ratajczak et al., 2016). More recently, the NMN transporter Slc12a8 was found to transport NMN directly into cells (Grozio et al., 2019; Wu & Sinclair, 2019) although it remains unclear which is the predominant way of bringing NMN into the cell. It also remains to be tested whether a *Drosophila* ortholog, *CG12773*, could have the same function in flies.

The attenuation of axon death signalling requires the NAD⁺ biosynthetic activity of NMNAT proteins (Avery et al., 2009; Martin et al., 2010; Sasaki et al., 2006; J. Wang et al., 2005; Yan et al., 2010). Metabolic aspects of NAD⁺ in neurodegeneration and axon death signalling have recently been comprehensively reviewed in (Sasaki, 2018). Importantly, genetic, and pharmacological modifications of NAD⁺ metabolism result in different levels of attenuation (Sasaki et al., 2016).

NMNAT proteins use either NMN or NaMN to generate NAD⁺ in an ATP-dependent manner (Figure 4). After injury, NMNAT protein levels drop, resulting in increased NMNAT substrates, (e.g., NaMN and/or NMN), and decreased NMNAT products (e.g., NAD⁺), but which one is crucial for axon death signalling?

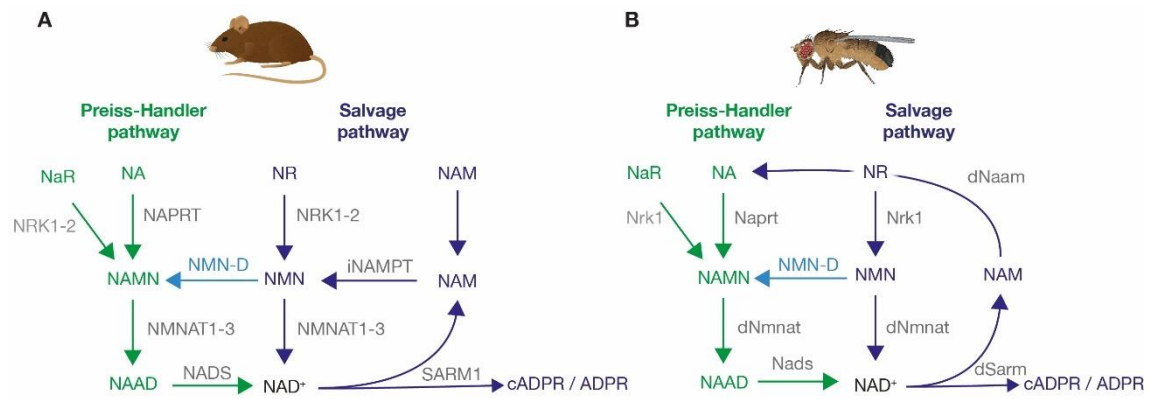


Figure 4. **A** mammalian NAD⁺ metabolic pathway. **B** *Drosophila* NAD⁺ metabolic pathway. In sky blue, NMN-Deamidase (NMN-D), a bacterial enzyme that can be expressed both in mammals and flies. Green, metabolites of the Preiss-Handler pathway; dark blue, metabolites of the salvage pathway; grey, enzymes, respectively. The *de novo* pathway is not shown. Adapted from Magdalena Kocia (unpublished).

While levels of NaMN seem to be negligible (Sasaki et al., 2016), levels of NMN are crucial: they temporally rise within 6 h after injury and seem to be an instructive signal (di Stefano et al., 2017; Figley et al., 2021; Loreto et al., 2015). Preventing this NMN rise results in long-term attenuation of axon death: either by the expression of WLD^S or modified NMNAT proteins that consume NMN to generate NAD⁺ or—interestingly—by the expression of a bacterial-specific enzyme, NMN-Deamidase (NMN-D) (Figure 4B), which consumes NMN but does not generate NAD⁺, both *in vitro* (di Stefano et al., 2015; Loreto et al., 2015; Sasaki et al., 2016) and *in vivo* (di Stefano et al., 2017, this study).

There is an alternative modification to keep NMN levels low in mammals: the pharmacological inhibition of NAMPT by FK866, either right before or immediately after injury, prevents the rise of NMN, which results in short-term to intermediate attenuation of axon death signalling (di Stefano et al., 2015; Sasaki et al., 2016).

In summary, distinct pharmacological or genetic manipulations that lead to lower levels of NMN also prevent axon death. Thus, the temporal rise of NMN after injury seems to be an instructive signal for axons to execute their destruction, at least in mammals. In flies, the role of NMN remains controversial as the lack of NAMPT (Gossmann et al., 2012) might cause NMN to have little or no role in the NAD⁺ biosynthetic pathway (Gerds et al., 2016). Additionally, the Gal4/UAS-mediated NMNd expression in *Drosophila* neurons preserves severed axons for 3–5 days after injury (Hsu et al., 2021) (see chapter 2 for more insights on this topic).

- **NMNAT product: nicotinamide adenine dinucleotide (NAD⁺)**

The involvement of NAD⁺ as a product of the biosynthetic activity of NMNAT proteins in axon death was observed right after the discovery of WLD^S: before or immediately after axonal injury, the exogenous supply of high levels of NAD⁺ leads to long-range attenuation of axon death signalling (Araki, 2004; J. Wang et al., 2005). Thus, axon death is triggered by NAD⁺ depletion in severed axons. Indeed, the estimated half-life of NAD⁺ by using isotope labelled NAD⁺ precursors is one hour in cultured HeLa cultured cells and 15 minutes to 15 hours in various mouse tissues, indicating the active nature of NAD⁺ consuming enzymes (Ichiyama et al., 1967; Rechsteiner et al., 1976; Sasaki et al., 2016). It is important to note that WLD^S or engineered NMNAT proteins do not generate higher levels of NAD⁺; they solely prevent the depletion thereof by a—yet

unknown—mechanism that inhibits an NAD⁺ consuming enzyme, which will be discussed further below (Gerdtts et al., 2013; Sasaki et al., 2016).

Wld^s got its foot in the door of axon death signalling and paved the way for several key discoveries related to NMNAT proteins. Levels and localization of the axonal survival factor NMNAT2/dNmnat are crucial for the survival or the degeneration of the axon. Its biosynthetic activity keeps levels of NMN as substrate low and prevents the depletion of NAD⁺ as the product (figure 3A).

Given the essential role of NMNAT proteins in axon death, an important question is how their turnover and half-life are regulated. What are the mechanisms regulating protein levels and therefore biosynthetic activity? Below, I will discuss the mechanisms crucial for NMNAT2 protein levels.

3) Atypical ubiquitin ligase complex

Following the cloning of *Wld^s* (Mack et al., 2001), the ubiquitin-proteasome system (UPS) was also found to be involved in the early stages of axon death (Q. Zhai et al., 2003). The subsequent discovery of NMNAT2 as a labile axon survival factor subjected to rapid turnover in axons (Gilley & Coleman, 2010), led to an attractive hypothesis: could the UPS be responsible for the rapid turnover of NMNAT2 in axons? The first evidence for the UPS system to be involved in axon death was found in *Drosophila*. The E3 ubiquitin ligase Highwire (Hiw) regulates the turnover of dNmnat (Neukomm et al., 2014; Xiong et al., 2012). Likewise, the mammalian homologue PAM/Highwire/RPM-1 (PHR1) also fine-tunes levels of NMNAT2 (Babetto et al., 2013). PHR1 belongs to an evolutionarily conserved, atypical SKP/Cullin/F-box (SCF)-type E3 ubiquitin ligase complex consisting of S-phase kinase-associated protein 1A (SKIP1A), PHR1 and F-box protein 45 (FBXO45) (Babetto et al., 2013; Yamagishi & Tessier-Lavigne, 2016). This atypical SCF complex regulates—through polyubiquitination and the proteasome—levels of NMNAT2, by explicitly targeting axoplasmic NMNAT2 for destruction (Desbois et al., 2018; Summers et al., 2018). The removal of either component slows down the turnover of NMNAT2, which results in attenuated axon death signalling (Figure 3A).

4) MAPK signalling

The mitogen-activated protein kinase (MAPK) signalling pathway is also involved in axon death signalling. It is activated within 5 min after axonal injury and culminates in the phosphorylation of c-Jun N-terminal kinases (JNKs): loss-of-function analyses revealed that a partially redundant MAPK cascade is required to execute the degeneration of axons after injury (e.g. MKK4, MLK, DLK, MKK4/7, JNK1/3, and SCG10) (Miller et al., 2009; Shin et al., 2012; Summers et al., 2018; Walker et al., 2017; Yang et al., 2015). The MAPK cascade limits levels of Nmnat2 by selectively degrading membrane-associated, palmitoylated NMNAT2 (Summers et al., 2018; Walker et al., 2017).

Interestingly, NMNAT2 levels are differentially regulated. MAPK signalling and the atypical ubiquitin ligase complex are essential for fine-tuning NMNAT2 levels. While MAPK signalling targets membrane-associated NMNAT2, the atypical ubiquitin ligase complex selectively degrades axoplasmic NMNAT2 (Milde, Fox, et al., 2013; Summers et al., 2018). The pharmacological inhibition of both mechanisms results in a substantial attenuation of axon

death signalling (Summers et al., 2018). This suggests that distinct axonal pools of NMNAT2 are differentially regulated (Figure 3A).

The above discoveries revealed a central and conserved function for NMNAT2/dNmnat. Levels of the labile axonal survival factor are dictated by three branches (Figure 3A): (i) continuous supply of NMNAT proteins by axonal transport, (ii) constant degradation of vesicle-bound NMNAT proteins by the MAPK pathway, and (iii) constant degradation of soluble NMNAT proteins by the atypical ubiquitin ligase complex.

In healthy uninjured axons, NMNAT protein levels are above threshold, ensuring low NMN and high NAD⁺ levels. *Vice versa*, the supply of NMNAT proteins by axonal transport is abrogated in injured axons. Therefore, NMNAT protein degradation by the MAPK pathway and the atypical ubiquitin ligase complex takes over. This results in below-threshold levels of NMNAT proteins. Likewise, levels of NMN temporally rise, whereas NAD⁺ levels drop.

So far, the execution of axon death signalling is solely initiated by below-threshold levels of NMNAT proteins. Any modification that sustains levels of NMNAT proteins—e.g., gain of NMNAT stability or loss of NMNAT protein degradation—ultimately attenuates axon death.

At this point, no mediator in axon death signalling had been identified that actively contributes to signalling, e.g., where loss-of-function mutations result in attenuated axon death signalling regardless of NMNAT protein levels. Below, I will discuss such mediators.

5) SARM1/dSarm

The first discovery of a loss-of-function mutation that attenuates axon death irrespective of NMNAT levels was made in *Drosophila*: through an unbiased forward-genetic screen for axon death defective mutants, several loss-of-function alleles of the gene *Drosophila* sterile alpha and armadillo motif (*dsarm*) were isolated (Figure 3). Mutations in *dsarm* block axon death for the life span of the fly (Osterloh et al., 2012), *dsarm* is therefore essential for injury-induced axon degeneration. Similarly, mutants or downregulation of the mammalian homologue *Sarm1* (also known as Ect4 or Myd88-5) harbour a potent attenuation of axon death signalling *in vitro* and *in vivo* (Gerdtts et al., 2013, 2015; Gilley et al., 2015; Osterloh et al., 2012). SARM1/dSarm is a toll-like receptor adaptor family member and is mainly expressed in the nervous system (Osterloh et al., 2012). Yet, it also functions in glial cells (McLaughlin et al., 2019), and the immune system (Panneerselvam et al., 2013).

SARM1/dSarm contains three evolutionarily conserved protein domains: an Armadillo/HEAT (ARM), a sterile alpha motif (SAM) (two in mammals and one in flies) and a Toll/interleukin-1 receptor homology (TIR) domain (Gerdtts et al., 2013; Osterloh et al., 2012). All three domains are essential for SARM1 function in mice (Gerdtts et al., 2013, 2015; Walker et al., 2017) and dSarm in *Drosophila* (Neukomm et al., 2017). The ARM domain keeps SARM1/dSarm inactive by the interaction of the N-terminal ARM domain with the C-terminal TIR domain, as previously reported in the *C. elegans* homologue TIR-1 (Chuang & Bargmann, 2005), and the SAM domain is necessary for SARM1 dimerisation (Gerdtts et al., 2015; Yang et al., 2015). After injury, an instructive signal leads to dimerization of the TIR domain, and consequently to the activation of SARM1 /Sarm1 (Gerdtts et al., 2013). Rather than harbouring signalling activity, the TIR domain contains an enzymatic activity to trigger rapid depletion of NAD⁺ (NADase activity) (Essuman et

al., 2017; Gerdts et al., 2015; Sasaki et al., 2016). This was further demonstrated with a point mutation in the catalytic site (E642A) that rendered the NADase inactive and eliminated the prodegenerative function of SARM1 (Essuman et al., 2017). Deletion of the auto-inhibitory ARM domain of SARM1 (dSarm^{ΔARM}) in flies (Neukomm et al., 2017) or mice (Gerdts et al., 2013) resulted in spontaneous axon degeneration (e.g. in the absence of injury) demonstrating that SARM1 is necessary and sufficient for axon degeneration. Importantly, the TIR domain NADase activity is evolutionarily conserved across flies, zebrafish and mice, where it cleaves NAD⁺ into NAM and ADP-ribose (ADPR) or cyclic ADPR (cADPR) with species-specific differences (Essuman et al., 2017). These findings support a model where, upon injury, SARM1/dSarm is activated and actively depletes NAD⁺ levels in severed axons. Therefore, SARM1/dSarm plays a central role in NAD⁺ depletion in severed axons after injury.

Recently, the crystal structure of the SARM1 was determined in different configurations, providing unprecedented insight into the structure of the protein based on isolated domains and full-length inactive SARM1 (Bratkowski et al., 2020; Figley et al., 2021; Jiang et al., 2020; Shi et al., 2022; Sporny et al., 2019). SARM1 is a pre-assembled octamer already in its inactive state (Figure 5) (Bratkowski et al., 2020). The enzyme can rapidly transition from an inactive to an active state upon injury. To keep SARM1 inactive, an ARM-TIR lock ensures that the TIR domains stay spatially separate to avoid NAD⁺ hydrolase activity. Consequently, the release of this lock happens through the ARM domain, as mutations in critical residues of the ARM domain are sufficient to allow the switch from inactive to catalytically active forms (Bratkowski et al., 2020; Sporny et al., 2019). The crystal structure of SARM1 has revealed more findings that will be further discussed in the following sections.

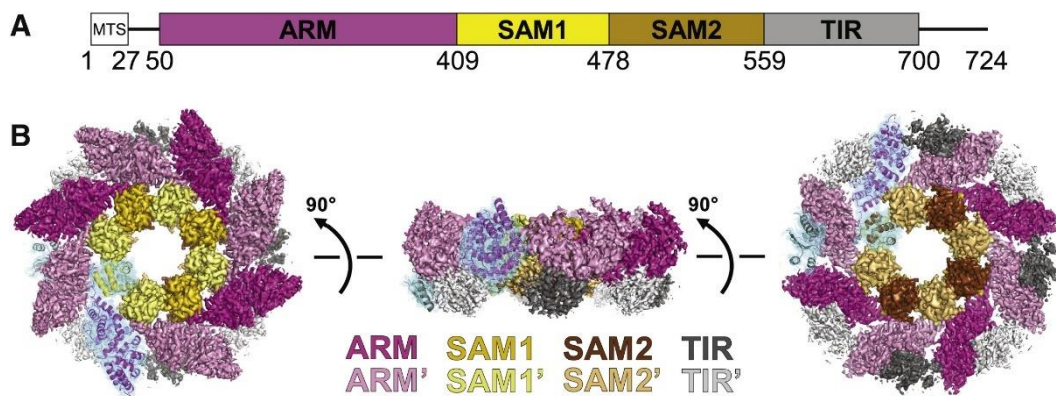


Figure 5. SARM1 domains and crystal structure. **A** Linear scheme of SARM1 domains, colour coded and with the amino acid numbers indicated. MTS, mitochondrial translocation sequence. **B** Cryo-EM map of SARM1. Prime (') labels are used to differentiate different copies of the same domain, and domains are colour coded with alternating dark (non-prime domains) and light (prime domains) shades: ARM (pink), SAM1 (yellow), SAM2 (brown), and TIR (grey). One monomer is shown as a cartoon representation enclosed by map density (cyan mesh) to better represent the path of the protein chain. Adapted from (Bratkowski et al., 2020).

6) Axundead

Recently, another essential mediator of axon death signalling has been identified in *Drosophila*. Several *axundead* (*axed*) mutants were isolated by another unbiased forward-genetic screen (Neukomm et al., 2017). Like *highwire* and *dsarm* mutants, mutations in *axed* attenuate axon death signalling for the lifespan of the fly (Figure 3B) (Neukomm et al., 2014, 2017; Osterloh et al., 2012). The *axed* gene consists of two isoforms (*axed^{long}* and *axed^{short}*), and both can rescue

axed mutants. Axed proteins are predominantly found in axons and synapses. Their levels increase 4–6 h post axotomy and return to baseline 24 h after injury, suggesting either a transient change in localization and/or levels in response to axonal injury. Axed contains two evolutionarily conserved domains: a BTB and a BACK domain, which suggests that Axed could dimerize and/or interact with Cullin ubiquitin ligases (Stogios & Privé, 2004). There are four mammalian paralogues (BTBD1, BTBD2, BTBD3, BTBD6), and it remains to be determined which paralogue(s) could have an active role in axon death in mammals (Neukomm et al., 2017). It has recently been described that SARM1 can interact with all four paralogues of Axed in mammals, in cultured NSC-34 cells. In addition, BTBD3 and BTBD6 were found at higher levels in a mouse model of Charcot-Marie-Tooth disease. Additionally, the knockdown of BTBD3 or BTBD6 delayed cell death triggered by a constitutively active SARM1 protein (Schmidt, 2020). Nevertheless, the precise mechanistic function of Axed remains currently unknown.

7) Calpains and Calpastatin

Calpains have recently been shown to be involved in axon death signalling (Figure 3A) (Yang et al., 2015). Calpains are Ca^{2+} -dependent non-lysosomal proteases, and they are involved in neuronal degeneration in TBI, cerebral ischaemia and AD (Saatman et al., 2010). Among the 15 mammalian isoforms, Calpain-1 and Calpain-2 are ubiquitously expressed, predominantly in the brain, and are present in both neurons and glia (Macqueen & Wilcox, 2014). Within minutes after experimental traumatic axonal injury (TAI), axonal Calpain activity is elevated (Büki et al., 1999). Vice versa, mice lacking Calpain-1/2 show a significant delay in axon death compared with wild-type mice (Yang et al., 2015).

Calpastatin is an inhibitor of Calpains *in vivo*. After axonal injury, levels of Calpastatin drop within 10 h, which correlates with the morphological degeneration of axons (Yang et al., 2013). In contrast, transgenic mice expressing human Calpastatin harbour robust attenuation of axon death in transected optic nerves in the CNS and sciatic nerves in the PNS (Ma et al., 2013).

Calpastatin-mediated regulation of Calpains is likely the most downstream cascade of axon death signalling. However, the mechanistic link between the above mediators of axon death signalling and Calpains in mammals, and whether Calpains are also involved in other species, remains to be determined.

VI. Advantages of different animal models

Flies harbour the unique advantage of unbiased forward-genetic screens. Axon death can easily be assessed *in vivo* in several neurons such as antennal or maxillary palp ablation, wing injuries, and during larval development by nerve crush (Rooney & Freeman, 2014). Moreover, by the use of optogenetics, the functional preservation of axons and their synapses can readily be assessed by a simple grooming assay (Hampel et al., 2015; Paglione et al., 2020).

Mice are frequently used for both *in vitro* and *in vivo* axon death assays: *in vitro* cultured neurons from superior cell ganglia (SCGs) and DRGs from the PNS, and retinal ganglion cells (RGCs) from the CNS, are subjected to axon death assays. Moreover, pharmacogenetic manipulation of metabolism can also be applied *in vitro*. Broadly used *in vivo* assays are optic nerve injuries (CNS) and sciatic nerve lesions (PNS).

Rats facilitate stereotaxic injections because of their larger brains, and lesions of optic or facial nerves and nerve roots can also be readily performed. Moreover, nerves are longer than those in mice, putting them closer to human axons, although human axons can still be 10-fold longer than their rat counterparts (Adalbert et al., 2005, 2012). Rats also provide more abundant sources of tissue for biochemical and proteomic studies.

Zebrafish provides a significant advantage with its powerful *in vivo* live imaging, as the complete time course of axon death, with the resolution of single axons, can readily be observed. It is important to mention that zebrafish offer the unique ability to visualize temporal Ca^{2+} events *in vivo*.

VII. Commonalities and differences across species

Genetic analyses in the above animal systems provided important insights over recent years. These findings led to the definition of an axon death signalling pathway. It is tempting to combine all analyses to define a core signalling cascade across multiple species. Yet these analyses also revealed subtle differences that should not be neglected. Below, I will highlight common features and species-specific axon death signalling differences among mice, flies and fish.

1) Conserved mediators

Ca^{2+} plays a crucial role in all model systems tested so far. Both Ca^{2+} entry into the axon after injury (first, rapid short-term Ca^{2+} wave) and the Ca^{2+} release from intracellular stores at the end of the lag phase (second, long-term Ca^{2+} wave) have been observed across multiple species. It is therefore likely that the first conserved mediator of axon death signalling is Ca^{2+} influx into severed axons.

NMNAT2/dNmnat in mice, fish and flies harbour an evolutionary conserved feature. As a labile axon survival factor, levels of NMNAT proteins matter: high or robust levels potentially protect severed axons from undergoing axon death, and low levels induce axon degeneration in all species tested (Y. Fang et al., 2012; Feng et al., 2010; Gilley & Coleman, 2010; Martin et al., 2010). Alongside NMNAT, its biosynthetic NAD^+ activity is also conserved across species.

Atypical ubiquitin ligase complex members, which regulate NMNAT protein levels, are conserved in mice and flies (SKIP1A, PHR1, FBXO45 in mice, and Hiw1 in flies). Interestingly, while the MAPK pathway plays a vital role in mice, it seems negligible in flies (Neukomm et al., 2017). Whether the fish homologues of the atypical ubiquitin ligase complex and the MAPK signalling cascade similarly regulate levels of NMNAT2 remains elusive.

The function of the dSarm/SARM1 homologues in flies and mice, and Sarm1 in fish (Tian et al., 2018), is also evolutionarily conserved. Loss-of-function mutants block axon death signalling, and the TIR domain of these species harbours the ability to pathologically degrade NAD^+ to produce Nam and ADPR or cADPR (Essuman et al., 2017).

It is equally important to note that species-specific pathway analyses revealed some remarkable differences. It indicates that we are far from fully understanding axon death signalling mechanisms. Below, I will briefly discuss these differences.

2) Differences across species

Mice lacking *Nmnat2* contain truncated axons during embryogenesis and die perinatally (Gilley et al., 2013). This lethality is partially rescued by the overexpression of *Wld^S*, and entirely by *Sarm1*^{-/-} mutants (Gilley et al., 2017). Therefore, SARM1 executes axon death following below-threshold levels of NMNAT2. SARM1 likely acts downstream of NMNAT2 (Figure 3A).

As mentioned, *Nmnat2*^{-/-} mice contain truncated axons during embryogenesis and die perinatally (Gilley et al., 2013). *Wld^S* mice and *Sarm1*^{-/-} are not the only candidates able to rescue both: surprisingly, the expression of the bacterial NMN-D does the same in a dosage-dependent manner (di Stefano et al., 2017). This finding suggests that, besides the pathological NAD⁺ consumption of SARM1, the temporal rise of NMN is also crucial for axon death signalling, after NMNAT2 has disappeared in severed axons (Figure 3A).

In flies, sensory neurons mutant for the sole *dnmnat* gene undergo rapid neurodegeneration, which, unlike in mammals, is not blocked by *dsarm*, but by *axed* mutants (Neukomm et al., 2017). These findings imply that neurodegeneration induced by below-threshold levels of dNmnat is not executed by dSarm, but by Axed. Similarly, axon and neurodegeneration induced by the expression of a constitutively active NADase version of dSarm lacking the inhibitory ARM domain (dSarm^{ΔARM}), which promotes rapid NAD⁺ depletion, is blocked by *axed* mutants. It suggests that Axed is also downstream of dSarm. Finally, axon and neurodegeneration induced together by *dnmnat* mutants and dSarm^{ΔARM} expression is also blocked by *axed* mutants, suggesting that axon death signalling converges on Axed to execute the disassembly of the axon (Figure 3B) (Neukomm et al., 2017).

In fish, axon death is attenuated by the overexpression of *Nmnat2* and *Wld^S* (Feng et al., 2010; Martin et al., 2010). Moreover, loss of *Sarm1* also attenuates axon death, suggesting that its function is conserved in fish (Tian et al., 2018). However, it remains to be seen whether below-threshold levels of *Nmnat2* are sufficient to trigger axon degeneration. Last but not least, the genetic interaction among Ca²⁺, NAMPT2 and SARM1 remains to be determined (Figure 3C).

Above, I have summarized conserved axon death mediators and I highlighted differences observed across species. Despite these subtle differences, it is tempting to extract a core axon death mechanism that could be evolutionarily conserved. It will be discussed below.

3) The axon degeneration instructive signal

When we wrote a review in 2019 (Llobet Rosell & Neukomm, 2019), very little was known about the initiation factor, the instructive trigger that would activate the axon dead signalling pathway to execute axon degeneration. We were left with speculations and wrote a whole paragraph about it. Within 4 years, the field has advanced a lot in that direction, and we are closer to answering the question “why and how do axons execute their disassembly?” than we were four years ago.

Currently, SARM1 appears as a central executioner of axon degeneration. The ratio between NMN and NAD⁺ seems to be crucial: under normal, healthy conditions, the ratio between NMN and NAD⁺ is highly in favour of NAD⁺ (NMN << NAD⁺), which is supported by the observation of lower axonal concentrations of NMN and higher concentrations of NAD⁺ (Figure 3A) (di Stefano

et al., 2015; Figley et al., 2021; Gilley et al., 2015; Sasaki et al., 2016, this study). Upon axonal injury, the survival factor NMNAT2 in the distal axon sharply declines due to its short half-life and lack of supply from the cell body (Gilley & Coleman, 2010) leading to a temporal accumulation of NMN. In addition, the NAD^+ *de novo* synthesis is halted, thus reducing the ratio ($\text{NMN} < \text{NAD}^+$). Below-threshold levels of NMNAT2 also fail to provide NMNAT2-mediated inhibition of SARM1, which gets activated and discharges the NADase activity, tipping the ratio even more towards NMN ($\text{NMN} \gg \text{NAD}^+$) (Figure 6) (di Stefano et al., 2015; Loreto et al., 2015).

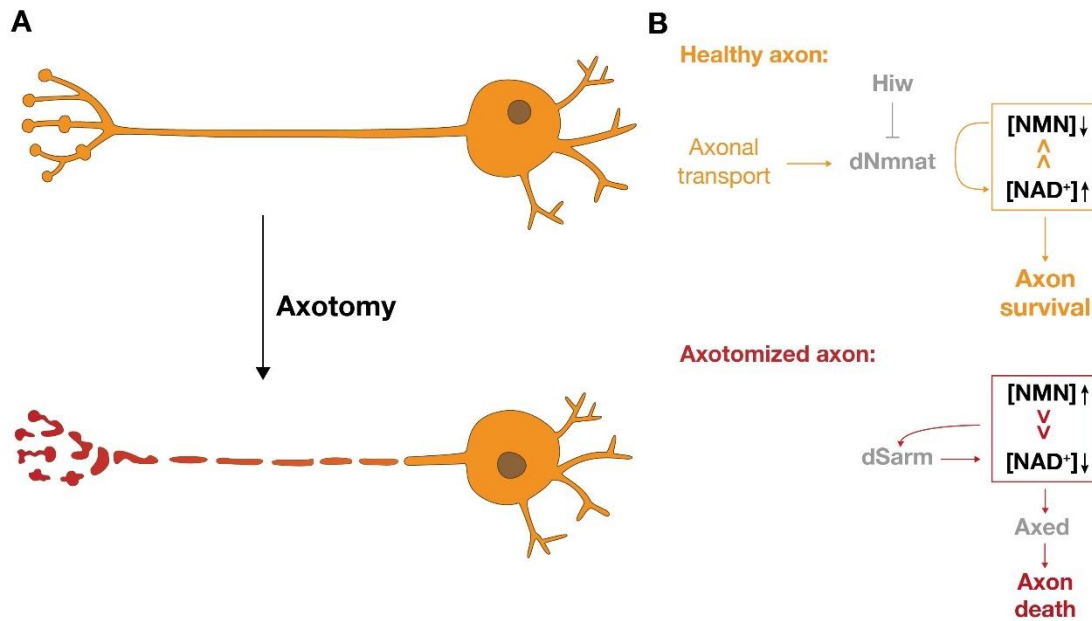


Figure 6. The ratio between NMN and NAD^+ is crucial in *Drosophila*. **A** Axons degenerate within one day after injury (axotomy) in normal conditions. **B** In healthy conditions (e.g., in the absence of axotomy), the ratio is highly in favour of NAD^+ . Upon axonal injury, the ratio dramatically shifts towards NMN, activating the signalling pathway to trigger axon degeneration.

As explained above, the accomplishment of elucidating the crystal structure of SARM1 led to the identification of the ARM-TIR lock. It also led to the identification of an allosteric pocket in SARM1 distant from the ARM-TIR lock site, but still in the ARM domain, that was shown to bind both NAD^+ and NMN (Figley et al., 2021; Jiang et al., 2020) suggesting that NAD^+ and NMN regulate SARM1 activity by binding in a competitive fashion to the ARM domain: in physiological conditions, NAD^+ is present in higher levels compared to NMN, thus NAD^+ would bind to the allosteric pocket keeping Sarm1 inactive; upon injury, the temporal accumulation of NMN results in replacement of the NAD^+ for NMN in the allosteric pocket and subsequently activate SARM1 to trigger axon degeneration. While these observations are essential, it remains unknown whether these structural observations can be reconciled *in vivo*.

VIII. Axon death signalling in disease

Mutations in human *Nmnat2* have been linked to foetal akinesia deformation sequence (FADS), and childhood-onset polyneuropathy and erythromelalgia (Huppke et al., 2019; Lukacs et al., 2019). These discoveries provide the first direct molecular evidence that axon death in WD is involved in a human axonal disorder. They support the idea that axonopathies are a major

contributor to certain human neurodegenerative diseases (Burke & O'Malley, 2013; Flatters et al., 2017; Hill et al., 2016; Vickers et al., 2009).

Wld^S and its capacity to slow down injury-induced axon degeneration offered the first opportunity to attenuate axonopathies in the absence of injury. Over recent years, distinct outcomes have been observed in a broad range of disease models, including extended life span, age-dependent effects, improved performance, or a lack of amelioration (Conforti et al., 2014). The promising neuroprotective function of Wld^S also led to the development of drugs to stabilize NMNAT proteins (Ali et al., 2017). However, while the efficacy of Wld^S or any other form of engineered NMNAT seems promising in specific models of neurological conditions, its therapeutic potential may be limited due to a gain-of-function protein: its efficacy relies on dosage, which could be challenging during long-term treatments (Mack et al., 2001). Moreover, Wld^S harbours age-dependent effects (Ferri et al., 2003), and while it can slow down axon death, it cannot entirely block it (Gilley et al., 2017). Therefore, alternative or complementary approaches would increase the chance of ameliorating axonopathies.

The manipulation of the NMN/NAD⁺ ratio could offer an attractive alternative. It could be achieved by pharmacological targeting of specific metabolic pathways, or by a simple oral supplement of NAD⁺ or its precursors. Preventing either NAD⁺ consumption or a temporal rise of NMN could serve as attractive strategies (Kaneko, 2006; Meyer zu Horste et al., 2011). However, without any specificity toward neuronal tissue, manipulating NAD⁺ metabolism also bears significant risks (Yaku et al., 2018).

The discovery of SARM1/dSarm has offered a novel and unique therapeutic opportunity. To block axon death signalling, SARM1 protein or its activity has to be decreased, rather than increased such as with NMNAT2. Like Wld^S, *Sarm1*^{-/-} mice offer a range of outcomes in mouse models of neurological conditions:

When axons are challenged by mechanical forces, *Sarm1*^{-/-} mice harbour reduced neurological deficits and a better functional outcome in a model of TBI (Henninger et al., 2016). *Sarm1*^{-/-} mice also contain significantly reduced axonal lesions in a model of TBI with impact acceleration of heads (Ziogas & Koliatsos, 2018). In addition, an *in vivo* gene therapy approach using an adeno-associated virus to deliver a dominant-negative version of SARM1 had similar effects in an injury-induced axon degeneration model to that in *Sarm1*^{-/-} mice (Geisler et al., 2019). These findings strongly suggest that SARM1 serves as a promising therapeutic target to ameliorate force-induced axonopathies.

In two models of CIPN (e.g., vincristine or paclitaxel), and metabolic-induced peripheral neuropathy, mice lacking *Sarm1* prevent the distal degeneration of myelinated axons and electrophysiological abnormalities (Geisler et al., 2016; Turkiew et al., 2017). These findings fuel hope that axonopathies caused by chemotherapy or by diabetes—the most common causes of peripheral neuropathies (Grisold et al., 2012; Juster-Switlyk & Smith, 2016)—could also be therapeutically targeted in patients to delay the progression of peripheral neuropathy, or even to prevent the neuronal injury from starting.

However, while SARM1 harbours the potential to ameliorate certain axonopathies, it is important to note that the lack of *Sarm1* does not suppress motor neuron degeneration in a mouse model of ALS (Peters et al., 2018), although some SARM1 variants were found to be

enriched in ALS patients (Bloom et al., 2022). It remains to be determined whether SARM1 is dispensable in other ALS mouse models.

So far, *Sarm1*^{-/-} mutants have beneficial effects in specific models of neurological conditions. It raises hope that SARM1 and other axon death mediators could serve as druggable targets to halt axon loss. Axon death signalling is an attractive pathway to develop therapies against, with the ultimate goal to prevent and treat axon loss in a broad range of neurological diseases.

SUMMARY OF AIMS AND GENERAL SCOPE OF THE THESIS

This thesis aims to better understand how injury-induced axon degeneration is mechanistically regulated and executed. For the reasons provided in the introduction, I ultimately hypothesised that the accumulation of NMN is the instructive signal *in vivo* in *Drosophila*. After injury, the accumulation of NMN should activate the axon death signalling pathway that executes axon degeneration (Chapters 3, 4). Additionally, I also sought to investigate the interacting proteins of Axed to better understand its mechanistic function in the axon death signalling pathway downstream of NAD⁺ depletion (Chapter 7).

To investigate the above hypotheses, I used cutting-edge *Drosophila* methods to investigate axon death genes that are required for the signalling pathway and the modulation of the NAD⁺ metabolic pathway. These techniques include the observation of injured axons in different sets of sensory neurons side-by-side with uninjured control axons to assess the morphological phenotype of the injured axons. They further facilitate the use of optogenetics to activate neurons—or severed axons—required and sufficient to perform antennal grooming as a read-out for circuit integrity (Chapter 2). Lastly, I used transfected *Drosophila* cultured cells to massively express and purify proteins of interest to subsequently analyse them for their NADase activity (Chapter 3), or purified proteins of interest from *Drosophila* fly heads to subject them to mass spectrometry to find new candidate interactors of Axed, among others (Chapter 7).

In addition, I contributed to two research articles as co-author, where I performed wing injuries to a set of different dSarm constructs (Chapter 5) and brain dissections to be analysed by a new 3D high-resolution microscope (Chapter 6).

Because axon death signalling is evolutionarily conserved across evolution, and not only activated after injury but also in a broad range of neurological diseases, it is of crucial interest to further understand the axon death mediators as well as to fill the missing gaps between them. My research could be of interest to discover novel therapeutical targets for a broad range of human axonopathies.

CHAPTER 2

Observation and analysis of axon death in injured neurons of *Drosophila melanogaster*



Tools to perform injuries and brain dissections (tweezers, micro scissors, slides, coverslips, and halocarbon oil).

1.1 Summary of the results

In this study, we described three protocols designed in the lab that can be used in the fly to explore injury-induced axon degeneration as well as functional loss of axons, dendrites and synapses: 1) the wing injury helps to observe the morphology of axon degeneration side by side with uninjured control axons in the same wing; 2) the antennal ablation assay removes the cell bodies of the olfactory receptor neurons (ORN) to study the morphology of the axon degeneration in the brain; and 3) grooming induced by optogenetics serves as a readout for synapse integrity before and after axonal injury of Johnston Organ (JO) neurons, that are required and sufficient for antennal grooming in flies. Representative results for each experiment are shown, including unpublished results (Figure 6), where we show for the first time that overexpression of dNmnat in the JO neurons (e.g., *dnmnat^{OE}*) leads to a preserved potent grooming behaviour 7 days after injury; in other words, the synapses of injured neurons overexpressing dNmnat remain circuit-integrated 1 week after injury (Paglione et al., 2020).

1.2 Personal contribution

In this study, I performed and analysed the experiments focused on the morphology of the axons (e.g., wing injury and antennal ablation of the ORNs). Together with Maria Paglione, Jean-Yves Chatton and Lukas Neukomm, we designed the experiments and wrote the manuscript and the script for the video (Paglione et al., 2020).

Video Article

Morphological and Functional Evaluation of Axons and their Synapses during Axon Death in *Drosophila melanogaster*

Maria Paglione^{*1}, Arnau Llobet Rosell^{*1}, Jean-Yves Chatton¹, Lukas J. Neukomm¹¹Department of Fundamental Neurosciences, University of Lausanne^{*}These authors contributed equallyCorrespondence to: Lukas J. Neukomm at lukas.neukomm@unil.chURL: <https://www.jove.com/video/60865>DOI: [doi:10.3791/60865](https://doi.org/10.3791/60865)Keywords: Neuroscience, Issue 157, *Drosophila*, Neurobiology, Wallerian Degeneration, injury-induced axon degeneration, axon death, genetics, optogenetics, behavior, microscopy, fluorescence

Date Published: 3/16/2020

Citation: Paglione, M., Rosell, A.L., Chatton, J.Y., Neukomm, L.J. Morphological and Functional Evaluation of Axons and their Synapses during Axon Death in *Drosophila melanogaster*. *J. Vis. Exp.* (157), e60865, doi:10.3791/60865 (2020).

Abstract

Axon degeneration is a shared feature in neurodegenerative disease and when nervous systems are challenged by mechanical or chemical forces. However, our understanding of the molecular mechanisms underlying axon degeneration remains limited. Injury-induced axon degeneration serves as a simple model to study how severed axons execute their own disassembly (axon death). Over recent years, an evolutionarily conserved axon death signaling cascade has been identified from flies to mammals, which is required for the separated axon to degenerate after injury. Conversely, attenuated axon death signaling results in morphological and functional preservation of severed axons and their synapses. Here, we present three simple and recently developed protocols that allow for the observation of axonal morphology, or axonal and synaptic function of severed axons that have been cut-off from the neuronal cell body, in the fruit fly *Drosophila*. Morphology can be observed in the wing, where a partial injury results in axon death side-by-side of uninjured control axons within the same nerve bundle. Alternatively, axonal morphology can also be observed in the brain, where the whole nerve bundle undergoes axon death triggered by antennal ablation. Functional preservation of severed axons and their synapses can be assessed by a simple optogenetic approach coupled with a post-synaptic grooming behavior. We present examples using a *highwire* loss-of-function mutation and by over-expressing *dnmnat*, both capable of delaying axon death for weeks to months. Importantly, these protocols can be used beyond injury; they facilitate the characterization of neuronal maintenance factors, axonal transport, and axonal mitochondria.

Video Link

The video component of this article can be found at <https://www.jove.com/video/60865/>

Introduction

The morphological integrity of neurons is essential for sustained nervous system function throughout life. The vast majority of the neuronal volume is taken by axons^{1,2}; thus life-long maintenance of particularly long axons is a major biological and bioenergetic challenge for the nervous system. Multiple axonal-intrinsic and glial-extrinsic support mechanisms have been identified, ensuring life-long axonal survival. Their impairment results in axon degeneration³, which is a common feature of nervous systems being challenged in disease, and by mechanical or chemical forces^{4,5}. However, the underlying molecular mechanisms of axon degeneration remain poorly understood in any context, making the development of efficacious treatments to block axon loss challenging. The development of effective therapies against these neurological conditions is important, as they create an enormous burden in our society⁶.

Injury-induced axon degeneration serves as a simple model to study how severed axons execute their own disassembly. Discovered by and named after Augustus Waller in 1850, Wallerian degeneration (WD) is an umbrella term that comprises two distinct, molecularly separable processes⁷. First, after axonal injury, axons separated from their cell bodies actively execute their own self-destruction (axon death) through an evolutionarily conserved axon death signaling cascade within one day after injury⁸. Second, surrounding glia and specialized phagocytes engage and clear the resulting axonal debris within three to five days. The attenuation of axon death signaling results in severed axons that remain preserved for weeks^{9,10,11,12}, while the attenuation of glial engulfment culminates in axonal debris which persists for weeks in vivo^{13,14,15}.

Research in flies, mice, rats and zebrafish revealed several evolutionarily conserved and essential mediators of axon death signaling⁸. Axon death mutants contain severed axons and synapses that fail to undergo axon death; they remain morphologically and functionally preserved for weeks, in the absence of cell body support^{9,10,12,13,16,17,18,19,20,21,22,23}. The discovery and characterization of these mediators led to the definition of a molecular pathway executing axon death. Importantly, axon death signaling is activated not only when the axon is cut, crushed or stretched^{24,25}; it also seems to be a contributor in distinct animal models of neurological conditions (e.g., where axons degenerate in an injury-independent manner⁴, yet with a range of beneficial outcomes^{4,8}). Therefore, understanding how axon death executes axon degeneration after injury might offer insights beyond a simple injury model; it could also provide targets for therapeutic intervention.

The fruit fly *Drosophila melanogaster* (*Drosophila*) has proven to be an invaluable system for axon death signaling. Research in the fly revealed four essential evolutionarily conserved axon death genes: *highwire* (*hiw*)^{11,14}, *dnmnat*^{12,26}, *dsarm*¹⁰ and *axundead* (*axed*)¹². The modification of these mediators — loss-of-function mutations of *hiw*, *dsarm* and *axed*, and over-expression of *dnmnat* — potentially blocks axon death for the life span of the fly. While severed wild type axons undergo axon death within 1 day, severed axons and their synapses lacking *hiw*, *dsarm* or *axed* remain not only morphologically, but also functionally preserved for weeks. Whether functional preservation can also be achieved through high levels of *dnmnat* remains to be determined.

Here, we will present three simple and recently developed protocols to study axon death (e.g., the morphology and function of severed axons and their synapses over time) in the absence of cell body support. We demonstrate how attenuated axon death results in severed axons which are morphologically preserved with a *hiw* loss-of-function mutation (*hiw*^{ΔN}) and how attenuated axon death results in severed axons and synapses that remain functionally preserved for at least 7 days with over-expression of *dnmnat* (*dnmnat*^{OE}). These protocols allow for the observation of individual axonal and synaptic morphology either in the central, or peripheral nervous system (CNS and PNS, respectively)^{13,14}, while the functional preservation of severed axons and their synapses in the CNS can be visualized by the use of a simple optogenetic setup combined with grooming as a behavioral readout¹².

Protocol

1. Observation of Axon Morphology During Axon Death in the PNS

1. Wing injury: partial injury of axon bundles
 1. Use 5 virgin females and 5 males from the right genotype (**Figure 4A**, P₀ generation) to perform crosses at room temperature (RT). Pass P₀ into new vials every 3–4 days. Collect freshly eclosed adult progeny (F₁ generation) daily and age them for 7–14 days.
 2. Anesthetize flies on CO₂ pads. Use micro scissors to cut the anterior wing vein roughly in the middle of the wing (**Figure 1A**). Use one wing for the injury and the other wing as an age-matched uninjured control. Apply one injury per wing, and make sure to get sufficient wings injured (approximately 15 wings).
NOTE: The whole wing can be cut through, but it is sufficient to cut only the anterior wing vein. This is the strongest part of the wing.
 3. Recover the flies in food-containing vials.
2. Wing dissection and visualization of axons
 1. Spread 10 μL of halocarbon oil 27 with a pipette along a whole glass slide (**Figure 1B**).
 2. Cut off the injured, as well as, the uninjured control wing at desired time points (e.g., 1 or 7 days post injury). Use micro scissors to cut, and tweezers to grab the wing. Mount maximal 4 wings into halocarbon oil 27 (**Figure 1B**) and cover them with a cover slide.
 3. Image the wing immediately using a spinning disk microscope. Acquire a series of optical sections along the z-axis with 0.33 μm step-size and compress z-stacks into a single file for subsequent analyses.
NOTE: Do not grab the anterior wing vein where cell bodies and axons are housed. Grab the wing at the center. The tissue in wings is not fixed; keep the time from mounting wings to imaging these under 8 min.

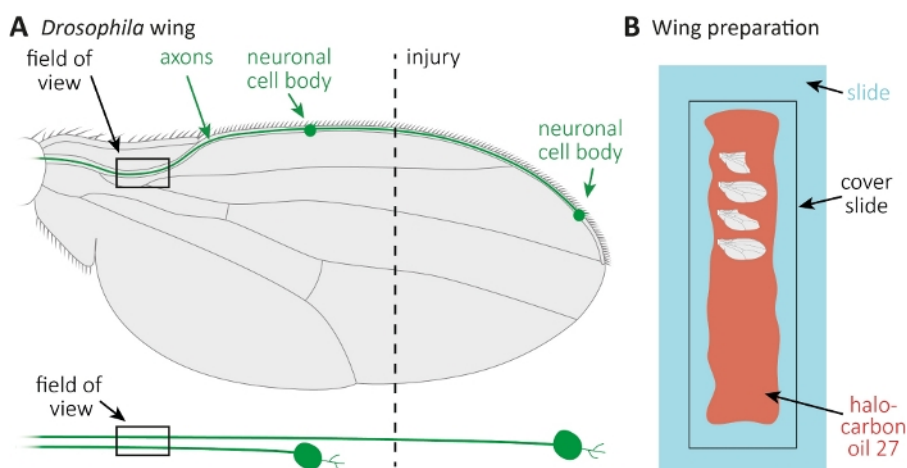


Figure 1: Observation of axon morphology during axon death in the wing. (A) Schematic fly wing with two sparsely GFP-labeled sensory neurons, which are also separately indicated below. The site of injury and the field of observation are indicated. (B) Schematic setup for wing imaging. Injured and uninjured control wings (grey) are mounted in halocarbon oil 27 (red) on a glass slide (light blue) and covered with a cover slide (black). [Please click here to view a larger version of this figure.](#)

2. Observation of Axon and Synapse Morphology During Axon Death in the CNS

1. Antennal ablation: injury of whole axon bundles
 1. Use 5 virgin females and 5 males from the right genotype (**Figure 5A**, P₀ generation) to perform crosses at RT. Pass P₀ into new vials every 3–4 days. Collect freshly eclosed adult progeny (F₁ generation) daily and let them age for 7 up to 14 days.

2. Anesthetize flies on CO₂ pads. Use tweezers to ablate the right 3rd antennal segment for unilateral ablation; or both left and right 3rd antennal segments for bilateral ablation (**Figure 2A-C**). This will remove GFP-labeled neuronal cell bodies, while their axonal projections remain in the CNS.
NOTE: Antennal ablation severs the whole axon bundle. If unilateral ablation is performed, the axon bundle on the contralateral side (the unablated antenna) serves as internal control. Make sure to perform sufficient antennal ablations (approximately 15 animals).
 3. Recover the flies in food-containing vials.
2. Brain dissection and visualization of axons
1. Mix silicone elastomer base (9 mL) and curing agent (1 mL) in a volume ratio of 10:1. Transfer each 5 mL mixture into a 35 mm tissue culture plate, and reduce air introduced by mixing with gentle agitation in the fume hood overnight. The mixture solidifies within 24 h.
NOTE: Dissection plates must be prepared only once and may be used multiple times.
 2. Anesthetize flies on CO₂ pads and decapitate adult heads using two tweezers at desired time points (e.g., 1 or 7 days after antennal ablation). Use one tweezer to grab the neck, and the other tweezer to fix the thorax. Gently pull the neck and head off the thorax.
NOTE: Leave decapitated heads on the CO₂ pad until the desired number is achieved, but make sure to proceed to the next step within 30 min.
 3. Transfer all heads into a 1.5 mL microcentrifuge tube containing 1 mL of fixing solution containing 4% paraformaldehyde (PFA) and 0.1% Triton X-100 in phosphate buffered saline (PBS) using tweezers that have been dipped into the fixing solution.
NOTE: Fly heads stick well on wet tweezers. It makes it feasible to transfer all heads readily into the microcentrifuge tube.
 4. Fix heads for 20 min with gentle agitation at RT. Put the microcentrifuge tube on ice, heads will gravitate to the bottom of the microcentrifuge tube. Remove the supernatant with a pipette and repeat this procedure with five 2 min washes with 1 mL of washing buffer containing 0.1% Triton X-100 in PBS with gentle agitation at RT, to remove residual fixing solution.
NOTE: Videos on how to dissect adult *Drosophila* brains are readily available²⁷.
 5. Transfer the heads with a glass pipette into a dissection plate filled with washing buffer. Use one tweezer to grab and pull the proboscis off the head, while holding the head with the other tweezer. This will leave a hole where the proboscis was attached to the exoskeleton.
 6. Use two tweezers to remove the exoskeleton between the hole and each compound eye. This will make it feasible to open the head structure with both tweezers, and to gently scratch out the brain within.
 7. Clean each brain by removing trachea or fat stuck to it (**Figure 2D**, top). Once the brain is cleaned, put it in a new microcentrifuge tube containing 1 mL of washing buffer on ice.
NOTE: Damaged or lost optic lobes will not affect the olfactory lobe in the center of the brain (**Figure 2D**, top).
 8. Replace washing buffer with 1 mL of fixing solution once all brains are collected and accumulated at the bottom of the microcentrifuge tube. Fix brains for 10 min with rocking at RT, followed by five 2 min washes in 1 mL of washing buffer with rocking at RT.
 9. Apply primary antibodies (1:500) in washing buffer overnight with rocking at 4 °C, followed by 10 washes over 2 h using 1 mL of washing buffer with rocking at RT.
 10. Apply secondary antibodies (1:500) in washing buffer 2 h with rocking at RT and wrap microcentrifuge tube in aluminum foil to block light. Keep the microcentrifuge tube covered with aluminum foil for the rest of the procedure. Apply ten washes with 1 mL of washing buffer over 2 h with rocking at RT.
 11. Remove the supernatant and use a single drop of antifade reagent to cover the brains in the microcentrifuge tube. Incubate brains for at least 30 min at 4 °C before preparing them for mounting and imaging.
 12. Prepare a cover slide, stick lab tape on it, and cut out a "T"-like shape from the tape (**Figure 2D**, bottom). The resulting space serves as area where the brain-containing antifade reagent²⁸ will be pipetted into, preferably into both chambers.
NOTE: Use a 20-200 µL pipette tip where 3 mm of the tip has been cut off to widen the opening of the pipette. This will make it feasible to pipette the brain-containing antifade reagent. Carefully cover the brains with a cover slide.
 13. Use clay to prepare two small even rolls. Ensure that the clay rolls are not higher than the height of a glass slide. Stick the clay rolls onto the glass slide (**Figure 2D**, bottom). Place the brain-containing cover slide sandwich onto the clay rolls.
NOTE: GFP-labeled axons and their synapses are located in the front of the brain. It is, therefore, easier to image them from the front. However, brains will either face up, or face down on the cover slide sandwich. Clay rolls serve as sandwich holders, and during imaging, the sandwich can be flipped upside down. This will make it feasible to acquire images from the front from every brain.
 14. Acquire a series of optical sections along the z-axis with 1.0 µm step-size using a confocal microscope, and compress z-stacks into a single file for subsequent analyses, to assess the number of axonal projections remaining intact.

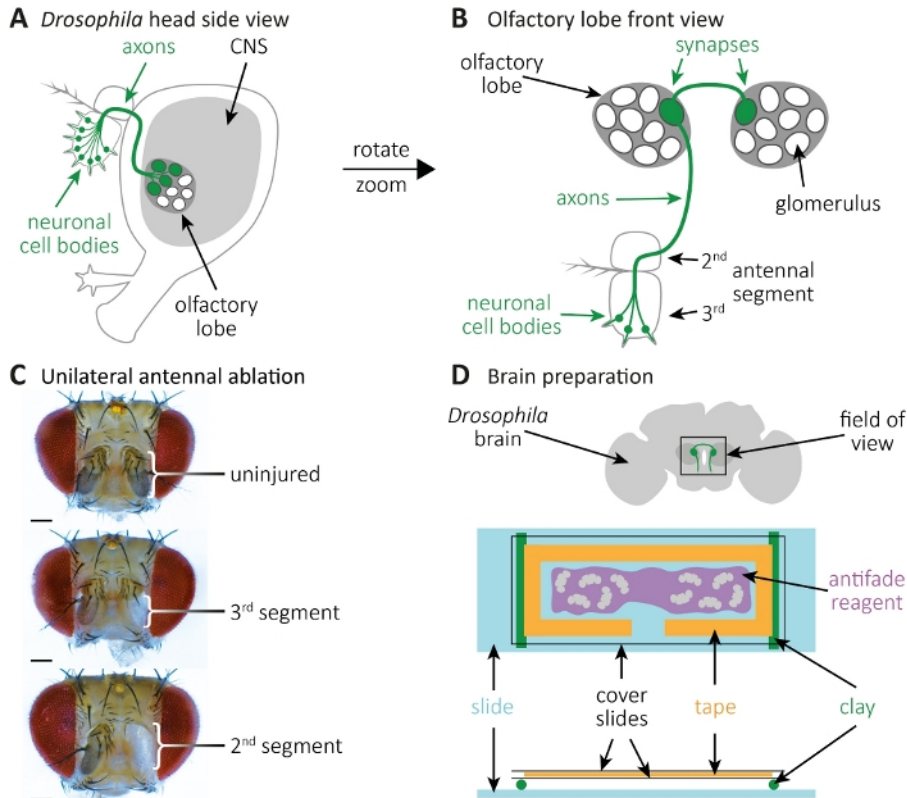


Figure 2: Observation of axon and synapse morphology during axon death in the brain. (A) Side view of a schematic fly head with GFP-labeled cell bodies, axons and synapses. (B) High-magnification front view of GFP-labeled olfactory receptor neurons and their axons and synapses. Cell bodies are housed in the 3rd antennal segment, and their axons project into the CNS. Axons form synapses in a glomerulus in the left olfactory lobe, cross the midline and form synapses in the glomerulus on the contralateral olfactory lobe. (C) Examples of fly heads with unilateral antennal ablation. Top: Uninjured control. Middle: Ablation of the 3rd antennal segment. Bottom: Ablation of the 2nd (and thus also 3rd) antennal segment. (D) Brain preparation. Top: Schematic dissected fly brain with indicated olfactory lobes and axonal projections in the field of view. Bottom: Schematic setup for brain imaging. Two clay rolls (green) are mounted onto a glass slide (light blue), they carry a cover slide sandwich, which contains fly brains (grey). Brains are mounted in antifade reagent (purple), surrounded by a lab tape (orange), and covered by two cover slides (black). [Please click here to view a larger version of this figure.](#)

3. Grooming Induced by Optogenetics as a Readout for Axon and Synapse Function

1. Optogenetic setup

1. Perform the optogenetic experiment in a dark room. Ensure that the setup consists of an 850 nm infrared (IR) LED spotlight to illuminate flies in the dark (Figure 3A), a flashing 660 nm red LED spotlight to activate neurons expressing CsChrimson, and a monochrome camera with a 700 nm longpass filter, which prevents the recording of red light flashes.
2. Use a 3D printer to generate a tiny circular behavior chamber with a diameter of 1 cm, cover it with a cover slide, and place an 860 nm emitter coupled to the red LED spotlight next to the chamber (Figure 3B).
NOTE: The emitter indicates when the red LED spotlight is on, thus activating the neurons.
3. Mount the LED spotlights and the camera on top of the chamber (Figure 3A, C).
4. Activate neurons by 10 Hz flashes during 10 s. The duration of activation can be adjusted according to the experimental design.

2. Preparing flies for optogenetics

1. Melt fly food in a microwave. After the food cooled down, before solidification, add 1:100 of 20 mM all trans-retinal in ethanol (EtOH) to a final concentration of 200 μ M. Mix well, and pour the food immediately into empty vials.
NOTE: Avoid adding all trans-retinal to hot food, this could result in less efficient optogenetics.
2. Cover vials containing solidified food with plugs or cotton balls. Wrap vials with aluminum foil. Then, store the food-containing vials in a dark, cold room.
3. Use 5 virgin females and 5 males (Figure 6A, generation P₀) from the right genotype to perform crosses at RT. Pass P₀ into new vials every 3–4 days. Collect freshly eclosed adult progeny (generation F₁) on a daily base and let them age for 7 up to 14 days in aluminum-covered vials containing 200 μ M all trans-retinal in fly food.
4. Collect flies by tapping them from food-containing vials into an empty vial with no food. Cool the vial down in ice-containing water for approximately 30 s. Flies will fall asleep. Put individual flies rapidly into small chambers covered with a cover slide (Figure 3B).
NOTE: As soon as flies warm up, they wake up. It is crucial to quickly spread individual flies into single chambers each. Avoid CO₂ pads to anaesthetize flies, this will impact their behavior.

- Perform optogenetics to elicit antennal grooming. Here, the protocol consists of the following intervals: 30 s where the red light is absent, followed by 10 s of red-light exposure at 10 Hz. Repeat this procedure three times in total, followed by an additional 30 s interval where the red light is absent^{12,29,30}.
NOTE: This protocol can be adjusted according to the experimental preference.
- Collect individual flies from each chamber on CO₂ pads. Subject them to antennal injury. Ablate both the left and the right 2nd antennal segments (**Figure 2C**). This will remove the cell bodies of Johnston's organ (JO) neurons, while the axonal projections remain in the CNS. Recover the flies in aluminum-covered vials containing 200 μ M all trans-retinal.
NOTE: For antennal grooming induced by optogenetics, the sensory neuron cell bodies are housed in the 2nd antennal segment (**Figure 2C**).
- At corresponding time points (e.g., 7 days post antennal ablation), subject flies to another grooming assay (go back to step 3.2.4).

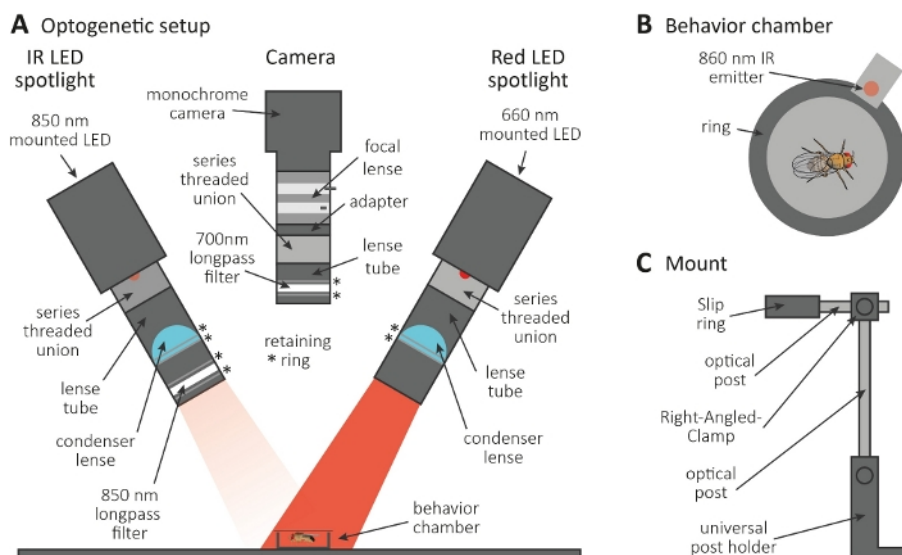


Figure 3: Optogenetic setup to induce grooming as a readout for axon and synapse function. (A) Illustration of assembled components required for optogenetics. Infrared (IR) LED spotlight, camera and red LED spotlight (from left to right, respectively). The components including a detailed description are listed in the **Table of Materials**. (B) Top view illustration of a behavior chamber including an IR emitter to indicate red LED spotlight activation. (C) Illustration of a single mount setup. A total of three mount setups are required for the two LED spotlights and the camera, respectively. [Please click here to view a larger version of this figure.](#)

Representative Results

Above, we described three methods to study the morphology and function of severed axons and their synapses. The first method allows for high-resolution observation of individual axons in the PNS. It requires clones generated by the MARCM technique^{14,31}. Here, we performed crosses to generate wild type and *highwire* mutant MARCM clones (**Figure 4A**). A simple cut in the middle of the wing induces axon injury of neurons housed distal (e.g., at the outer side of the wing), while proximal neurons (e.g., between the cut site and the thorax) remain uninjured. This approach makes it feasible to observe axon death side-by-side of uninjured control axons in the same nerve bundle (**Figure 1A**, **Figure 4B**). Here, we used a genetic background resulting in low numbers of GFP-labeled clones (e.g., two in each experiment¹⁴). We present examples of 1 and 7 days after injury of wild type axons, to provide examples of control axons, axons undergoing axon death, and axonal fragments being cleared by surrounding glia, respectively. In addition, we repeated axonal injury in *highwire* mutants where we analyzed the outcome 7 days after injury.

Uninjured control wings harbor two wild-type clones, thus two GFP-labeled wild-type axons (**Figure 4B**, wild type, uninjured control). One day after cutting the middle of the wing by the use of micro scissors, axon death is induced in GFP-labeled axons where cell bodies are distal to the cut site, while axons from proximally housed cell bodies serve as an internal control within the same nerve bundle (**Figure 4B**, wild type, 1 day post injury). Note the axonal debris trace in the upper part indicated by the arrow. 7 days after axonal injury, GFP-labeled axonal debris is cleared by surrounding glia, while GFP labeled uninjured control axons remain in the nerve bundle (**Figure 4B**, wild type, 7 days post injury, arrow). In contrast, *highwire* mutant axons that have been severed for 7 days remain morphologically preserved, consistent with previous findings^{11,14} (**Figure 4B**, *highwire*, 7 days post injury, arrow). These results demonstrate the powerful visual resolution of the *Drosophila* wing. Axon death can be observed side-by-side of uninjured controls in the same nerve bundle. While wild-type axons undergo axon death within 1 day after injury and the resulting debris is cleared within 7 days, axon death deficient *highwire* mutants remain morphologically preserved for 7 days.

A Wild type:

$w, hs-FLP^{12}, FRT19A$; $dpr1-Gal4, 5xUAS-mCD8::GFP$ / CyO \otimes $w, hs-FLP^{12}, tub-Gal80, FRT19A$; $dpr1-Gal4, 5xUAS-Gal4, 5xUAS-mCD8::GFP, ase-FLP^{12}$ / Y ; CyO

$w, hs-FLP^{12}, FRT19A$; $dpr1-Gal4, 5xUAS-mCD8::GFP$ / CyO ; $w, hs-FLP^{12}, tub-Gal80, FRT19A$; $dpr1-Gal4, 5xUAS-Gal4, 5xUAS-mCD8::GFP, ase-FLP^{12}$ / Y ; CyO

highwire:

$w, hs-FLP^{12}, hiw^{M1}, FRT19A$ / $FM7a, B$; $dpr1-Gal4, 5xUAS-mCD8::GFP$ / CyO \otimes $w, hs-FLP^{12}, tub-Gal80, FRT19A$; $dpr1-Gal4, 5xUAS-Gal4, 5xUAS-mCD8::GFP, ase-FLP^{12}$ / Y ; CyO

$w, hs-FLP^{12}, hiw^{M1}, FRT19A$ / $FM7a, B$; $dpr1-Gal4, 5xUAS-mCD8::GFP$ / CyO ; $w, hs-FLP^{12}, tub-Gal80, FRT19A$; $dpr1-Gal4, 5xUAS-Gal4, 5xUAS-mCD8::GFP, ase-FLP^{12}$ / Y ; CyO

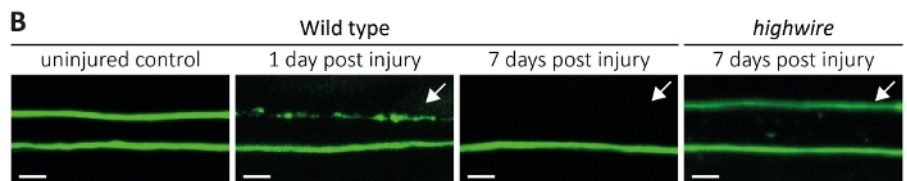


Figure 4: Approach to study axon death of GFP-labeled sensory neuron axons in the wing. (A) Schematic crosses to generate wild type and *highwire* clones in the wing (P₀ and F₁ generation, respectively). Virgin females are on the left, males on the right. See **Table of Materials** for genotype details. (B) Examples of control and injured GFP-labeled axons. The field of view is indicated in (Figure 1A). From left to right: uninjured wild type control axons, wild type axons 1-day post injury, wild type axons 7 days post injury, *highwire* mutant axons 7 days post injury, respectively. Arrows indicate severed axons, Scale bar = 5 μm. [Please click here to view a larger version of this figure.](#)

The second method describes how to visualize whole axon bundles projecting into the CNS where they form synapses, which belong to neurons housed in both left and right antennae (Figure 2A-C). Here, we performed crosses to generate wild type and *highwire* mutant MARCM clones (Figure 5A). Uninjured, GFP-labeled axons and their synapses can be visualized over the course of days to weeks, in the absence of injury (Figure 5B, Wild type, uninjured control). Alternatively, animals can be subjected to 3rd antennal segment ablation, and severed GFP-labeled axons and their synapses can be observed during a time course over hours to days. We focused on 7 days after antennal ablation, because at this time point, axons and their synapses have undergone axon death, and resulting debris is cleared by surrounding glia. If unilateral ablation of the right antenna is performed, then the right axon bundle is severed and will disassemble and the resulting debris is fully cleared 7 days after injury (Figure 5B, wild type, unilateral ablation, 7 days post injury, arrows), consistent with previous findings¹³. Alternatively, both the right and the left antennae can be ablated, which will sever both axon bundles, and 7 days after injury, axons and their synapses disappeared (Figure 5B, wild type, bilateral ablation, 7 days post injury, arrow). In contrast, unilateral ablation of the right antennae in *highwire* mutants results in severed axons that remain preserved 7 days post injury, consistent with previous findings^{11,14} (Figure 5B, *highwire*, unilateral ablation, 7 days post injury, arrow). These results demonstrate that severed wild-type axons undergo axon death and the resulting debris is cleared within 7 days, while axon death deficient *highwire* mutants fail to undergo axon death and remain morphologically preserved for 7 days.

A Wild type:

$w, hs-FLP^{12}, FRT19A$ \otimes $w, hs-FLP^{12}, tub-Gal80, FRT19A$; $OR22a-Gal4, 5xUAS-mCD8::GFP$ / CyO ; $ey-FLP^6$ / $TM3, Sb, e$

$w, hs-FLP^{12}, FRT19A$ / $w, hs-FLP^{12}, tub-Gal80, FRT19A$; $OR22a-Gal4, 5xUAS-mCD8::GFP$ / $+$; $ey-FLP^6$ / $+$

highwire:

$w, hs-FLP^{12}, hiw^{M1}, FRT19A$ / $FM7a, B$ \otimes $w, hs-FLP^{12}, tub-Gal80, FRT19A$; $OR22a-Gal4, 5xUAS-mCD8::GFP$ / CyO ; $ey-FLP^6$ / $TM3, Sb, e$

$w, hs-FLP^{12}, hiw^{M1}, FRT19A$ / $w, hs-FLP^{12}, tub-Gal80, FRT19A$; $OR22a-Gal4, 5xUAS-mCD8::GFP$ / $+$; $ey-FLP^6$ / $+$

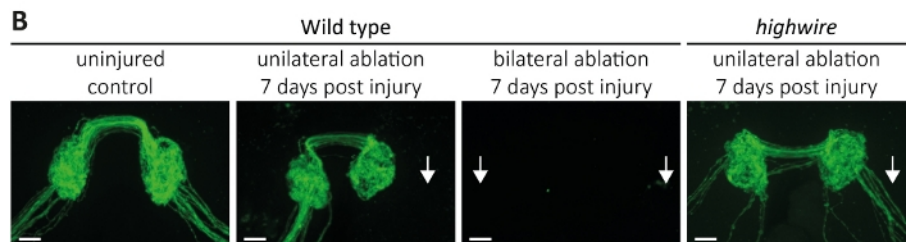


Figure 5: Approach to study axon death of GFP-labeled sensory neuron axons in the brain. (A) Schematic crosses to generate wild type and *highwire* clones in the brain (P₀ and F₁ generation, respectively). Virgin females are on the left, males on the right. See **Table of Materials** for genotype details. (B) Examples of control and injured GFP-labeled axons. From left to right: uninjured wild type controls, wild type 7 days post unilateral antennal ablation, wild type 7 days post bilateral antennal ablation, and *highwire* mutants 7 days post unilateral antennal ablation, respectively. Arrows indicate severed axon bundles, Scale bar = 10 μm. [Please click here to view a larger version of this figure.](#)

The third method allows for the observation of functional preservation of severed axons and their synapses in the CNS. It relies on the manipulation of a subset of JO neurons housed in the 2nd antennal segment which are sufficient to induce antennal grooming. Expression of a red-shifted channelrhodopsin (CsChrimson) in JO neurons, combined with dietary supplementation of all trans-retinal, is sufficient to elicit a simple post-synaptic grooming behavior upon red light exposure^{12,30}. Here, we performed crosses to generate wild type JO neurons, and JO neurons over-expressing *dnmnat* (*dnmnat*^{OE}) (Figure 6A). Wild type flies or flies containing JO neurons with attenuated axon death (*dnmnat*^{OE}), both harbor a potent grooming behavior before injury. However, 7 days post injury (e.g., bilateral ablation of the 2nd antennal segment), grooming fails to be elicited by optogenetics in wild type flies due to injury-induced axon and synapse degeneration, while animals with attenuated axon death continue to groom (Figure 6B, Movie 1,2). Attenuated axon death is therefore capable of functionally preserving severed axons and their synapses for 7 days.

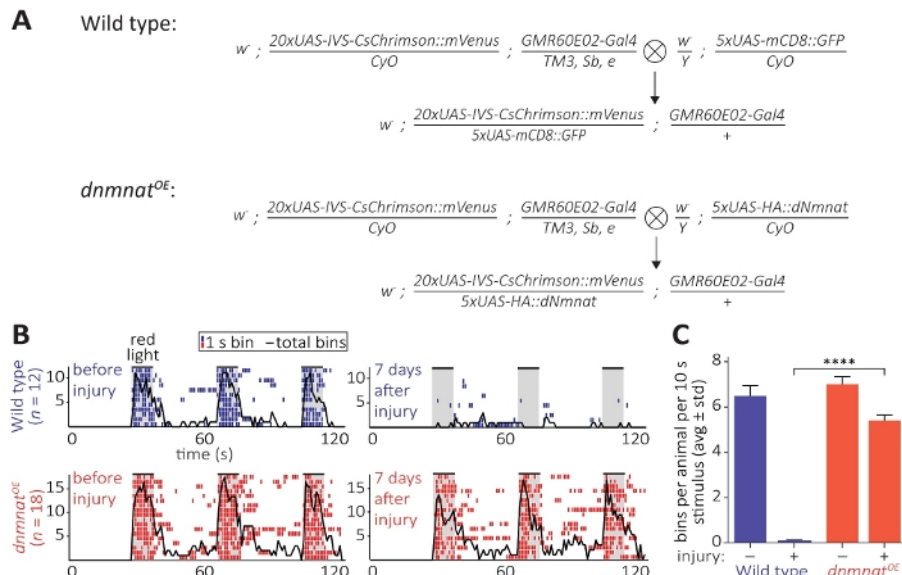


Figure 6: Approach to visualize axonal and synaptic function after axotomy. (A) Schematic crosses to generate wild type and *dnmnat* over-expressing JO sensory neurons (P₀ and F₁ generation, respectively). Virgin females are on the left, males on the right. See **Table of Materials** for genotype details. **(B)** Individual ethograms of grooming behavior induced by optogenetics. Top: individual ethograms of wild type flies before and 7 days after injury (blue). Bottom: individual ethograms of flies over-expressing *dnmnat* (*dnmnat*^{OE}) in JO neurons before and 7 days after injury (red). Each bin indicates at least 1 grooming behavior within 1 s. The black line indicates the sum of all bins. **(C)** Quantification of grooming behavior. Data is shown as average ± standard deviation, p > 0.001 (one-way ANOVA, multiple comparison with Tukey's post hoc test). [Please click here to view a larger version of this figure.](#)

Movie 1: Representative wild type grooming behavior elicited by optogenetics before and 7 days after antennal ablation. [Please click here to download this video.](#)

Movie 2: Representative grooming behavior elicited by optogenetics in flies over-expressing *dnmnat* in JO neurons before and 7 days after antennal ablation. [Please click here to download this video.](#)

Discussion

The protocols described here allow for the robust and reproducible observation of morphology as well as function of axons and their synapses separated from their cell bodies in *Drosophila*. The wing assay facilitates the observation of axon death side-by-side of uninjured control axons in the PNS¹⁴, while the antennal assay facilitates the observation of whole nerve bundles of GFP-labeled axons and their synapses, to assess both morphology and function in the brain (CNS)¹². There are critical steps and certain advantages for each approach to study morphology that have to be taken into consideration when designing experiments.

To observe axon morphology in the PNS in the wing, experiments can be readily performed, because of the transparency of the wing: it allows to bypass dissection and immunohistochemistry. However, due to the lack of fixation, the wings have to be imaged immediately after mounting¹⁴. Currently, two distinct Gal4 drivers are frequently used, either *ok371Gal4* or *dpr1Gal4*, and both references offer distinct approaches to quantify degeneration^{14,26}. Sparse labeling of a few neurons is recommended, by using "Mosaic Analysis with a Repressible Cell Marker (MARCM)"^{14,31}, as the resolution of axonal morphology is unprecedented. In contrast, the observation of synapses is not possible in wings, they are located in the ventral nerve cord inside the thorax of the flies. Furthermore, additional axonal markers cannot be visualized by immunohistochemistry: the waxy cuticle makes it impossible for the diffusion of fixatives and antibodies into the underlying tissue.

To observe axon and synapse morphology in the CNS, brain dissections have to be performed. They offer the advantage of visualizing additional axonal and synaptic markers by the use of immunohistochemistry, and synapses can be observed alongside axons in the same field of view^{10,13}. A large collection of characterized olfactory receptor neuron (ORN) Gal4 drivers is readily available³², and frequently, *OR22aGal4* is the driver of choice. For antennal ablation, cell bodies of OR22a neurons are housed in the 3rd segment (Figure 2B). A fluorescence intensity-based quantification is used to quantify the degeneration of either axons or synapses¹³. Conversely, experiments are time consuming due to brain dissection and antibody staining.

To visualize axonal and synaptic function after axotomy, optogenetics is used to trigger antennal grooming: it serves as a readout for functional preservation of severed axons and their synapses¹². The grooming circuit and corresponding sensory, inter- and motoneuron Gal4 drivers have been thoroughly described^{29,30}. *GMR60E02Gal4* labels a subset of Johnston's organ (JO) sensory neurons, which are required and sufficient for grooming^{29,30}. For antennal ablation, cell bodies of JO neurons are housed in the 2nd antennal segment (**Figure 2B**). An optogenetic setup can readily be built from scratch, or an existing setup adjusted. Importantly, experiments have to be performed in a dark room, and flies thus visualized with an infrared (IR) LED spotlight. When using CsChrimson as a channel, it is crucial to supply the food with all trans-retinal and a red LED spotlight to activate JO neurons²⁹. Alternatively, blue light-sensitive channels and a blue LED spotlight, or the TrpA1 channel and temperature can be used for neuronal activation^{29,33}. The quantification of grooming behavior has already been described^{12,29}.

When these assays are used to specifically study axon death, it is important to note that the phenotype of morphological or functional preservation should be robust over time. There are cases where axon death leads to a consistent yet less pronounced phenotype in morphological preservation^{34,35}, and whether such a phenotype translates into functional preservation remains to be determined.

Axon death phenotypes have also been observed in neurons during development of *Drosophila* larvae, where nerves were crushed rather than injured^{11,23}. Here, we specifically focused on adult *Drosophila* neurons which completed development. In this context, the use of RNA interference³⁶, or tissue-specific CRISPR/Cas9³⁷ can readily be implemented. Importantly, the above techniques can be used in an axon death independent context: they facilitate the characterization of neuronal maintenance factors³⁸, axonal transport³⁹, age-dependent axonal mitochondria changes⁴⁰, and morphology of axonal mitochondria⁴¹.

Disclosures

The authors declare that they have nothing to disclose.

Acknowledgments

We would like to thank the entire Neukomm lab for contributions. This work was supported by a Swiss National Science Foundation (SNSF) Assistant Professor award (grant 176855), the International Foundation for Research in Paraplegia (IRP, grant P180), SNSF Spark (grant 190919) and by support from the University of Lausanne and the Department of Fundamental Neurosciences (État de Vaud) to L.J.N.

References

1. Matsuda, W. et al. Single Nigrostriatal Dopaminergic Neurons Form Widely Spread and Highly Dense Axonal Arborizations in the Neostriatum. *The Journal of Neuroscience: The Official Journal of the Society for Neuroscience*. **29** (2), 444-453 (2009).
2. Wedel, M. J. A Monument of Inefficiency: The Presumed Course of the Recurrent Laryngeal Nerve in Sauropod Dinosaurs. *Acta Palaeontologica Polonica*. **57** (2), 251-256 (2012).
3. Mariano, V., Dominguez-Iturza, N., Neukomm, L. J., Bagni, C. Maintenance mechanisms of circuit-integrated axons. *Current Opinion in Neurobiology*. **53**, 162-173 (2018).
4. Conforti, L., Gilley, J., Coleman, M. P. Wallerian degeneration: an emerging axon death pathway linking injury and disease. *Nature reviews Neuroscience*. **15** (6), 394-409 (2014).
5. Neukomm, L. J., Freeman, M. R. Diverse cellular and molecular modes of axon degeneration. *Trends in Cell Biology*. **24** (9), 515-523 (2014).
6. Gustavsson, A. et al. Cost of disorders of the brain in Europe 2010. *European Neuropsychopharmacology: The Journal of the European College of Neuropsychopharmacology*. **21** (10), 718-779 (2011).
7. Waller, A. Experiments on the Section of the Glossopharyngeal and Hypoglossal Nerves of the Frog, and Observations of the Alterations Produced Thereby in the Structure of Their Primitive Fibres. *Philosophical Transactions of the Royal Society of London*. **140**, 423-429 (1850).
8. Rosell, A. L., Neukomm, L. J. Axon death signalling in Wallerian degeneration among species and in disease. *Open Biology*. **9** (8), 190118 (2019).
9. Mack, T. G. et al. Wallerian degeneration of injured axons and synapses is delayed by a Ube4b/Nmnat chimeric gene. *Nature Neuroscience*. **4** (12), 1199-1206 (2001).
10. Osterloh, J. M. et al. dSarm/Sarm1 is required for activation of an injury-induced axon death pathway. *Science (New York, NY)*. **337** (6093), 481-484 (2012).
11. Xiong, X. et al. The highwire ubiquitin ligase promotes axonal degeneration by tuning levels of nmnat protein. *PLoS Biology*. **10** (12), e1001440 (2012).
12. Neukomm, L. J. et al. Axon Death Pathways Converge on Axundead to Promote Functional and Structural Axon Disassembly. *Neuron*. **95** (1), 78-91 (2017).
13. MacDonald, J. M. et al. The *Drosophila* cell corpse engulfment receptor Draper mediates glial clearance of severed axons. *Neuron*. **50** (6), 869-881 (2006).
14. Neukomm, L. J., Burdett, T. C., Gonzalez, M. A., Zuchner, S., Freeman, M. R. Rapid in vivo forward genetic approach for identifying axon death genes in *Drosophila*. *Proceedings of the National Academy of Sciences of the United States of America*. **111** (27), 9965-9970 (2014).
15. Lu, T.Y. et al. Axon degeneration induces glial responses through Draper-TRAF4-JNK signalling. *Nature Communications*. **8**, 14355 (2017).
16. Lunn, E. R., Perry, V. H., Brown, M. C., Rosen, H., Gordon, S. Absence of Wallerian Degeneration does not Hinder Regeneration in Peripheral Nerve. *The European Journal of Neuroscience*. **1** (1), 27-33 (1989).
17. Adalbert, R. et al. A rat model of slow Wallerian degeneration (Wld(S)) with improved preservation of neuromuscular synapses. *The European Journal of Neuroscience*. **21** (1), 271-277 (2005).
18. Martin, S. M., O'Brien, G. S., Portera-Cailliau, C., Sagasti, A. Wallerian degeneration of zebrafish trigeminal axons in the skin is required for regeneration and developmental pruning. *Development (Cambridge, England)*. **137** (23), 3985-3994 (2010).
19. Feng, Y. et al. Overexpression of Wld(S) or Nmnat2 in Mauthner Cells by Single-Cell Electroporation Delays Axon Degeneration in Live Zebrafish. *Journal of Neuroscience Research*. **88** (15), 3319-3327 (2010).

20. Gilley, J., Coleman, M. P. Endogenous Nmnat2 is an essential survival factor for maintenance of healthy axons. *PLoS Biology*. **8** (1), e1000300 (2010).
21. Babetto, E., Beirowski, B., Russler, E. V., Milbrandt, J., DiAntonio, A. The Phr1 ubiquitin ligase promotes injury-induced axon self-destruction. *Cell Reports*. **3** (5), 1422-1429 (2013).
22. Gerdtz, J., Summers, D. W., Sasaki, Y., DiAntonio, A., Milbrandt, J. Sarm1-mediated axon degeneration requires both SAM and TIR interactions. *The Journal of Neuroscience*. **33** (33), 13569-13580 (2013).
23. Gerdtz, J., Brace, E. J., Sasaki, Y., DiAntonio, A., Milbrandt, J. SARM1 activation triggers axon degeneration locally via NAD⁺ destruction. *Science (New York, NY)*. **348** (6233), 453-457 (2015).
24. Bridge, P. M. et al. Nerve crush injuries--a model for axonotmesis. *Experimental Neurology*. **127** (2), 284-290 (1994).
25. Maxwell, W. L., Bartlett, E., Morgan, H. Wallerian Degeneration in the Optic Nerve Stretch-Injury Model of Traumatic Brain Injury: A Stereological Analysis. *Journal of Neurotrauma*. **32** (11), 780-790 (2015).
26. Fang, Y., Soares, L., Teng, X., Geary, M., Bonini, N. M. A novel Drosophila model of nerve injury reveals an essential role of Nmnat in maintaining axonal integrity. *Current Biology*. **22** (7), 590-595 (2012).
27. *Janelia Farm Adult Drosophila Brain Dissection*. <https://www.janelia.org/project-team/flylight/protocols> (2015).
28. Mowiol mounting medium. *Cold Spring Harbor Protocols*. **2006** (1), (2006).
29. Seeds, A. M. et al. A suppression hierarchy among competing motor programs drives sequential grooming in Drosophila. *eLife*. **3**, e02951 (2014).
30. Hampel, S., Franconville, R., Simpson, J. H., Seeds, A. M. A neural command circuit for grooming movement control. *eLife*. **4**, e08758 (2015).
31. Lee, T., Luo, L. Mosaic analysis with a repressible cell marker for studies of gene function in neuronal morphogenesis. *Neuron*. **22** (3), 451-461 (1999).
32. Vosshall, L. B., Wong, A. M., Axel, R. An olfactory sensory map in the fly brain. *Cell*. **102** (2), 147-159 (2000).
33. Hampel, S., McKellar, C. E., Simpson, J. H., Seeds, A. M. Simultaneous activation of parallel sensory pathways promotes a grooming sequence in Drosophila. *eLife*. **6**, (2017).
34. Farley, J. E. et al. Transcription factor Pebbled/RREB1 regulates injury-induced axon degeneration. *Proceedings of the National Academy of Sciences of the United States of America*. **23** (6), (2018).
35. Wang, H. et al. Rapid depletion of ESCRT protein Vps4 underlies injury-induced autophagic impediment and Wallerian degeneration. *Science Advances*. **5** (2), (2019).
36. Dietzl, G. et al. A genome-wide transgenic RNAi library for conditional gene inactivation in Drosophila. *Nature*. **448** (7150), 151-156 (2007).
37. Port, F. et al. A large-scale resource for tissue-specific CRISPR mutagenesis in Drosophila. *bioRxiv*. **102**, 636076 (2019).
38. Vagnoni, A., Hoffmann, P. C., Bullock, S. L. Reducing Lissencephaly-1 levels augments mitochondrial transport and has a protective effect in adult Drosophila neurons. *Journal of Cell Science*. **129** (1), 178-190 (2016).
39. Vagnoni, A., Bullock, S. L. A cAMP/PKA/Kinesin-1 Axis Promotes the Axonal Transport of Mitochondria in Aging Drosophila Neurons. *Current Biology*. **28** (8), 1265-1272, (2018).
40. Cao, X. et al. In vivo imaging reveals mitophagy independence in the maintenance of axonal mitochondria during normal aging. *Aging Cell*. **16** (5), 1180-1190 (2017).
41. Smith, G. A. et al. Glutathione S-Transferase Regulates Mitochondrial Populations in Axons through Increased Glutathione Oxidation. *Neuron*. **103** (1), 52-65 (2019).

Materials List for:

Morphological and Functional Evaluation of Axons and their Synapses during Axon Death in *Drosophila melanogaster*

Maria Paglione^{*1}, Arnau Llobet Rosell^{*1}, Jean-Yves Chatton¹, Lukas J. Neukomm¹

¹Department of Fundamental Neurosciences, University of Lausanne

*These authors contributed equally

Correspondence to: Lukas J. Neukomm at lukas.neukomm@unil.ch

URL: <https://www.jove.com/video/60865>

DOI: [doi:10.3791/60865](https://doi.org/10.3791/60865)

Materials

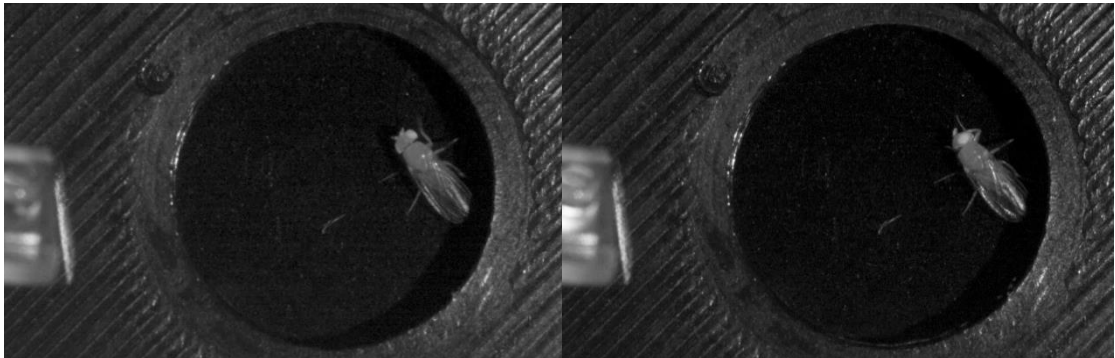
Name	Company	Catalog Number	Comments
Tweezers (high precision, ultra fine)	EMS	78520-5	Antennal ablation
MicroPoint Scissors (5-mm cutting edge)	EMS	72933-04	Wing injury
1.5 mL microcentrifuge tube	Eppendorf	30120086.0000	
35mm tissue culture dish	Sarstedt	83.3900	
Cover Slips, Thickness 1	Thermo Scientific™	BB02400600A113MNT0	
Superfrost Microscope Slides	Thermo Scientific™	AA00008032E00MNT10	
High-Sensitivity USB 2.0 CMOS Camera, 1280 x 1024, Global Shutter	Thorlabs	DCC1240M	Camera setup
SM1 Retaining Ring for Ø1" Lens Tubes and Mounts	Thorlabs	SM1RR	
25mm 1/1.2" C mount Lens	Tamron	M112FM25	
Adapter with External M27 x 0.5 Threads and Internal SM1 Threads	Thorlabs	SM1A36	
Aspheric Condenser Lens, Ø25 mm, f=20.1 mm, NA=0.60, ARC: 650-1050 nm	Thorlabs	ACL2520U-B	
Ø25.0 mm Premium Longpass Filter, Cut-On Wavelength: 700 nm	Thorlabs	FELH0700	
SM1 (1.035"-40) Coupler, External Threads, 0.5" Long	Thorlabs	SM1T2	
SM1 Lens Tube Without External Threads, 1" Long, Two Retaining Rings Included	Thorlabs	SM1M10	
850 nm, 900 mW (Min) Mounted LED, 1200 mA	Thorlabs	M850L3	IR LED spotlight
SM1 (1.035"-40) Coupler, External Threads, 0.5" Long	Thorlabs	SM1T2	
SM1 Lens Tube Without External Threads, 2" Long, Two Retaining Rings Included	Thorlabs	SM1M20	
Aspheric Condenser Lens, Ø25 mm, f=20.1 mm, NA=0.60, ARC: 650-1050 nm	Thorlabs	ACL2520U-B	
Ø25.0 mm Premium Longpass Filter, Cut-On Wavelength: 850 nm	Thorlabs	FELH0850	
SM1 Retaining Ring for Ø1" Lens Tubes and Mounts	Thorlabs	SM1RR	

660 nm, 940 mW (Min) Mounted LED, 1200 mA	Thorlabs	M660L4	Red LED spotlight
Aspheric Condenser Lens, Ø25 mm, f=20.1 mm, NA=0.60, ARC: 650-1050 nm	Thorlabs	ACL2520U-B	
SM1 (1.035"-40) Coupler, External Threads, 0.5" Long	Thorlabs	SM1T2	
SM1 Lens Tube Without External Threads, 2" Long, Two Retaining Rings Included	Thorlabs	SM1M20	
15 V, 2.4 A Power Supply Unit with 3.5 mm Jack Connector for One K- or T-Cube	Thorlabs	KPS101	LED control
T-Cube LED Driver, 1200 mA Max Drive Current	Thorlabs	LEDD1B	
150 mm x 300 mm x 12.7 mm Aluminum Breadboard, M6 Double-Density Taps	Thorlabs	MB1530/M	Mount base
Ø12.7 mm Universal Post Holder, Spring-Loaded Locking Thumbscrew, L = 75 mm	Thorlabs	UPH75/M	Mount, 3x (IR LED, red LED, cam)
Ø1.20" Slip Ring for SM1 Lens Tubes and C-Mount Extension Tubes, M4 Tap	Thorlabs	SM1RC/M	
Ø12.7 mm Optical Post, SS, M4 Setscrew, M6 Tap, L = 150 mm	Thorlabs	TR150/M	
Ø12.7 mm Optical Post, SS, M4 Setscrew, M6 Tap, L = 40 mm	Thorlabs	TR40/M	
Right-Angle Clamp for Ø1/2" Posts, 5 mm Hex	Thorlabs	RA90/M	
M6 x 1.0 Stainless Steel Cap Screw, 16 mm Long, Pack of 25	Thorlabs	SH6MS16	screws for mount onto base
USB-6001 14-Bit 20 kS/s Multifunction I/O and NI-DAQmx	National Instruments	782604-01	Red LED spotlight controller
20k Ohm 1 Gang Linear Panel Mount Potentiometer	TT Electronics/BI	P230-2EC22BR20K	fintuner for indicator
IR (860nm) emitter, 100 mA radial	Osram	475-1365-ND	Red light indicator
cable	-	-	Misc
All-trans retinal	Sigma	R2625	
Ethanol absolute	Vwr	20821.296	
Halocarbon Oil 27	Sigma	H8773	
Mowiol	Merk	81381	
Paraformaldehyde	Sigma	F8775	
Phosphate buffered saline (PBS)	Sigma	P5493	
Sylgard 184 silicone elastomer base	Dow Corning Corp	4019862	
Sylgard 184 silicone elastomer curing agent	Dow Corning Corp	4019862	
Triton X-100	Sigma	T8787	
Chicken anti-GFP antibodies	Rockland	600-901-215	Antibodies
Goat Dylight anti-Chicken	Abcam	ab96947	
FM7a, B	BDSC	RRID:BDSC_785	X chromosome
FRT19A[hs-neo]	BDSC	RRID:BDSC_1709	

hiw[ΔN]	BDSC	RRID:BDSC_51637	
hs-FLP[12]	BDSC	RRID:BDSC_1929	
tub-Gal80[LL1]	BDSC	RRID:BDSC_5132	
w[1118]	BDSC	RRID:BDSC_3605	
20xUAS-IVS-CsChrimson::mVenus	BDSC	RRID:BDSC_55135	2nd chromosome
5xUAS-Gal4[12B]	Kyoto	RRID:Kyoto_108492	
5xUAS-HA::dnmnat	BDSC	RRID:BDSC_39702	
5xUAS-mCD8::GFP[LL5]	BDSC	RRID:BDSC_5134	
ase-FLP[2d]	Freeman laboratory	Neukomm et al., 2014 (PNAS)	
CyO	BDSC	RRID:BDSC_2555	
dpr1-Gal4	BDSC	RRID:BDSC_25083	
OR22a-Gal4	BDSC	RRID:BDSC_9952	
ey-FLP[6]	BDSC	RRID:BDSC_5577	3rd chromosome
GMR60E02-Gal4	BDSC	RRID:BDSC_39250	
TM3,Sb,e	BDSC	RRID:BDSC_3644	

CHAPTER 3

The NAD⁺ precursor NMN activates dSarm to trigger axon degeneration in *Drosophila*



A resting and an antennal-grooming fly (left and right, respectively). Antennal grooming is performed with the forelegs. The grooming behaviour is controlled by an LED on the left side of each picture (left, OFF, right, ON, respectively).

2.1 Summary of the results

In this study, we demonstrate how the metabolite NMN, the precursor of NAD⁺, binds to and activates dSarm to execute axon degeneration both *in vitro* and *in vivo*. We demonstrate how a bacterial enzyme, NMN-Deamidase (NMN-D), when expressed in *Drosophila*, can keep NMN levels lower and that lower NMN levels are sufficient to preserve the morphology of injured axons for the lifespan of the flies. The synapses from injured axons remain circuit-integrated for at least two weeks. We describe for the first time how the expression of NAMPT—a second source of NMN synthesis—results in faster axonal degeneration after injury. We also demonstrate how NMN activates the NADase enzyme dSarm, and how preventing it can result in long-term protection. We finally show how neurodegeneration triggered by the loss of *nmnat*, is substantially delayed with the expression of NMN-D. Overall, these findings contribute to a better understanding of the injury-induced axon degeneration signalling pathway. Our manuscript is under consideration in *eLife* and will be resubmitted in mid-October 2022.

2.2 Personal contribution

Together with Andrea Loreto and Lukas Neukomm, we conceived the study and designed the experiments. We collaborated with the group of Giuseppe Orsomando (Ancona, Italy) to perform the enzymatic assays, and with the Metabolomics Platform of the University of Lausanne to perform the metabolic analyses. Maria Paglione performed the optogenetics assay for the CRISPR/Cas9 knockouts; Magdalena Kocia collected the heads of mNAMPT overexpression analysed by the Metabolomics Platform; Jon Gilley performed the NADase assays. I performed and analysed the rest of the experiments. I also wrote the manuscript together with Lukas Neukomm.

1 **The NAD⁺ precursor NMN activates dSarm to trigger axon degeneration in *Drosophila***

2

3

4 Arнау Llobet Rosell^{1,+}, Maria Paglione^{1,+}, Jonathan Gilley², Magdalena Kocia^{1,+}, Giulia
5 Perillo³, Massimiliano Gasparrini⁴, Lucia Cialabrini⁴, Nadia Raffaelli⁴, Carlo Angeletti⁵,
6 Giuseppe Orsomando⁵, Pei-Hsuan Wu³, Michael P. Coleman², Andrea Loreto^{2,6}, Lukas J.
7 Neukomm^{1,*}

8

9

10 1 Department of Fundamental Neurosciences, University of Lausanne, Rue du Bugnon 9,
11 1005 Lausanne VD, Switzerland

12

13 2 John van Geest Centre for Brain Repair, Department of Clinical Neurosciences, University
14 of Cambridge, Forvie Site, Robinson Way, Cambridge, CB2 0PY, United Kingdom

15

16 3 Department of Genetic Medicine and Development, University of Geneva, Rue Michel-
17 Servet 1, CH-1211 Geneva, Switzerland

18

19 4 Department of Agricultural, Food and Environmental Sciences, Polytechnic University of
20 Marche, Via Brecce Bianche, Ancona 60131, Italy

21

22 5 Department of Clinical Sciences, Section of Biochemistry, Polytechnic University of
23 Marche, Via Ranieri 67, Ancona 60131, Italy

24

25 6 Current address: Department of Physiology, Anatomy and Genetics, Kavli Institute for
26 NanoScience Discovery, Oxford Parkinson's Disease Centre, University of Oxford, South
27 Parks Road, Oxford, OX1 3QU, United Kingdom

28

29 ⁺ Lemanic Neuroscience Doctoral School (LNDS)

30

31 * Author of correspondence:

32 lukas.neukomm@unil.ch

33 +41 21 692 52 88

34

35 **Abstract**

36

37 Axon degeneration contributes to the disruption of neuronal circuit function in diseased
38 and injured nervous systems. Severed axons degenerate following the activation of an
39 evolutionarily conserved signaling pathway, which culminates in the activation of SARM1 in
40 mammals to execute the pathological depletion of the metabolite NAD⁺. SARM1 NADase
41 activity is activated by the NAD⁺ precursor nicotinamide mononucleotide (NMN). In
42 mammals, keeping NMN levels low potentially preserves axons after injury. However, it
43 remains unclear whether NMN is also a key mediator of axon degeneration and dSarm
44 activation in flies. Here, we demonstrate that lowering NMN levels in *Drosophila* through
45 the expression of a newly generated prokaryotic NMN-Deamidase (NMN-D) preserves
46 severed axons for months and keeps them circuit-integrated for weeks. NMN-D alters the
47 NAD⁺ metabolic flux by lowering NMN, while NAD⁺ remains unchanged *in vivo*. Increased
48 NMN synthesis, by the expression of mouse nicotinamide phosphoribosyltransferase
49 (mNAMPT), leads to faster axon degeneration after injury. We also show that NMN-
50 induced activation of dSarm mediates axon degeneration *in vivo*. Finally, NMN-D delays
51 neurodegeneration caused by loss of the sole NMN-consuming and NAD⁺-synthesizing
52 enzyme dNmnat. Our results reveal a critical role for NMN in neurodegeneration in the fly,
53 which extends beyond axonal injury. The potent neuroprotection by reducing NMN levels is
54 similar to the interference with other essential mediators of axon degeneration in
55 *Drosophila*.

56

57

58 Introduction

59

60 The elimination of large portions of axons is a widespread event in the developing nervous
61 system (Neukomm and Freeman, 2014; Riccomagno and Kolodkin, 2015). Axon
62 degeneration is also an early hallmark of nervous system injury and a common feature of
63 neurodegenerative diseases (Coleman and Höke, 2020; Mariano et al., 2018; Merlini et al.,
64 2022). Understanding the underlying molecular mechanisms may facilitate the
65 development of treatments to block axon loss in acute or chronic neurological conditions.

66 Wallerian degeneration is a well-established, evolutionarily conserved, and simple
67 system to study how injured axons execute their self-destruction (Llobet Rosell and
68 Neukomm, 2019; Waller, 1850). Upon axonal injury (axotomy), distal axons separated from
69 their soma degenerate within a day. Axotomy activates a signaling pathway (programmed
70 axon degeneration, or axon death) that actively executes the self-destruction of severed
71 axons. Induced signaling culminates in the activation of sterile alpha and TIR motif-
72 containing protein 1 (dSarm and SARM1 in flies and mice, respectively) (Gerdts et al., 2013;
73 Osterloh et al., 2012). As NADase, once activated, dSarm/SARM1 executes the pathological
74 depletion of nicotinamide adenine dinucleotide (NAD⁺) in severed axons, culminating in
75 catastrophic fragmentation (Essuman et al., 2017; Figley et al., 2021; Gerdts et al., 2015).
76 Initially thought to be activated only after injury, evidence accumulated over recent years
77 that axon death signaling is also activated in many non-injury neurological disorders (Figley
78 and DiAntonio, 2020; Hopkins et al., 2021).

79 In mammals, SARM1 activation is tightly controlled by metabolites in the NAD⁺
80 biosynthetic pathway. The labile enzyme nicotinamide mononucleotide
81 adenylyltransferase 2 (NMNAT2) is constantly transported into the axon, where it is
82 degraded by the E3 ubiquitin ligase PAM-Highwire-Rpm-1 (PHR1) and mitogen-activated
83 protein kinase (MAPK) signaling (Babetto et al., 2013; Gilley and Coleman, 2010; Walker et
84 al., 2017). This steady state results in sufficient NMNAT2 that consumes nicotinamide
85 mononucleotide (NMN) to synthesize NAD⁺. Upon axonal injury, axonal transport halts.
86 Subsequently, NMNAT2 is rapidly degraded. It leads to a temporal rise of axonal NMN and
87 a halt in NAD⁺ biosynthesis (di Stefano et al., 2017, 2015; Loreto et al., 2021, 2015). NMN
88 and NAD⁺ compete by binding to an allosteric pocket in the SARM1 armadillo-repeat (ARM)
89 domain, which is crucial for SARM1 activation. While a rise in NMN activates SARM1 by
90 inducing its conformational change (Bratkowski et al., 2020; Figley et al., 2021; Zhao et al.,
91 2019), NAD⁺ prevents this activation by competing for the same pocket in the ARM domain
92 (Jiang et al., 2020). This competitive binding occurs at physiologically relevant levels of
93 NMN and NAD⁺ (Angeletti et al., 2022).

94 Previous studies have shown that expression of the prokaryotic enzyme PncC—also
95 known as NMN-Deamidase (NMNd)—converts NMN to nicotinic acid mononucleotide
96 (NaMN) (Galeazzi et al., 2011), prevents SARM1 activation and preserves severed axons in
97 mammals and zebrafish: for instance, axons with NMNd remain preserved up to 96 h in
98 murine neuronal cultures (di Stefano et al., 2015; Loreto et al., 2015; Sasaki et al., 2016),

99 24 h in zebrafish and 3 weeks in mice (di Stefano et al., 2017). It remains currently unclear
100 whether NMNd expression levels determine the extent of preservation.

101 Much of this mechanism of axon death signaling is conserved in *Drosophila* (Llobet
102 Rosell and Neukomm, 2019). However, flies harbor some notable differences. A single
103 *dnmnat* gene provides a cytoplasmic and nuclear splice protein variant; consequently,
104 *dnmnat* disruption results in cellular dNmnat loss (Ruan et al., 2015). dNmnat turnover is
105 regulated solely by the E3 ubiquitin ligase Highwire (Hiw) (Xiong et al., 2012) but not by
106 MAPK signaling (Neukomm et al., 2017). Furthermore, the BTB/Back domain-containing
107 Axundead (Axed) executes catastrophic fragmentation downstream of NAD⁺ depletion,
108 while the mammalian paralog(s) remain to be identified (Neukomm et al., 2017).

109 The role of NMN in axon degeneration in *Drosophila* is controversial. Flies lack
110 nicotinamide phosphoribosyltransferase (NAMPT) (Gossmann et al., 2012). NMN might,
111 therefore, be a dispensable intermediate in the NAD⁺ biosynthetic pathway, thus playing a
112 minor role as a mediator of axon degeneration (Gerdtts et al., 2016). The Gal4/UAS-
113 mediated NMNd expression in *Drosophila* neurons preserves severed axons for 3–5 days
114 after injury (Hsu et al., 2021). It contrasts with the phenotype of other axon death signaling
115 mediators, such as loss-of-function mutations in *hiw*, *dsarm*, and *axed*, as well as over-
116 expression of *dnmnat* (*dnmnat*^{OE}), all of which harbor severed axons that remain preserved
117 for weeks to months (Fang et al., 2012; Neukomm et al., 2017, 2014; Osterloh et al., 2012).
118 Therefore, the role of NMN as an axon death mediator in *Drosophila* remains to be formally
119 determined.

120 Here, we report that NMN is an essential mediator of injury-induced axon degeneration
121 in *Drosophila*. Genetic modifications resulting in low NMN levels protect severed axons for
122 the lifespan of the fly, while the addition of an extra NMN synthesizing activity forces axons
123 to undergo faster degeneration after injury. NMN induces the dSarm NADase activity,
124 demonstrating its role as a crucial activator *in vivo*.

125

126

127

128 Results

129

130 Robust expression of prokaryotic NMN-Deamidase in *Drosophila*

131 Mutations in *hiw*, *dsarm*, or *axed* attenuate axon death signaling resulting in morphological
132 preservation of severed axons for approximately 50 days, the average lifespan of *Drosophila*
133 (Neukomm et al., 2017, 2014; Osterloh et al., 2012). In contrast, neuronal expression of
134 prokaryotic NMN-Deamidase (NMNd) to consume NMN results in less than 10 % of severed
135 axons being preserved at 7 days post axotomy (dpa) (Hsu et al., 2021). We performed an
136 established wing injury assay to confirm this observation (Paglione et al., 2020). Briefly, a
137 subset of GFP-labeled sensory neurons (e.g., *dpr1-Gal4* MARCM clones) expressing NMNd
138 (Hsu et al., 2021) or GFP were subjected to axotomy in 5–7-day old flies with one wing being
139 partially injured and the other serving as an uninjured control (Figure 1 – figure
140 supplement 1A). At 7 dpa, we quantified uninjured control axons, axonal debris and severed
141 intact axons, respectively (Figure 1 – figure supplement 1B, left), and calculated the
142 percentage of protected severed axons (Figure 1 – figure supplement 1B, right). We
143 observed a 40 % preservation of severed axons with NMNd (Figure 1 – figure supplement 1,
144 genotypes in Table 1 – source data 1). The modest increase of preservation in our hands is
145 probably due to higher NMNd levels caused by higher Gal4 levels in *dpr1* than *elav* (Hsu et
146 al., 2021). However, the expression of NMNd fails to attenuate axon death signaling to the
147 extent of axon death mutants, suggesting that NMN does not play an essential role in
148 activating axon death supported by the absence of the NMN-synthesizing enzyme Nampt
149 in flies (Gossmann et al., 2012). Alternatviely, NMNd expression and the resulting NMN
150 consumption is simply not sufficient for potent attenuation of axon death signaling and
151 preservation of severed axons.

152 Based on the above observations, we decided to generate an N-terminal GFP-tagged
153 NMN-Deamidase (GFP::NMN-D) to increase protein stability (Rücker et al., 2001). Plasmids
154 with GFP-tagged wild-type and enzymatically dead versions of NMN-Deamidase were
155 generated (di Stefano et al., 2017, 2015), under the control of the UAS regulatory sequence
156 (*UAS-GFP::NMN-D*, and *UAS-GFP::NMN-D^{dead}*, respectively). We found that wild-type and
157 enzymatically dead NMN-D enzymes are equally expressed in S2 cells, as detected by our
158 newly generated anti-PncC/NMNd/NMN-D antibodies (Materials & Methods, Figure 1–
159 figure supplement 2). Notably, we observed two immunoreactivities per lane, with the
160 lower band being a potential degradation product.

161 The similar expression of the NMN-D enzymes prompted us to use the plasmids to
162 generate transgenic flies by targeted insertion (*attP40* landing site). To compare *in vivo*
163 expression levels, NMN-D, NMN-D^{dead}, and NMNd were expressed with pan-cellular *actin-*
164 *Gal4*. We found that NMN-D and NMN-D^{dead} immunoreactivities were significantly stronger
165 than NMNd (Figure 1 – figure supplement 2B, C). In addition, GFP immunoreactivity was
166 also detected in NMN-D and NMN-D^{dead}, confirming the robust expression of the newly
167 generated tagged proteins (Figure 1A). These results show that our newly generated GFP-
168 tagged NMN-D variants are substantially stronger expressed than NMNd *in vivo*.

169

170 **Neuronal NMN-D expression blocks injury-induced axon degeneration for the lifespan**
171 **of *Drosophila***

172 The lower-expressed NMNd resulted in a 40% preservation in our wing injury assay. We
173 repeated the injury assay to assess the preservation of our newly generated and higher-
174 expressed NMN-D variants. While severed axons with GFP or NMN-D^{dead} degenerated,
175 axons with NMN-D remained fully preserved at 7 dpa (Figure 1B, C, Figure 1 – figure
176 supplement 3). This contrasts with the weaker preservation of axons with lower NMNd
177 expression (Figure 1 – figure supplement 1). Similarly, strong preservation was seen in
178 cholinergic olfactory receptor neurons (ORNs), where severed axons with NMN-D remained
179 preserved at 7 dpa (Figure 1D). We extended the ORN injury assay and found preservation
180 at 10, 30, and 50 dpa (Figure 1E). While quantifying the precise number of axons is
181 technically not feasible, severed preserved axons were observed in all 10, 30, and 50 dpa
182 brains, albeit fewer at later time points (MacDonald et al., 2006). Thus, high levels of NMN-
183 D confer robust protection of severed axons for multiple neuron types for the entire
184 lifespan of *Drosophila*.

185

186 **NMN-D alters the NAD⁺ metabolic flux to lower NMN in fly heads**

187 Before measuring the effect of NMN-D on the NAD⁺ metabolic flux, we measured the
188 activities of the various NAD⁺ biosynthetic enzymes in fly heads (Figure 2 – figure
189 supplement 1A, Figure 2A) (Amici et al., 2017; Zamporlini et al., 2014). We confirmed that
190 NAD⁺ can be synthesized from nicotinamide (NAM), nicotinamide riboside (NR), and
191 quinolinate. However, the *Drosophila* Qaprt homolog that catalyzes the conversion from
192 quinolinate to nicotinic acid mononucleotide (NaMN) remains to be identified (Katsyuba et
193 al., 2018). We also confirmed the absence of NAMPT activity (Figure 2 – figure
194 supplement 1A) (Gossmann et al., 2012). In addition, we confirmed the expression of genes
195 involved in NAD⁺ synthesis and axon death signaling that are involved in NAD⁺ metabolism
196 by measuring respective mRNA abundance in fly heads by qRT-PCR (Figure 2 – figure
197 supplement 1B). We note that the expression and activity of NAD⁺ metabolic enzymes can
198 be readily detected fly heads.

199 Next, we wanted to know whether the sole expression of NMN-D can change the NAD⁺
200 metabolic flux *in vivo* (Figure 2A). We compared levels of metabolites in heads by LC-
201 MS/MS among samples that expressed NMN-D and NMN-D^{dead} (Figure 2B) (van der Velpen
202 et al., 2021). Consistent with robust NMN-D activity, NMN levels were 6-fold lower and
203 NaMN 12-fold higher. We also found significantly higher NaAD and NaR levels.
204 Importantly, all other metabolites remained unchanged, including NAD⁺ (Figure 2B).

205 Prompted by such a significant change in the NAD⁺ metabolic flux, we wondered
206 whether the change could alter the expression of genes involved in NAD⁺ metabolism or
207 axon death signaling. However, besides the expected significant increase of the Gal4-
208 mediated expression of NMN-D and NMN-D^{dead}, we did not observe any notable changes
209 (Figure 2 – figure supplement 2). Our observations demonstrate that the expression of

210 NMN-D alone is sufficient to change the NAD⁺ metabolic flux, thereby significantly
211 lowering NMN levels without affecting NAD⁺ in *Drosophila* heads; they serve as an excellent
212 tissue for metabolic analyses.

213

214 **Low axonal NMN preserves synaptic connectivity for weeks after injury**

215 Mutations that attenuate axon death signaling robustly suppress the morphological
216 degeneration after axotomy. They also preserve synaptic connectivity. We have previously
217 demonstrated that synaptic connectivity of severed axons with attenuated axon death
218 remains preserved for at least 14 days using an established optogenetic assay (Neukomm
219 et al., 2017; Paglione et al., 2020). Briefly, mechanosensory chordotonal neurons in the
220 Johnston's organ (JO), whose cell bodies are in the 2nd segment of adult antennae, are
221 required and sufficient for antennal grooming (Hampel et al., 2015; Seeds et al., 2014). The
222 JO-specific expression of CsChrimson combined with a red-light stimulus can specifically
223 and robustly induce antennal grooming.

224 We used this assay to test individual flies before bilateral antennal ablation (ctl) and at
225 7 dpa (Figure 3). Flies expressing GFP in JO neurons failed to elicit antennal grooming
226 following red-light exposure at 7 dpa (Figure 3, Video 1). In contrast, flies with JO-specific
227 NMN-D expression continued to elicit antennal grooming at 7 dpa (Figure 3, Video 2).
228 Remarkably, the evoked grooming behavior remained equally robust at 14 dpa (Figure 3 –
229 figure supplement 1). Preservation of synaptic connectivity depended on low NMN levels,
230 as flies expressing NMN-D^{dead} in JO neurons failed to elicit antennal grooming upon red-
231 light exposure at 7 dpa (Figure 3, Video 3). Our findings demonstrate that lowering NMN
232 potently attenuates axon death signaling, which is sufficient to preserve synaptic
233 connectivity of severed axons and synapses for weeks after injury.

234

235 **mNAMPT-expressing axons degenerate faster after injury**

236 Two enzymatic reactions synthesize NMN in mammals: NAMPT-mediated NAM and
237 NRK1/2-mediated NR consumption. *Drosophila* lacks NAMPT activity, and NMN synthesis
238 relies solely on Nrk-mediated NR consumption (Figure 2 – figure supplement 1A). We
239 hypothesized that mouse NAMPT (mNAMPT) expression could increase NMN synthesis
240 and, therefore, lead to faster injury-induced axon degeneration *in vivo* (Figure 4A). We
241 generated transgenic flies harboring mNAMPT under the control of UAS by targeted
242 insertion (*attP40*). Western blots revealed proper expression of mNAMPT in fly heads
243 (Figure 4B).

244 We then tested the effect of mNAMPT on the NAD⁺ metabolic flux *in vivo*. Surprisingly,
245 NAM, NMN, and NAD⁺ levels remained unchanged under physiological conditions
246 (Figure 4C). However, we noticed 3-fold higher NR and a moderate but significant elevation
247 of ADPR and cADPR levels upon mNAMPT overexpression (Figure 4C). We also asked
248 whether mNAMPT impacts on NAD⁺ homeostasis thereby altering the expression of axon
249 death or NAD⁺ synthesis genes. Besides the expected significant increase in the Gal4-

250 mediated expression of *mNAMPT*, we did not observe any notable changes at the mRNA
251 level (Figure 4 – figure supplement 1).

252 Although *mNAMPT* expression failed to elevate NMN under physiological conditions, we
253 hypothesized that *mNAMPT* could boost NMN levels after injury because of the following
254 observations in mammals: *NMNAT2* is labile and rapidly degraded in severed axons (Gilley
255 and Coleman, 2010), while *NAMPT* persists much longer (di Stefano et al., 2015). We
256 speculated that in flies, in severed axons *dNmnat* declines similarly, but not *mNAMPT*.
257 Consequentially, NMN accumulates. Strikingly, in our wing injury assay, while axons with
258 GFP showed signs of degeneration starting from 6 hours post axotomy (hpa), *mNAMPT*
259 expression resulted in significantly faster axon degeneration with signs of degeneration at
260 4 hpa (Figure 4D, E). This accelerated degeneration is likely linked to increased NMN
261 production, but other mechanisms cannot be excluded as there is no increase in NMN
262 under physiological conditions.

263 We next asked whether the faster degeneration of *mNAMPT*-expressing severed axons
264 requires axon death genes. While mutations in *dsarm* and *hiw* completely blocked the
265 degeneration of severed axons expressing *mNAMPT*, *axed* showed a partial preservation of
266 60% at 12 hours after injury (Figure 4F). Importantly, *axed* mutants, in the absence of
267 *mNAMPT* expression, showed a similar preservation within the first 12 hours (Figure 4 –
268 figure supplement 2). This preservation remained unchanged at 7 dpa, suggesting that
269 *mNAMPT* expression does not change the preservation provided by *axed*, *dsarm*, and *hiw*
270 (Figure 4 – figure supplement 2, Figure 4G). Our observations support that elevated NMN
271 levels require axon death signaling to initiate the degeneration of severed axons.

272 Overall, our data suggest that NMN accumulation after injury triggers axon
273 degeneration in *Drosophila* through the axon death pathway. To the best of our knowledge,
274 we provide the first direct *in vivo* demonstration that an additional source of NMN
275 synthesis—by the expression of *mNAMPT*—accelerates injury-induced axon degeneration.
276

277 **NMN activation of dSarm NADase is required for axon degeneration *in vivo***

278 We have shown that low NMN attenuates injury-induced axon degeneration, while a more
279 rapid accumulation of NMN, due to expression of *mNAMPT*, results in faster injury-induced
280 axon degeneration. A cell-permeable form of NMN (CZ-48) binds to and activates *SARM1*
281 by changing its conformation (Zhao et al., 2019). Crystal structures of the ARM domain of
282 *dSarm* (*dSarm*^{ARM}), as well as the full-length human *SARM1* (*hSARM1*), support the
283 observation that NMN acts as a ligand for *dSarm*^{ARM} (Figley et al., 2021; Gu et al., 2021).
284 NMN binding to the ARM domain requires a critical residue, lysine 193 (K193), to induce a
285 conformational change in the ARM domain of *dSarm/SARM1*. Consistent with this, a
286 mutation of the lysine residue (e.g., K193R) results in a dominant-negative injury-induced
287 axon degeneration phenotype in murine cell cultures (Bratkowski et al., 2020; Figley et al.,
288 2021; Geisler et al., 2019; Loreto et al., 2021; Zhao et al., 2019).

289 To confirm whether NMN activates *dSarm* *in vitro* and *in vivo*, we generated *dsarm*
290 constructs encoding wild-type and the human K193R-equivalent K450R mutation. Crucially,

291 an isoform we used previously, dSarm(D), fails to fully rescue the *dsarm*⁸⁹⁶ defective axon
292 death phenotype (Figure 5 – figure supplement 1A, B) (Neukomm et al., 2017). Therefore,
293 among the eight distinct *dsarm* transcripts, which all contain the ARM, SAM, and TIR
294 domains, we chose the shortest coding isoform, *dsarm*(E) (Figure 6 – figure supplement 1A).
295 We generated untagged and C-terminal FLAG-tagged dSarm(E), with and without K450R,
296 under the control of UAS and confirmed the FLAG-tagged proteins are expressed at similar
297 levels in S2 cells (Figure 5A). We also directly tested the immunopurified FLAG-tagged
298 proteins for constitutive and NMN-inducible NADase activity (Figure 5B). While wild-type
299 and K450R dSarm(E) had similar constitutive activities in the presence of 25 μM NAD⁺
300 alone, we found that only wild-type NADase activity was induced further with the addition
301 of 50 μM NMN. At the same time, K450R remained essentially unchanged (Figure 5C). This
302 confirmed the critical role of K450 in NMN-dependent activation of the dSarm NADase,
303 equivalent to the role of K193 in hSARM1 (Figley et al., 2021; Loreto et al., 2021).

304 Next, we generated transgenic flies expressing tagged and untagged wild-type and
305 mutant dSarm(E) variants—by targeted insertion of the *UAS-dsarm*(E) plasmids (*attP40*)—
306 and confirmed pan-cellular expression of the FLAG-tagged variants by immunoblotting
307 (Figure 5D). We used all variants for *dsarm*⁸⁹⁶ axon death defective rescue experiments in
308 our wing injury assay. We found that the expression of wild-type dSarm(E) (both tagged
309 and untagged) almost entirely rescued *dsarm*⁸⁹⁶ mutants, whereas dSarm(E^{K450R}) proteins
310 completely failed to rescue the phenotype at 7 dpe (Figure 5E). We demonstrate that a non-
311 inducible NADase variant, dSarm(E^{K450R}), in the absence of wild-type dSarm, fails to
312 execute injury-induced axon degeneration *in vivo*.

313

314 **The preservation of severed axons provided by NMN-D is partially reverted by RNAi-** 315 **mediated knockdown of Nadsyn**

316 We have now established that NMN activates dSarm to trigger the degeneration of severed
317 axons in *Drosophila*. While NMN induces a conformational change in a pocket of the ARM
318 domain, NAD⁺ prevents this activation by competing for the same pocket (Bratkowski et
319 al., 2020; Figley et al., 2021; Jiang et al., 2020; Zhao et al., 2019). We therefore wanted to
320 test whether the preservation provided by lower NMN is reverted by a simultaneous
321 reduction of NAD⁺ synthesis. We generated NMN-D-expressing neurons containing RNAi-
322 mediated knockdown of Nadsyn (*nadsyn*^{RNAi}). At 7 dpa, the 100 % preservation provided by
323 NMN-D was partially reduced to 60 % by *nadsyn*^{RNAi} *in vivo* (Figure 5 – figure supplement 2).
324 This observation supports the degenerative NMN and the protective NAD⁺ function by
325 activating and inhibiting dSarm in injury-induced axon degeneration in *Drosophila*.

326

327 **Low NMN delays neurodegeneration triggered by loss of *dnmnat***

328 Lowering levels of NMN confers very robust protection against axon degeneration in
329 *Drosophila*, similar to that achieved by targeting other mediators of axon degeneration,
330 such as *hiw*, *dsarm*, *axed*, and the over-expression of *dnmnat* (*dnmnat*^{OE}) (Fang et al., 2012;

331 Neukomm et al., 2017, 2014; Osterloh et al., 2012; Paglione et al., 2020; Xiong et al., 2012).
332 We therefore assessed the genetic interaction among these regulators *in vivo*.

333 The current model, supported by our data, predicts that NMN accumulation occurs
334 upstream of dSarm activation. Consistent with this, the induced expression of
335 constitutively active dSarm lacking its inhibitory ARM domain (dSarm^{ΔARM}) is sufficient to
336 pathologically deplete NAD⁺, triggering axon- and neurodegeneration in the absence of
337 injury (Essuman et al., 2017; Neukomm et al., 2017). We asked whether lowering levels of
338 NMN can delay or prevent neurodegeneration induced by dSarm^{ΔARM}-mediated NAD⁺
339 depletion. *dsarm*^{ΔARM} clones with forced NAD⁺ depletion rapidly degenerated within 5 days
340 after adults were born (days post eclosion, dpe) (Figure 6A). As expected, lowering NMN
341 levels by NMN-D in *dsarm*^{ΔARM} clones did not alter the kinetics of neurodegeneration
342 (Figure 6A). These observations further support that NMN accumulation occurs upstream
343 of dSarm activation, and that once neuronal NAD⁺ is low, neurodegeneration cannot be
344 halted by low NMN.

345 We also asked whether lowering NMN interferes with loss-of-function mutations of
346 *axed*, *dsarm*, double mutants, *hiw*, and *dnmnat*^{OE}. As expected, the attenuated axon death
347 phenotype of low NMN did not change in these mutant backgrounds at 7 dpe (Figure 6B).

348 Loss-of-function mutations in *dnmnat* also activate axon death signaling, leading to
349 neurodegeneration in the absence of injury (Neukomm et al., 2017). dNmnat is the sole
350 enzyme with NAD⁺ biosynthetic activity in *Drosophila*. *dnmnat*¹ mutant clones lack NMN
351 consumption and NAD⁺ synthesis (Zhai et al., 2006), and they degenerate with similar
352 kinetics as *dsarm*^{ΔARM} clones (Neukomm et al., 2017). We asked whether low NMN levels
353 can delay or prevent *dnmnat*¹-induced neurodegeneration. Surprisingly, although not
354 expected to restore NAD⁺ synthesis, lowering NMN levels significantly delayed
355 neurodegeneration (Figure 6C). Between 1–5 dpe, while clones with *dnmnat*¹ fully
356 degenerated, NMN-D expressing *dnmnat*¹ clones remained morphologically intact, similar
357 to controls. After 5 days, these clones gradually started to deteriorate (Figure 6C). This
358 protective delay of neurodegeneration depends on lowering NMN levels, as the expression
359 of NMN-D^{dead} completely failed to protect *dnmnat*¹ neurons (Figure 6C).

360 To confirm that NMN-D delays *dnmnat*¹-mediated neurodegeneration, we wanted to
361 generate tissue-specific CRISPR/Cas9 *dnmnat* knockouts. CRISPR/Cas9 tools significantly
362 facilitate genetics in *Drosophila*. Instead of using mutants in a specific genomic locus,
363 mutations are generated by co-expressing Cas9 and *sgRNAs*.

364 First, we generated transgenic flies harboring *tRNA*-flanked *sgRNAs* to target four
365 distinct loci in *dnmnat* under the control of UAS (Port and Bullock, 2016). We made similar
366 transgenic flies to target all other axon death genes (Figure 6 – figure supplement 1A). We
367 then tested our novel tools for their ability to attenuate axon death by assessing preserved
368 axonal morphology (Figure 6 – figure supplement 1B) and synaptic connectivity after injury
369 (Figure 6 – figure supplement 1C). We found that the preservation depended on the
370 combination of the tissue (e.g., Gal4 driver) and the Cas9 source (e.g., *UAS-cas9* vs. *actin*–

371 *cas9*). Our observations highlight that the combination of Cas9 and *sgRNAs* must be
372 carefully determined in each tissue targeted by CRISPR/Cas9.

373 We then asked whether *dnmnat^{sgRNAs}* can trigger neurodegeneration by analyzing
374 neuronal survival (Figure 6 – figure supplement 1D) and synaptic connectivity over time
375 (Figure 6 – figure supplement 1E). Notably, we observed synthetic lethality in *UAS–*
376 *dnmnat^{sgRNAs} actin–Cas9* flies; we thus used *UAS–cas9*. Neurons with CRISPR/Cas9-targeted
377 *dnmnat* degenerated as fast as *dnmnat¹* mutants (Figure 6 – figure supplement 1D). In line
378 with these findings, we observed reduced synaptic connectivity in 7- and 14-day-old flies
379 (Figure 6 – figure supplement 1E). We also found the expression of NMN-D in *dnmnat^{sgRNAs}*
380 clones resulted in similar neuroprotection as observed with *dnmnat¹* mutants. They
381 remained morphologically intact during the first 5 days and then gradually degenerated
382 (Figure 6 – figure supplement 1F). Therefore, NMN-D can also delay neurodegeneration in
383 CRISPR/Cas9-targeted *dnmnat* clones by preventing NMN accumulation.

384 Taken together, our *in vivo* results suggest that in the absence of *dnmnat*, NMN-D
385 prevents NMN accumulation and therefore delays neurodegeneration. However, neurons
386 subsequently degenerate because NAD⁺ synthesis halts, and NAD⁺ gradually decays below
387 the threshold of survival. Similarly, NMN-D fails to delay neurodegeneration when
388 dSarm^{ΔARM} forcefully depletes NAD⁺. These results support the role of NMN as an activator
389 rather than an executioner in axon death signaling.

390

391 Discussion

392

393 Here we investigate how lowering of the NAD⁺ precursor metabolite NMN influences axon
394 survival in *Drosophila*, using robust expression of prokaryotic NMN-D, as demonstrated
395 with newly generated anti-PncC/NMNd antibodies. When expressed, NMN-D consumes
396 NMN to synthesize NaMN in *Drosophila* heads. While the preservation by NMN-D could in
397 principle reflect an inhibitory effect of NaMN (Sasaki et al., 2021), the additional
398 acceleration of degeneration by mNAMPT strongly argues that NMN is a key mediator of
399 dSarm-driven axon degeneration. In the context of injury-induced axon degeneration,
400 neuronal expression of NMN-D to keep NMN low is sufficient to block axon death signaling:
401 severed axons with NMN-D remain morphologically preserved for the lifespan of flies, and
402 circuit-integrated for weeks after injury. Notably, the NMN-D-mediated change of the
403 NAD⁺ metabolic flux does not alter axon death or NAD⁺ synthesis gene expression,
404 highlighting the usefulness of the NMN-D tool in *Drosophila*.

405 Neurodegeneration induced by dNmnat depletion is also delayed by low NMN levels.
406 Our data indicate that NMN is a key mediator of axon degeneration in *Drosophila*, acting as
407 an activator of dSarm in the axon death pathway *in vivo*. This is consistent with
408 observations in mammals (Bratkowski et al., 2020; di Stefano et al., 2015; Zhao et al., 2019)
409 and with previously reported direct binding of NMN to the dSarm ARM domain (Figley et
410 al., 2021).

411 The discovery and characterization of the axon death signaling pathway revealed four
412 major players mediating axonal degeneration in *Drosophila*. Loss-of-function mutations in
413 *hiw*, *dsarm*, and *axed*, as well as *dnmnat* over-expression robustly inhibit injury-induced
414 axon degeneration (Fang et al., 2012; Neukomm et al., 2017, 2014; Osterloh et al., 2012;
415 Xiong et al., 2012). We now show that lowering NMN levels has an equally potent
416 protective effect, adding NMN as an additional mediator to the signaling pathway.
417 Synaptic connectivity of severed axons is also preserved for weeks, comparable to *hiw*,
418 *dsarm*, and *axed* mutants (Neukomm et al., 2017), and *dnmnat* over-expression (Paglione et
419 al., 2020).

420 Our demonstration of NMN as a mediator of axon degeneration in *Drosophila* addresses
421 an important question in the field. While recent discoveries confirm the original finding of a
422 pro-degenerative action of NMN (di Stefano et al., 2015), the role of NMN in axon
423 degeneration has also been questioned, especially in *Drosophila*. Given the absence of
424 NAMPT in flies, it is tempting to speculate that NMN—as a minor intermediate of the NAD⁺
425 metabolic pathway—is not a primary mediator in injury-induced axon degeneration (Gerdtts
426 et al., 2016). However, we provide compelling evidence that NMN is not only present in flies
427 as previously reported (Lehmann et al., 2017) but that its accumulation causes axon
428 degeneration. In line with other studies, we show further proof that NMN acts as an
429 activator of dSarm *in vitro* by using a new *dsarm* isoform, *dsarm(E)*, which is fully functional
430 in axon death signaling. Its non-inducible variant, dSarm(E^{K450R}) fails to rescue the
431 attenuated axon degeneration phenotype in neurons lacking *dsarm*. Together with the

432 reported dominant negative effect of SARM1(^{K193R}) in mice (Geisler et al., 2019), our
433 observations further support that NMN activation of dSarm also occurs *in vivo*.

434 The previously published NMNd revealed partially protected axons 7 days after injury in
435 the wing (Hsu et al., 2021), while our NMN-D extends preservation to 50 days. This
436 difference is likely due to the N-terminal GFP tag in GFP::NMN-D, which can increase
437 protein stability (Rücker et al., 2001). This is supported by our newly generated anti-PncC
438 antibodies and suggests that NMN-D expression levels dictate the reduction of NMN, and
439 therefore the preservation of severed axons.

440 We also demonstrate that increasing the synthesis of NMN provokes a faster
441 degeneration of severed axons *in vivo*, which requires all axon death mediators. Mammals
442 synthesize NMN with two distinct enzymatic reactions: NR consumption by NRK1/2 and
443 NAM consumption by NAMPT, both ensuring NMN supply. In *Drosophila*, NAMPT activity is
444 absent, and NMN appears to be synthesized by NrK alone, yet dietary NMN
445 supplementation might also contribute to NMN levels (Yoshino et al., 2018). We used
446 mNAMPT as an extra source of NMN synthesis. However, in contrast to the NMN-D-
447 induced change in the NAD⁺ metabolic flux, mNAMPT had only a minor impact under
448 physiological conditions. It is challenging to measure the specific axonal rise in NMN after
449 injury *in vivo*. However, NMNAT2 is rapidly disappearing in severed axons (Gilley and
450 Coleman, 2010), and so is dNmnat in *Drosophila* axons and synapses (Xiong et al., 2012),
451 through PHR1 and Hiw, respectively, while NAMPT persists longer (di Stefano et al., 2015).
452 It is therefore likely that persisting mNAMPT in severed *Drosophila* axons continues NMN
453 synthesis, leading to faster NMN accumulation, dSarm activation, and faster axon
454 degeneration.

455 While NMN activates dSarm by inducing a conformational change in a pocket of the
456 inhibitory ARM domain, NAD⁺ competes for the same pocket, acting as an inhibitor of
457 dSarm activation (Jiang et al., 2020). Our simultaneous manipulation of NMN and NAD⁺
458 levels (by NMN-D expression and *nadsyn*^{RNAi}, respectively) further supports that this
459 competition is crucial in *Drosophila* to regulate dSarm activity and, consequentially, axon
460 degeneration after axotomy *in vivo*.

461 Finally, we expanded our investigations beyond injury, by looking at NMN in a model of
462 neurodegeneration. dNmnat is essential for NAD⁺ synthesis. While neuronal clones with
463 mutant *dnmnat*² start to degenerate after they are born, intriguingly, co-expression of
464 NMN-D resulted in a preserved neuronal morphology for at least 5 days, before
465 degeneration started with similar kinetics. Our results suggest that a rise in NMN, rather
466 than the lack of NAD⁺ biosynthesis, is a trigger for neurons to degenerate also in this
467 model, at least within the first 5 days. Once NAD⁺ levels drop beyond neuronal survival,
468 neurons eventually degenerate. This is supported by observation with forced NAD⁺
469 depletion by dSarm^{ΔARM} (Neukomm et al., 2017) and inhibition of NAD⁺ biosynthesis in
470 murine neurons with FK866 (di Stefano et al., 2015). Still, it is surprising to observe that
471 neurons lacking NAD⁺ synthesis can survive for days. It suggests either that the NAD⁺

472 turnover is slower than expected (Liu et al., 2018) or mechanisms are in place to
473 compensate for NAD⁺ loss, at least in the short term.

474 In conclusion, NMN is a potent mediator of axon- and neurodegeneration in *Drosophila*.
475 Our newly developed NMN-D tool will be useful in many degenerative aspects beyond
476 injury, such as in axon morphogenesis and maintenance (Izadifar et al., 2021) and in
477 dendrite pruning (Ji et al., 2022). Our metabolic analyses further demonstrate that
478 *Drosophila* serves as an excellent model system to study NAD⁺ metabolism *in vivo*.
479

480 **Figure legends**

481

482 **Figure 1. Neuronal expression of prokaryotic NMN-D preserves the morphology of**
483 **severed axons for the lifespan in *Drosophila*.** **A** Equal expression of wild-type and
484 enzymatic dead NMN-D enzymes, respectively. Western blots with anti-PncC and anti-GFP
485 immunoreactivities (red and green, respectively). **B** Low NMN results in severed wing
486 sensory neuron axons that remain morphologically preserved at 7 dpa. Examples of control
487 and 7 dpa. **C** Axon death quantification. % preservation of injured axons at 7 dpa, average \pm
488 standard error of the mean ($n = 15$ wings). **D** Low NMN results in severed axons of olfactory
489 receptor neurons that remain morphologically preserved at 7 dpa. Examples of control and
490 7 dpa (arrows, site of unilateral ablation). Lower right, % of brains with severed preserved
491 axon fibers. **E** Low NMN results in severed axons that remain morphologically preserved for
492 50 days. Representative pictures of 10, 30, and 50 dpa, from a total of 10 brains imaged for
493 each condition (arrows, site of unilateral ablation). Lower right, % of brains with severed
494 preserved axon fibers.

495

496 **Figure 1 – figure supplement 1. Partial preservation of severed axons at 7 dpa by**
497 **previously published NMN-Deamidase (NMNd).** **A** Control and 7 days post axotomy
498 (7 dpa) examples of GFP- and NMNd-expressing axons in the wing injury assay. Cell bodies
499 in the cut-off distal wing are immediately counted to determine severed axons. After injury,
500 the number of neuronal cell bodies (cb) that remain attached in the proximal wing–
501 displayed in the upper right corner of each example–indicates how many uninjured, thus
502 expected axons remain in the nerve bundle. **B** Axon death quantification. Left: average
503 numbers of uninjured control, debris, and severed intact axons (white, gray, and black,
504 respectively; $n = 15$ wings). Right: % preservation of injured axons at 7 dpa, average \pm
505 standard error of the mean ($n = 15$ wings).

506

507 **Figure 1 – figure supplement 2. Increased NMN-D detected by anti-PncC antibodies.**
508 **A** NMN-D expression and detection by anti-PncC antibodies in S2 cells. **B** Increased levels
509 of NMN-D compared to NMNd in heads of *Drosophila*. Arrow, predicted NMN-Deamidase;
510 arrowhead, potential degradation product. **C** Quantification of Western blot PncC-
511 immunoreactivity by densitometry. 2 heads / lane; mean \pm standard deviation ($n = 4$); a.u.,
512 arbitrary units. One-way ANOVA with Tukey's multiple comparisons test. *** = $p < 0.001$,
513 ns, not significant, = $p > 0.05$.

514

515 **Figure 1 – figure supplement 3. Quantification of axonal phenotypes.** Average numbers
516 of uninjured control, debris, and severed intact axons (white, gray, and black, respectively;
517 $n = 15$ wings, 7 dpa – and +, respectively).

518

519

520 **Figure 2. Pan-cellular NMN-D expression alters the flux of NAD⁺ metabolites to lower**
521 **NMN in heads of *Drosophila*.** **A** *Drosophila* NAD⁺ metabolic pathway. Black, metabolites;
522 grey, enzymes; blue, prokaryotic NMN-D, respectively. **B** The expression of NMN-D results
523 in lower NMN and higher NaMN, NaAD, and NaR levels, respectively. **C** % NMN / NAD⁺
524 ratio. Extracted metabolites from 50 heads, mean ± standard deviation ($n = 4$). Dots,
525 individual measurements. One-way ANOVA with Tukey's multiple comparisons test, ****
526 = $p < 0.0001$, ns = $p > 0.05$.

527

528 **Figure 2 – figure supplement 1. Enzymatic activity and expression levels of NAD⁺**
529 **synthesis and axon death genes.** **A** Enzymatic activities of NAD⁺ metabolic pathway
530 proteins in extracts of *Drosophila* heads. Qaprt-like: quinolinate phosphoribosyltransferase-
531 like activity, catalyzes quinolinate to NaMN from the de novo NAD⁺ synthesis pathway. The
532 identity of *Drosophila* Qaprt remains currently unknown (REF Katsyuba 2018, Nature).
533 Values are listed as mean ± standard deviation ($n = 2$). **B** mRNA abundance of axon death
534 and NAD⁺ synthesis genes normalized to *α-tubulin 84B* in *Drosophila* heads. Amplicon
535 primers covered all isoforms of each gene tested ($n = 3$). One-way ANOVA with Tukey's
536 multiple comparisons test, **** = $p < 0.0001$. nd, not determined.

537

538 **Figure 2 – figure supplement 2. Lower NMN does not alter mRNA abundance of axon**
539 **death or NAD⁺ synthesis genes in *Drosophila* heads.** Data is shown as box and dot plots (n
540 = 3). Amplicon primers covered all isoforms of each gene tested. One-way ANOVA with
541 Tukey's multiple comparisons test, **** = $p < 0.0001$, ns = $p > 0.05$.

542

543 **Figure 3. Low neuronal NMN preserves synaptic connectivity at 7 dpa.** Antennal
544 grooming induced by red light. Left: ethograms of uninjured control (ctl) and 7 dpa flies.
545 Gray bars, 10 s red light; colored boxes, bins; black line, sum of bins ($n = 15$ flies). Right:
546 average bins per fly during 10 s red-light exposure ($n = 15$ flies). Two-tailed t-student test,
547 **** = $p < 0.0001$, ns = $p > 0.05$.

548

549 **Figure 3 – figure supplement 1. Low neuronal NMN preserves synaptic connectivity for**
550 **weeks after injury.** Antennal grooming induced by red light. Left: ethograms of uninjured
551 control (ctl), 7 and 14 dpa flies. Gray, 10 s red light; blue boxes; bins; black line, sum of bins
552 ($n = 15$ flies). Right: average bins per fly during 10 s red-light exposure ($n = 15$ flies). Two-
553 tailed t-student test, ** = $p < 0.01$, ns = $p > 0.05$.

554

555 **Video 1.**

556 Examples of red light-stimulated wild-type flies expressing CsChrimson and GFP in JO
557 neurons, uninjured and at 7 dpa.

558

559 **Video 2.**

560 Examples of red light-stimulated wild-type flies expressing CsChrimson and GFP::NMN-D
561 in JO neurons, uninjured and at 7 dpa.

562

563 **Video 3.**

564 Examples of red light-stimulated wild-type flies expressing CsChrimson and GFP::NMN-
565 D^{dead} in JO neurons, uninjured and at 7 dpa.

566

567 **Figure 4. Faster injury-induced axon degeneration through mammalian NAMPT**
568 **expression. A** *Drosophila* NAD⁺ metabolic pathway. Black, metabolites; grey, enzymes;
569 blue, mouse NAMPT (mNAMPT). **B** Detection of mNAMPT expression in heads by Western
570 blot. **C** Subtle changes in NAD⁺ metabolic flux by mNAMPT expression in fly heads.
571 Genotypes indicated in B. Extracted metabolites from 50 heads, mean ± standard deviation
572 ($n = 4$). Dots, individual measurements. One-way ANOVA with Tukey's multiple
573 comparisons test. **D** The expression of mNAMPT results in faster axon degeneration after
574 injury. Examples of injured axons at 4 hours post axotomy (hpa). **E** % preservation of
575 injured axons within 12 hours post axotomy (hpa), average ± standard error of the mean (n
576 = 20 wings). Multiple unpaired t-tests. **F** Faster axon degeneration by mNAMPT expression
577 requires axon death genes. % preservation of injured axons within 12 hpa, average ±
578 standard error of the mean ($n = 10$ wings) **G** % preservation of injured axons at 7 dpa,
579 average ± standard error of the mean ($n = 15$ wings) **** = $p < 0.0001$, *** = $p < 0.001$, * = p
580 < 0.01, ns = $p > 0.05$.

581

582 **Figure 4 – figure supplement 1. mNAMPT expression does not alter mRNA abundance**
583 **of axon death or NAD⁺ synthesis genes in *Drosophila* heads.** Data is shown as box and
584 dot plots ($n = 3$). Amplicon primers covered all isoforms of each gene tested. One-way
585 ANOVA with Tukey's multiple comparisons test, **** = $p < 0.0001$, ns = $p > 0.05$.

586

587 **Figure 4 – figure supplement 2. Preservation provided by *axed* is not altered by the**
588 **expression of mNAMPT.** % preservation of injured axons within 12 hpa and at 7 dpa (left
589 and right, respectively). Average ± standard error of the mean ($n = 20$ wings). One-way
590 ANOVA with Tukey's multiple comparisons test, ns = $p > 0.05$.

591

592 **Figure 5. NMN inducibility of dSarm NADase is required for axon degeneration *in vivo*.**
593 **A** Expression and detection of wild-type and K450R dSarm(E) variants in S2 cells.
594 **B** Immunoblot of immunopurified dSarm(E)::FLAG and dSarm(E^{K450R})::FLAG. Known
595 amounts of immunopurified human SARM1 (hSARM1) were used to quantify the levels of
596 immunopurified dSarm(E); 12.5 ng = 154.5 fmol hSARM1; 25 ng = 309 fmol hSARM1
597 **C** NADase activity of dSarm. Left: NADase activity (mol NAD consumed / min / mol dSarm)
598 of immunopurified dSarm(E)::FLAG and dSarm(E^{K450R})::FLAG in the presence of 25 μM
599 NAD⁺, or 25 μM NAD⁺ + 50 μM NMN. Right: degree of MNM induction (fold-change relative
600 to NAD⁺ alone). Mean ± standard error of mean ($n = 7$). Control immunoprecipitations

601 (using extracts from *Actin-Gal4* transfected S2 cells) revealed no non-specific NAD⁺-
602 consuming activity on equivalent amounts of bead / antibody complexes compared to that
603 used in the dSarm(E) activity assays ($n = 7$). Multiple paired t-test with false discovery rate
604 (FDR) correction. **D** Equal expression levels of dSarm(E) variants in *Drosophila* heads.
605 **E** Rescue experiments of dSarm(E) variants in *dsarm*⁸⁹⁶ mutant clones. dSarm(E) rescues,
606 while dSarm(E^{K450R}) fails to rescue the *dsarm*⁸⁹⁶ axon death defective phenotype.
607 % preservation of severed axons at 7 dpa, average \pm standard error of mean ($n = 15$ wings).
608 ns = $p > 0.05$, * = $p < 0.05$.

609

610 **Figure 5 – figure supplement 1. Partial rescue of *dsarm*⁸⁹⁶ axon death defective**
611 **phenotype by dSarm(D) isoform.** **A** dSarm(D)::GFP is not detected by GFP
612 immunoreactivity in Western blots of fly heads. **B** Expression of dSarm(D) and
613 dSarm(D)::GFP partially rescues the *dsarm*⁸⁹⁶ axon death defective phenotype.
614 % preservation of injured axons at 7 dpa, average \pm standard error of the mean ($n = 15$
615 wings).

616

617 **Figure 5 – figure supplement 2. Preservation of severed axons provided by NMN-D**
618 **requires Nadsyn.** **A** *Drosophila* NAD⁺ metabolic pathway. Black, metabolites; grey,
619 enzymes; blue, NMN-D; red prohibition, *nadsyn*^{RNAi}. **B** The preservation provided by NMN-
620 D is partially reverted by *nadsyn*^{RNAi}. % preservation of injured axons at 7 dpa, average \pm
621 standard error of the mean ($n = 15$ wings).

622

623 **Figure 6. Low neuronal NMN delays neurodegeneration triggered by the loss of**
624 ***dnmnat*.** **A** Low NMN fails to prevent neurodegeneration triggered by dSarm ^{Δ ARM}-
625 mediated NAD⁺ depletion. Top: examples of cell bodies and axons at 5 days post eclosion
626 (dpe). Bottom: quantification of intact cell bodies, average \pm 95 % confidence interval (CI),
627 ($n = 10$ wings). **B** Epistasis analysis of low NMN with axon death signaling genes. Low NMN
628 does not alter *axed*, *dsarm*, *hiw*, or *dnmnat* overexpression (+ *dnmnat*^{OE}) phenotypes in the
629 wing injury assay. % preservation of injured axons at 7 dpa, average \pm standard error of the
630 mean ($n = 15$ wings). **C** Low NMN delays neurodegeneration triggered by the loss of
631 *dnmnat*. Top: examples of cell bodies and axons at 5 dpe. Bottom: quantification of intact
632 cell bodies, average \pm 95 % CI, ($n = 10$ wings). Multiple unpaired t-tests. All tests are
633 compared to the control group (e.g., black dots). **** = $p < 0.0001$, *** = $p < 0.001$, * = $p <$
634 0.05.

635

636 **Figure 6 – figure supplement 1. Newly generated *sgRNAs* targeting axon death genes.**
637 **A** Targets and orientation of axon death gene *sgRNAs*. Schematic genomic loci and
638 indicated isoforms. Black arrows, *sgRNA* target and orientation. **B** Preservation of severed
639 axons by attenuated axon death CRISPR/Cas9 tools depends on Cas9 source.
640 % preservation of severed axons (average \pm 95 % CI) at 7 dpa ($n = 15$ wings). **C** Preservation
641 of synaptic connectivity after injury by attenuated axon death CRISPR/Cas9 tools depends

642 on Cas9 source. Quantification of bins, average \pm standard deviation ($n = 15$ flies). Two-way
643 ANOVA with Tukey's multiple comparisons test. **D** Activation of axon death by targeting
644 *dnmnat* with CRISPR/Cas9 phenocopies *dnmnat*¹ mutants (*dnmnat*^{sgRNAs} + *UAS-cas9*).
645 Quantification of intact cell bodies, average \pm 95 % CI ($n = 10$ wings). Multiple unpaired t-
646 tests. All tests are compared to the control group (e.g., black dots). **E** Activation of axon
647 death by targeting *dnmnat* with CRISPR/Cas9 reduces evoked grooming behavior over time
648 (*dnmnat*^{sgRNAs} + *UAS-cas9*). Quantification of bins, average \pm standard deviation ($n = 15$
649 flies). Two-way ANOVA with Tukey's multiple comparisons test. **F** Low NMN delays
650 degeneration in CRISPR/Cas9-targeted *dnmnat* neurons (*dnmnat*^{sgRNAs} + *UAS-cas9*).
651 Quantification of intact cell bodies, average \pm 95 % CI ($n = 10$ wings). Multiple unpaired t-
652 tests. All tests are compared to the control group (e.g., black dots). **** = $p > 0.0001$, ***
653 = $p < 0.001$, ** = $p > 0.01$, * = $p < 0.05$.

654

655 **Table 1 – source data 1. Genotypes in each display item.** Abbreviations: *mCD8::GFP* =
656 *UAS-mCD8::GFP*, *dpr1* = *dpr1-Gal4*

657

658 **Source data legends**

659

660 **Figure 1 – source data 1. A** Raw unedited Western blots and uncropped blots with relevant
661 bands clearly labeled. **C** Raw data of quantified preserved severed axons.

662

663 **Figure 1 – figure supplement 1 – source data 1. B** Raw data of quantified preserved
664 severed axons.

665

666 **Figure 1 – figure supplement 2 – source data 1. A** Raw unedited Western blots and
667 uncropped blots with relevant bands clearly labeled. **B** Raw unedited Western blots and
668 uncropped blots with relevant bands clearly labeled. **C** Raw data of Western blot
669 quantification.

670

671 **Figure 1 – figure supplement 3 – source data 1. C** Raw data of quantified preserved
672 severed axons.

673

674 **Figure 2 – source data 1. B** Raw data of metabolomic measurement.

675

676 **Figure 2 – figure supplement 1 – source data 1. A** Raw data of enzymatic activity. **B** Raw
677 data of qRT-PCR.

678

679 **Figure 2 – figure supplement 2 – source data 1.** Raw data of qRT-PCR.

680

681 **Figure 3 – source data 1.** Raw data of grooming.

682

683 **Figure 3 – figure supplement 1 – source data 1.** Raw data of grooming.

684

685 **Figure 4 – source data 1. B** Raw unedited Western blots and uncropped blots with relevant
686 bands clearly labeled. **C** Raw data of metabolomic measurement. **E** Raw data of quantified
687 preserved severed axons. **F** Raw data of quantified preserved severed axons. **G** Raw data of
688 quantified preserved severed axons.

689

690 **Figure 4 – figure supplement 1 – source data 1.** Raw data of qRT-PCR.

691

692 **Figure 4 – figure supplement 2 – source data 1.** Raw data of quantified preserved severed
693 axons.

694

695 **Figure 5 – source data 1. A** Raw unedited Western blots and uncropped blots with relevant
696 bands clearly labeled. **B** Raw unedited Western blots and uncropped blots with relevant
697 bands clearly labeled. **C** Raw data of NADglo assay. **D** Raw unedited Western blots and

698 uncropped blots with relevant bands clearly labeled. **E** Raw data of quantified preserved
699 severed axons.

700

701 **Figure 5 – figure supplement 1 – source data 1. A** Raw unedited Western blots and
702 uncropped blots with relevant bands clearly labeled. **B** Raw data of quantified preserved
703 severed axons.

704

705 **Figure 5 – figure supplement 2 – source data 1. B** Raw data of quantified preserved
706 severed axons.

707

708 **Figure 6 – source data 1. A** Raw data of quantified intact neuronal cell bodies. **B** Raw data
709 of quantified preserved severed axons. **C** Raw data of quantified intact neuronal cell bodies.

710

711 **Figure 6 – figure supplement 1 – source data 1. B** Raw data of quantified preserved
712 severed axons. **C** Raw data of grooming. **D** Raw data of quantified intact neuronal cell
713 bodies. **E** Raw data of grooming. **F** Raw data of quantified intact neuronal cell bodies.

714

715

716 **Acknowledgments**

717

718 We thank Dr. Jemeen Sreedharan for support in generating transgenic flies, and Dr. Julijana
719 Ivanisevic and Dr. Hector Gallart-Ayala from the Metabolomics Unit at University of
720 Lausanne for metabolic analyses. This work was supported by a UK Biotechnology and
721 Biological Sciences Research Council (BBSRC) / AstraZeneca Industrial Partnership award
722 (BB/S009582/1a) to JG; funds from the Italian Grant RSA 2018-20 from UNIVPM to GO; a Sir
723 Henry Wellcome Postdoctoral Fellowship from the Wellcome Trust (210904/Z/18/Z) to AL;
724 the John and Lucille van Geest Foundation to MPC; and Swiss National Science Foundation
725 SNSF Assistant Professor awards (PP00P3_176855 and PP00P3_211015), the International
726 Foundation for Research in Paraplegia (P180), and SNSF Spark (190919) to LJN.

727

728

729

730 **Materials & Methods**

731

732 **Fly genetics**

733 Flies (*Drosophila melanogaster*) were kept on Nutri-Fly Bloomington Formulation (see
734 resources table) with dry yeast at 20 °C unless stated otherwise. The following genders
735 were scored as progeny from MARCM crosses: females (X chromosome); and males &
736 females (autosomes, chromosomes 2L, 2R, 3L, and 3R). We did not observe any gender-
737 specific differences in clone numbers or axon death phenotype. Gender and genotypes are
738 listed in Table S1.

739

740 **NAD-related enzymes assay**

741 Sample extraction: Fly heads (previously collected and frozen, 50 weighed heads per
742 sample) were ground in liquid N₂ and sonicated after resuspension in 200-250 µl of 50 mM
743 Tris-HCl pH 7.5, 0.3 M NaCl, 1 mM PMSF, and 2 µg/ml each of aprotinin, leupeptin,
744 chimostatin, pepstatin and antipain. The suspension was centrifuged at 40000 g for 20 min
745 at 4 °C. The supernatant was passed through a G-25 column (GE Healthcare) equilibrated
746 with 50 mM Tris-HCl pH 7.5, 0.3 M NaCl to remove low molecular weight compounds that
747 interfere with the enzymatic assays. Protein contents were measured with the Bio-Rad
748 Protein Assay.

749

750 Nampt, Nrk, Naprt, and Qaprt activities: Enzymes were assayed according to (Zamporlini
751 et al., 2014) with minor modifications. Briefly, their formed reaction products, either NMN
752 or NaMN, were converted to NAD using ancillary enzymes PncC (bacterial NMN
753 deamidase), NadD (bacterial NaMN adenyltransferase), and NadE (bacterial NAD
754 synthase), followed by quantification of NAD with a fluorometric cycling assay (Zamporlini
755 et al., 2014).

756 First, mononucleotide products were converted to NaAD in dedicated assay mixtures as
757 described below.

758 *Nampt:* The assay mixture consisted of ethanol buffer (30 mM HEPES/KOH pH 8.0, 1 % v/v
759 ethanol, 8.4 mg/ml semicarbazide), 40 mM HEPES/KOH pH 7.5, 10 mM KF, 10 mM MgCl₂,
760 2.5 mM ATP, 0.3 mM NAM, 2 mM PRPP, 6 U/ml ADH, 0.067 mg/ml BSA, 1 U/ml NadD,
761 0.03 U/ml PncC, in a final volume of 100 µl.

762 *Nrk:* The assay mixture was similar to the one of NAMPT, lacking PRPP, with 2 mM NR
763 instead of NAM, and with 5 µM FK866.

764 *Naprt:* The assay mixture included ethanol buffer, 40 mM HEPES/KOH pH 7.5, 10 mM KF,
765 20 mM MgCl₂, 2.5 mM ATP, 2 mM PRPP, 0.5 mM NA, 6 U/ml ADH, 0.067 mg/ml BSA and
766 1 U/m NadD.

767 *QaPRT:* The assay mixture included ethanol buffer, 30 mM potassium phosphate buffer
768 pH 7.0, 10 mM KF, 5 mM MgCl₂, 2.5 mM ATP, 2 mM PRPP, 0.3 mM QA, 6 U/ml ADH,
769 0.067 mg/ml BSA and 1 U/ml NadD.

770 Second, aliquots of the assay mixtures were withdrawn at different incubation times at
771 37 °C, treated with perchloric acid to stop the reactions, and incubated in a NadE mixture to
772 transform NaAD into NAD. Third, NAD was quantified with fluorometric cycling
773 (Zamporlini et al., 2014).

774

775 dNaam activity: NA was converted to NaAD by the consecutive actions of the ancillary
776 enzymes PncB (bacterial NaPRT) and NadD. The reaction mixture consisted of ethanol
777 buffer, 40 mM HEPES/KOH pH 7.5, 10 mM KF, 10 mM MgCl₂, 2.5 mM ATP, 2 mM PRPP,
778 0.3 mM NAM, 6 U/ml ADH, 0.067 mg/ml BSA, 0.5 U/ml PncB and 1 U/ml NadD. A control
779 mixture was prepared in the absence of NAM. The generated NaAD was converted to NAD
780 which was quantified as described above.

781

782 dNmnat and NaDS activities: Enzymatic activities were determined by directly measuring
783 the newly synthesized NAD as follows:

784 dNmnat: The assay mixture consisted of 40 mM HEPES/KOH pH 7.5, 10 mM KF, 1 mM DTT,
785 25 mM MgCl₂, 1 mM ATP, 1 mM NMN. NMN was omitted in a control mixture.

786 NaDS: the assay mixture included 50 mM HEPES/KOH pH 7.5, 10 mM KF, 50 mM KCl, 5 mM
787 MgCl₂, 4 mM ATP, 20 mM glutamine, 1 mM NaAD. NaAD was omitted in a control mixture.
788 The dNmnat and NaDS assay mixtures were incubated at 37 °C, aliquots were withdrawn
789 and immediately subjected to acidic treatment to stop the reaction at various times. The
790 newly synthesized NAD was quantified as described above.

791

792 One Unit (U) above refers to the amount of enzyme that forms 1 μmol/min of product at
793 the indicated temperature, under conditions of initial velocity, e.g., less than 20 % of
794 substrate consumption. Other activity values are reported as pmol/hour/50 heads of
795 product formed and are means ± standard deviation of two independent experiments. The
796 ancillary bacterial enzymes PncC, NadD, and NadE were prepared as described (Zamporlini
797 et al., 2014), whereas *Staphylococcus aureus* PncB was prepared according to (Amici et al.,
798 2017).

799

800 **NAD⁺ metabolite quantification by LC-MS/MS**

801 Sample extraction: Fly heads (50 per sample) were extracted with 125 μl of ice-cold
802 methanol containing stable isotope-labeled (e.g., internal standard or ISTD) metabolites.
803 Sample extracts were vortexed and centrifuged (15 min, 14000 rpm at 4 °C). The resulting
804 supernatant was collected and evaporated to dryness in a vacuum concentrator (LabConco,
805 Missouri, US). Sample extracts were reconstituted in 50 μl of ddH₂O prior to LC-MS/MS
806 analysis.

807

808 LC-MS/MS: Extracted samples were analyzed by Liquid Chromatography coupled with
809 tandem mass spectrometry (LC-MS/MS) in positive electrospray ionization (ESI) mode. An
810 Agilent 1290 Infinite (Agilent Technologies, Santa Clara, California, US) ultra-high

811 performance liquid chromatography (UHPLC) system was interfaced with Agilent 6495 LC-
812 MS QqQ system equipped with an Agilent Jet Stream ESI source. This LC-MS/MS was used
813 to quantify the intermediates implicated in NAD⁺ *de novo synthesis* and *salvage pathways*
814 (van der Velpen et al., 2021).

815 The separation of NAD⁺ metabolites implicated in salvage and Preiss-Handler pathway was
816 carried out using the Scherzo SMC18 (3 μm 2.0 mm x 150 mm) column (Imtakt, MZ-
817 Analysentechnik, Mainz, Germany). The two mobile phases were composed of 20 mM
818 ammonium formate and 0.1 % formic acid in ddH₂O (= A) and acetonitrile: ammonium
819 formate 20 mM and 0.1 % formic acid (90:10, v/v) (= B). The gradient elution started at
820 100 % A (0 - 2 min), reaching 100 % B (2 - 12 min), then 100 % B was held for 3 min and
821 decreased to 100 % A in 1 min following for an isocratic step at the initial conditions (16 -
822 22 min). The flow rate was 200 μl/min, the column temperature 30 °C and the sample
823 injection volume 2 μl. To avoid sample carry-over, the injection path was cleaned after each
824 injection using a strong solvent (0.2 % formic acid in methanol) followed by a weak solvent
825 (0.2 % formic acid in ddH₂O).

826 AJS ESI source conditions operating in positive mode were set as follows: dry gas
827 temperature 290 °C, nebulizer 45 psi and flow 12 l/min, sheath gas temperature 350 °C and
828 flow 12 l/min, nozzle voltage +500 V, and capillary voltage +4000 V. Dynamic Multiple
829 Reaction Monitoring (DMRM) acquisition mode with a total cycle of 600 ms was used
830 operating at the optimal collision energy for each metabolite transition.

831

832 Data processing: Data was processed using Mass Hunter Quantitative (Agilent). For
833 absolute quantification, the calibration curve and the internal standard spike were used to
834 determine the response factor. Linearity of the standard curves was evaluated using a 14-
835 point range; in addition, peak area integration was manually curated and corrected where
836 necessary. Concentration of metabolites were corrected for the ratio of peak area between
837 the analyte and the ISTD, to account for matrix effects.

838

839 **S2 cell culture**

840 *Drosophila* Schneider cells (S2) are sold and authenticated by Thermo Fisher (R69007). The
841 Master Seed Bank has been tested for contamination of bacteria, yeast, mycoplasma, and
842 virus and has been characterized by isozyme and karyotype analysis. S2 cells were
843 maintained at 26 °C in *Drosophila* Schneider's medium (Thermo Fisher) supplemented with
844 10 % Fetal Bovine Serum (Thermo Fisher) and 1xPenicillin-Streptomycin (Thermo Fisher). 8
845 x 10⁵ cells were plated out in 10 mm plates 24 h prior to transfection. Cells were co-
846 transfected with either *UAS-dsarm(E)::flag*, *UAS-dsarm(E^{K193R})::flag*, *UAS-GFP::NMN-*
847 *Deamidase*, or *UAS-GFP::NMN-Deamidase^{dead}* constructs and *pAc-GAL4* (Addgene) to a
848 final concentration of 10 μg DNA/well using Mirus TransIT-Insect (Mirus Bio). 48 h post-
849 transfection, cells were harvested with the original medium in tubes on ice. Cells were
850 centrifuged at 5000 g for 30 s, the supernatant discarded, the cells resuspended in 5 ml of
851 cold PBS and centrifuged again at 5000 g for 30 s. After discarding the supernatant, cells

852 were resuspended in 300 µl/plate of cold KHM lysis buffer (110 mM CH₃CO₂K, 20 mM
853 HEPES pH 7.4, 2 mM MgCl₂, 0.1 mM digitonin, Complete inhibitor EDTA free (Roche)) and
854 incubated for 10 min at 4 °C while briefly vortexing for 5 s and up-and-down pipetting 5
855 times every minute. Samples were then centrifuged at 3000 rpm for 5 min to pellet cell
856 debris. Protein concentration of the supernatant was determined using the BCA protein
857 quantification assay (ThermoFischer).

858

859 **PncC antibody generation**

860 Rabbit anti-PncC antibodies were generated by Lubioscience under a proprietary protocol.
861 The immunogen used was purified from *Escherichia coli*, strain K12, corresponding to the
862 full protein sequence of NMN-D. The amino acid sequence is the following:

863 MTDSELMQLSEQVGOALKARGATVTTAESCTGGWVAKVITDIAGSSAWFERGFVTYSNEAK
864 AQMIGVREETLAQHGAVSEPVVVEMAIGALKAARADYAVSISGIAGPDGGSEEKPVGVWFAF
865 ATARGEGITRRECFSGDRDAVRRQATAYALQTLWQQFLQNT

866

867 **Western blot**

868 Sample preparation:

869 *Fly heads*: whole fly heads were lysed in Laemmli buffer (2 heads/10 µl) and 10 µl loaded per
870 well.

871 *S2 cells*: Protein concentration was determined as described above, and 20 µg of protein
872 prepared in Laemmli buffer and loaded per well.

873

874 Sample run: 4-12 % surePAGE™ gels (genescrpt) were used with MOPS running buffer (for
875 higher molecular weight proteins) or MES running buffer (for lower molecular weight
876 proteins). Gels were subjected to 200 V. A molecular weight marker Precision Plus
877 Protein™ Kaleidoscope™ Prestained Protein Ladder was used (Biorad). Proteins were
878 transferred to PVDF membranes with the eBlot® L1 system using eBlot® L1 Transfer Stack
879 supports (Genscript) and the resulting membranes were washed three times with TBS-T
880 (Tris-buffered saline containing 0.1 % Tween® 20 (Merk)). Membranes were blocked with
881 5 % milk (Carl-Roth) in TBS-T at room temperature (RT) for 1 h. Membranes were incubated
882 at 4 °C with corresponding primary antibodies overnight (O/N) . Membranes were washed
883 three times with TBS-T for 10 min and incubated with secondary antibodies in 5 % milk in
884 TBS-T at RT during 1 h. Membranes were washed three times with TBS-T for 10 min.

885

886 Antibody concentrations:

887 *Primary antibodies*: 1:5000 rabbit anti-GFP (Abcam, ab6556), 1:15000 mouse anti-Tubulin
888 (Sigma), 1:5000 rabbit anti-Tubulin (Abcam, T9026), 1:2000 rabbit anti-PncC
889 (LubioScience, established in this study), 1:1000 mouse anti-FLAG (Sigma, F3165), 1:500
890 mouse anti-Syntaxin (DSHB, 8c3), 1:2000 anti-NAMPT (Merk, MABS465).

891 *Secondary antibodies*: 1:10000 goat anti-rabbit IgG (H+L) Dylight 800 (ThermoFisher,
892 A32735), 1:10000 goat anti-mouse IgG (H+L) Dylight 800 (ThermoFisher, A32730), 1:10000

893 goat anti-rabbit IgG (H+L) Dylight 680 (ThermoFisher, A32734), 1:10000 goat anti-mouse
894 IgG (H+L) Dylight 680 (ThermoFisher, A32729), 1:10000 goat anti-rat IgG (H+L) Dylight 800
895 (ThermoFisher, sa510024).

896

897 Signal acquisition: Fluorescent signals were acquired using Odyssey® DLx (LI-COR). Images
898 were quantified by densitometric analysis using ImageJ (NIH).

899

900 **Injury (axotomy) assays**

901 Wing injury: Flies were kept at 20 °C for 5-7 days prior axotomy, unless stated otherwise.
902 Axotomy was performed using a modification of a previously described protocol (Paglione
903 et al., 2020). One wing per anesthetized fly was cut approximately in the middle. The distal,
904 cut-off part of the wing was mounted in Halocarbon Oil 27 on a microscopy slide, covered
905 with a coverslip, and immediately used to count the amount of cut-off cell bodies (as
906 readout for the number of injured axons) under an epifluorescence microscope. Flies were
907 returned to individual vials. At 0, 2, 4, 6, 8, 10 and 12 h post axotomy (hpa), or 7 days post
908 axotomy (dpa), wings were mounted onto a slide, and imaged with a spinning disk
909 microscope to assess for intact or degenerated axons, as well as the remaining uninjured
910 control axons.

911

912 Antennal ablation: Adults were aged at 20 °C for 5-7 days before performing antennal
913 ablation (Paglione et al., 2020). Unilateral antennal ablation (e.g., removal of one antenna)
914 was performed using high precision and ultra-fine tweezers, and flies returned to vial for
915 the appropriate time. The ablation of 3rd antennal segments did not damage the rest of the
916 head or lead to fly mortality. At corresponding time points, adult brain dissections were
917 performed as described (Paglione et al., 2020): decapitated heads were fixed in 4 %
918 formaldehyde in PTX (0.5 % Triton X-100 in PBS) for 20 min, and washed 3 x 10 min with
919 PTX. Brain dissections were performed in PTX, and dissected brains were fixed in 4 %
920 formaldehyde in PTX for 10 min, followed by 1 h of blocking in 10 % normal goat serum
921 (Jackson Immuno) in PTX and an O/N incubation with the following primary antibodies at
922 4 °C in blocking solution: 1:500 chicken anti-GFP (Rockland), and 1:150 mouse anti-nc82
923 (DSHB, nc82). Brains were then washed 3x 10 min with PTX at RT, and incubated with
924 secondary antibodies in PTX at RT for 2 h: 1:200 Dylight 488 goat anti-chicken (abcam,
925 ab96947), and 1:200 AlexaFluor 546 goat anti-mouse (ThermoFisher, a-11030). Brains were
926 washed 3 x 10 min with PTX at RT, and mounted in Vectashield for microscopy.

927

928 **Time course of degenerating neurons**

929 Wings of aged flies (0 – 10 days post eclosion (dpe)) were observed and imaged with a
930 spinning disk microscope to assess for intact or degenerated neurons and axons.

931

932 **Transgenesis**

933 The plasmids listed below were generated and used for PhiC31 integrase-mediated
934 targeted transgenesis (Bestgene) ($5\times UAS$, w^+ marker). *attP40* target site: *UAS-GFP::NMN-*
935 *Deamidase*, *UAS-GFP::NMN-Deamidase^{dead}*, *UAS-dsarm(E)*, *UAS-dsarm(E)::flag*, *UAS-*
936 *dsarm(E^{K450R})*, *UAS-dsarm(E^{K450R})::flag*, *UAS-mNAMPT*. *VK37* target site: *UAS-*
937 *4x(tRNA::axed^{sgRNAs})*, *UAS-4x(tRNA::hiw^{sgRNAs})*, *UAS-4x(tRNA::dsarm^{sgRNAs})*, *UAS-*
938 *4x(tRNA::dnmna^{sgRNAs})*. All plasmids are available as *.gb files on Addgene.

939

940 **Optogenetics**

941 Crosses were performed on standard cornmeal agar containing 200 μ M all-*trans* retinoic
942 acid in aluminum-wrapped vials to keep the progeny in the dark (Paglione et al., 2020).
943 CsChrimson experiments were performed in the dark, and flies were visualized for
944 recording using an 850 nm infrared light source at 2 mW/cm² intensity (Mightex, Toronto,
945 CA). For CsChrimson activation, 656 nm red light at 6 mW/cm² intensity (Mightex) was
946 used. Red light stimulus parameters were delivered using a NIDAQ board controlled
947 through Bonsai (<https://open-ephys.org/>). Exclusion criteria: to avoid spontaneous
948 grooming behavior, during the recording, flies that groomed within the first 30 s were
949 excluded from the analysis. Red-light stimulation (10 Hz for 10 s) was followed by a 30 s
950 interstimulus recovery (3 repetitions in total). Flies were recorded, and videos were
951 manually analyzed using VLC player (<http://www.videolan.org/>). Grooming activity
952 (ethogram) was plotted as bins (1 bin, grooming event(s) per second). Ethograms were
953 visualized using R (<https://cran.r-project.org/>). The ablation of 2nd antennal segments did
954 neither damage the head nor lead to fly mortality. Flies that died during the analysis
955 window (7 – 15 dpa) were excluded.

956

957 **In-cell NAD-glo of dSarm proteins for NADase assay**

958 Immunoprecipitation: S2 cells cell lysates (see above) were protein-quantified with the BCA
959 protein assay and diluted to 500 ng/ μ l in ice-cold KHM buffer. Lysates were mixed with
960 20 μ g/ml mouse anti-FLAG[®] M2 monoclonal antibody (Sigma-Aldrich, F3165) and 50 μ l/ml
961 of pre-washed Pierce magnetic protein A/G beads (Thermo Fisher Scientific, 88802) and
962 incubated overnight at 4 °C with rotation. After incubation, beads were washed 3x with
963 KHM buffer and 1x with PBS and resuspended in 1 mg/ml BSA in PBS (with protease
964 inhibitors, Merk, 11873580001).

965

966 NADase assays: A series of test assays were first performed to define appropriate test
967 conditions. Optimized reaction conditions were as follows: 25 μ l reactions (overall 1x PBS)
968 contained 40 fmol/ μ l dSarm(E) protein together with 25 μ M NAD⁺ \pm 50 μ M NMN. Reactions
969 were kept on ice while being set up. Reactions were performed with the recombinant
970 dSarm(E) still attached to beads and bead suspensions were thoroughly mixed prior to
971 addition to the reactions. Constitutive (basal) NAD⁺ consumption was measured from
972 reactions containing NAD⁺ alone as the difference between starting levels (0 mins) and
973 levels remaining after incubating for between 80 and 120 min at 25 °C, and NAD⁺

974 consumption in the presence of 50 μ M NMN was calculated after incubating for between 40
975 and 120 min (times were dependent on variant activity in each sample). Reactions were
976 mixed once during the incubation to resuspend the beads. NAD⁺ levels were measured
977 using the NAD/NADH-Glo™ assay. 5 μ l aliquots of reaction were removed immediately
978 after setting up (whilst still on ice), to obtain precise starting levels (0 min) in individual
979 reactions, and again after the defined times listed above. Aliquots were then mixed with
980 2.5 μ l of 0.4 M HCl, to stop the reaction, and neutralised by mixing with 2.5 μ l 0.5 M Tris
981 base after 10 min. Neutralised samples were subsequently diluted 1 in 50 in a buffer
982 consisting of 50 % PBS, 25 % 0.4 M HCL, 25 % 0.5 M Tris base to bring the NAD⁺. NAD⁺
983 concentrations down to the linear range of detection for the NAD/NADH-Glo™ assay. 10 μ l
984 of the diluted sample was then mixed with 10 μ l of NAD/NADH-Glo™ detection reagent on
985 ice in wells of a 384-well white polystyrene microplate (Corning). Once all reactions had
986 been set up the plate was moved to a GloMax® Explorer plate reader (Promega) and
987 incubated for 40 min at 25 °C before reading for luminescence. NAD⁺ concentrations were
988 determined from a standard curve generated from a dilution series of NAD⁺ and NAD⁺
989 consumption rates were converted to mol of NAD⁺ consumed per min per mol of dSarm(E)
990 protein (mol/min/mol dSarm) (Gilley et al., 2021). Individual data points for each separate
991 protein preparation are the means of two or three technical replicates. No non-specific
992 activity was detected on bead/antibody complexes in control immunoprecipitations using
993 extracts from *Actin-Gal4* transfected S2 cells (based on $n = 5$).

994

995 **Quantitative PCR with reverse transcription and RNA quantification**

996 Total RNA from forty fly heads for each genotype was isolated with TRIzol LS Reagent
997 (Invitrogen, 10296010). The isolated RNA was treated with TURBO DNase (Invitrogen,
998 AM2238) at 37°C for 20 min and purified using RNA Clean & Concentrator-5 (Zymo
999 Research, R1015). First strand cDNA was synthesized using random hexamers (Invitrogen,
1000 N8080127) and SuperScript IV first-strand synthesis system (Invitrogen, 18091050).
1001 Quantitative PCR was performed for each sample using PowerUp SYBR green master mix
1002 (Applied Biosystems, A25741) with technical triplicates for both +RT and -RT for each
1003 genotype in MicroAmp optical 96-well reaction plates (Applied Biosystems, 4306737) and
1004 QuantStudio 1 real-time PCR system (Applied Biosystems). Relative transcript abundance
1005 was calculated using the $\Delta\Delta$ Ct method. α -tubulin, an mRNA that remains unchanged in
1006 mutant and transgenic flies based on qPCR analysis, was used for normalization. Error bars
1007 represent standard deviations. Statistical significance was calculated using the one-way
1008 ANOVA test. The post hoc Tukey test was performed for statistically different groups
1009 determined by the ANOVA test (p value < 0.05). The resulting p values from the Tukey test
1010 are reported.

1011 Primers used (forward and reverse, respectively, 200–500 bp amplicons, all isoforms
1012 included):

1013 *NMN-D*: TCGTGCTGATTATGCCGTGT, AAAAGCAAACCAGGTGC

1014 *mNAMPT*: TGGGGTGAAGACCTGAGACA, TGGCAGCAACTTGTAGCCTT

1015 *dsarm*: AGGAGAACATGGCCAAGACG, GTTGTCAATTGCCCGCCT
1016 *axed*: CATTCCCTACCGCGCTCACA, TTTGGTGCTGGTTGGTCAGT
1017 *hiw*: CTCACCCAGCGTCAGAAGTT, CCATTGGCTCCAATCCAGGT
1018 *dnmnat*: TTGCTGTTCCAGGCCTATGG, CAACGTGGAGCTCACCTCAT
1019 *dnaam*: CAATGGACGCCTGTTTCACG, TTCGTATCGAAGGCGAA
1020 *dnrk*: GCGTGTCCCATGGAGCAATA, AGCCACGATTCGGAGAAGTA
1021 *naprt*: TCCTATGCCATCGCATTCCC, TTGGCGGACTGTTCTCAGAC
1022 *nadsyn*: AATATGCTGGTGGACGTGGG, GGCGATTAAGAAGGCCACC

1023

1024 **Replicates**

1025 For all experiments, at least 3 biological replicates were performed for each genotype
1026 and/or condition. No inclusion/exclusion criteria was applied except for optogenetics, which
1027 is stated in the subsection "optogenetics" of materials and methods.

1028

1029 **Software and statistics**

1030 Image-J and photoshop was used to process wing and ORN pictures. Software for
1031 optogenetics is included in the optogenetics section. Graphpad prism 9 was used to
1032 perform all the statistical analysis. For tests applying a false discovery rate (FDR) correction,
1033 the adjusted p value we report is the q value.

1034

1035 **Source data**

1036 The following R code was used to generate ethograms from excel files.

1037

```
1038 library(readxl)
1039 nm_n_7 <- read_excel("nm_n 7 days.xlsx")
1040 head(nm_n_7)
1041 # custom function using image to emulate an ethograph
1042 ethogram <- function(zeroOneMatrix, color='skyblue',xlab='behaviour',ylab='animals'){
1043   m <- as.matrix(zeroOneMatrix)
1044   m[m == 0] <- NA
1045   nAnimals <- nrow(m)
1046   nTimeSlots <- ncol(m)
1047   image(x=1:nTimeSlots,
1048         y=1:nAnimals,
1049         z=t(m[nAnimals:1,]),
1050         col=c(color),
1051         xlab=xlab,
1052         ylab=ylab,
1053         yaxt = 'n')
1054 }
```

1055

```

1056 # let's plot
1057 ethogram(nmn_7, color='lightskyblue1')
1058
1059 data_t = t(nmn_7)
1060 head(data_t)
1061 colnames(data_t) = rev(c(1:ncol(data_t)))
1062 rownames(data_t) = c(1:nrow(data_t))
1063 head(data_t)
1064 data_long <- reshape2::melt(data_t)
1065 colnames(data_long) = c("Time", "Animal", "Val")
1066 data_long$Val <- factor(data_long$Val)
1067 head(data_long)
1068
1069 data_zeros = data.frame(data_t)
1070 data_zeros[is.na(data_zeros)] <- 0
1071 rs = rowSums(data_zeros)
1072 rs
1073 data_sum = data.frame(Time=c(1:length(rs)), Count=rs)
1074 head(data_sum)
1075 library(ggplot2)
1076 e2 = ggplot() +
1077   geom_tile(data_long, mapping=aes(x = data_long$Time, y = data_long$Animal,
1078   fill=data_long$Val), color="white", size=0.5) +
1079   labs(x="behaviour", y="animals", title="OPTO") +
1080   theme_bw() + theme(axis.text.x=element_text(size=9, angle=0, vjust=0.3),
1081     axis.text.y=element_text(size=9),
1082     plot.title=element_text(size=11)) +
1083   theme(panel.border=element_blank()) +
1084   scale_fill_manual(values=c("skyblue")) +
1085   geom_line(data_sum, mapping=aes(x=data_sum$Time, y=data_sum$Count),
1086   color="black", size=0.7)
1087 e2
1088
1089 Transparent reporting guidelines
1090 We followed the ARRIVE guidelines for reporting work involving fly research.

```

1091 **References**

1092

- 1093 Amici A, Grolla AA, del Grosso E, Bellini R, Bianchi M, Travelli C, Garavaglia S, Sorci L,
1094 Raffaelli N, Ruggieri S, Genazzani AA, Orsomando G. 2017. Synthesis and Degradation
1095 of Adenosine 5'-Tetraphosphate by Nicotinamide and Nicotinate
1096 Phosphoribosyltransferases. *Cell Chem Biol* **24**:553-564.e4.
1097 doi:10.1016/j.chembiol.2017.03.010
- 1098 Angeletti C, Amici A, Gilley J, Loreto A, Trapanotto AG, Antoniou C, Merlini E, Coleman
1099 MP, Orsomando G. 2022. SARM1 is a multi-functional NAD(P)ase with prominent base
1100 exchange activity, all regulated by multiple physiologically-relevant NAD metabolites.
1101 *iScience* 103812. doi:10.1016/J.ISCI.2022.103812
- 1102 Babetto E, Beirowski B, Russler E, Milbrandt J, DiAntonio A. 2013. The Phr1 Ubiquitin
1103 Ligase Promotes Injury-Induced Axon Self-Destruction. *Cell Rep* **3**:1422-1429.
1104 doi:10.1016/j.celrep.2013.04.013
- 1105 Bratkowski M, Xie T, Thayer DA, Brown SP, Bai X, Correspondence SS, Lad S, Mathur P,
1106 Yang Y-S, Danko G, Burdett TC, Danao J, Cantor A, Kozak JA, Sambashivan S. 2020.
1107 Structural and Mechanistic Regulation of the Pro-degenerative NAD Hydrolase
1108 SARM1. doi:10.1016/j.celrep.2020.107999
- 1109 Coleman MP, Höke A. 2020. Programmed axon degeneration: from mouse to mechanism
1110 to medicine. *Nature Reviews Neuroscience* 2020 21:4 21:183-196. doi:10.1038/s41583-
1111 020-0269-3
- 1112 di Stefano M, Loreto A, Orsomando G, Mori V, Zamporlini F, Hulse RP, Webster J,
1113 Donaldson LF, Gering M, Raffaelli N, Coleman MP, Gilley J, Conforti L. 2017. NMN
1114 Deamidase Delays Wallerian Degeneration and Rescues Axonal Defects Caused by
1115 NMNAT2 Deficiency In Vivo. *Curr Biol* **27**:784-794. doi:10.1016/J.CUB.2017.01.070
- 1116 di Stefano M, Nascimento-Ferreira I, Orsomando G, Mori V, Gilley J, Brown R, Janeckova L,
1117 Vargas ME, Worrell LA, Loreto A, Tickle J, Patrick J, Webster JRM, Marangoni M, Carpi
1118 FM, Pucciarelli S, Rossi F, Meng W, Sagasti A, Ribchester RR, Magni G, Coleman MP,
1119 Conforti L. 2015. A rise in NAD precursor nicotinamide mononucleotide (NMN) after
1120 injury promotes axon degeneration. *Cell Death Differ* **22**:731-742.
1121 doi:10.1038/cdd.2014.164
- 1122 Essuman K, Summers DW, Sasaki Y, Mao X, DiAntonio A, Milbrandt J. 2017. The SARM1
1123 Toll/Interleukin-1 Receptor Domain Possesses Intrinsic NAD+ Cleavage Activity that
1124 Promotes Pathological Axonal Degeneration. *Neuron* **93**:1334-1343.e5.
1125 doi:10.1016/j.neuron.2017.02.022
- 1126 Fang Y, Soares L, Teng X, Geary M, Bonini NM. 2012. A novel drosophila model of nerve
1127 injury reveals an essential role of Nmnat in maintaining axonal integrity. *Current*
1128 *Biology* **22**:590-595. doi:10.1016/j.cub.2012.01.065
- 1129 Figley MD, DiAntonio A. 2020. The SARM1 axon degeneration pathway: control of the NAD
1130 + metabolome regulates axon survival in health and disease. *Curr Opin Neurobiol*
1131 **63**:59-66. doi:10.1016/J.CONB.2020.02.012
- 1132 Figley MD, Gu W, Nanson JD, Shi Y, Sasaki Y, Cunnea K, Malde AK, Jia X, Luo Z, Saikot FK,
1133 Mosaiab T, Masic V, Holt S, Hartley-Tassell L, McGuinness HY, Manik MK, Bosanac T,
1134 Landsberg MJ, Kerry PS, Mobli M, Hughes RO, Milbrandt J, Kobe B, DiAntonio A, Ve T.
1135 2021. SARM1 is a metabolic sensor activated by an increased NMN/NAD+ ratio to
1136 trigger axon degeneration. *Neuron* **109**:1118-1136.e11.
1137 doi:10.1016/J.NEURON.2021.02.009

1138 Galeazzi L, Bocci P, Amici A, Brunetti L, Ruggieri S, Romine M, Reed S, Osterman AL,
1139 Rodionov DA, Sorci L, Raffaelli N. 2011. Identification of nicotinamide mononucleotide
1140 deamidase of the bacterial pyridine nucleotide cycle reveals a novel broadly conserved
1141 amidohydrolase family. *Journal of Biological Chemistry* **286**:40365–40375.
1142 doi:10.1074/JBC.M111.275818/ATTACHMENT/D6160550-8D69-4B53-BB35-
1143 9BABA AF1B120/MMC1.PDF

1144 Geisler S, Huang SX, Strickland A, Doan RA, Summers DW, Mao X, Park J, DiAntonio A,
1145 Milbrandt J. 2019. Gene therapy targeting SARM1 blocks pathological axon
1146 degeneration in mice. *J Exp Med* **216**:294–303. doi:10.1084/JEM.20181040

1147 Gerdts J, Brace EJ, Sasaki Y, DiAntonio A, Milbrandt J. 2015. Supplementary Materials for
1148 SARM1 activation triggers axon degeneration locally via NAD + destruction. *Science*
1149 (1979) **348**:453–458. doi:10.1126/science.1258366

1150 Gerdts J, Summers DW, Milbrandt J, DiAntonio A. 2016. Axon Self-Destruction: New Links
1151 among SARM1, MAPKs, and NAD+ Metabolism. *Neuron* **89**:449–460.
1152 doi:10.1016/J.NEURON.2015.12.023

1153 Gerdts J, Summers DW, Sasaki Y, DiAntonio A, Milbrandt J. 2013. Sarm1-Mediated Axon
1154 Degeneration Requires Both SAM and TIR Interactions. *Journal of Neuroscience*
1155 **33**:13569–13580. doi:10.1523/JNEUROSCI.1197-13.2013

1156 Gilley J, Coleman MP. 2010. Endogenous Nmnat2 Is an Essential Survival Factor for
1157 Maintenance of Healthy Axons. *PLoS Biol* **8**. doi:10.1371/journal.pbio.1000300

1158 Gilley J, Jackson O, Pipis M, Estiar MA, Al-Chalabi A, Danzi MC, van Eijk KR, Goutman SA,
1159 Harms MB, Houlden H, Iacoangeli A, Kaye J, Lima L, Genomics QS, Ravits J, Rouleau
1160 GA, Schüle R, Xu J, Züchner S, Cooper-Knock J, Gan-Or Z, Reilly MM, Coleman MP.
1161 2021. Enrichment of SARM1 alleles encoding variants with constitutively hyperactive
1162 NADase in patients with ALS and other motor nerve disorders. *Elife* **10**.
1163 doi:10.7554/ELIFE.70905

1164 Gossmann TI, Ziegler M, Puntervoll P, de Figueiredo LF, Schuster S, Heiland I. 2012. NAD+
1165 biosynthesis and salvage – a phylogenetic perspective. *FEBS J* **279**:3355–3363.
1166 doi:10.1111/J.1742-4658.2012.08559.X

1167 Gu W, Luo Z, Vonnrhein C, Jia X, Ve T, Nanson JD, Kobe B. 2021. Crystal structure
1168 determination of the armadillo repeat domain of Drosophila SARM1 using MIRAS
1169 phasing. *urn:issn:2053-230X* **77**:364–373. doi:10.1107/S2053230X21006786

1170 Hampel S, Franconville R, Simpson JH, Seeds AM. 2015. A neural command circuit for
1171 grooming movement control. *Elife* **4**. doi:10.7554/eLife.08758

1172 Hopkins EL, Gu W, Kobe B, Coleman MP. 2021. A Novel NAD Signaling Mechanism in Axon
1173 Degeneration and its Relationship to Innate Immunity. *Front Mol Biosci* **8**:662.
1174 doi:10.3389/FMOLB.2021.703532/BIBTEX

1175 Hsu JM, Kang Y, Corty MM, Mathieson D, Peters OM, Freeman MR. 2021. Injury-Induced
1176 Inhibition of Bystander Neurons Requires dSarm and Signaling from Glia. *Neuron*
1177 **109**:473-487.e5. doi:10.1016/J.NEURON.2020.11.012

1178 Izadifar A, Courchet J, Virga DM, Verreet T, Hamilton S, Ayaz D, Misbaer A,
1179 Vandenbogaerde S, Monteiro L, Petrovic M, Sachse S, Yan B, Erfurth ML, Dascenco D,
1180 Kise Y, Yan J, Edwards-Faret G, Lewis T, Polleux F, Schmucker D. 2021. Axon
1181 morphogenesis and maintenance require an evolutionary conserved safeguard
1182 function of Wnk kinases antagonizing Sarm and Axed. *Neuron* **109**:2864-2883.e8.
1183 doi:10.1016/J.NEURON.2021.07.006

1184 Ji H, Sapar ML, Sarkar A, Wang B, Han C. 2022. Phagocytosis and self-destruction break
1185 down dendrites of *Drosophila* sensory neurons at distinct steps of Wallerian
1186 degeneration. *Proceedings of the National Academy of Sciences* **119**:e2111818119.
1187 doi:10.1073/PNAS.2111818119

1188 Jiang Y, Liu T, Lee CH, Chang Q, Yang J, Zhang Z. 2020. The NAD⁺-mediated self-inhibition
1189 mechanism of pro-neurodegenerative SARM1. *Nature* 2020 **588**:7839 **588**:658–663.
1190 doi:10.1038/s41586-020-2862-z

1191 Katsyuba E, Mottis A, Zietak M, de Franco F, van der Velpen V, Gariani K, Ryu D, Cialabrini
1192 L, Matilainen O, Liscio P, Giacchè N, Stokar-Regenscheit N, Legouis D, de Seigneux S,
1193 Ivanisevic J, Raffaelli N, Schoonjans K, Pellicciari R, Auwerx J. 2018. De novo NAD⁺
1194 synthesis enhances mitochondrial function and improves health. *Nature* 2018 **563**:7731
1195 **563**:354–359. doi:10.1038/s41586-018-0645-6

1196 Lehmann S, Loh SHY, Martins LM. 2017. Enhancing NAD⁺ salvage metabolism is
1197 neuroprotective in a PINK1 model of Parkinson's disease. *Biol Open* **6**:141–147.
1198 doi:10.1242/BIO.022186

1199 Liu L, Su X, Quinn WJ, Hui S, Krukenberg K, Frederick DW, Redpath P, Zhan L, Chellappa K,
1200 White E, Migaud M, Mitchison TJ, Baur JA, Rabinowitz JD. 2018. Quantitative Analysis
1201 of NAD Synthesis-Breakdown Fluxes. *Cell Metab* **27**:1067–1080.e5.
1202 doi:10.1016/J.CMET.2018.03.018/ATTACHMENT/E65ADC78-6B59-4551-8797-
1203 BF40EC13843D/MMC1.PDF

1204 Llobet Rosell A, Neukomm LJ. 2019. Axon death signalling in Wallerian degeneration
1205 among species and in disease. *Open Biol* **9**:190118. doi:10.1098/rsob.190118

1206 Loreto A, Angeletti C, Gu W, Osborne A, Nieuwenhuis B, Gilley J, Merlini E, Arthur-Farraj P,
1207 Amici A, Luo Z, Hartley-Tassell L, Ve T, Desrochers LM, Wang Q, Kobe B, Orsomando
1208 G, Coleman MP. 2021. Neurotoxin-mediated potent activation of the axon
1209 degeneration regulator SARM1. *Elife* **10**. doi:10.7554/ELIFE.72823

1210 Loreto A, di Stefano M, Gering M, Conforti L. 2015. Wallerian Degeneration Is Executed by
1211 an NMN-SARM1-Dependent Late Ca²⁺ Influx but Only Modestly Influenced by
1212 Mitochondria. *Cell Rep* **13**:2539–2552. doi:10.1016/j.celrep.2015.11.032

1213 MacDonald JM, Beach MG, Porpiglia E, Sheehan AE, Watts RJ, Freeman MR. 2006. The
1214 *Drosophila* Cell Corpse Engulfment Receptor Draper Mediates Glial Clearance of
1215 Severed Axons. *Neuron* **50**:869–881. doi:10.1016/j.neuron.2006.04.028

1216 Mariano V, Domínguez-Iturza N, Neukomm LJ, Bagni C. 2018. Maintenance mechanisms of
1217 circuit-integrated axons. *Curr Opin Neurobiol* **53**:162–173.
1218 doi:10.1016/J.CONB.2018.08.007

1219 Merlini E, Coleman MP, Loreto A. 2022. Mitochondrial dysfunction as a trigger of
1220 programmed axon death. *Trends Neurosci* **45**:53–63. doi:10.1016/J.TINS.2021.10.014

1221 Neukomm LJ, Burdett TC, Gonzalez MA, Züchner S, Freeman MR. 2014. Rapid in vivo
1222 forward genetic approach for identifying axon death genes in *Drosophila*. *Proceedings*
1223 *of the National Academy of Sciences* **111**:9965–9970. doi:10.1073/pnas.1406230111

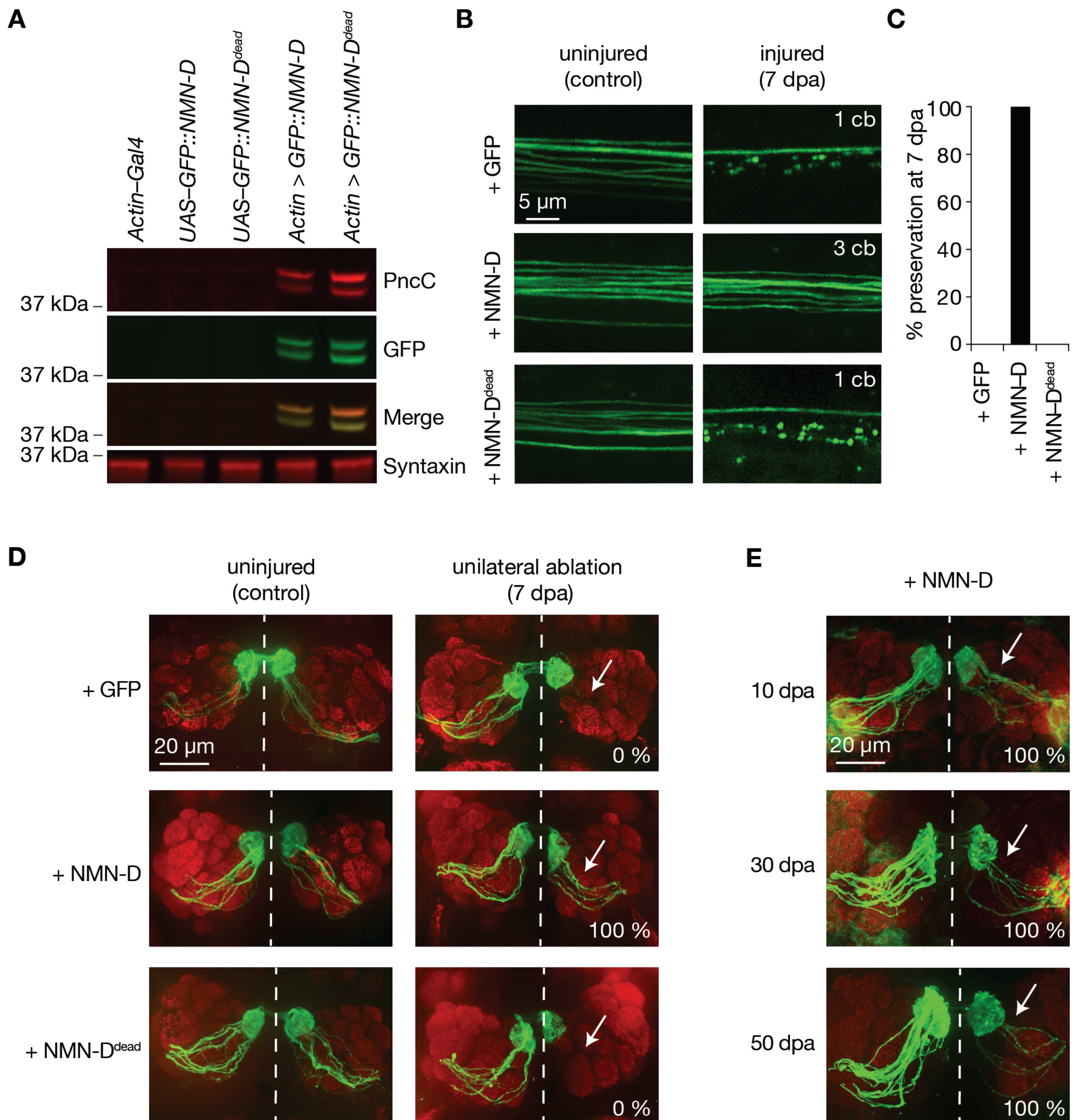
1224 Neukomm LJ, Burdett TC, Seeds AM, Hampel S, Coutinho-Budd JC, Farley JE, Wong J,
1225 Karadeniz YB, Osterloh JM, Sheehan AE, Freeman MR. 2017. Axon Death Pathways
1226 Converge on Axundead to Promote Functional and Structural Axon Disassembly.
1227 *Neuron* **95**:78–91.e5. doi:10.1016/j.neuron.2017.06.031

1228 Neukomm LJ, Freeman MR. 2014. Diverse cellular and molecular modes of axon
1229 degeneration. *Trends Cell Biol* **24**:515–523. doi:10.1016/j.tcb.2014.04.003

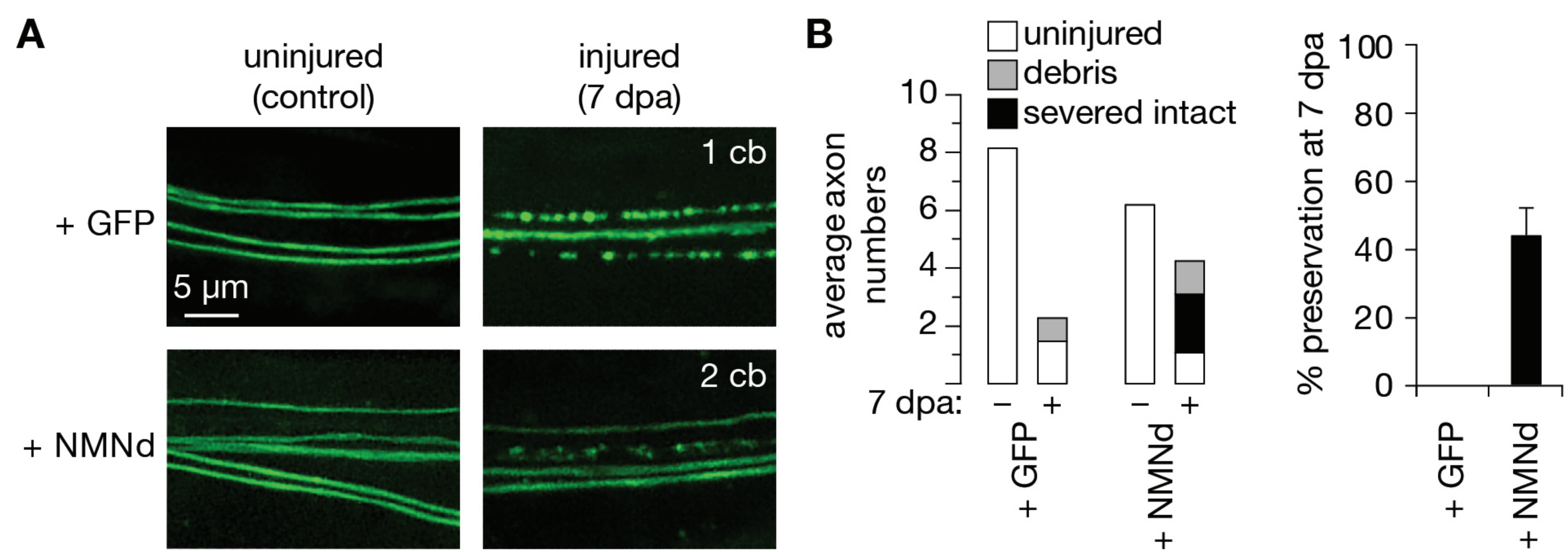
1230 Osterloh JM, Yang J, Rooney TM, Fox AN, Adalbert R, Powell EH, Sheehan AE, Avery MA,
1231 Hackett R, Logan MA, MacDonald JM, Ziegenfuss JS, Milde S, Hou YJ, Nathan C, Ding
1232 A, Brown RH, Conforti L, Coleman M, Tessier-Lavigne M, Züchner S, Freeman MR.
1233 2012. dSarm/Sarm1 is required for activation of an injury-induced axon death pathway.
1234 *Science (1979)* **337**:481–484. doi:10.1126/science.1223899
1235 Paglione M, Llobet Rosell A, Chatton JY, Neukomm LJ. 2020. Morphological and Functional
1236 Evaluation of Axons and their Synapses during Axon Death in *Drosophila*
1237 *melanogaster*. *J Vis Exp* 60865. doi:10.3791/60865
1238 Port F, Bullock SL. 2016. Augmenting CRISPR applications in *Drosophila* with tRNA-flanked
1239 sgRNAs. *Nat Methods* **13**:852–854. doi:10.1038/nmeth.3972
1240 Riccomagno MM, Kolodkin AL. 2015. Sculpting Neural Circuits by Axon and Dendrite
1241 Pruning. <http://dx.doi.org/10.1146/annurev-cellbio-100913-013038> **31**:779–805.
1242 doi:10.1146/ANNUREV-CELLBIO-100913-013038
1243 Ruan K, Zhu Y, Li C, Brazill JM, Zhai RG. 2015. Alternative splicing of *Drosophila* Nmnat
1244 functions as a switch to enhance neuroprotection under stress. *Nat Commun* **6**:10057.
1245 doi:10.1038/ncomms10057
1246 Rucker E, Schneider G, Steinhäuser K, Löwer R, Hauber J, Stauber RH. 2001. Rapid
1247 evaluation and optimization of recombinant protein production using GFP tagging.
1248 *Protein Expr Purif* **21**:220–223. doi:10.1006/PREP.2000.1373
1249 Sasaki Y, Nakagawa T, Mao X, DiAntonio A, Milbrandt J. 2016. NMNAT1 inhibits axon
1250 degeneration via blockade of SARM1-mediated NAD⁺ depletion. *Elife* **5**.
1251 doi:10.7554/ELIFE.19749
1252 Sasaki Y, Zhu J, Shi Y, Gu W, Kobe B, Ve T, DiAntonio A, Milbrandt J. 2021. Nicotinic acid
1253 mononucleotide is an allosteric SARM1 inhibitor promoting axonal protection. *Exp*
1254 *Neurol* **345**:113842. doi:10.1016/J.EXPNEUROL.2021.113842
1255 Seeds AM, Ravbar P, Chung P, Hampel S, Midgley FM, Mensh BD, Simpson JH. 2014. A
1256 suppression hierarchy among competing motor programs drives sequential grooming
1257 in *Drosophila*. *Elife* **3**:e02951. doi:10.7554/ELIFE.02951
1258 van der Velpen V, Rosenberg N, Maillard V, Teav T, Chatton JY, Gallart-Ayala H, Ivanisevic
1259 J. 2021. Sex-specific alterations in NAD⁺ metabolism in 3xTg Alzheimer's disease
1260 mouse brain assessed by quantitative targeted LC-MS. *J Neurochem* **159**:378–388.
1261 doi:10.1111/JNC.15362
1262 Walker LJ, Summers DW, Sasaki Y, Brace E, Milbrandt J, DiAntonio A. 2017. MAPK
1263 signaling promotes axonal degeneration by speeding the turnover of the axonal
1264 maintenance factor NMNAT2. *Elife* **6**. doi:10.7554/eLife.22540
1265 Waller A. 1850. Experiments on the Section of the Glossopharyngeal and Hypoglossal
1266 Nerves of the Frog, and Observations of the Alterations Produced Thereby in the
1267 Structure of Their Primitive, Source: Philosophical Transactions of the Royal Society of
1268 London.
1269 Xiong X, Hao Y, Sun K, Li J, Li X, Mishra B, Soppina P, Wu C, Hume RI, Collins CA. 2012. The
1270 Highwire Ubiquitin Ligase Promotes Axonal Degeneration by Tuning Levels of Nmnat
1271 Protein. *PLoS Biol* **10**:1–18. doi:10.1371/journal.pbio.1001440
1272 Yoshino J, Baur JA, Imai S ichiro. 2018. NAD⁺ Intermediates: The Biology and Therapeutic
1273 Potential of NMN and NR. *Cell Metab* **27**:513–528. doi:10.1016/J.CMET.2017.11.002
1274 Zamporlini F, Ruggieri S, Mazzola F, Amici A, Orsomando G, Raffaelli N. 2014. Novel assay
1275 for simultaneous measurement of pyridine mononucleotides synthesizing activities

1276 allows dissection of the NAD(+) biosynthetic machinery in mammalian cells. *FEBS J*
1277 **281**:5104–5119. doi:10.1111/FEBS.13050
1278 Zhai RG, Cao Y, Hiesinger PR, Zhou Y, Mehta SQ, Schulze KL, Verstreken P, Bellen HJ.
1279 2006. Drosophila NMNAT maintains neural integrity independent of its NAD synthesis
1280 activity. *PLoS Biol* **4**:2336–2348. doi:10.1371/journal.pbio.0040416
1281 Zhao ZY, Xie XJ, Li WH, Liu J, Chen Z, Zhang B, Li T, Li SL, Lu JG, Zhang Liangren, Zhang Li
1282 he, Xu Z, Lee HC, Zhao YJ. 2019. A Cell-Permeant Mimetic of NMN Activates SARM1
1283 to Produce Cyclic ADP-Ribose and Induce Non-apoptotic Cell Death. *iScience* **15**:452.
1284 doi:10.1016/J.ISCI.2019.05.001
1285

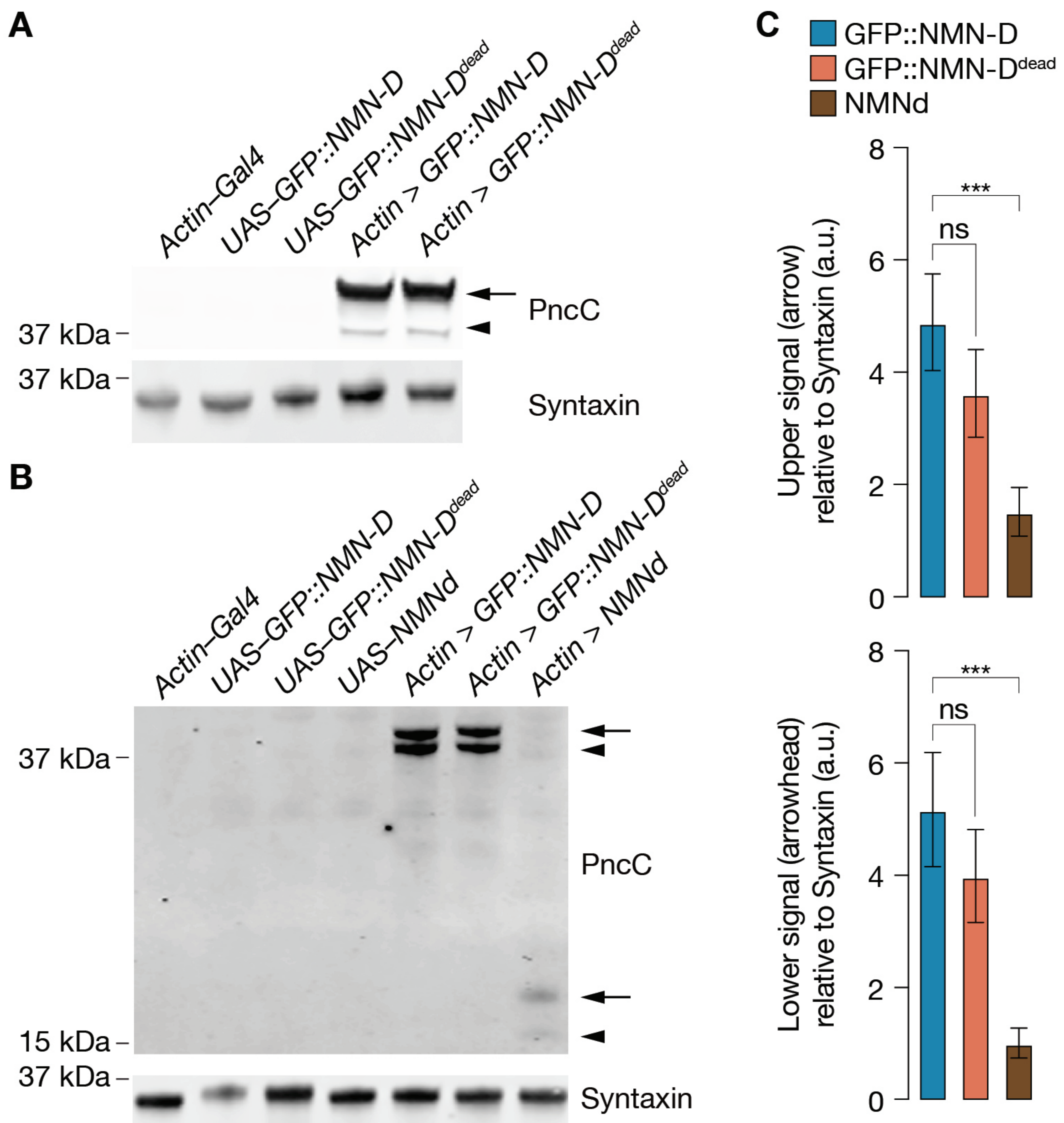
Llobet Rosell *et al.*, Figure 1



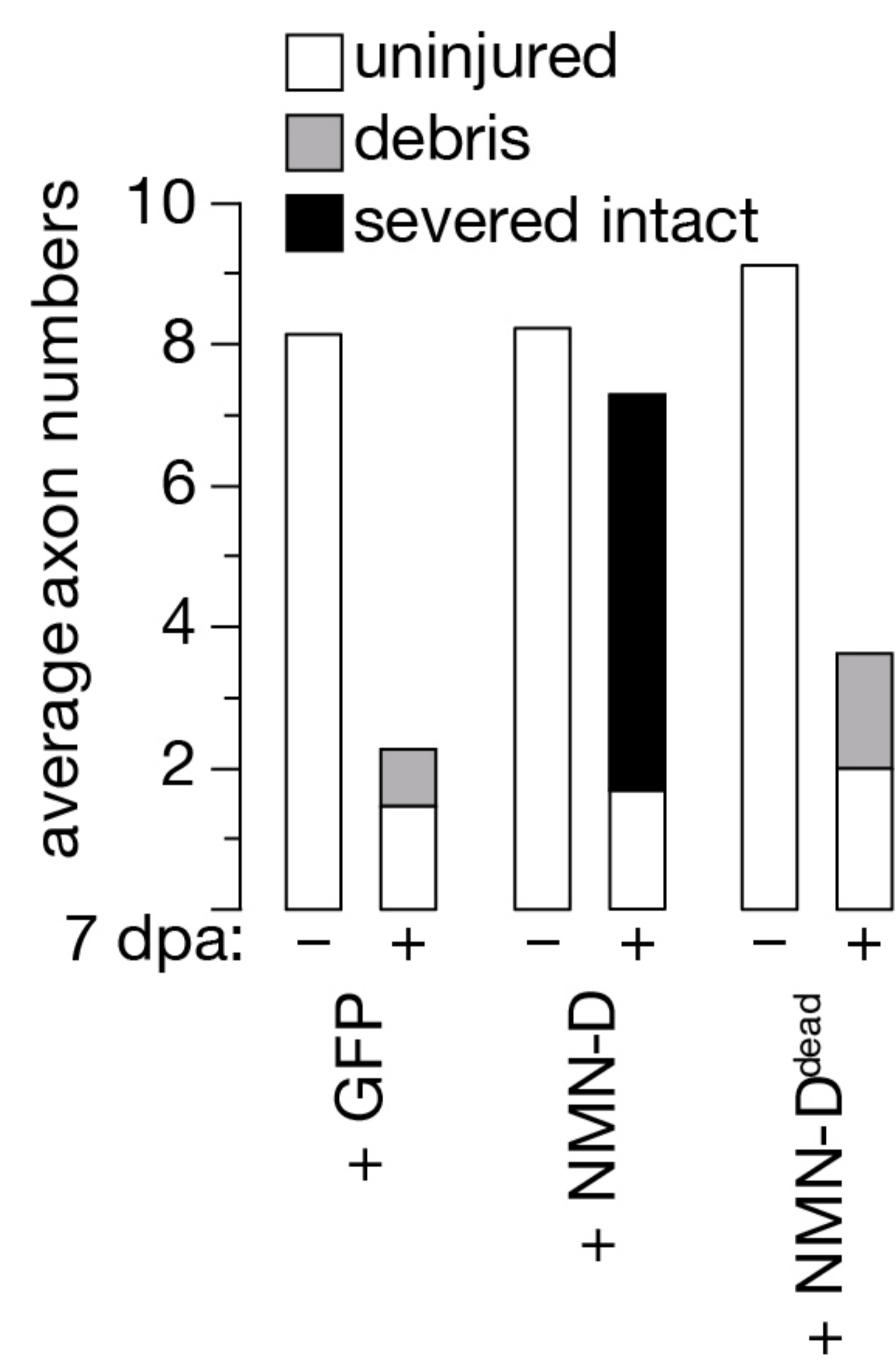
Llobet Rosell *et al.*, Figure 1 – figure supplement 1



Llobet Rosell *et al.*, Figure 1 – figure supplement 2

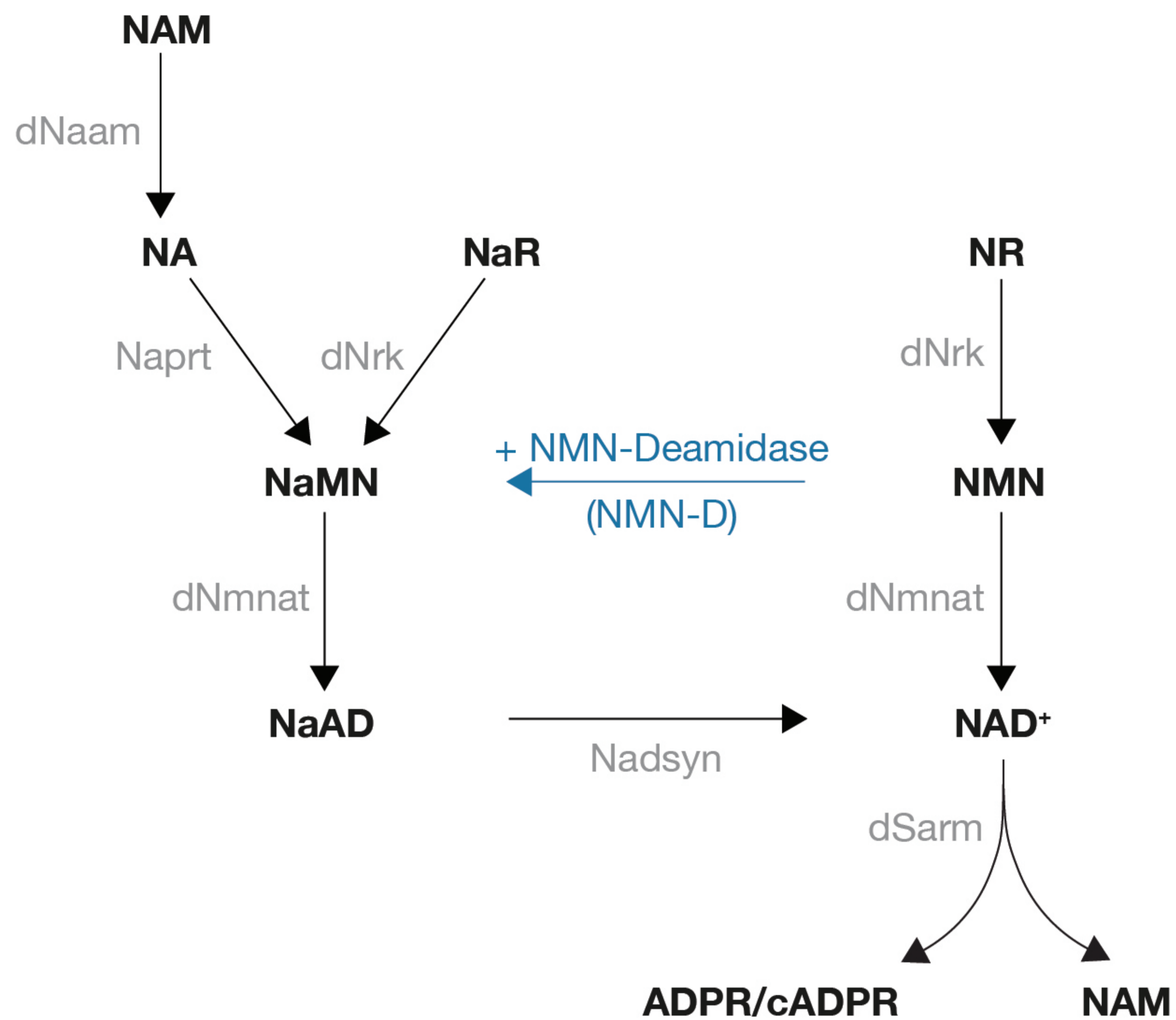


Llobet Rosell *et al.*, Figure 1 – figure supplement 3

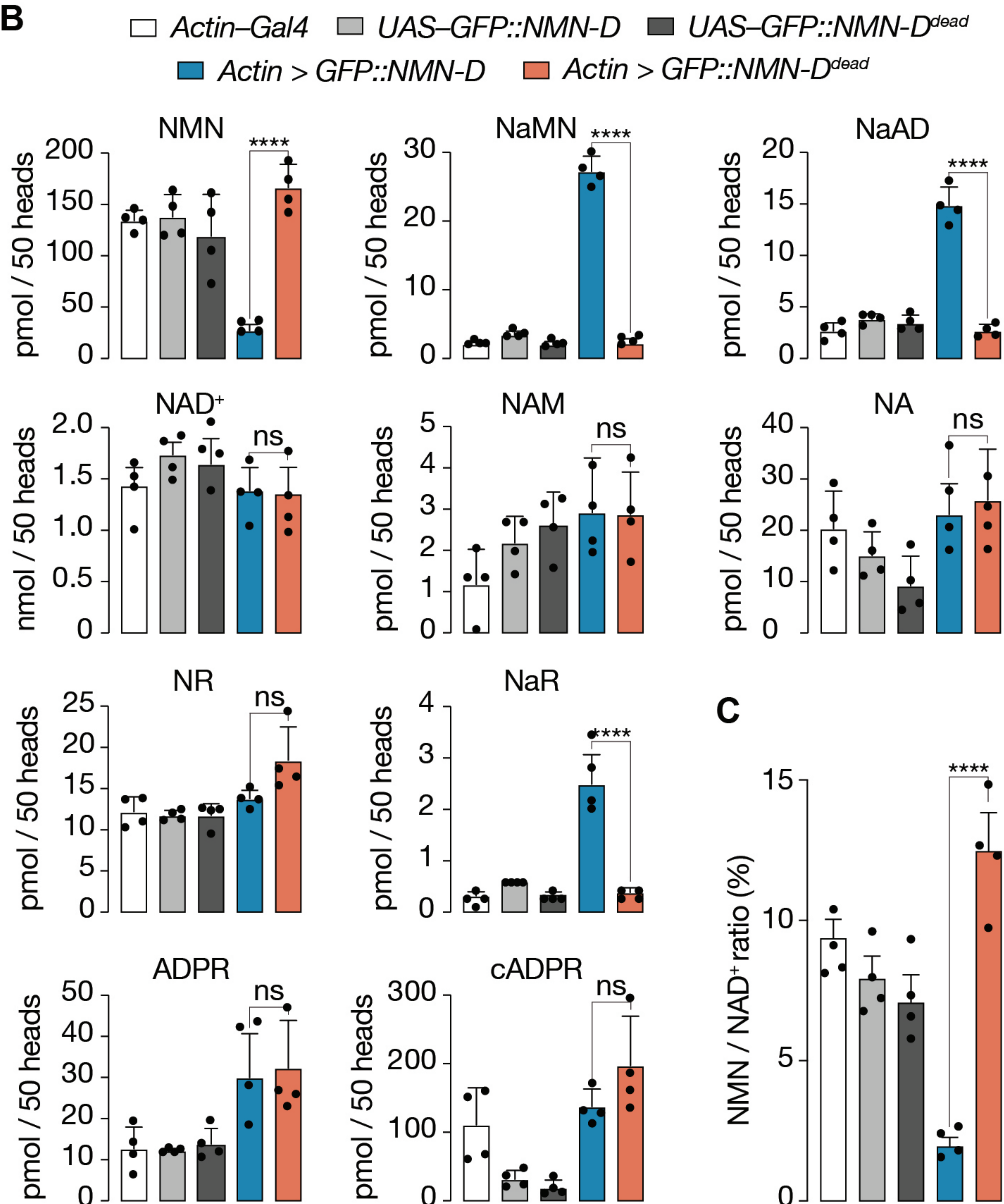


Llobet Rosell *et al.*, Figure 2

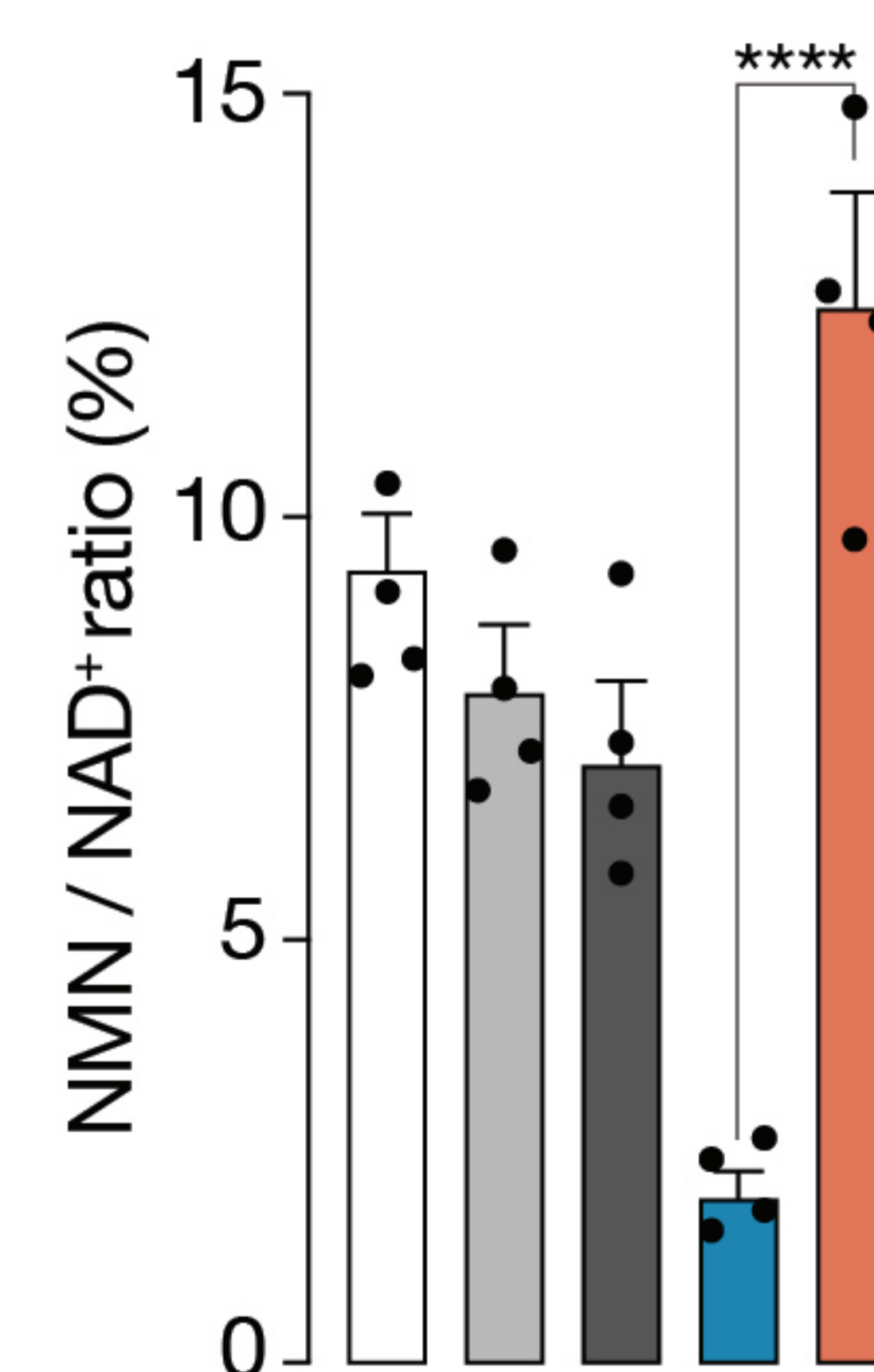
A



B



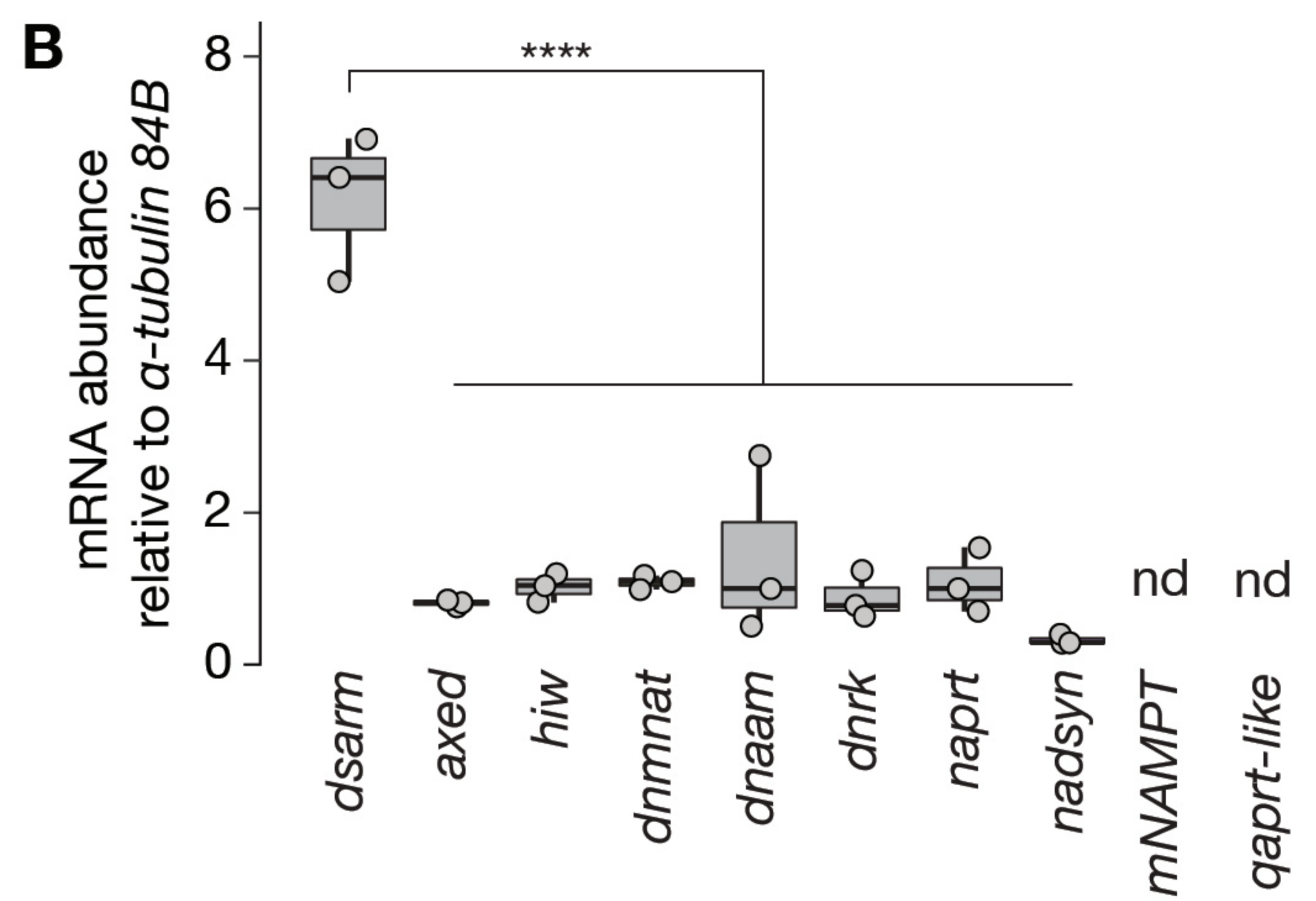
C



Llobet Rosell *et al.*, Figure 2 – figure supplement 1

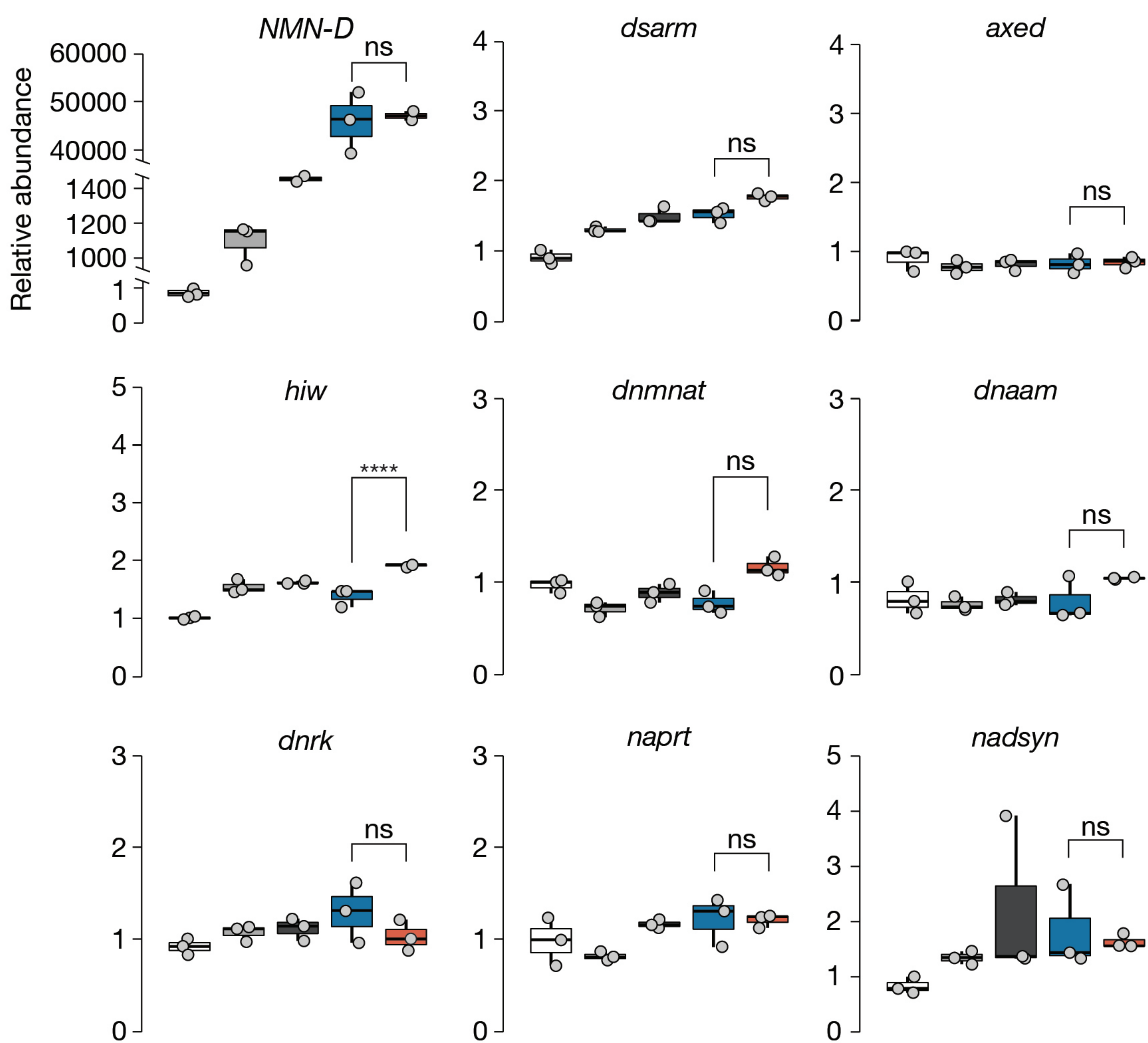
A

Enzyme	pmol / h / 50 heads
dNaam	33795 ± 19771
Naprt	1.23 ± 1.73
dNrk	10.91 ± 7.10
dNmnat	2.19 ± 1.23
Nadsyn	205.5 ± 194.4
mNampt	not detected
Qaprt-like	4.85 ± 1.82

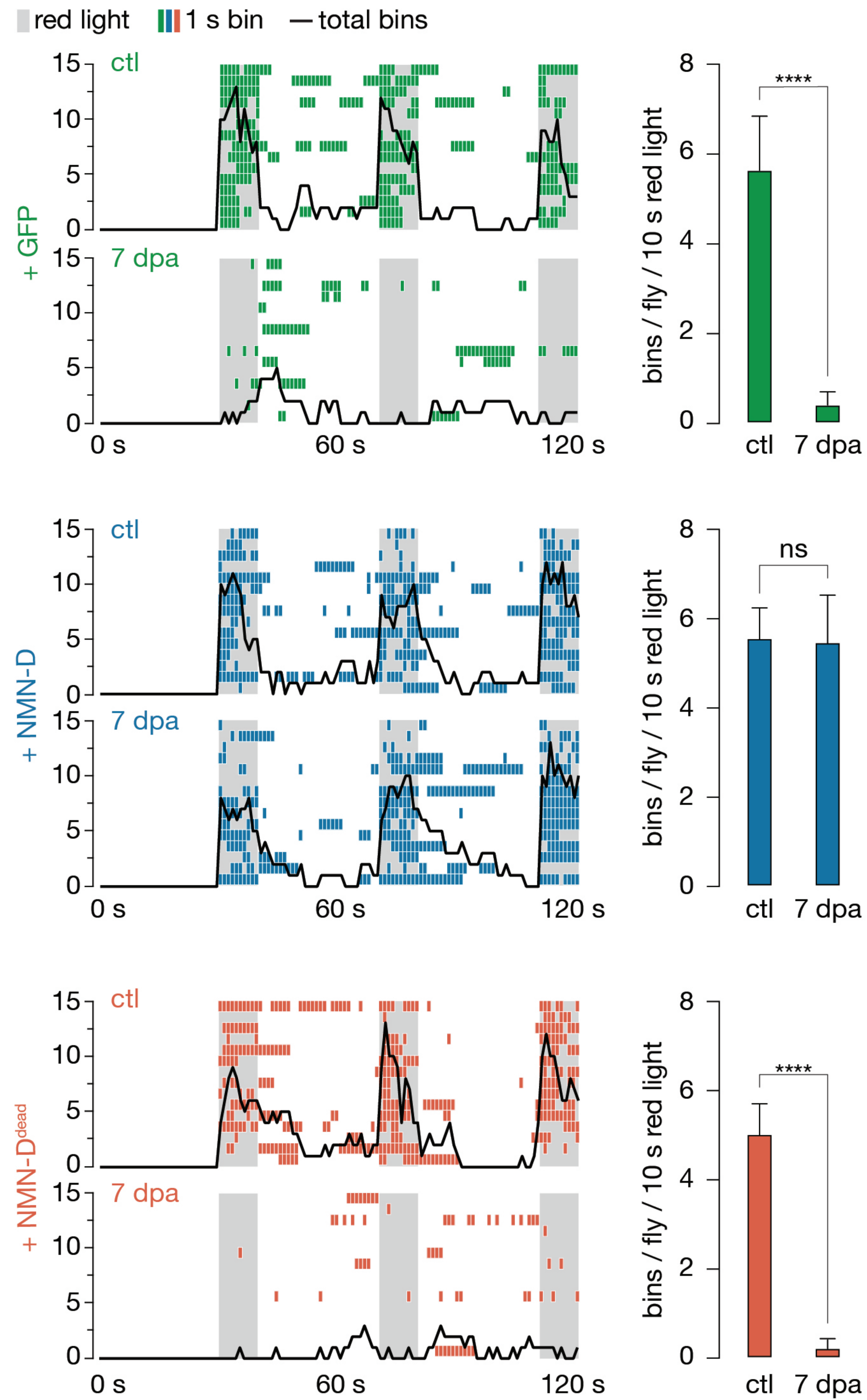


Llobet Rosell *et al.*, Figure 2 – figure supplement 2

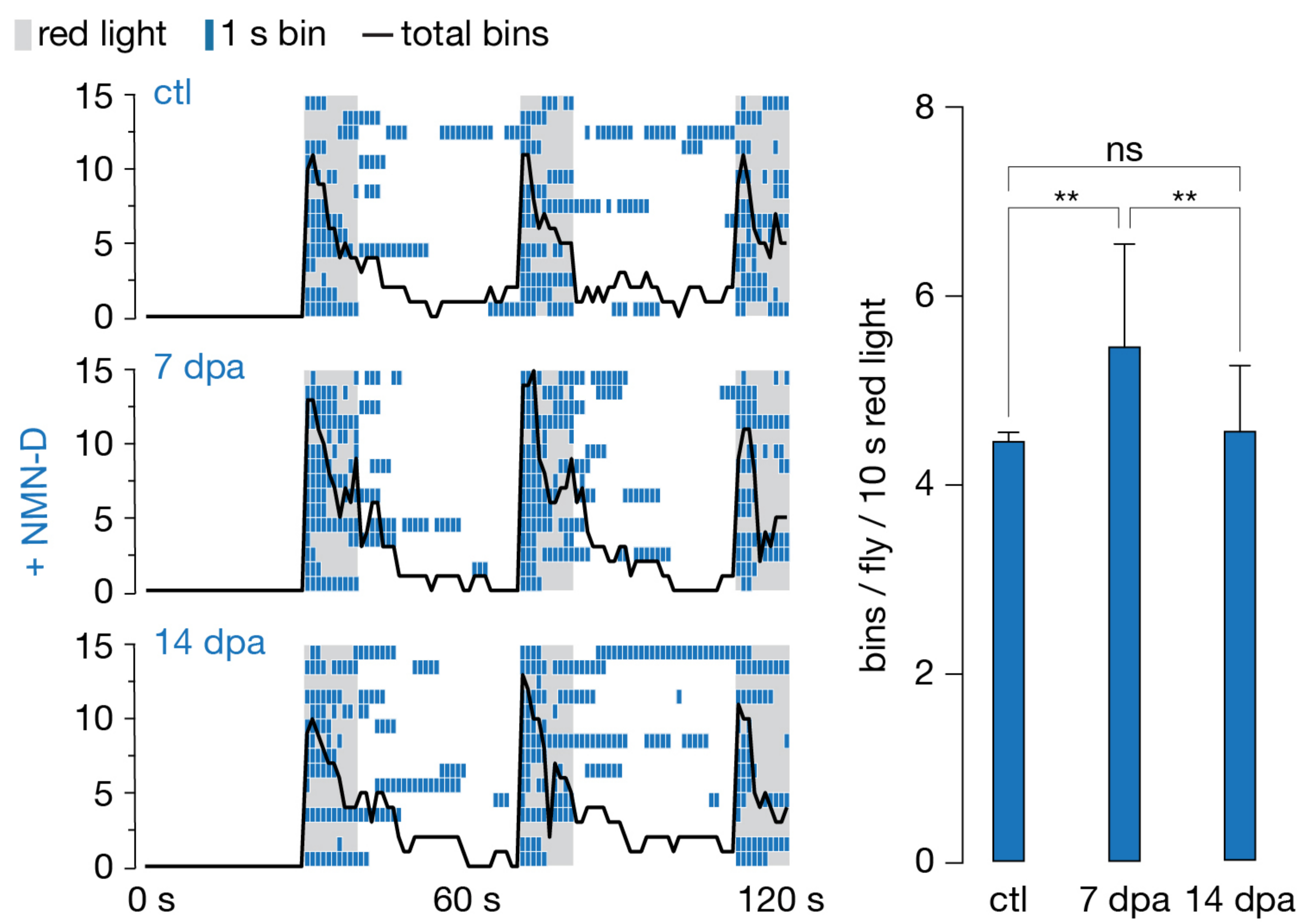
□ *Actin-Gal4* □ *UAS-NMN-D* ■ *UAS-NMN-D^{dead}* ■ *Actin > NMN-D* ■ *Actin > NMN-D^{dead}*

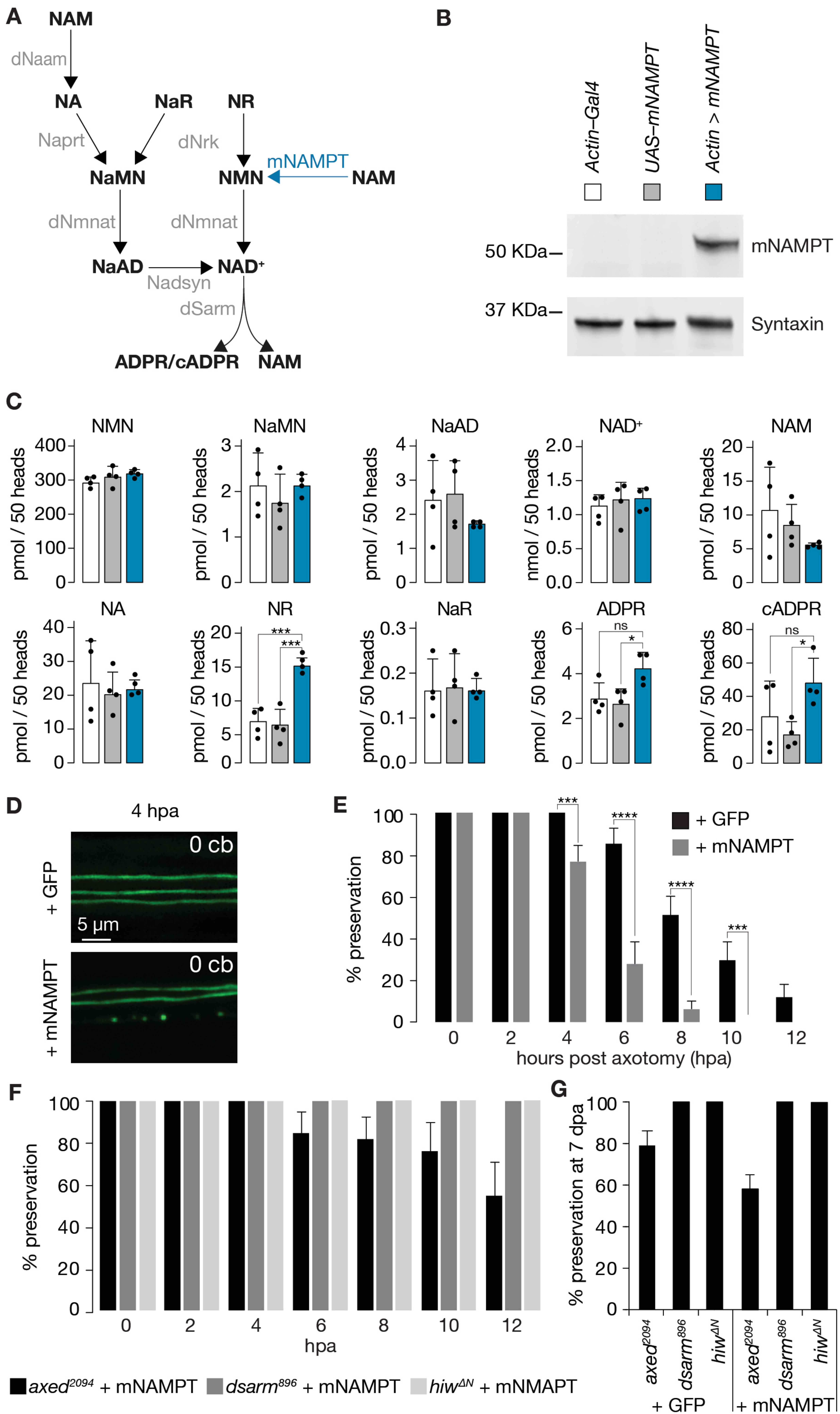


Llobet Rosell *et al.*, Figure 3

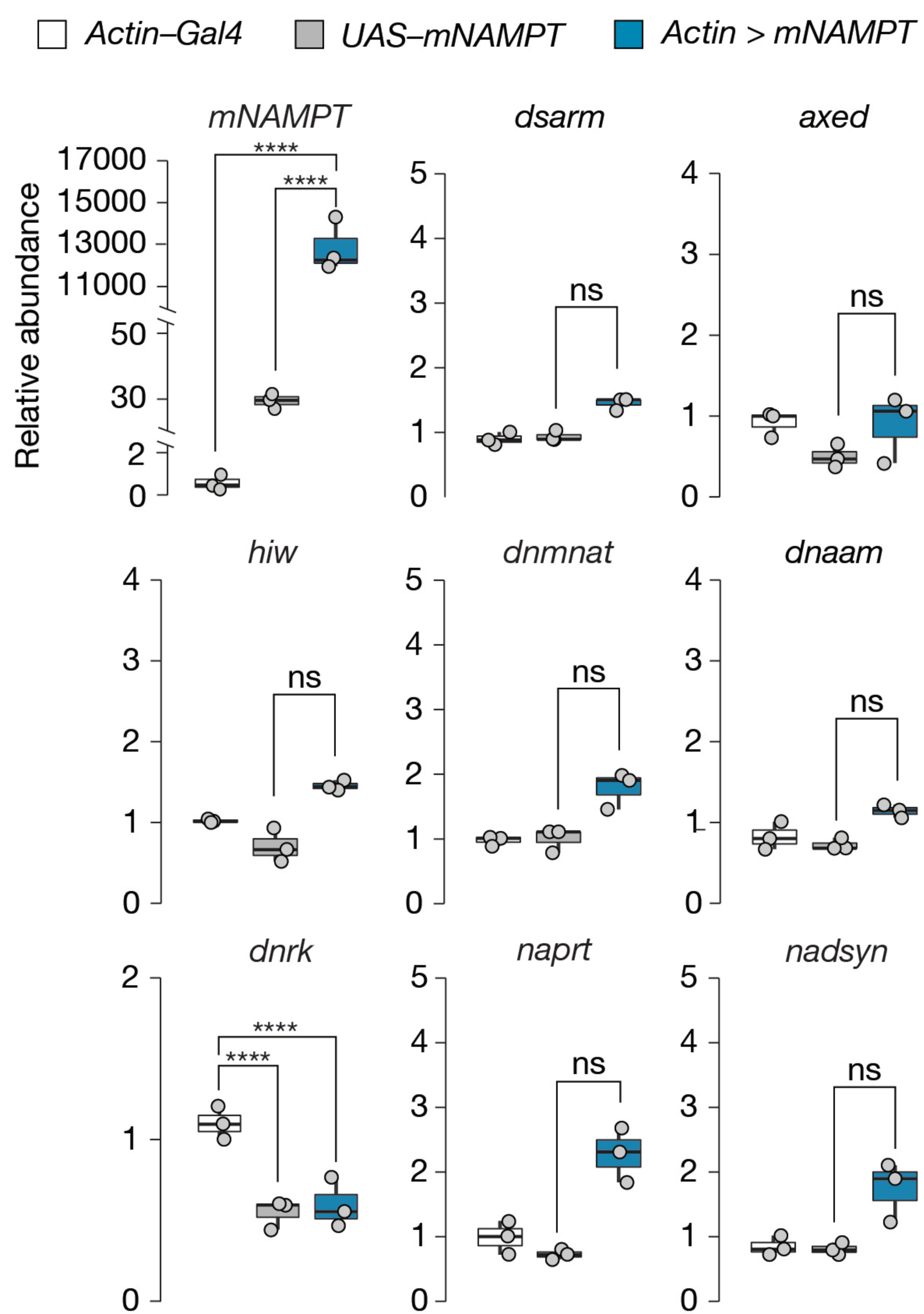


Llobet Rosell *et al.*, Figure 3 – figure supplement 1

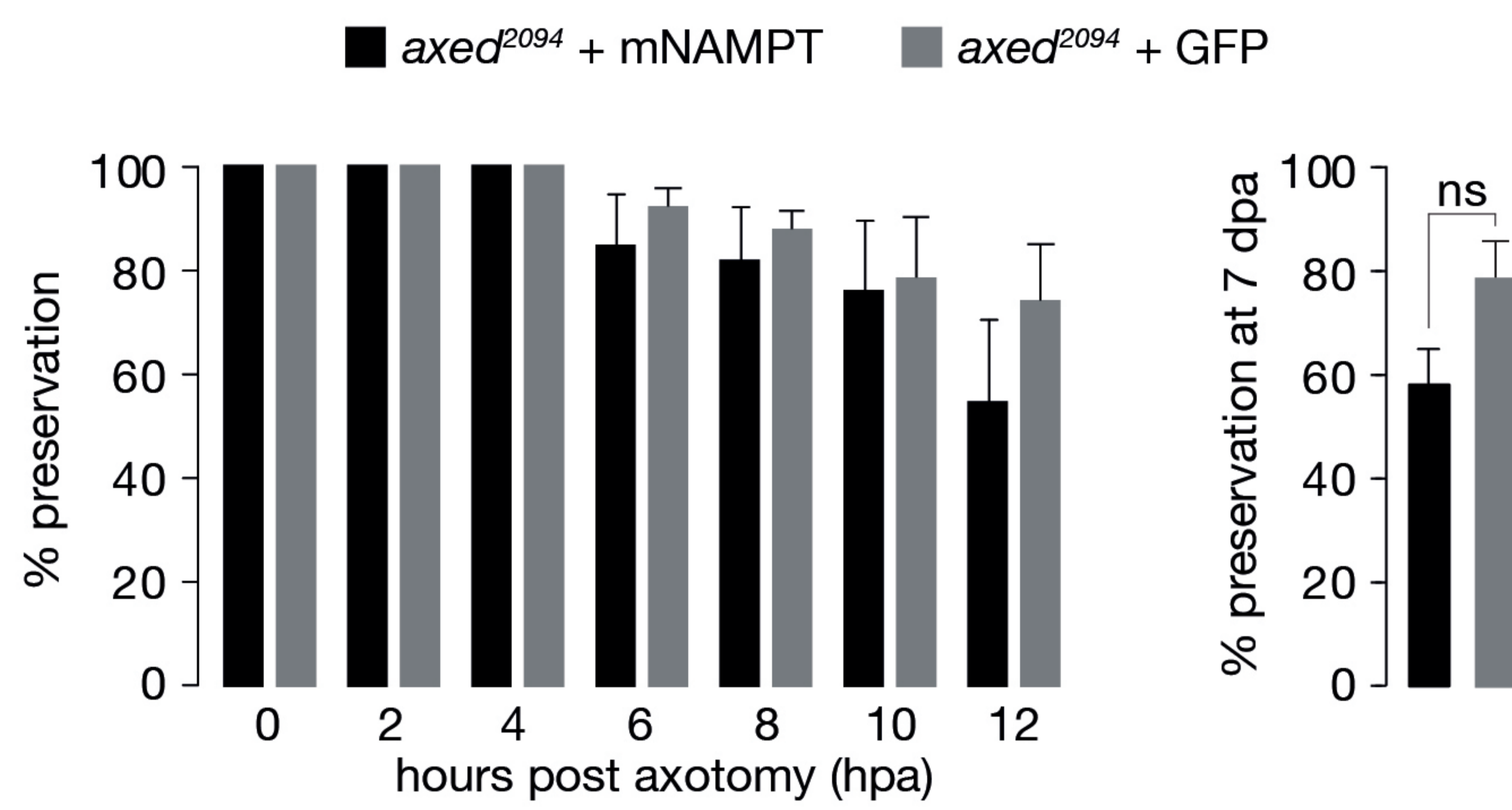


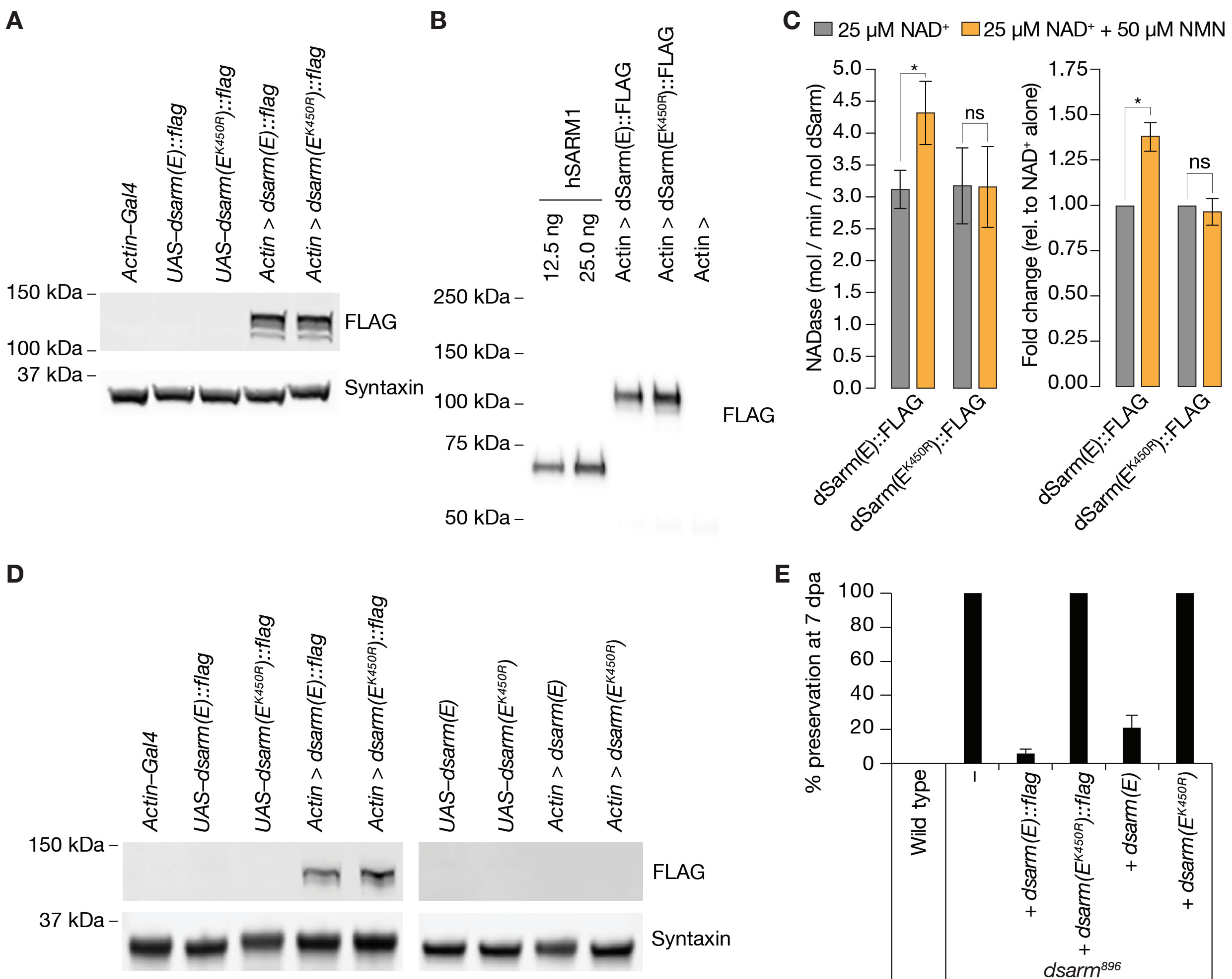


Llobet Rosell *et al.*, Figure 4 – figure supplement 1



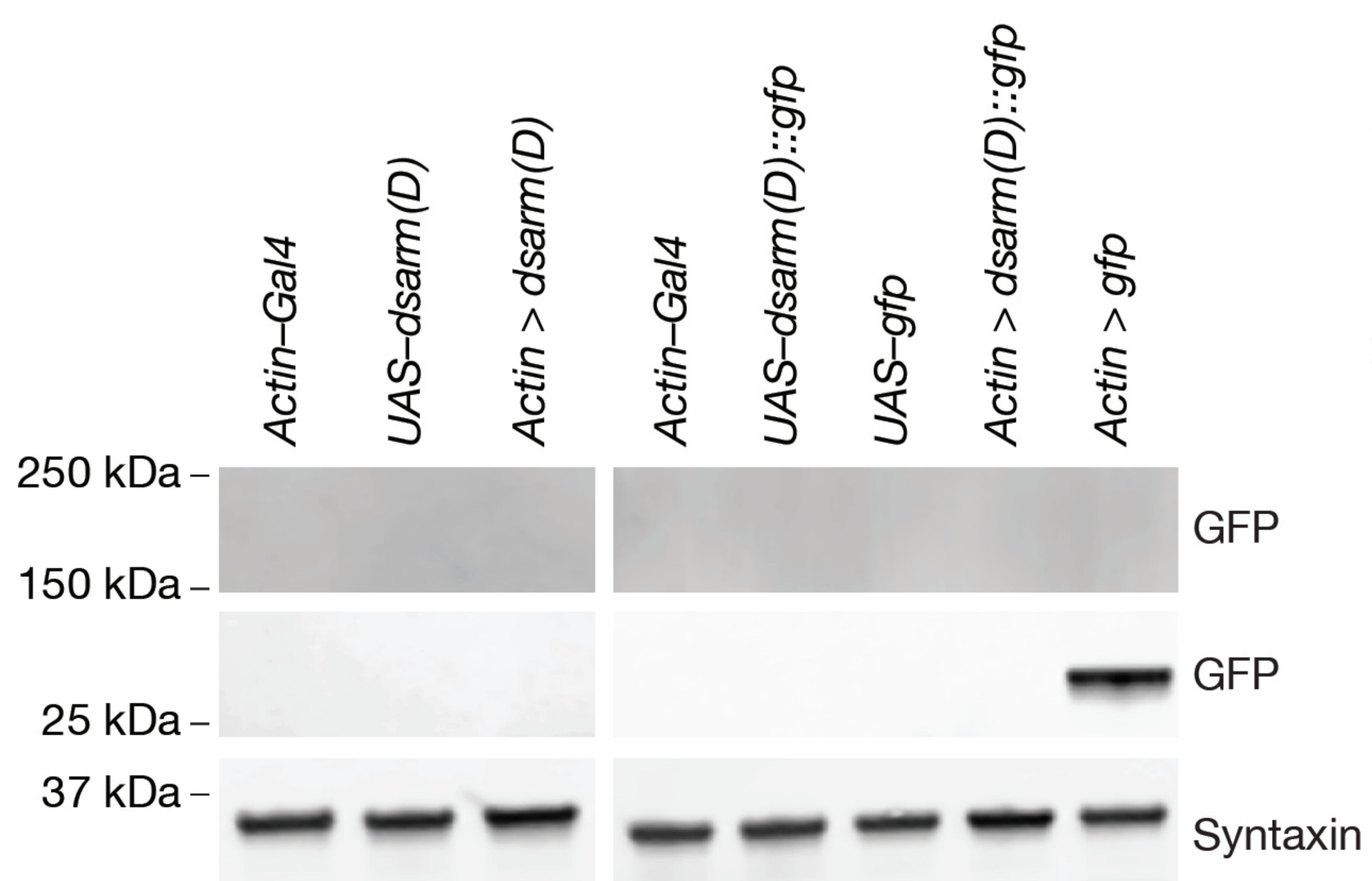
Llobet Rosell *et al.*, Figure 4 – figure supplement 2



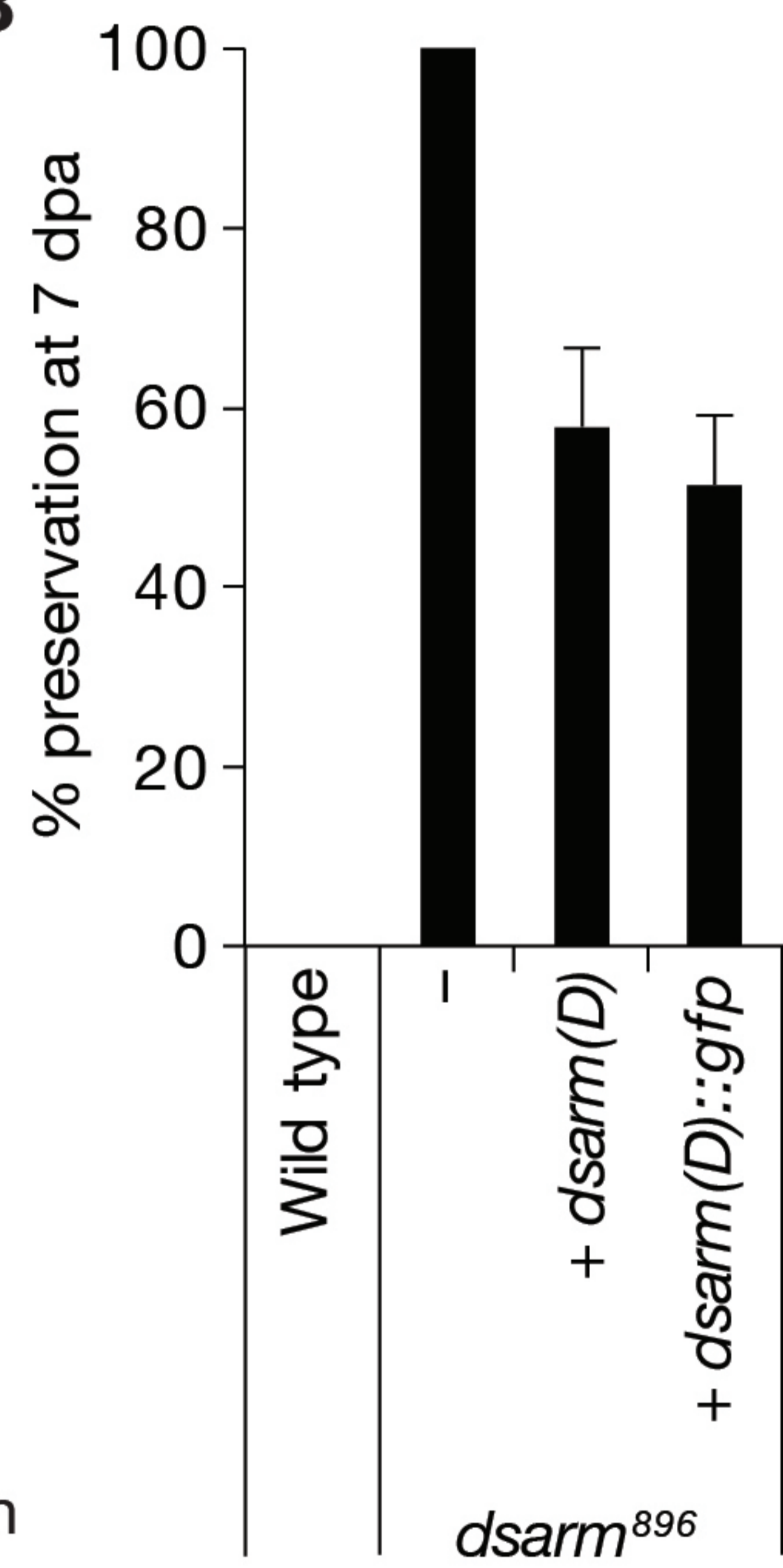


Llobet Rosell *et al.*, Figure 5 – figure supplement 1

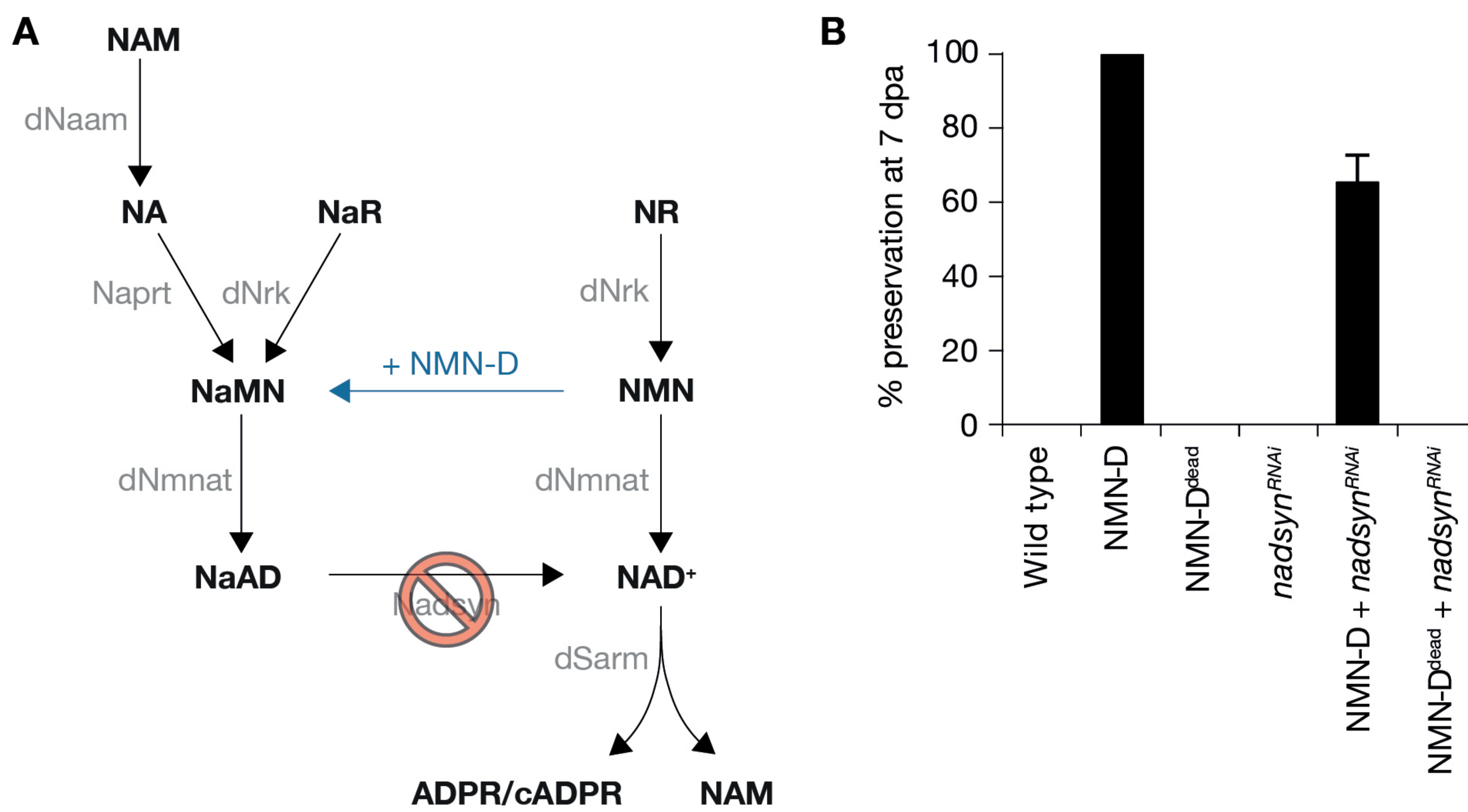
A



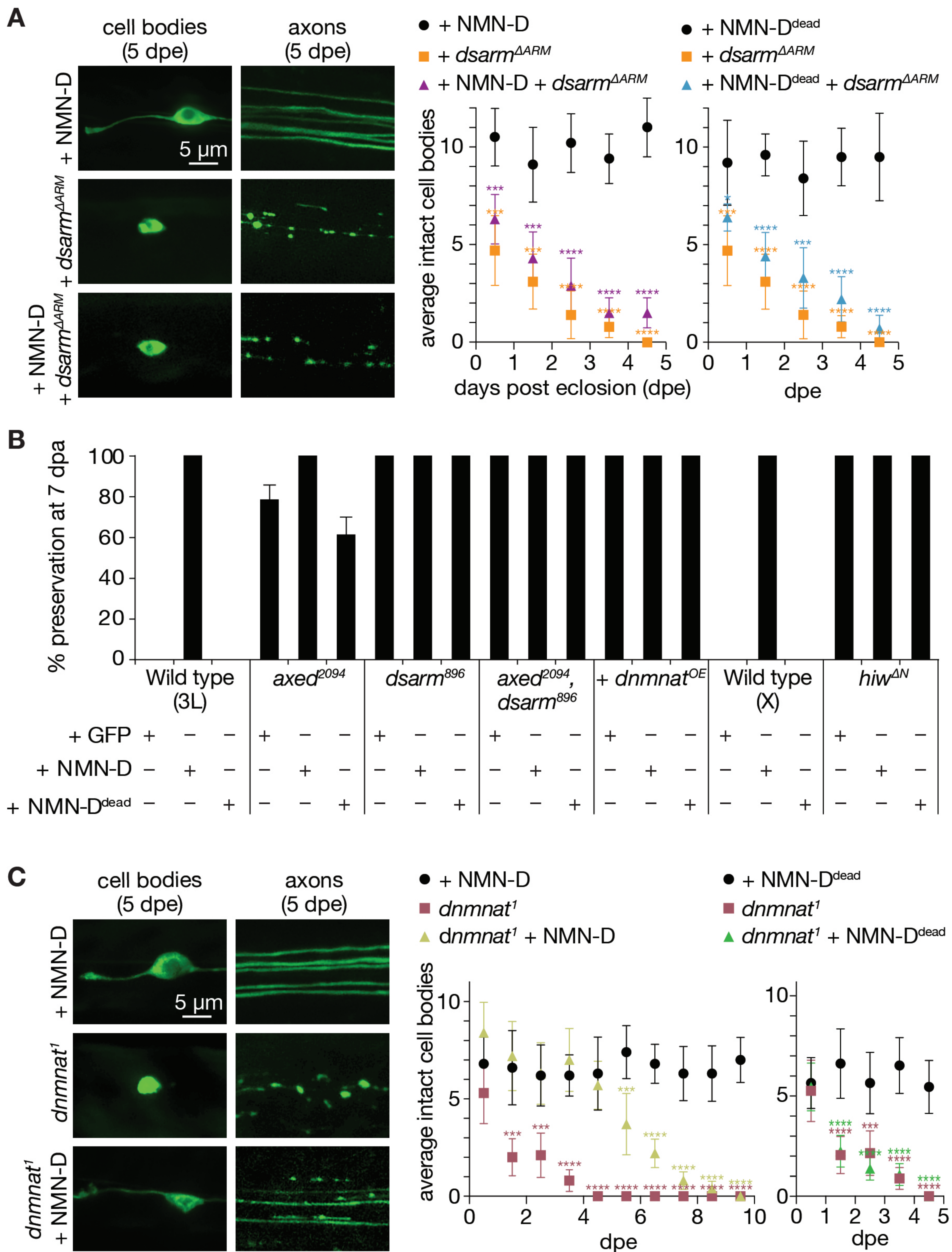
B

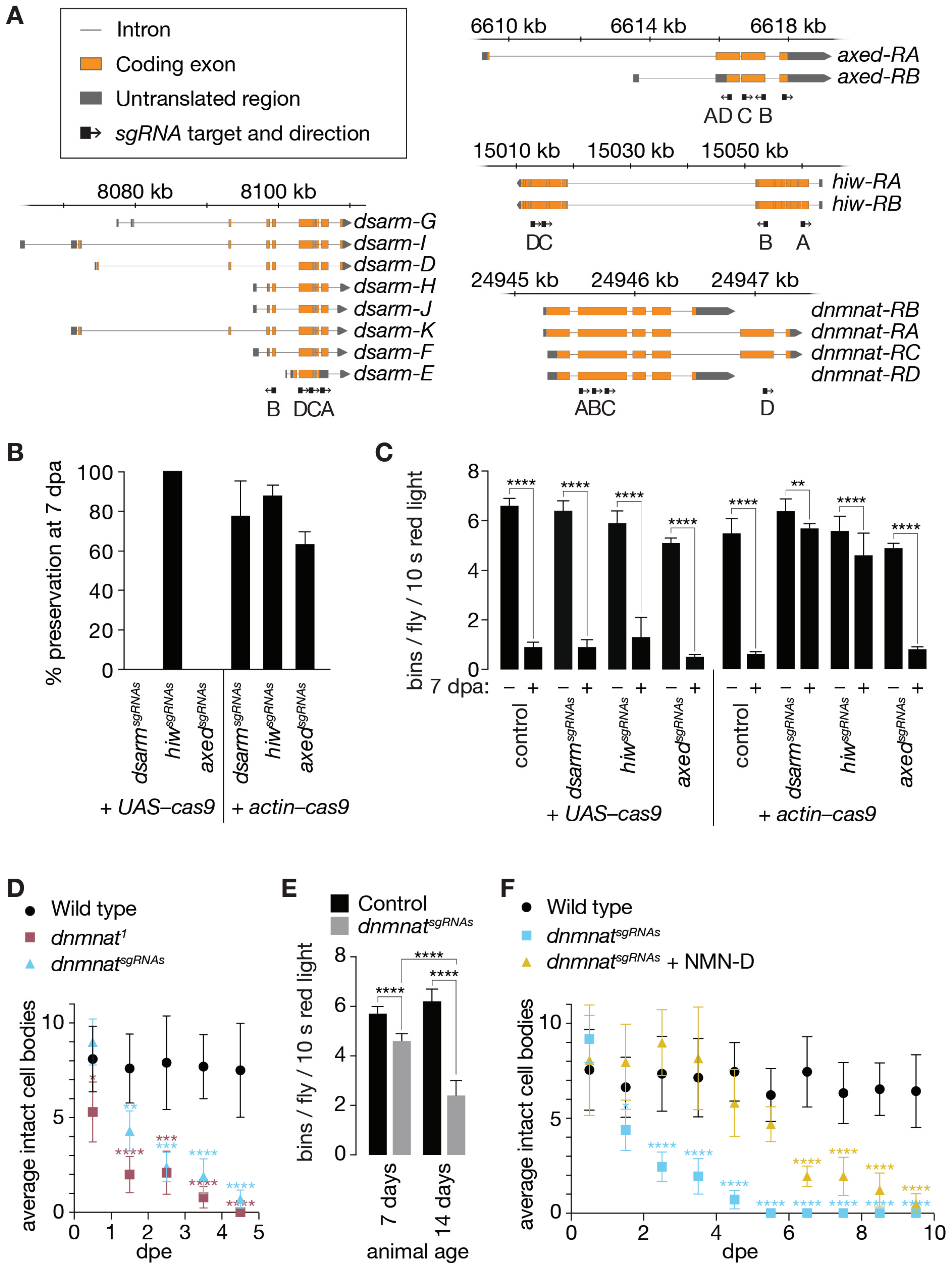


Llobet Rosell *et al.*, Figure 5 – figure supplement 2



Llobet Rosell *et al.*, Figure 6





Main Figures

Figure 1

A *actin-Gal4*: w; *actin-Gal4*/+;

A *UAS-NMN-D*: w; 5xUAS-GFP::*NMN-Deamidase*/+;

A *UAS-NMN-D^{dead}*: w; 5xUAS-GFP::*NMN-Deamidase^{dead}*/+;

A *actin > NMN-D*: w; *actin-Gal4* /5xUAS-GFP::*NMN-Deamidase*;

A *actin > NMN-D^{dead}*: w; *actin-Gal4* /5xUAS-GFP::*NMN-Deamidase^{dead}*;

B-C *GFP*: w; *dpr1,mCD8::GFP,aseFLP^{2b}* /UAS-GFP ; *FRT2A/tub Gal80,FRT2A*

B-C *NMN-D*: w; *dpr1,mCD8::GFP,aseFLP^{2b}* /5xUAS-GFP::*NMN-Deamidase* ; *FRT2A/tub Gal80,FRT2A*

B-C *NMN-D^{dead}*: w; *dpr1,mCD8::GFP,aseFLP^{2b}* /5xUAS-GFP::*NMN-Deamidase^{dead}* ; *FRT2A/tub Gal80,FRT2A*

D *GFP*: w; *OR22a-Gal4*, 5xUAS-*mCD8::GFP* /UAS-GFP

D *NMN-D^{dead}*: w; *OR22a-Gal4*, 5xUAS-*mCD8::GFP* /5xUAS-GFP::*NMN-Deamidase^{dead}*

D-E *NMN-D*: w; *OR22a-Gal4*, 5xUAS-*mCD8::GFP* /5xUAS-GFP::*NMN-Deamidase*

Figure 1 - figure supplement 1

A-B *GFP*: w; *dpr1,mCD8::GFP,aseFLP^{2b}* /UAS-GFP ; *FRT2A/tub Gal80,FRT2A*

A-B *NMNd*: w; *dpr1,mCD8::GFP,aseFLP^{2b}* /5xUAS-*NMN-Deamidase* ; *FRT2A/tub Gal80,FRT2A*

Figure 1 - figure supplement 2

B *actin-Gal4*: w; *actin-Gal4*/+;

B *UAS-NMN-D*: w; 5xUAS-GFP::*NMN-Deamidase*/+;

B *UAS-NMN-D^{dead}*: w; 5xUAS-GFP::*NMN-Deamidase^{dead}*/+;

B *UAS-NMNd*: w; 5xUAS-*NMN-Deamidase*/+;

B-C *actin > NMN-D*: w; *actin-Gal4* /5xUAS-GFP::*NMN-Deamidase*;

B-C *actin > NMN-D^{dead}*: w; *actin-Gal4* /5xUAS-GFP::*NMN-Deamidase^{dead}*;

B-C *actin > NMNd*: w; *actin-Gal4* /5xUAS::*NMN-Deamidase*;

Figure 1 - figure supplement 3

GFP: w; *dpr1,mCD8::GFP,aseFLP^{2b}* /UAS-GFP ; *FRT2A/tub Gal80,FRT2A*

NMN-D: w; *dpr1,mCD8::GFP,aseFLP^{2b}* /5xUAS-GFP::*NMN-Deamidase* ; *FRT2A/tub Gal80,FRT2A*

NMN-D^{dead}: w; *dpr1,mCD8::GFP,aseFLP^{2b}* /5xUAS-GFP::*NMN-Deamidase^{dead}* ; *FRT2A/tub Gal80,FRT2A*

Figure 2

B *actin-Gal4*: w; *actin-Gal4*/+;

B *UAS-NMN-D*: w; 5xUAS-GFP::*NMN-Deamidase*/+;

B *UAS-NMN-D^{dead}*: w; 5xUAS-GFP::*NMN-Deamidase^{dead}*/+;

B *actin > NMN-D*: w; *actin-Gal4* /5xUAS-GFP::*NMN-Deamidase*;

B *actin > NMN-D^{dead}*: w; *actin-Gal4* /5xUAS-GFP::*NMN-Deamidase^{dead}*;

Figure 2 - figure supplement 1

A-B *Wild type*: Canton special (Canton-S).

Figure 2 - figure supplement 2

B *actin-Gal4*: w; *actin-Gal4*/+;

B *UAS-NMN-D*: w; 5xUAS-GFP::*NMN-Deamidase*/+;

B *UAS-NMN-D^{dead}*: w; 5xUAS-GFP::*NMN-Deamidase^{dead}*/+;

B *actin > NMN-D*: w; *actin-Gal4* /5xUAS-GFP::*NMN-Deamidase*;

B *actin > NMN-D^{dead}*: w; *actin-Gal4* /5xUAS-GFP::*NMN-Deamidase^{dead}*;

Figure 3

GFP: w; 20xUAS IVS *CsChrimson::mVenus* /UAS-GFP ; *GMR60E02 Gal4* /+

NMN-D: w; 20xUAS IVS *CsChrimson::mVenus* /5xUAS-GFP::*NMN-Deamidase* ; *GMR60E02 Gal4* /+

NMN-D^{dead}: w; 20xUAS IVS *CsChrimson::mVenus* /5xUAS-GFP::*NMN-Deamidase^{dead}* ; *GMR60E02 Gal4* /+

Figure 3 - figure supplement 1

NMN-D: w; 20xUAS IVS *CsChrimson::mVenus* /5xUAS-GFP::*NMN-Deamidase* ; *GMR60E02 Gal4* /+

Video 1

GFP: w; 20xUAS IVS *CsChrimson::mVenus* /UAS-GFP ; *GMR60E02 Gal4* /+

Video 2

NMN-D: w; 20xUAS IVS CsChrimson::mVenus /5xUAS-GFP::NMN-Deamidase ; GMR60E02 Gal4 /+

Video 3

NMN-D^{dead}: w; 20xUAS IVS CsChrimson::mVenus /5xUAS-GFP::NMN-Deamidase^{dead} ; GMR60E02 Gal4 /+

Figure 4

B-C actin-Gal4: w; actin-Gal4/+;

B-C UAS-mNAMPT: w; 5xUAS-mNAMPT/+;

B-C actin > UAS-mNAMPT: w; actin-Gal4 /UAS-mNAMPT;

D-E GFP: w; dpr1,mCD8::GFP,aseFLP^{2b} /UAS-GFP ; FRT2A/tub Gal80,FRT2A

D-E mNAMPT: w; dpr1,mCD8::GFP,aseFLP^{2b} /5xUAS-mNAMPT ; FRT2A/tub Gal80,FRT2A

F-G mNAMPT + axed²⁰⁹⁴: w; dpr1,mCD8::GFP,aseFLP^{2b} /5xUAS-mNAMPT ; axed²⁰⁹⁴ , FRT2A/tub Gal80,FRT2A

F-G mNAMPT + dsarm⁸⁹⁶: w; dpr1,mCD8::GFP,aseFLP^{2b} /5xUAS-mNAMPT ; dsarm⁸⁹⁶ , FRT2A/tub Gal80,FRT2A

F-G mNAMPT + hiw^{ΔN}: w,tub Gal80,FRT19A/w,hiw^{ΔN},FRT19A ; dpr1,mCD8::GFP,aseFLP^{2d} /5xUAS-mNAMPT

G GFP + axed²⁰⁹⁴: w; dpr1,mCD8::GFP,aseFLP^{2b} /UAS-GFP ; axed²⁰⁹⁴ ,FRT2A/tub Gal80,FRT2A

G GFP + dsarm⁸⁹⁶: w; dpr1,mCD8::GFP,aseFLP^{2b} /UAS-GFP ; dsarm⁸⁹⁶ ,FRT2A/tub Gal80,FRT2A

G GFP + hiw^{ΔN}: w,tub Gal80,FRT19A/w,hiw^{ΔN},FRT19A ; dpr1,mCD8::GFP,aseFLP^{2d} /UAS-GFP ;

Figure 4 - figure supplement 1

actin-Gal4: w; actin-Gal4/+;

UAS-mNAMPT: w; 5xUAS-mNAMPT/+;

actin > UAS-mNAMPT: w; actin-Gal4 /UAS-mNAMPT;

Figure 4 - figure supplement 2

mNAMPT + axed²⁰⁹⁴: w; dpr1,mCD8::GFP,aseFLP^{2b} /5xUAS-mNAMPT ; axed²⁰⁹⁴ , FRT2A/tub Gal80,FRT2A

GFP + axed²⁰⁹⁴: w; dpr1,mCD8::GFP,aseFLP^{2b} /UAS-GFP ; axed²⁰⁹⁴ ,FRT2A/tub Gal80,FRT2A

Figure 5

D actin-Gal4: w; actin-Gal4/+;

D uas-dsarm(E)::flag: w; 5xUAS-dsarm(E)::flag /+;

D uas-dsarm(E^{K450R})::flag: w; 5xUAS-dsarm(E^{K450R})::flag /+;

D actin > dsarm(E)::flag: w; actin-Gal4 /5xUAS-dsarm(E)::flag;

D actin > dsarm(E^{K450R})::flag: w; actin-Gal4 /5xUAS-dsarm(E^{K450R})::flag

D uas-dsarm(E): w; 5xUAS-dsarm(E) /+;

D uas-dsarm(E^{K450R}): w; 5xUAS-dsarm(E^{K450R}) /+;

D actin > dsarm(E): w; actin-Gal4 /5xUAS-dsarm(E);

D actin > dsarm(E^{K450R}): w; actin-Gal4 /5xUAS-dsarm(E^{K450R})

E Wild type: w; dpr1,mCD8::GFP,aseFLP^{2b} /+ ; FRT2A/tub Gal80,FRT2A

E dsarm⁸⁹⁶: w; dpr1,mCD8::GFP,aseFLP^{2b} /+ ; dsarm⁸⁹⁶ ,FRT2A/tub Gal80,FRT2A

E dsarm⁸⁹⁶ + dsarm(E)::flag: w; dpr1,mCD8::GFP,aseFLP^{2b} /dsarm(E)::flag; dsarm⁸⁹⁶ ,FRT2A/tub Gal80,FRT2A

E dsarm⁸⁹⁶ + dsarm(E^{K450R})::flag: w; dpr1,mCD8::GFP,aseFLP^{2b} /dsarm(E^{K450R})::flag; dsarm⁸⁹⁶ ,FRT2A/tub Gal80,FRT2A

E dsarm⁸⁹⁶ + dsarm(E): w; dpr1,mCD8::GFP,aseFLP^{2b} /dsarm(E); dsarm⁸⁹⁶ ,FRT2A/tub Gal80,FRT2A

E dsarm⁸⁹⁶ + dsarm(E^{K450R}): w; dpr1,mCD8::GFP,aseFLP^{2b} /dsarm(E^{K450R}); dsarm⁸⁹⁶ ,FRT2A/tub Gal80,FRT2A

Figure 5 - figure supplement 1

A actin-Gal4: w; actin-Gal4/+;

A uas-dsarm(D): w; 5xUAS-dsarm(D) /+;

A actin > dsarm(D): w; actin-Gal4 /5xUAS-dsarm(D);

A uas-dsarm(D)::GFP: w; 5xUAS-dsarm(D)::GFP /+;

A uas-GFP: w; UAS-GFP /+;

A actin > dsarm(D)::GFP: w; actin-Gal4 /5xUAS-dsarm(D)::GFP;

A actin > GFP: w; actin-Gal4 /UAS-GFP

B Wild type: w; dpr1,mCD8::GFP,aseFLP^{2b} /+ ; FRT2A/tub Gal80,FRT2A

B dsarm⁸⁹⁶: w; dpr1,mCD8::GFP,aseFLP^{2b} /+ ; dsarm⁸⁹⁶ ,FRT2A/tub Gal80,FRT2A

B dsarm⁸⁹⁶ + dsarm(D): w; dpr1,mCD8::GFP,aseFLP^{2b} /dsarm(D); dsarm⁸⁹⁶ ,FRT2A/tub Gal80,FRT2A

B dsarm⁸⁹⁶ + dsarm(D)::GFP: w; dpr1,mCD8::GFP,aseFLP^{2b} /dsarm(D)::GFP; dsarm⁸⁹⁶ ,FRT2A/tub Gal80,FRT2A

Figure 5 - figure supplement 2

B Wild type: *w ; dpr1,mCD8::GFP,aseFLP^{2b} /+ ; FRT2A/tub Gal80,FRT2A*
B NMN-D: *w ; dpr1,mCD8::GFP,aseFLP^{2b} , 5xUAS-GFP::NMN-Deamidase /+ ; FRT2A/tub Gal80,FRT2A*
B NMN-D^{dead}: *w ; dpr1,mCD8::GFP,aseFLP^{2b} , 5xUAS-GFP::NMN-Deamidase^{dead} /+ ; FRT2A/tub Gal80,FRT2A*
B nadsyn^{RNAi}: *w ; dpr1,mCD8::GFP,aseFLP^{2b} /UAS-nadsyn^{RNAi} ; FRT2A/tub Gal80,FRT2A*
B NMN-D + nadsyn^{RNAi}: *w ; dpr1,mCD8::GFP,aseFLP^{2b} , 5xUAS-GFP::NMN-Deamidase /UAS-nadsyn^{RNAi} ; FRT2A/tub Gal80,FRT2A*
B NMN-D^{dead} + nadsyn^{RNAi}: *w ; dpr1,mCD8::GFP,aseFLP^{2b} , 5xUAS-GFP::NMN-Deamidase^{dead} /UAS-nadsyn^{RNAi} ; FRT2A/tub Gal80,FRT2A*

Figure 6

A NMN-D: *w ; dpr1,mCD8::GFP,aseFLP^{2b} /5xUAS-GFP::NMN-Deamidase ; FRT2A/tub Gal80,FRT2A*
A NMN-D^{dead}: *w ; dpr1,mCD8::GFP,aseFLP^{2b} /5xUAS-GFP::NMN-Deamidase^{dead} ; FRT2A/tub Gal80,FRT2A*
A dsarm^{ΔARM}: *w ; dpr1,mCD8::GFP,aseFLP^{2b} , dsarm^{ΔARM} /+ ; FRT2A/tub Gal80,FRT2A*
A NMN-D + dsarm^{ΔARM}: *w ; dpr1,mCD8::GFP,aseFLP^{2b} , dsarm^{ΔARM} /5xUAS-GFP::NMN-Deamidase ; FRT2A/tub Gal80,FRT2A*
A NMN-D^{dead} + dsarm^{ΔARM}: *w ; dpr1,mCD8::GFP,aseFLP^{2b} , dsarm^{ΔARM} /5xUAS-GFP::NMN-Deamidase^{dead} ; FRT2A/tub Gal80,FRT2A*
B 3L + GFP: *w ; dpr1,mCD8::GFP,aseFLP^{2b} /UAS-GFP ; FRT2A/tub Gal80,FRT2A*
B 3L + NMN-D: *w ; dpr1,mCD8::GFP,aseFLP^{2b} /5xUAS-GFP::NMN-Deamidase ; FRT2A/tub Gal80,FRT2A*
B 3L + NMN-D^{dead}: *w ; dpr1,mCD8::GFP,aseFLP^{2b} /5xUAS-GFP::NMN-Deamidase^{dead} ; FRT2A/tub Gal80,FRT2A*
B axed²⁰⁹⁴ + GFP: *w ; dpr1,mCD8::GFP,aseFLP^{2b} /UAS-GFP ; axed²⁰⁹⁴ , FRT2A/tub Gal80,FRT2A*
B axed²⁰⁹⁴ + NMN-D: *w ; dpr1,mCD8::GFP,aseFLP^{2b} /5xUAS-GFP::NMN-Deamidase ; axed²⁰⁹⁴ , FRT2A/tub Gal80,FRT2A*
B axed²⁰⁹⁴ + NMN-D^{dead}: *w ; dpr1,mCD8::GFP,aseFLP^{2b} /5xUAS-GFP::NMN-Deamidase^{dead} ; axed²⁰⁹⁴ , FRT2A/tub Gal80,FRT2A*
B dsarm⁸⁹⁶ + GFP: *w ; dpr1,mCD8::GFP,aseFLP^{2b} /UAS-GFP ; dsarm⁸⁹⁶ , FRT2A/tub Gal80,FRT2A*
B dsarm⁸⁹⁶ + NMN-D: *w ; dpr1,mCD8::GFP,aseFLP^{2b} /5xUAS-GFP::NMN-Deamidase ; dsarm⁸⁹⁶ , FRT2A/tub Gal80,FRT2A*
B dsarm⁸⁹⁶ + NMN-D^{dead}: *w ; dpr1,mCD8::GFP,aseFLP^{2b} /5xUAS-GFP::NMN-Deamidase^{dead} ; dsarm⁸⁹⁶ , FRT2A/tub Gal80,FRT2A*
B axed²⁰⁹⁴ , dsarm⁸⁹⁶ + GFP: *w ; dpr1,mCD8::GFP,aseFLP^{2b} /UAS-GFP ; axed²⁰⁹⁴ , dsarm⁸⁹⁶ , FRT2A/tub Gal80,FRT2A*
B axed²⁰⁹⁴ , dsarm⁸⁹⁶ + NMN-D: *w ; dpr1,mCD8::GFP,aseFLP^{2b} /5xUAS-GFP::NMN-Deamidase ; axed²⁰⁹⁴ , dsarm⁸⁹⁶ , FRT2A/tub Gal80,FRT2A*
B axed²⁰⁹⁴ , dsarm⁸⁹⁶ + NMN-D^{dead}: *w ; dpr1,mCD8::GFP,aseFLP^{2b} /5xUAS-GFP::NMN-Deamidase^{dead} ; axed²⁰⁹⁴ , dsarm⁸⁹⁶ , FRT2A/tub Gal80,FRT2A*
B dnmnat^{OE} + GFP: *w ; dpr1,mCD8::GFP,aseFLP^{2b} /5xUAS-dnmnat ; FRT2A/tub Gal80,FRT2A*
B dnmnat^{OE} + NMN-D: *w ; dpr1,mCD8::GFP,aseFLP^{2b} , 5xUAS-GFP::NMN-Deamidase /5xUAS-dnmnat ; FRT2A/tub Gal80,FRT2A*
B dnmnat^{OE} + NMN-D^{dead}: *w ; dpr1,mCD8::GFP,aseFLP^{2b} , 5xUAS-GFP::NMN-Deamidase^{dead} /5xUAS-dnmnat ; FRT2A/tub Gal80,FRT2A*
B X + GFP: *w,tub Gal80,FRT19A/w,FRT19A ; dpr1,mCD8::GFP,aseFLP^{2d} /UAS-GFP ;*
B X + NMN-D: *w,tub Gal80,FRT19A/w,FRT19A ; dpr1,mCD8::GFP,aseFLP^{2d} /5xUAS-GFP::NMN-Deamidase ;*
B X + NMN-D^{dead}: *w,tub Gal80,FRT19A/w,FRT19A ; dpr1,mCD8::GFP,aseFLP^{2d} /5xUAS-GFP::NMN-Deamidase^{dead} ;*
B hiw^{ΔN} + GFP: *w,tub Gal80,FRT19A/w,hiw^{ΔN} , FRT19A ; dpr1,mCD8::GFP,aseFLP^{2d} /UAS-GFP ;*
B hiw^{ΔN} + NMN-D: *w,tub Gal80,FRT19A/w,hiw^{ΔN} , FRT19A ; dpr1,mCD8::GFP,aseFLP^{2d} /5xUAS-GFP::NMN-Deamidase ;*
B hiw^{ΔN} + NMN-D^{dead}: *w,tub Gal80,FRT19A/w,hiw^{ΔN} , FRT19A ; dpr1,mCD8::GFP,aseFLP^{2d} /5xUAS-GFP::NMN-Deamidase^{dead} ;*
C NMN-D: *w ; dpr1,mCD8::GFP,aseFLP^{2e} /5xUAS-GFP::NMN-Deamidase ; FRT82B/FRT82B,tub Gal80*
C NMN-D^{dead}: *w ; dpr1,mCD8::GFP,aseFLP^{2e} /5xUAS-GFP::NMN-Deamidase^{dead} ; FRT82B/tub Gal80,FRT82B*
C dnmnat¹: *w ; dpr1,mCD8::GFP,aseFLP^{2e} /+ ; FRT82B,dnmnat¹ /FRT82B,tub Gal80*
C dnmnat¹ + NMN-D: *w ; dpr1,mCD8::GFP,aseFLP^{2e} , 5xUAS-GFP::NMN-Deamidase /+ ; FRT82B,dnmnat¹ /FRT82B,tub Gal80*
C dnmnat¹ + NMN-D^{dead}: *w ; dpr1,mCD8::GFP,aseFLP^{2e} /5xUAS-GFP::NMN-Deamidase^{dead} ; FRT82B,dnmnat¹ /FRT82B,tub Gal80*

Figure 6 - figure supplement 1

B dsarm^{sgRNAs} + UAS-Cas9: *w ; dpr1,mCD8::GFP,aseFLP^{2b} , UAS-Cas9 /10xUAS-4x(tRNA::sgRNA)^{dsarm} ; FRT2A/tub Gal80,FRT2A*
B hiw^{sgRNAs} + UAS-Cas9: *w ; dpr1,mCD8::GFP,aseFLP^{2b} , UAS-Cas9 /10xUAS-4x(tRNA::sgRNA)^{hiw} ; FRT2A/tub Gal80,FRT2A*
B axed^{sgRNAs} + UAS-Cas9: *w ; dpr1,mCD8::GFP,aseFLP^{2b} , UAS-Cas9 /10xUAS-4x(tRNA::sgRNA)^{axed} ; FRT2A/tub Gal80,FRT2A*
B dsarm^{sgRNAs} + actin-Cas9: *w,actin-Cas9/Y ; dpr1,mCD8::GFP,aseFLP^{2b} /10xUAS-4x(tRNA::sgRNA)^{dsarm} ; FRT2A/tub Gal80,FRT2A*
B hiw^{sgRNAs} + actin-Cas9: *w,actin-Cas9/Y ; dpr1,mCD8::GFP,aseFLP^{2b} /10xUAS-4x(tRNA::sgRNA)^{hiw} ; FRT2A/tub Gal80,FRT2A*
B axed^{sgRNAs} + actin-Cas9: *w,actin-Cas9/Y ; dpr1,mCD8::GFP,aseFLP^{2b} /10xUAS-4x(tRNA::sgRNA)^{axed} ; FRT2A/tub Gal80,FRT2A*
C,E control + UAS-Cas9: *w, 20xUAS IVS CsChrimson::mVenus /Y ; UAS-Cas9 /+ ; GMR60E02 Gal4 /+*
C dsarm^{sgRNAs} + UAS-Cas9: *w, 20xUAS IVS CsChrimson::mVenus /Y ; UAS-Cas9 /10xUAS-4x(tRNA::sgRNA)^{dsarm} ; GMR60E02 Gal4 /+*
C hiw^{sgRNAs} + UAS-Cas9: *w, 20xUAS IVS CsChrimson::mVenus /Y ; UAS-Cas9 /10xUAS-4x(tRNA::sgRNA)^{hiw} ; GMR60E02 Gal4 /+*
C axed^{sgRNAs} + UAS-Cas9: *w, 20xUAS IVS CsChrimson::mVenus /Y ; UAS-Cas9 /10xUAS-4x(tRNA::sgRNA)^{axed} ; GMR60E02 Gal4 /+*
C control + actin-Cas9: *y,actin-Cas9,w /Y ; 20xUAS IVS CsChrimson::mVenus /+ ; GMR60E02 Gal4 /+*
C dsarm^{sgRNAs} + actin-Cas9: *y,actin-Cas9,w /Y ; 20xUAS IVS CsChrimson::mVenus /10xUAS-4x(tRNA::sgRNA)^{dsarm} ; GMR60E02 Gal4 /+*
C hiw^{sgRNAs} + actin-Cas9: *y,actin-Cas9,w /Y ; 20xUAS IVS CsChrimson::mVenus /10xUAS-4x(tRNA::sgRNA)^{hiw} ; GMR60E02 Gal4 /+*
C axed^{sgRNAs} + actin-Cas9: *y,actin-Cas9,w /Y ; 20xUAS IVS CsChrimson::mVenus /10xUAS-4x(tRNA::sgRNA)^{axed} ; GMR60E02 Gal4 /+*
D-E Wild type: *w ; dpr1,mCD8::GFP,aseFLP^{2e} /+ ; FRT82B/FRT82B,tub Gal80*
D dnmnat¹: *w ; dpr1,mCD8::GFP,aseFLP^{2e} /+ ; FRT82B,dnmnat¹ /FRT82B,tub Gal80*
D-E dnmnat^{sgRNAs}: *w ; dpr1,mCD8::GFP,aseFLP^{2e} , UAS-Cas9 /10xUAS-4x(tRNA::sgRNA)^{dnmnat} ; FRT82B/FRT82B,tub Gal80*
D dnmnat^{sgRNAs} + UAS-Cas9: *w, 20xUAS IVS CsChrimson::mVenus /Y ; UAS-Cas9 /10xUAS-4x(tRNA::sgRNA)^{dnmnat} ; GMR60E02 Gal4 /+*
E dnmnat^{sgRNAs} + NMN-D: *w ; dpr1,mCD8::GFP,aseFLP^{2e} , UAS-Cas9 /5xUAS-GFP::NMN-Deamidase, 10xUAS-4x(tRNA::sgRNA)^{dnmnat} ; FRT82B/FRT82B,tub Gal80*

CHAPTER 4

Additional experiments to chapter 3



A female and a male fly, left and right respectively.

3.1 Summary of the results

In this section, I will discuss results obtained with NMN-D in *Drosophila* that are not included in the *eLife* manuscript.

3.2 Methods

RNAi: flies of the correct genotype (e.g., with RNAi solely in clonal wing sensory neurons) were obtained from synchronously set-up crosses. The previous chapter describes the methods required for injury and the quantification of severed axons.

Life span assay: flies of the correct genotype were obtained from synchronously set up crosses and collected within 24 h after eclosion using CO₂ anaesthesia. Males and non-virgin females were placed separately in narrow vials (10 individuals/vial, 10 vials/genotype, and sex) containing Bloomington Formulation fly food. Flies were kept at 20 °C. Dead and alive flies were counted every 2 days. Flies were transferred to fresh vials twice a week without anaesthesia.

3.3 Results

4) Low NMN-mediated protection requires Nads activity

In the introduction and chapter 2 I explained and demonstrated how vital the ratio between NMN and NAD⁺ is: in a healthy axon NMN is low and NAD⁺ high, while after injury, NMN levels raise while NAD⁺ synthesis is halted (due to the absence of dNmnat), and subsequently, NAD⁺ is rapidly degraded (by dSarm).

In *Drosophila*, dNmnat is the bottleneck of NAD⁺ biosynthetic activity (Figure 4) (Gilley & Coleman, 2010). dNmnat consumes NMN to synthesise NAD⁺. Notably, it also consumes NaMN to synthesise NaAD, which NAD⁺ synthase (Nads) then consumes to synthesise NAD⁺ (Figure 4). The expression of NMN-D shifts the metabolic flux from NMN to NaMN (e.g., towards the Preiss-Handler pathway). Therefore, the main NAD⁺ biosynthetic activity relies on NaAD consumption by Nads. This scenario facilitates testing whether both NMN and NAD⁺ compete to regulate dSarm activation *in vivo*.

In mammals, NMN promotes, while NAD⁺ prevents the activation of SARM1 *in vitro* (Figley et al., 2021; Zhao et al., 2019). I have demonstrated *in vivo* that lowering NMN with unchanged NAD⁺ does not activate dSarm after injury, severed axons remain preserved at 7 dpa, in NMN-D expressing flies, NAD⁺ synthesis relies on Nads; therefore, by targeting Nads by RNAi, I hypothesise that NAD⁺ levels are also lowered (Figure 7A). NMN-D flies with *Nads^{RNAi}* should have lower NMN and NAD⁺. Thus, dSarm could get activated, resulting in NAD⁺ depletion and at least the partial degeneration of axons after injury (e.g., a partial reversion of the protective phenotype).

To test whether the knockdown of Nads (e.g., *Nads^{RNAi}*) modifies injury-induced axon degeneration, I performed wing injuries in wild-type flies or flies expressing NMN-D ± *Nads^{RNAi}*. The reduction of Nads in NMN-D-expressing neurons partially reverted the preservation by NMN-D approximately by 40% at 7 dpa (Figure 7B). This result suggests that NMN promotes

whereas NAD⁺ inhibits dSarm activation *in vivo* in *Drosophila*. Thus, dSarm/SARM1 acts as an evolutionarily conserved NMN/NAD⁺ sensor.

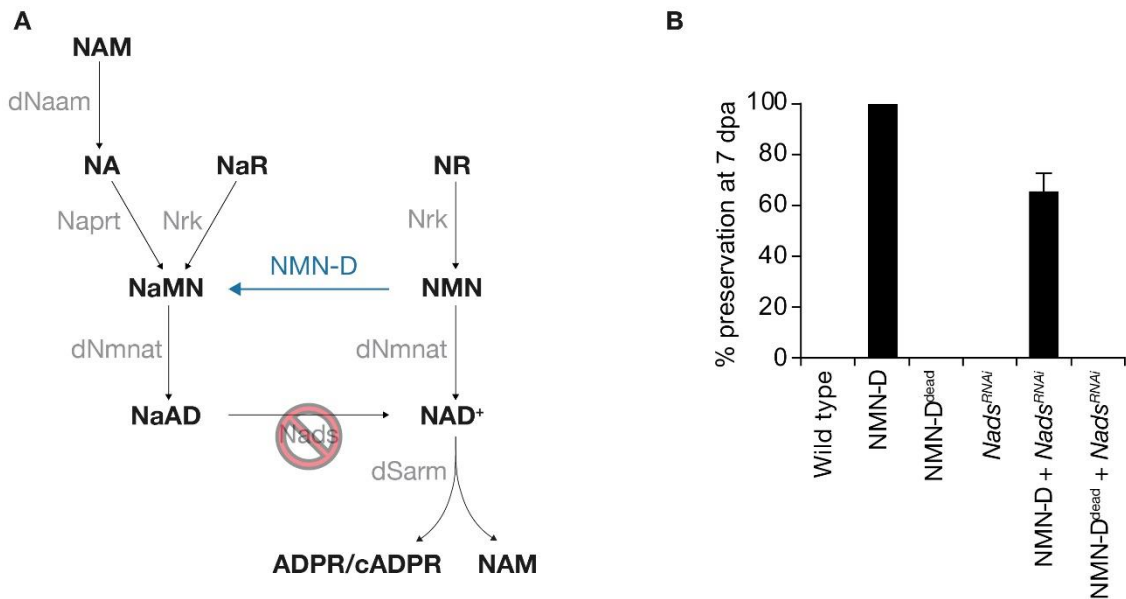


Figure 7. NMN-D-mediated protection of severed axons requires Nads activity. **A** NAD⁺ metabolic pathway in *Drosophila* with indicated expression of NMN-D and RNAi-mediated knockdown of Nads (blue and red, respectively). **B** Axon death quantification of the wing injury assay. % preservation of injured axons at 7 dpa, average \pm standard error of the mean ($n = 15$ wings).

5) Low NMN does not influence the life span of *Drosophila*

Ageing and age-related diseases are closely related to decreased NAD⁺ levels (Hou et al., 2019a, 2019b; McReynolds et al., 2020). In *in vivo* studies, the administration of NAD⁺ precursors such as NAM, NMN or NR, or the manipulation of enzymes of the NAD⁺ metabolic pathway such as *Drosophila* nicotinamidase (dNaam) improve health and extend the life span (Balan et al., 2008; E. F. Fang et al., 2017; Imai & Guarente, 2014; Mitchell et al., 2018; Shade, 2020b; Yoshino et al., 2018).

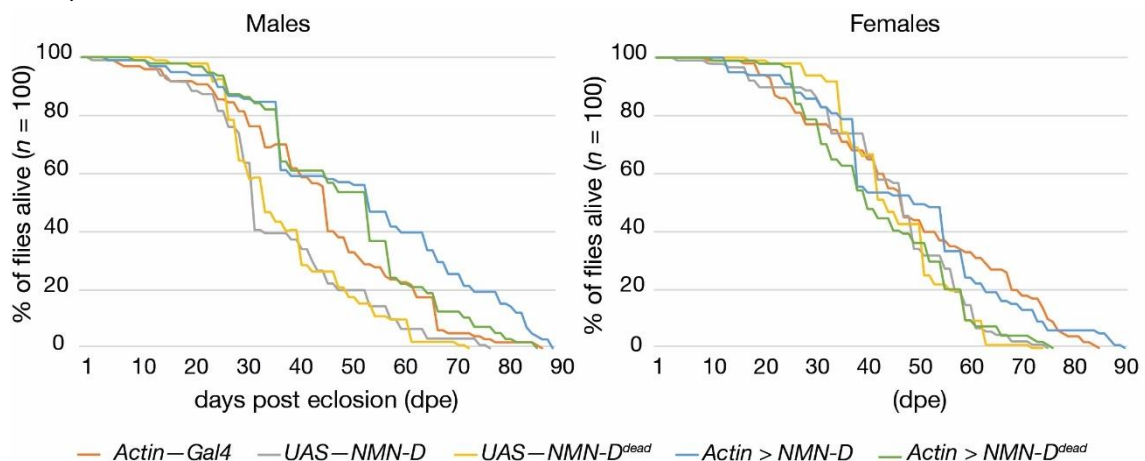


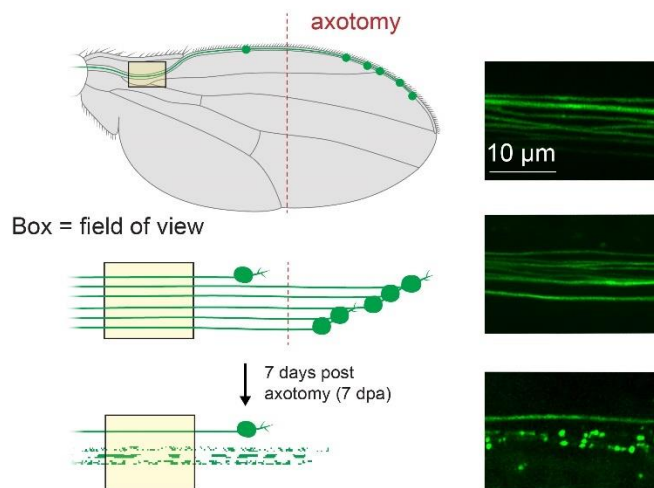
Figure 8. NMN-D expression does not influence *Drosophila* life span. Survival curves for male and female adult flies expressing NMN-D (blue) or NMN-D^{dead} (green) ubiquitously via the Actin-Gal4 driver. The driver alone, *Actin-Gal4* (orange), or the transgenes alone, UAS-NMN-D (grey) and UAS-NMN-D^{dead} (yellow) were used as controls.

Because the expression of NMN-D in *Drosophila* modifies the metabolic flux resulting in a change of several metabolites of the NAD⁺ metabolic pathway (e.g., lower NMN, higher NaMN, *etc.*), I sought to determine whether NMN-D alters the life span of flies. NMN-D or NMN-D^{dead} were ubiquitously expressed (*Actin > NMN-D* and *Actin > NMN-D^{dead}* respectively), and the life span compared to controls (e.g., *Actin-Gal4*, *UAS-NMN-D* or *UAS-NMN-D^{dead}*). Neither overall differences were observed, nor sex-specific impacts (Figure 8).

Although *Actin > NMN-D* males showed a slight trend towards a longer life span, they die similarly to the rest of the genotypes. This trend is not observed in females (Figure 8). This observation suggests that although NMN-D expression alters the NAD⁺ metabolic flux, the life span of the flies is not affected.

CHAPTER 5

Divergent signaling requirements of dSarm in injury-induced degeneration and developmental glial phagocytosis



Scheme of the wing injury assay on the left, with 63x pictures of GFP expressing neurons on the right, before and after injury.

4.1 Summary of the results

In this study, *Herrmann et al.* describe how dSarm contains divergent signalling requirements in injury-induced axon degeneration and Toll-like receptor (TLR)-mediated developmental glial phagocytosis (Herrmann et al., 2022). The authors first designed several knock-in constructs of dSarm lacking different domains to compare their functional requirements: the TIR domain NAD⁺ hydrolase activity of dSarm is required to activate injury-induced axon degeneration in ORNs. Surprisingly, the TIR domain alone (dSarm^{TIR}) is sufficient to trigger axon degeneration in an injury-independent manner. Nevertheless, that is not the case in sensory neurons of the wing, where all the domains of dSarm are required for the degeneration of injured axons. The different behaviour of dSarm^{TIR} in ORNs and wing sensory neurons remains an open question that is addressed in the discussion of the article (Herrmann et al., 2022).

In contrast, dSarm signalling in glia requires NADase activity (e.g., the TIR domain) but not its oligomerizing domain (e.g., the SAM domain) as dSarm still functions without oligomerization. It is in stark contrast to injury-induced axon degeneration. Finally, the MAP3K Apoptosis signal-regulated kinase 1 (Ask1) functions downstream of dSarm in developmental TLR signal transduction, but not in injury-induced axon degeneration (Herrmann et al., 2022).

4.2 Personal contribution


In this study, I performed and analysed the experiment on the wing sensory neurons. Kelsey Hermann generated and shared the constructs, and I performed the wing injuries. I contributed to the experimental design together with Lukas Neukomm, Kelsey Hermann and Heather Brohier. I also wrote the section of the manuscript related to that experiment together with Lukas Neukomm (Herrmann et al., 2022).

RESEARCH ARTICLE

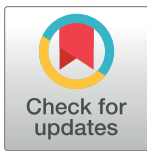
Divergent signaling requirements of dSARM in injury-induced degeneration and developmental glial phagocytosis

Kelsey A. Herrmann¹ , Yizhou Liu¹ , Arnau Llobet-Rosell² , Colleen N. McLaughlin¹, Lukas J. Neukomm² , Jaeda C. Coutinho-Budd³ , Heather T. Broihier¹ *

1 Department of Neurosciences, Case Western Reserve University School of Medicine, Cleveland, Ohio, United States of America, **2** Department of Fundamental Neurosciences, University of Lausanne, Lausanne, Switzerland, **3** Department of Neuroscience, University of Virginia, Charlottesville, Virginia, United States of America

 These authors contributed equally to this work.

* heather.broihier@case.edu



OPEN ACCESS

Citation: Herrmann KA, Liu Y, Llobet-Rosell A, McLaughlin CN, Neukomm LJ, Coutinho-Budd JC, et al. (2022) Divergent signaling requirements of dSARM in injury-induced degeneration and developmental glial phagocytosis. *PLoS Genet* 18(6): e1010257. <https://doi.org/10.1371/journal.pgen.1010257>

Editor: Fengwei Yu, National University of Singapore, SINGAPORE

Received: January 3, 2022

Accepted: May 13, 2022

Published: June 23, 2022

Copyright: © 2022 Herrmann et al. This is an open access article distributed under the terms of the [Creative Commons Attribution License](https://creativecommons.org/licenses/by/4.0/), which permits unrestricted use, distribution, and reproduction in any medium, provided the original author and source are credited.

Data Availability Statement: All relevant data are within the paper and its [Supporting information files](#).

Funding: This work was supported by a Swiss National Science Foundation SNSF Assistant Professor award (176855), the International Foundation for Research in Paraplegia (P180), and SNSF Spark (190919) to L.J.N., and by R21NS110397, R01NS120689, and R01NS095895 to H.T.B. The funders had no role in study design,

Abstract

Elucidating signal transduction mechanisms of innate immune pathways is essential to defining how they elicit distinct cellular responses. Toll-like receptors (TLR) signal through their cytoplasmic TIR domains which bind other TIR domain-containing adaptors. dSARM/SARM1 is one such TIR domain adaptor best known for its role as the central axon degeneration trigger after injury. In degeneration, SARM1's domains have been assigned unique functions: the ARM domain is auto-inhibitory, SAM-SAM domain interactions mediate multimerization, and the TIR domain has intrinsic NAD⁺ hydrolase activity that precipitates axonal demise. Whether and how these distinct functions contribute to TLR signaling is unknown. Here we show divergent signaling requirements for dSARM in injury-induced axon degeneration and TLR-mediated developmental glial phagocytosis through analysis of new knock-in domain and point mutations. We demonstrate intragenic complementation between reciprocal pairs of domain mutants during development, providing evidence for separability of dSARM functional domains in TLR signaling. Surprisingly, dSARM's NAD⁺ hydrolase activity is strictly required for both degenerative and developmental signaling, demonstrating that TLR signal transduction requires dSARM's enzymatic activity. In contrast, while SAM domain-mediated dSARM multimerization is important for axon degeneration, it is dispensable for TLR signaling. Finally, dSARM functions in a linear genetic pathway with the MAP3K Ask1 during development but not in degenerating axons. Thus, we propose that dSARM exists in distinct signaling states in developmental and pathological contexts.

Author summary

Following injury, severed axons are actively destroyed by a protein called SARM1, or dSARM in *Drosophila*. It was recently shown that dSARM/SARM1 accomplishes this feat

data collection and analysis, decision to publish, or preparation of the manuscript.

Competing interests: The authors have declared that no competing interests exist.

by degrading the key coenzyme NAD^+ , leading to energetic collapse in the axon. This was surprising since dSARM/SARM1 is a TIR-domain containing protein, and as such, was thought to act exclusively as an adaptor in Toll receptor-mediated pathways. We recently uncovered a developmental role for dSARM in glia where it promotes engulfment of dying neurons. To understand the relationship between this function for dSARM and its better-known function in axon degeneration, we set out to (1) compare the enzymatic requirement of dSARM in both settings, and (2) determine if signaling mechanisms are the same. To address these questions, we used CRISPR to generate new dSARM knock-in alleles. We find that the NAD^+ hydrolase activity of dSARM is absolutely required for both its axon degeneration function and its signaling function. Pointing to differences in dSARM-mediated pathways in the two contexts, we provide evidence that Ask1 kinase is required for dSARM signaling in glia but not for axon degeneration. Thus, we propose that the NAD^+ hydrolase activity of dSARM leads to Ask1 activation and subsequent signal transduction.

Introduction

Brain homeostasis is maintained by cell-intrinsic and cell-extrinsic surveillance mechanisms. During normal development, a commonly cited estimate is that 50% of neurons die, and injury can precipitate the death of even more. The prevalence of neuron and neurite death during development highlights the importance of defining underlying molecular mechanisms as well as those active in phagocytic glia that engulf and dispose of neuronal corpses.

Wallerian degeneration is a specific type of axon degeneration in which the axon distal to an axotomy degenerates [1]. A spontaneous mouse mutant, Wallerian Degeneration Slow (Wld^{S}), exhibits markedly delayed axon degeneration [2,3]. This phenotype argues that axon degeneration is an active process and not passive wasting of the injured nerve. The Wld^{S} mutation is a tandem triplication of the NAD^+ synthetic enzyme Nicotinamide mononucleotide adenyl transferase 1 (*Nmnat1*) and Ubiquitination factor e4b (*Ube4b*) [4]. While NAD^+ levels normally plummet following injury [5], NAD^+ depletion is blocked by Wld^{S} [6–9], hinting at a regulatory role for NAD^+ in the decision to degenerate across evolution [10].

The discovery that Wallerian degeneration is an active destructive process prompted forward genetic screens for loss-of-function (LOF) mutants in which axons are protected following injury. *Drosophila* SARM1 was identified in such a screen as its loss confers robust protection of distal axons following axotomy [11]. Mice lacking SARM1 exhibit preservation of severed axons for weeks following injury [11,12], demonstrating conservation of function. Underscoring the importance of NAD^+ , SARM1 drives axonal death via intrinsic NAD^+ hydrolase activity that is proposed to culminate in metabolic catastrophe [13,14]. *SARM1* encodes a protein with an N-terminal ARM domain, two tandem SAM domains, and a C-terminal TIR domain. Biochemical and genetic studies indicate that the TIR domain contains NAD^+ hydrolase activity, the SAM domains are responsible for multimerization, and the ARM domain mediates auto-inhibition [12–16]. Recent structural studies provide a high-resolution view of SARM1 structure and demonstrate that it assembles into an octamer mediated by SAM domain oligomerization [17–19]. In its inactive conformation, the TIR domain is bound by the inhibitory ARM domain, while SARM1 activation leads to release of this auto-inhibition [18–22]. The TIR domains cleave NAD^+ once released by the ARM domain in response to an increase in the NMN/ NAD^+ ratio [23].

SARM1 was first identified as an innate immune adaptor protein [24,25] and regulates neurodevelopment [16,26–30]. We recently demonstrated that dSARM is a component of a glial Toll receptor pathway required for clearance of neuronal corpses [29]. Loss of Toll-6 pathway components results in accumulation of apoptotic debris in the developing brain and early-onset neurodegeneration. The identification of this developmental function for dSARM raises important questions. To what extent are dSARM-mediated signaling mechanisms conserved between axon degeneration and glial phagocytic pathways? Specifically, is SAM domain-mediated multimerization and/or the NAD⁺ hydrolase activity of dSARM necessary for TLR-dependent signaling? And are dSARM's downstream signaling mechanisms conserved in development and degeneration?

To date, functions of individual SARM1 domains have been assigned largely via *in vitro* assays and *in vivo* overexpression paradigms [12–15,17–22]. Given caveats associated with overexpression experiments, we interrogated SARM1 signaling requirements by mutating the endogenous locus. We used CRISPR/Cas9-mediated genome engineering to generate a *dSARM* knockout allele by replacing exons containing the ARM, SAM, and TIR domains with an attP recombination target. We then recombined in a series of domain mutants as well as a catalytically inactive point mutant (E1170A) and assessed the contributions of each domain to injury-induced degeneration and developmental phagocytosis. We find that the E1170A allele exhibits long-lived protection of axons following injury, demonstrating that dSARM's NAD⁺ hydrolase activity accounts for its pro-degenerative function *in vivo*. Unexpectedly, the TIR-only allele can drive spontaneous axon degeneration over the course of days, indicating that SAM-mediated multimerization is not essential for dSARM activity in the absence of ARM domain-mediated inhibition. We next analyzed these new *dSARM* alleles in glial TLR signaling and find that dSARM's NAD⁺ hydrolase activity is essential for this role. In contrast, the SAM domain is dispensable for signaling in glia. Finally, we explored signaling downstream of dSARM in glia and present evidence that dSARM functions through the MAP3K Ask1 in glia but not in degenerating axons. These findings argue that dSARM has distinct signaling modes in degenerative and non-degenerative signaling pathways.

Results

Genome engineering of the *dSARM* locus

We sought to compare functional requirements of dSARM domains in developmental and degenerative contexts *in vivo* and so undertook a CRISPR/Cas9-mediated genome engineering approach. Using CRISPR/Cas9, we precisely deleted the ARM, SAM, and TIR domain-encoding exons of *dSARM* and replaced them with an attP site to create a founder knock-out allele (*dSARM*^{KO}, Fig 1A–1D) [31,32]. We then utilized phiC31-mediated DNA integration at the attP site to create a series of *dSARM* alleles (Fig 1E–1G) [33]. These alleles retain endogenous intron-exon structure and differ only in the presence of a 50 nucleotide attR site in the intron preceding exon 17 and a 34 nucleotide loxP site in the intron succeeding exon 21/22 (exon numbering from FlyBase; Fig 1G). We successfully generated the following four domain mutants: *dSARM*^{ARM-TIR}, *dSARM*^{ARM-SAM}, *dSARM*^{TIR}, and *dSARM*^{SAM}, which are each named for the domain(s) present in the allele (Fig 1H). To test the function of dSARM's NAD⁺ hydrolase activity in signaling, we mutated a key glutamic acid in the active site to alanine, which is equivalent to dSARM E893A in isoform E and human SARM1 E642A (*dSARM*^{E1170A}, [14]; [34]). All of these new *dSARM* alleles are homozygous lethal. *dSARM*^{KO}, *dSARM*^{ARM-TIR}, *dSARM*^{ARM-SAM}, *dSARM*^{SAM}, and *dSARM*^{E1170A} animals die as wandering third-instar larvae (L3). The lethality of *dSARM*^{E1170A} animals indicates that the NAD⁺ hydrolase activity serves an essential developmental function. Interestingly, the lethal phase of *dSARM*^{TIR} homozygotes is

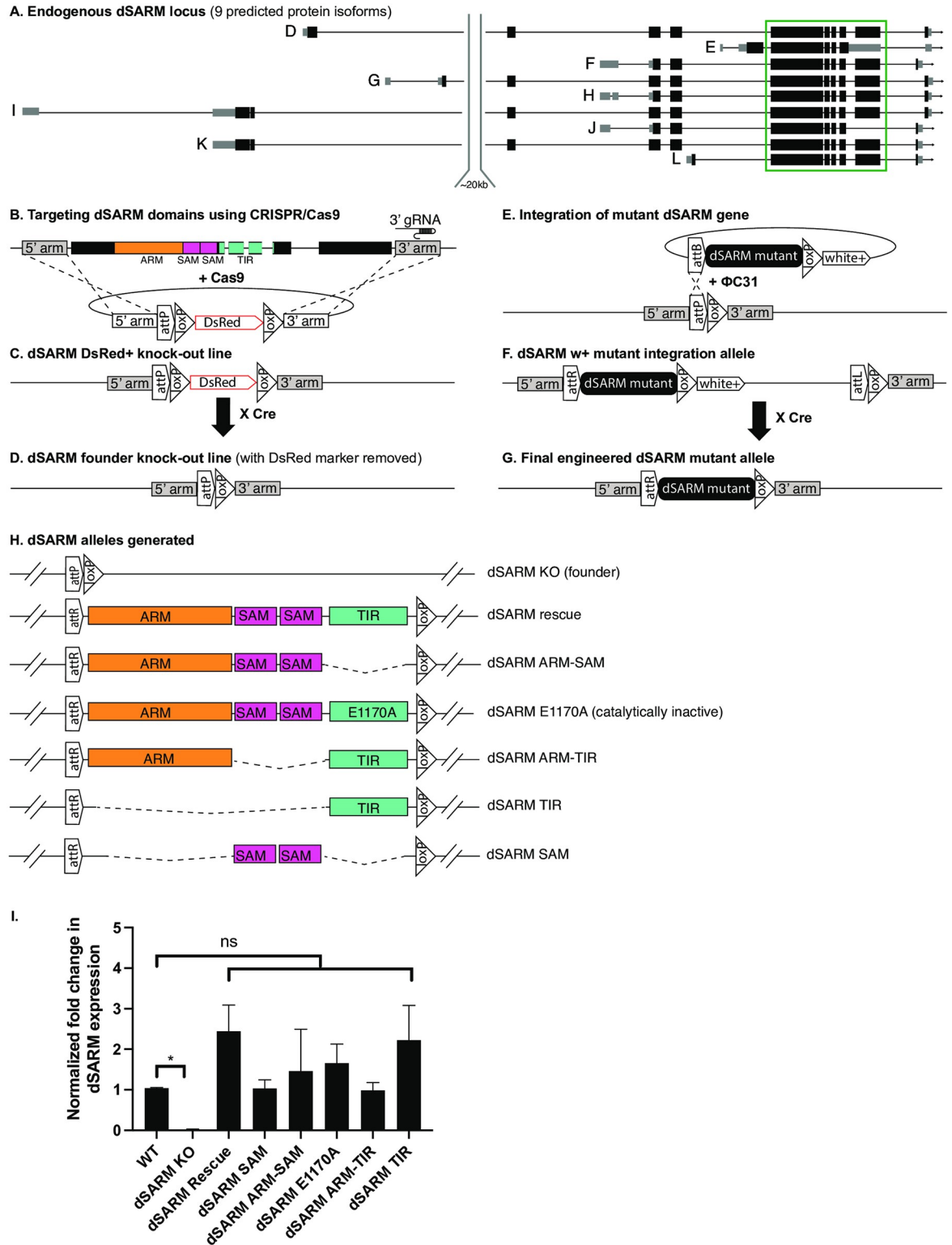


Fig 1. Genome engineering of the dSARM locus. (A) dSARM has 9 predicted isoforms. We designed a CRISPR/Cas9 strategy to knock out the ARM, SAM, and TIR domain encoding exons (boxed in green) in all isoforms. (B) A CRISPR/Cas9-induced homology-directed repair gene-targeting approach is used to delete the domain-encoding exons of dSARM. We identified a gRNA target sequence in the 3' intron immediately following the exons in the green box in A. The homology-directed repair donor DNA plasmid contains 5' and 3' homologous arms flanking dSARM domains, a loxP-flanked DsRed selection marker, and an attP site of phiC31. The ARM (orange),

SAM (magenta), and TIR (teal) domains are overlaid onto the dSARM locus. (C) In the “dSARM DsRed+ knock-out line”, the domain-encoding exons are replaced by the attP-loxP-DsRed-loxP cassette. (D) In the final *dSARM* founder knock-out line, the DsRed marker is removed by Cre recombinase, leaving attP and loxP sequences. (E) Genomic DNA is engineered to incorporate desired modifications (“*dSARM* mutant”) in the pGE-attB-w+ integration vector. The *dSARM* mutant is integrated into the founder line through phi-C31-mediated DNA integration via attP/attB recombination. (F) The resulting “dSARM w+ mutant integration allele” has the engineered mutant *dSARM* gene at its original genomic locus together with white+ and vector sequences. (G) w+ and extraneous vector sequences are removed by Cre recombinase to generate the “final engineered *dSARM* mutant allele” containing the engineered mutant flanked by attR and loxP sites in the adjacent introns. (H) A schematic showing the *dSARM* alleles that were generated. (I) qRT-PCR analysis of relative *dSARM* mRNA levels average \pm SEM: wild type (Oregon R) (n = 28): 1.04 \pm 0.01; *dSARM*^{KO} (n = 4): 0.02 \pm 0.01; *dSARM*^{Rescue} (n = 4): 2.45 \pm 0.64; *dSARM*^{E1170A} (n = 4): 1.66 \pm 0.47; *dSARM*^{ARM-SAM} (n = 4): 1.46 \pm 1.03; *dSARM*^{TIR} (n = 4): 2.23 \pm 0.85; *dSARM*^{ARM-TIR} (n = 4): 0.99 \pm 0.18; *dSARM*^{SAM} (n = 4): 1.03 \pm 0.21 Error bars are SEM.

<https://doi.org/10.1371/journal.pgen.1010257.g001>

at the first-instar larval stage (L1), suggesting that this allele has gain-of-function (GOF) activity. We also generated a *SARM*^{Rescue} line by recombining back in wild-type sequences (Fig 1H). *dSARM*^{Rescue} homozygotes are viable and fertile, serving as a control for the overall strategy. Alleles were validated by a combination of PCR and sequencing. Notably, after three rounds of injections into roughly 900 embryos, we were unable to recover *dSARM*^{SAM-TIR} transformants. This allele likely caused dominant lethality, as suggested by published work indicating that the ARM domain prevents unregulated activation of multimerized TIR domains [12,16]. To assay *dSARM* transcript abundance in mutant lines, we performed quantitative RT-PCR on first- or second-instar larvae, before the lethal phase of these animals. While *dSARM* transcripts are undetectable in the *dSARM*^{KO} founder line, we find normal levels of *dSARM* transcripts in all knock-in alleles (Fig 1I), indicating that stable transcripts are produced. Moreover, as shown below, we demonstrate intragenic complementation between pairs of alleles containing reciprocal domains demonstrating that the domain mutants are expressed and functional.

Loss of dSARM’s NADase activity affords long-lived protection of injured ORN axons

We employed these *dSARM* alleles to test domain requirements of dSARM in axon degeneration. We undertook a MARCM-based approach to evaluate them in an olfactory receptor neuron (ORN) axotomy model, the same paradigm in which dSARM’s role in axon degeneration was first uncovered [11]. In this genetic method, GFP-labeled homozygous mutant clones are generated in a heterozygous background. Since OR22a cell bodies are housed in the third antennal segment, distal axons can be readily detached from neuronal soma by removing the antenna. By performing a unilateral antennal ablation, the uninjured side serves as an internal control whereby the number of axons on the uninjured side are compared to the number on the injured side to quantify axon degeneration.

We removed antennae in animals 7 days post-eclosion (DPE) and assessed axon protection 7 days post injury (DPI). To test if the knock-out/knock-in strategy itself interfered with wild-type dSARM function, we assayed whether homozygous *dSARM*^{Rescue} mutant clones display normal axon degeneration following injury (Fig 2A, 2B and 2I). We find complete axon degeneration at 7 DPI in *dSARM*^{Rescue} clones. In contrast, *dSARM*^{KO} clones display protection equivalent to a pre-existing *dSARM* allele (*dSARM*⁸⁹⁶; [11]; Fig 2C, 2D and 2I). Together, the behavior of the knockout and rescue alleles validates our strategy.

Structural and functional studies demonstrate that the TIR domain of SARM1 has intrinsic NADase activity and that this enzymatic activity is essential for axon degeneration [13–15,18,22,35,36]. Our new *dSARM* knock-in mutants enable critical *in vivo* tests of the function of dSARM’s catalytic activity and protein domains that to date have been largely assigned via

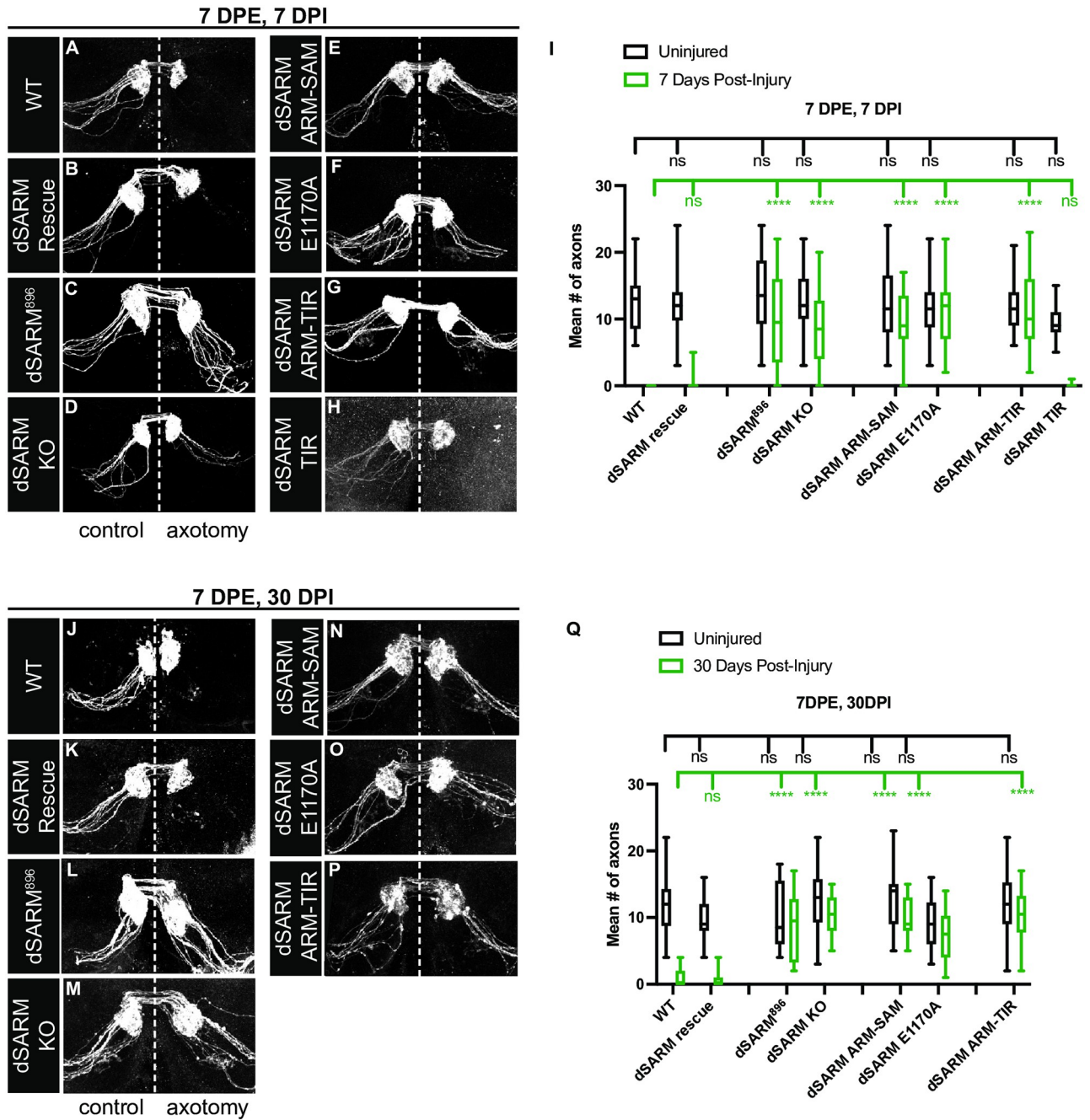


Fig 2. Loss of dSARM's NADase activity affords long-lived protection of injured ORN axons. (A-H) Representative z-projections of OR22a ORNs of the indicated genotypes labeled with anti-GFP. The control side is on the left and the axotomized side is on the right. These animals were injured 7-day post-eclosion (7 DPE) and analyzed at 7-days post-injury (7 DPI). (I) Quantification of mean number of axons on uninjured control (black) and 7 days post-injury (green). Mean number of axons on uninjured control, injured sides: wild type (FRT2A) (n = 25): 12.32, 0.00; dSARM⁸⁹⁶ (n = 24): 13.92, 9.75; dSARM^{Rescue} (n = 30): 12.33, 0.40; dSARM^{KO} (n = 32): 12.56, 8.34; dSARM^{ARM-SAM} (n = 34): 12.42, 9.00; dSARM^{E1170A} (n = 24): 11.71, 11.26; dSARM^{TIR} (n = 35): 9.46, 0.04; dSARM^{ARM-TIR} (n = 24): 11.76, 10.89. (J-P) Representative z-projections of OR22a ORNs of the indicated genotypes labeled with anti-GFP. The control side is on the left and the axotomized side is on the right. These animals were injured 7 DPE and analyzed at 30 DPI. (Q) Quantification of mean number of axons on uninjured control (black) and 7 days post-injury (green). Mean number of axons on uninjured control, injured sides: wild type (FRT2A) (n = 30): 11.77, 1.10; dSARM⁸⁹⁶ (n = 20): 9.95, 8.80; dSARM^{Rescue} (n = 26): 9.27, 0.77; dSARM^{KO} (n = 28): 12.61, 10.29; dSARM^{ARM-SAM} (n = 22): 12.81, 10.00; dSARM^{E1170A} (n = 27): 9.32, 7.32; dSARM^{ARM-TIR} (n = 22): 11.91, 10.86. Error bars represent min and max data points. n.s. is not significantly different. ****, p < 0.0001.

<https://doi.org/10.1371/journal.pgen.1010257.g002>

in vitro assays and *in vivo* overexpression paradigms. We interrogated requirements of the TIR domain in general as well as the NAD⁺ hydrolase activity in particular [14]. We find that both $dSARM^{ARM-SAM}$, in which the entire TIR domain is deleted, and $dSARM^{E1170A}$, in which a key glutamic acid residue in the active site is mutated, provide perfect protection of distal axons at 7 DPI indicating a strict requirement for dSARM's NADase activity in axon degeneration (Fig 2E, 2F and 2I). These findings differ somewhat from those in a recently published study [27] (see Discussion). We next tested whether SAM-mediated multimerization is required for degeneration by analyzing the phenotype of $dSARM^{ARM-TIR}$ mutant clones. The SAM domains are important for dSARM's pro-degeneration function *in vivo* since distal axons are fully protected in $dSARM^{ARM-TIR}$ mutant axons (Fig 2G and 2I). Finally, we analyzed whether the TIR domain alone is sufficient for axon degeneration or whether it requires regulation via ARM and SAM domains. Surprisingly, $dSARM^{TIR}$ mutant axons appear to exhibit timely degeneration of distal ORN axons (Fig 2H and 2I), indicating that the TIR domain alone is sufficient to drive injury-induced degeneration in this paradigm. However, the GFP fluorescence of both injured and un-injured ORN $dSARM^{TIR}$ mutant clones is weaker than in controls (Fig 2H), a phenotype explored in more detail below.

We assayed the ability of our new dSARM alleles to provide extended protection to severed ORN axons at 30 days following an injury induced at 7 DPE. We find that both $dSARM^{KO}$ and $dSARM^{E1170A}$ mutant axons are fully protected from degeneration 30 DPI (Fig 2M, 2O and 2Q), demonstrating that the NADase activity of dSARM is essential for long-lived protection. $dSARM^{ARM-TIR}$ mutant axons were also protected at 7 DPI (Fig 2G and 2I), but we wondered if this allele might retain low-level function reflected in axon loss at 30 DPI. However, $dSARM^{ARM-TIR}$ mutant clones are also fully protected at 30 DPI (Fig 2P and 2Q), arguing that SAM-mediated multimerization is essential for dSARM activation when both ARM auto-inhibitory and TIR domains are present. These findings provide strong *in vivo* support for recent structural studies demonstrating that the NAD⁺ hydrolase activity of SARM1 is positively regulated by SAM-SAM domain interactions and negatively regulated by ARM domain-mediated inhibition [17–23].

$dSARM^{ARM-SAM}$ has dominant-negative activity following injury

The octameric structure of SARM1 raises the possibility that mutants disrupting domain stoichiometry might display dominant-negative effects by inhibiting TIR domain multimerization [12]. Thus, we tested if reducing the number of TIR domains relative to ARM and SAM domains would slow axon degeneration. Normally, degeneration of distal ORN axons is efficient, with little debris remaining by 24 h post-injury (1 DPI; Fig 3A). Instead of counting axons, we quantified total axonal debris in these experiments to better capture axon fragmentation observed shortly after injury.

Using OR22aGal4 to drive UAS-mCD8::GFP in ORNs, we find that axons in whole animal $dSARM^{KO}$ heterozygotes degenerate as quickly as in controls, indicating that loss of one copy of dSARM does not delay axon degeneration (Fig 3B and 3E). We next tested whether $dSARM^{E1170A}$ or $dSARM^{ARM-SAM}$ heterozygous axons exhibit delayed degeneration since they alter either TIR domain number ($dSARM^{ARM-SAM}$) relative to ARM-SAM domains or TIR domain enzymatic activity ($dSARM^{E1170A}$). Interestingly, while $dSARM^{E1170A}$ heterozygotes degenerate as rapidly as controls, axon degeneration in $dSARM^{ARM-SAM}$ heterozygotes is incomplete at 1 DPI (Fig 3A, 3C, 3D and 3E). Axons do degenerate in all backgrounds by 2 DPI (Fig 3F–3J). We propose that $dSARM^{ARM-SAM}$ has modest dominant-negative activity because each octamer contains more auto-inhibitory ARM domains than TIR domains, which delays the formation of TIR-TIR dimers. The most parsimonious explanation of the finding that $dSARM^{E1170A}$

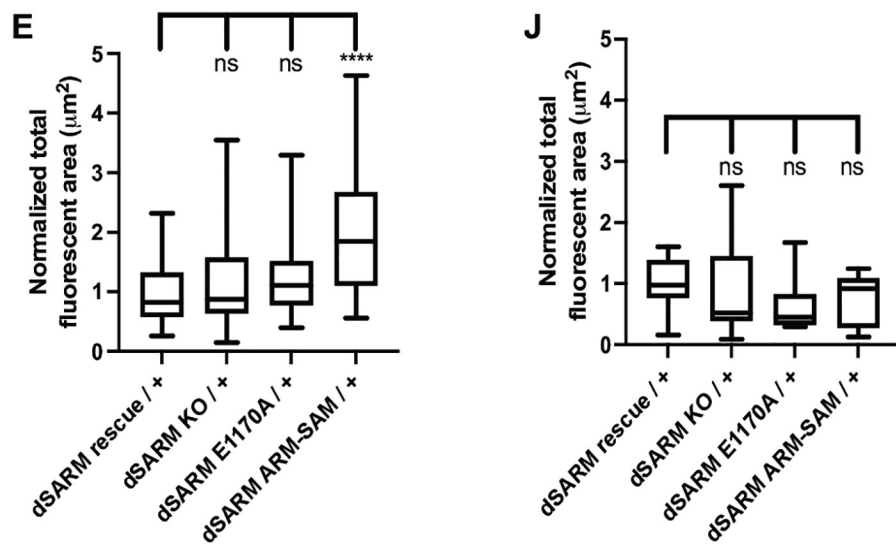
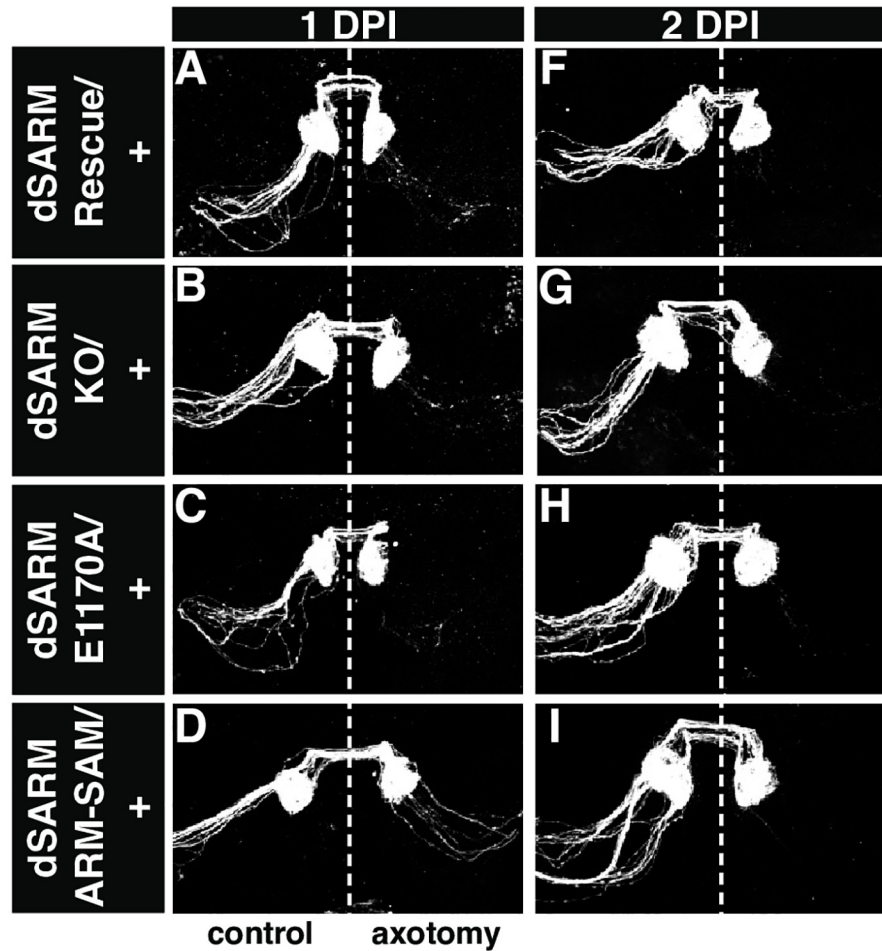


Fig 3. *dSARM*^{ARM-SAM} has dominant-negative activity following injury. (A-D, F-I) Representative z-projections of OR22a ORNs of the indicated genotypes labeled with anti-GFP. The control side is on the left and the axotomized side is on the right. These animals were injured 7 DPE and analyzed at 1 day (A-D) and 2 days (F-I) post-injury. (E) Quantification of total fluorescent area of debris on injured side at 1 DPI: dSARM^{Rescue} (n = 37): 1.00, dSARM^{KO} (n = 31): 1.16, dSARM^{E1170A} (n = 31): 1.27, and dSARM^{ARM-SAM} (n = 31): 2.07. (J) Quantification of total fluorescent

area of debris on injured side at 2 DPI: dSARM^{Rescue} (n = 14): 1.00, dSARM^{KO} (n = 12): 0.90, dSARM^{E1170A} (n = 13): 0.62, and dSARM^{ARM-SAM} (n = 11): 0.72. Error bars represent min and max data points. n.s. is not significantly different. ****, $p < 0.0001$.

<https://doi.org/10.1371/journal.pgen.1010257.g003>

is not a dominant-negative allele is that loss of NADase activity in one TIR monomer does not interfere with the NADase activity of other TIR monomers.

***dSARM*^{TIR} mutant ORN clones exhibit injury-independent axon degeneration**

While imaging 7 DPE animals, we noticed that both the uninjured and injured *dSARM*^{TIR} clones were less bright than the other genotypes and required more laser power to acquire an equivalent image, suggesting the possibility that the TIR domain alone caused axon degeneration. This prompted us to quantify the intensity of mutant clones for all alleles over time in the absence of injury.

First, we analyzed at 1 DPE (Fig 4A–4C) and found that *dSARM*^{TIR} mutant axons were already approximately 40% less bright than controls. Next, we looked at 7 DPE and found that *dSARM*^{TIR} mutant clones were approximately 55% less bright than controls (Fig 4D–4F). At 10 DPE the appearance of *dSARM*^{TIR} axons continued to wane, with an intensity 70% less than that of control genotypes (Fig 4G–4I). None of the other *dSARM* alleles affected fluorescence intensity at any of these time points. When we compared axon intensity among the three time points for *dSARM*^{TIR} mutant clones, we found a steady loss of axon integrity (Fig 4J), indicating that without ARM and SAM domains, the TIR domain drives axon loss over the course of 10 days. We speculate that without ARM domain-mediated inhibition, the TIR domains are free to associate with each other, cleave NAD⁺ and drive degeneration, but do so over a slower time scale than when they are tethered together by SAM domains. Together, these data argue that in ORN axons, SAM domain-mediated TIR multimerization drives high-level NADase activity to drive rapid axon degeneration on the order of hours following an acute injury. On the other hand, TIR monomers, or low frequency formation of TIR dimers, have low-level NADase activity capable of spontaneous axon degeneration over the course of 10 days.

We were intrigued by the unexpected finding that *dSARM*^{TIR} mutant ORN clones exhibit injury-induced degeneration (Fig 2H–2I). To look more carefully at the timing of injury-induced degeneration in these clones, we assessed axon degeneration 12 hours after injury. We performed the experiment at 1 DPE so that the mutant clones still appeared relatively healthy and quantified axons 12 h following axotomy in order to uncover small differences in timing. Surprisingly, we found no difference in degeneration rate in *dSARM*^{TIR} mutant clones relative to *dSARM*^{Rescue} clones (S1A–S1C Fig), arguing that free TIR domains can support timely injury-induced axon degeneration in neurons that are already undergoing slow and steady spontaneous degeneration.

All *dSARM* domains are required for degeneration of injured wing sensory axons

To extend the observations in the ORN injury assay in a second axotomy model, we tested our engineered mutations in a previously described MARCM-based approach in wing sensory neurons [37]. In this paradigm, flies are aged for 5–7 DPE before being subjected to injury: one wing is partially injured, while the other serves as an uninjured control [38]. At the day of injury, the number of cell bodies is counted in the cut-off wing, which indicates how many

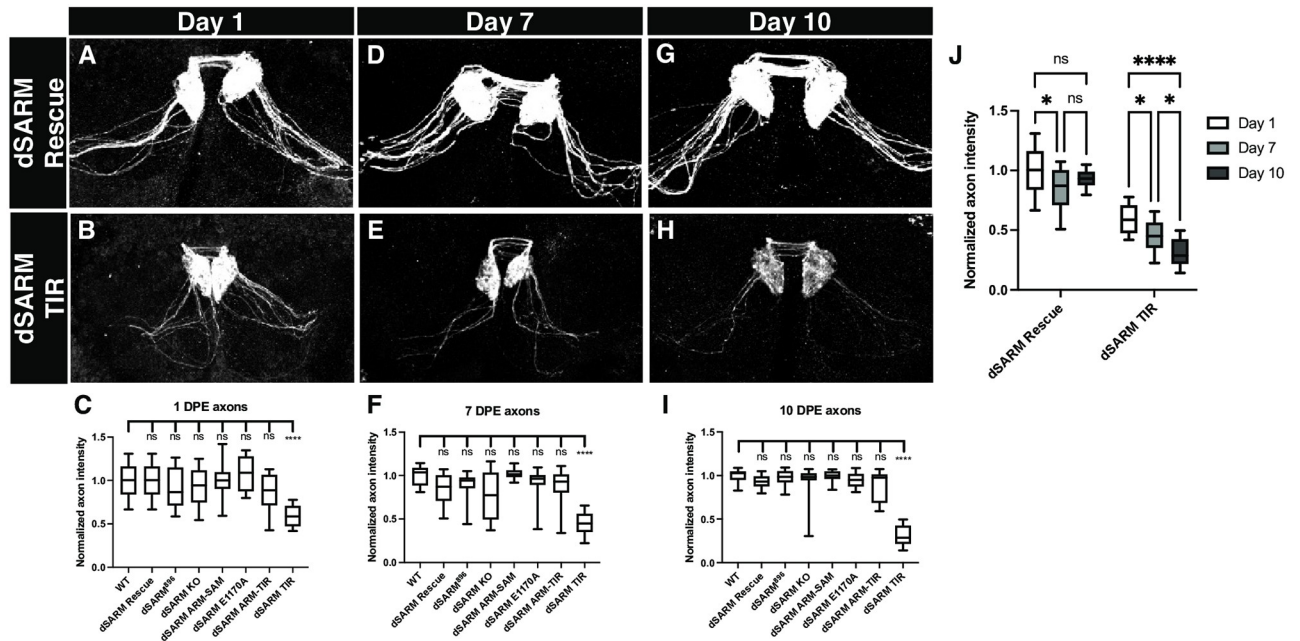


Fig 4. *dSARM^{TIR}* mutant clones exhibit injury-independent axon degeneration. (A,B) Representative z-projections of OR22a ORNs of the indicated genotypes labeled with anti-GFP at 1DPE. (C) Normalized mean axon intensity at 1 DPE: wild type (FRT2A): 1.00, dSARM⁸⁹⁶: 0.90, dSARM^{Rescue}: 1.00, dSARM^{KO}: 0.92, dSARM^{E1170A}: 1.09, dSARM^{ARM-SAM}: 1.00, dSARM^{TIR}: 0.59, and dSARM^{ARM-TIR}: 0.88. (D,E) Representative z-projections of OR22a ORNs of the indicated genotypes labeled with anti-GFP at 7 DPE. (F) Normalized mean axon intensity at 7 DPE: wild type (FRT2A): 1.00, dSARM⁸⁹⁶: 0.88, dSARM^{Rescue}: 0.85, dSARM^{KO}: 0.77, dSARM^{E1170A}: 0.92, dSARM^{ARM-SAM}: 1.03, dSARM^{TIR}: 0.45, and dSARM^{ARM-TIR}: 0.86. (G,H) Representative z-projections of OR22a ORNs of the indicated genotypes labeled with anti-GFP at 10 DPE. (I) Normalized mean axon intensity at 10 DPE: wild type (FRT2A): 1.00, dSARM⁸⁹⁶: 0.98, dSARM^{Rescue}: 0.93, dSARM^{KO}: 0.93, dSARM^{E1170A}: 0.94, dSARM^{ARM-SAM}: 0.99, dSARM^{TIR}: 0.30, and dSARM^{ARM-TIR}: 0.88. (J) Normalized mean axon intensity over time in dSARM^{Rescue} compared to dSARM^{TIR}. dSARM^{Rescue}: 1.00 (1DPE), 0.85 (7DPE), and 0.93 (10 DPE) and dSARM^{TIR}: 0.59 (1 DPE), 0.45 (7DPE), and 0.30 (10 DPE). Error bars represent min and max data points. N = 16 for each genotype. n.s. is not significantly different. *, p < 0.05. ****, p < 0.0001.

<https://doi.org/10.1371/journal.pgen.1010257.g004>

axons are severed. At 7 DPI, the injured and control wings are assessed for axonal phenotypes. In the injured examples, the number of neuronal cell bodies (cb) that were not cut off are indicated in the upper right corner as readout of uninjured axons (Fig 5A). The phenotypes (e.g., uninjured control axons, axonal debris, and severed intact axons, respectively) were quantified (Fig 5B), and the percentage of protected severed axons assessed at 7 DPI (Fig 5C).

We observed 100% protection of injured axons in *dSARM^{KO}* clones, while axons in *dSARM^{Rescue}* clones fully degenerated (Fig 5A, 5B and 5C). *dSARM^{E1170A}* and *dSARM^{ARM-SAM}* also failed to execute injury-induced axon degeneration, further confirming the necessity of the NAD⁺ hydrolase activity in axon degeneration (Fig 5B and 5C). *dSARM^{ARM-TIR}* mutant clones displayed equivalent axon protection to *dSARM^{KO}*, supporting that SAM-SAM multimerization is indispensable for dSARM activation after injury (Fig 5B and 5C). Lastly, we investigated the behavior of the TIR-only *dSARM* allele, which displayed both spontaneous and injury-induced axon degeneration in injured ORNs. In *dSARM^{TIR}* wing mutant clones, we did not observe signs of spontaneous degeneration, and clones showed full protection at 7 DPI (Fig 5B and 5C). These findings suggest that in the absence of ongoing spontaneous degeneration as in ORNs, the TIR domain does not support rapid injury-induced degeneration. Why the TIR-only mutant behaves differently in olfactory receptor neurons versus wing sensory neurons remains an open question that we speculate relates to differential timing of clone induction in the two systems (see Discussion). Taken together, these findings indicate

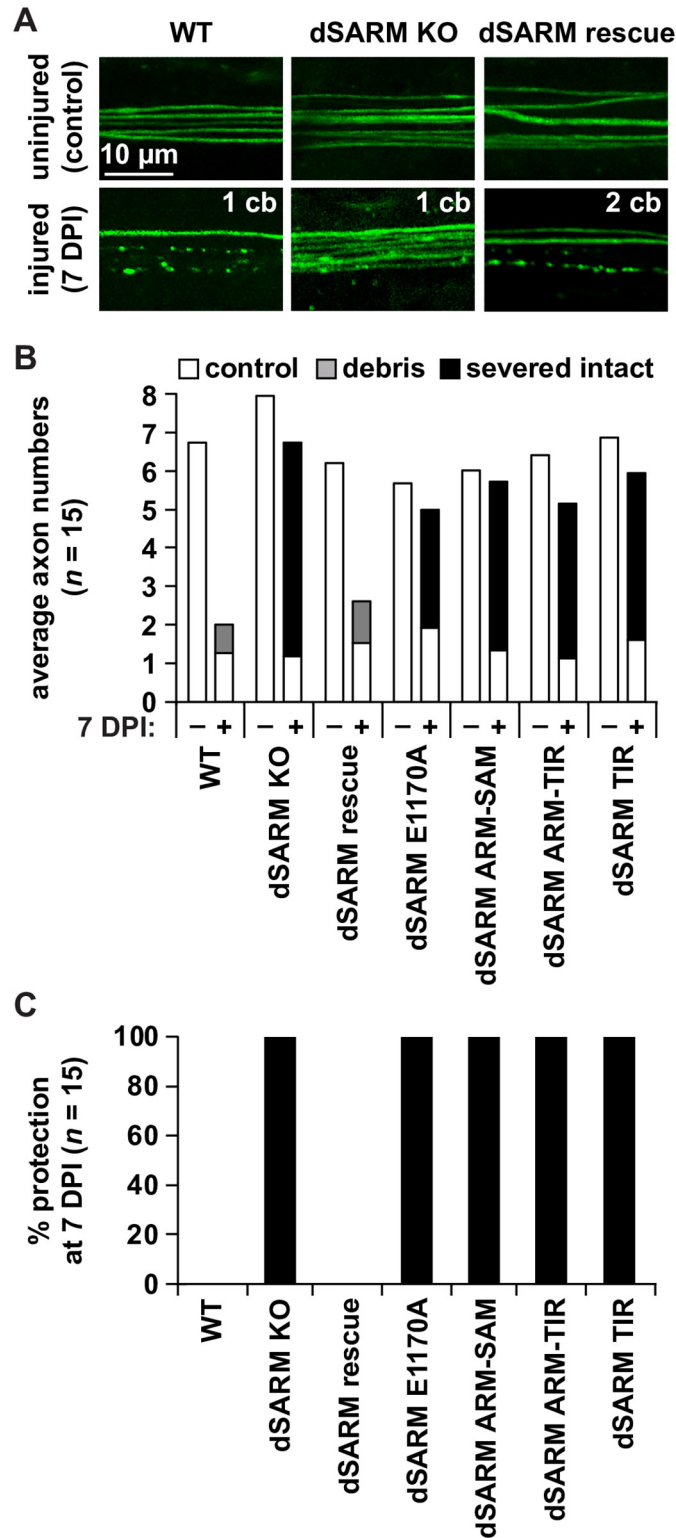


Fig 5. Full length dSARM is needed to trigger axon degeneration. (A) Representative pictures of control and 7 DPI axons of WT, dSARM KO and dSARM rescue. (B) Quantification of average axonal scores of uninjured control, debris, and severed intact axons (white, gray, and black, respectively). (C) Percentage of preserved severed axons at 7 DPI. N = 15 animals for each genotype.

<https://doi.org/10.1371/journal.pgen.1010257.g005>

that the NADase activity and SAM domain-mediated oligomerization are necessary for dSARM to activate and function as a neurodegenerative agent in injury-induced axon degeneration.

dSARM signaling in glia requires its NADase activity, but not its SAM domains

We recently uncovered a requirement for a glial dSARM-mediated TLR pathway in clearing neuronal debris during development. In loss-of-function (LOF) mutants of Toll-6, FoxO or dSARM, levels of Dcp-1-positive apoptotic debris are increased in the L3 brain [29]. We demonstrated that this pathway promotes phagocytosis by activating transcription of the key engulfment receptor Draper (Drpr) in a specific population of neuronal cell body-associated glia called cortex glia [39]. The discovery of a function for dSARM as a TLR pathway component raised important questions: (1) is dSARM multimerization required for TLR signaling? (2) does dSARM act solely as a TIR adaptor in this pathway or is its NAD⁺ hydrolase activity required? And (3) to what extent is signaling downstream of dSARM conserved in development versus degeneration? We previously demonstrated that RNAi-mediated knockdown of *dSARM* in cortex glia results in an identical increase in Dcp-1 debris as observed in *dSARM* nulls, while pan-neuronal dSARM knockdown does not affect corpse clearance [29]. Thus, the Dcp-1 phenotype observed in *dSARM* alleles can be attributed solely to dSARM's function in cortex glia.

To investigate functional requirements of individual dSARM domains in this pathway, we quantified the amount of Dcp-1 debris in L3 brains in all new *dSARM* alleles. For all alleles except *dSARM*^{TIR} (see below), we conducted this analysis at early L3 before the lethal phase of these animals. We developed an Imaris imaging pipeline to automate and standardize debris quantification, where to account for differences in brain size, Dcp-1 puncta count is normalized to individual brain lobe volume (see [Materials and methods](#); Dcp-1 puncta visible as white spots in brain lobes in [Fig 6](#)). Using this method, we find that neuronal corpses are cleared normally in *dSARM*^{Rescue} animals as evidenced by normal levels of Dcp-1 puncta in this background ([Fig 6A, 6B and 6H](#)). In contrast, we observe a roughly two-fold increase in apoptotic debris in *dSARM*^{KO} homozygotes relative to *dSARM*^{Rescue} animals ([Fig 6C and 6H](#)). This phenotype is consistent with that observed in the original *dSARM* LOF alleles and also with RNAi-mediated *dSARM* knockdown in cortex glia [29]. The phenotypes of the rescue and knockout in apoptotic debris clearance establishes the utility of our dSARM allelic series in dissecting signaling requirements of dSARM domains in this glial pathway.

We continued by interrogating the contributions of individual dSARM domains to developmental signaling. We find excessive neuronal debris in both *dSARM*^{ARM-SAM} and *dSARM*^{SAM} homozygotes ([Fig 6D, 6G and 6H](#)), indicating a TIR domain requirement in TLR signaling. Moreover, *dSARM*^{E1170A} homozygotes display an equivalent increase in Dcp-1 debris ([Fig 6E and 6H](#)), indicating that the NAD⁺ hydrolase activity is essential for the signaling role of dSARM in this setting. We next tested whether SAM-mediated dSARM multimerization is required by quantifying Dcp-1 puncta in *dSARM*^{ARM-TIR} homozygotes. Strikingly, apoptotic debris remains at control levels in *dSARM*^{ARM-TIR} mutants ([Fig 6F and 6H](#)), indicating that the SAM domain is dispensable for dSARM's signaling role. We wanted to test whether *dSARM*^{TIR} homozygotes display a glial phagocytosis phenotype at the L3 stage, but these mutants do not live this stage of development. Thus, we quantified apoptotic debris at L1. *dSARM*^{TIR} homozygotes display a roughly two-fold increase in neuronal debris relative to *dSARM*^{Rescue} animals at this stage ([Fig 6I–6K](#)). Given the likely GOF activity observed in *dSARM*^{TIR} mutants, it is unclear whether the increased debris in these animals reflects dSARM

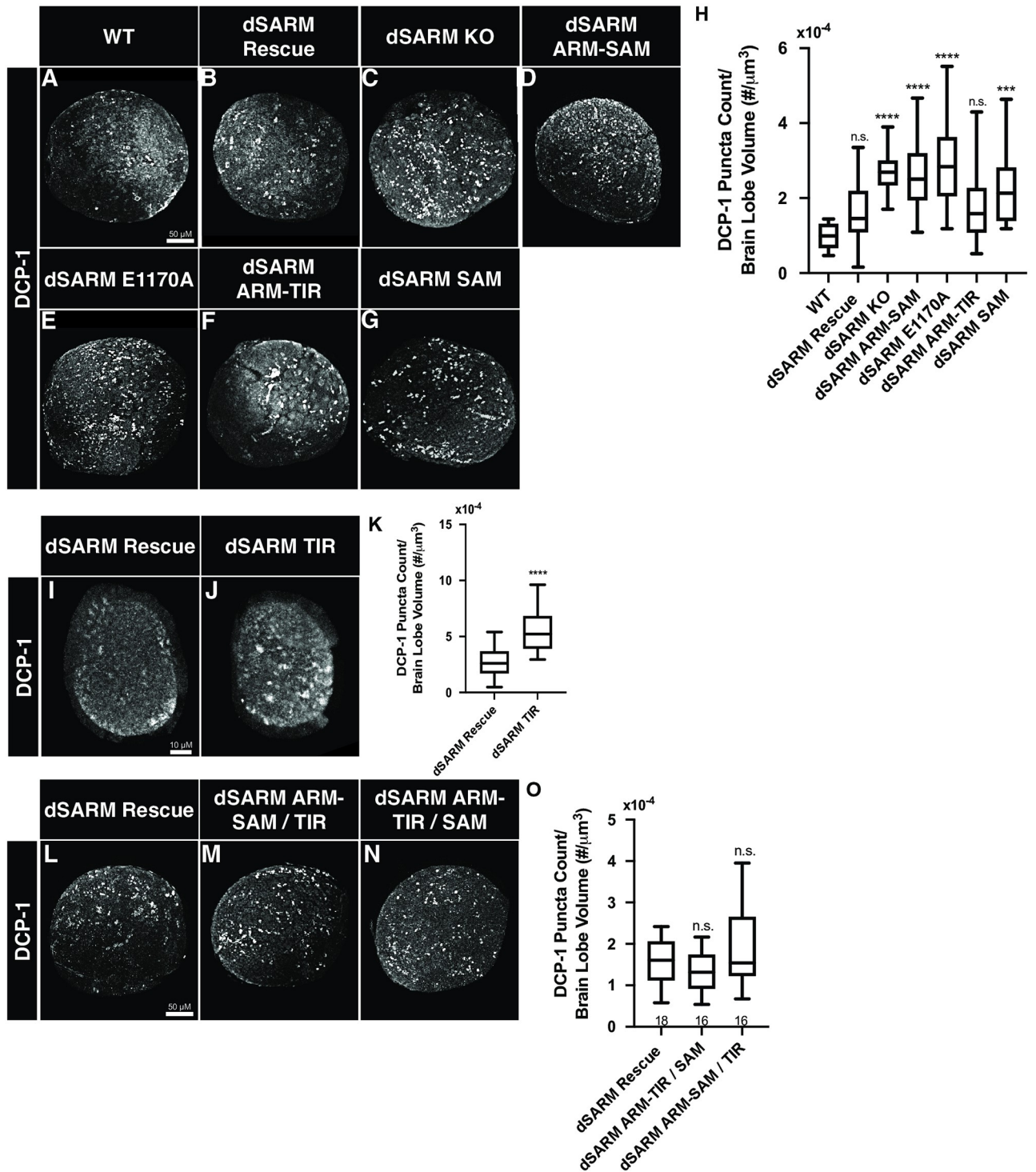


Fig 6. dSARM signaling in glia requires its NADase activity, but not its SAM domains. (A-G, I-J, and L-N) Representative z-projections of brain lobes of the indicated genotypes labeled with anti-Dcp-1. (H) Quantification of the number of Dcp-1 puncta normalized to brain lobe volume: wild type (Oregon R) (n = 28): 9.82×10^{-5} , dSARM^{Rescue} (n = 80): 1.64×10^{-4} , dSARM^{KO} (n = 30): 2.73×10^{-4} , dSARM^{ARM-SAM} (n = 20): 2.69×10^{-4} , dSARM^{E1170A} (n = 28): 2.91×10^{-4} , dSARM^{ARM-TIR} (n = 38): 1.75×10^{-4} , and dSARM^{SAM} (n = 17): 2.35×10^{-4} . (K) Quantification of the number of Dcp-1 puncta normalized to brain lobe volume: dSARM^{Rescue} (n = 26): 2.61×10^{-4} , and dSARM^{TIR} (n = 34): 5.22×10^{-4} . (O) Quantification of the number of Dcp-1 puncta normalized to brain lobe volume: dSARM^{Rescue} (n = 18): 1.57×10^{-4} , dSARM^{ARM-SAM/TIR} (n = 16): 1.92×10^{-4} , and dSARM^{ARM-TIR/SAM} (n = 16): 1.32×10^{-4} . n values can be found on each graph. n.s., not significant; *, p < 0.05; **, p < 0.01; ***, p < 0.001; ****, p < 0.0001.

<https://doi.org/10.1371/journal.pgen.1010257.g006>

function in cortex glia or increased neuronal death caused by a different mechanism. Regardless, these data imply that isolated TIR domains are insufficient to carry out dSARM's function in cortex glia. To test if *dSARM^{TIR}* behaves as a dominant allele in this assay, we tested if *dSARM^{TIR}* heterozygotes display increased levels of Dcp-1 debris at the L3 stage. We find normal levels of Dcp-1 debris in *dSARM^{TIR}* heterozygotes and in the rest of our new dSARM alleles (S3 Fig), demonstrating that none of the alleles have dominant activity in this context. These experiments suggest two main conclusions. (1) The finding that *dSARM^{ARM-TIR}* behaves as a null in injury-induced axon degeneration yet supports developmental signaling indicates a differential requirement for the SAM domains these two contexts. (2) The enzymatic activity of dSARM is essential for signaling, thus extending the known roles of the NADase activity of dSARM to signal transduction.

In pathological axon degeneration, the ARM, SAM, and TIR domains have all been assigned unique, separable functions. The extent to which these domains are distinct functional elements in TLR signal transduction has not been investigated. Intragenic complementation provides a classic genetic test of domain separability [40], and the generation of a series of complementary domain mutants of dSARM (Fig 1H) provides a unique opportunity to investigate this question. We generated *dSARM^{ARM-SAM}/dSARM^{TIR}* and *dSARM^{ARM-TIR}/dSARM^{SAM}* heteroallelic animals to test whether the domains can complement each other and restore wild-type dSARM function. We find that heteroallelic combinations of both pairs of reciprocal mutants are viable until the mid-pupal stage, while all homozygous mutants die as wandering third-instar larvae. The finding that ARM-SAM suppresses the early lethality observed in TIR-only homozygotes argues that ARM-SAM inhibits the GOF activity observed in this allele in trans. To look more specifically at the function of these reciprocal pairs of mutants in signaling, we quantified Dcp-1 apoptotic debris. We find that Dcp-1 counts are at wild-type levels in both heteroallelic combinations (Fig 6L–6O). This result is not surprising in the case of *dSARM^{ARM-TIR}/dSARM^{SAM}*, since *dSARM^{ARM-TIR}* homozygotes do not display a debris clearance phenotype. However, the rescue of debris clearance in *dSARM^{ARM-SAM}/dSARM^{TIR}* animals indicates that the ARM and TIR domains need not be covalently bound to restore wild-type dSARM function in a TLR pathway. Together, these findings indicate that the ARM, SAM, and TIR domains have separable functions during development and that the ARM domain can restrain the activity of the TIR domain in trans.

The MAP3K Ask1 is required for glial TLR signaling, but not for axon degeneration

The discovery that dSARM's NADase activity is required for pro-phagocytic signaling begs the question of how information is transmitted by dSARM's enzymatic activity. As a first step toward answering this question, we sought to identify downstream signaling components. We hypothesized that dSARM activation engages a MAPK cascade in cortex glia, a model initially based on Toll-6 signal transduction in motorneurons, where Toll-6 and dSARM drive JNK activation [30]. We looked for evidence of MAPK involvement in cortex glia, focusing first on the *Drosophila* MAP3K Ask1. Ask1 was a particularly attractive candidate because elegant genetic analyses in *C. elegans* demonstrated that Tir-1 (the worm homolog of dSARM/SARM1) activates Nsy-1 (the worm homolog of Ask1) to specify asymmetric odorant receptor expression [16]. More recently, dSARM and Ask1 have both been shown to be required to block vesicle trafficking after nerve injury [27].

To test for Ask1 involvement in glial TLR signaling, we investigated whether RNAi-mediated silencing of Ask1 in cortex glia increases Dcp-1 debris in the L3 brain. Indeed, reducing Ask1 expression in cortex glia resembles loss of dSARM and results in a two-fold increase in

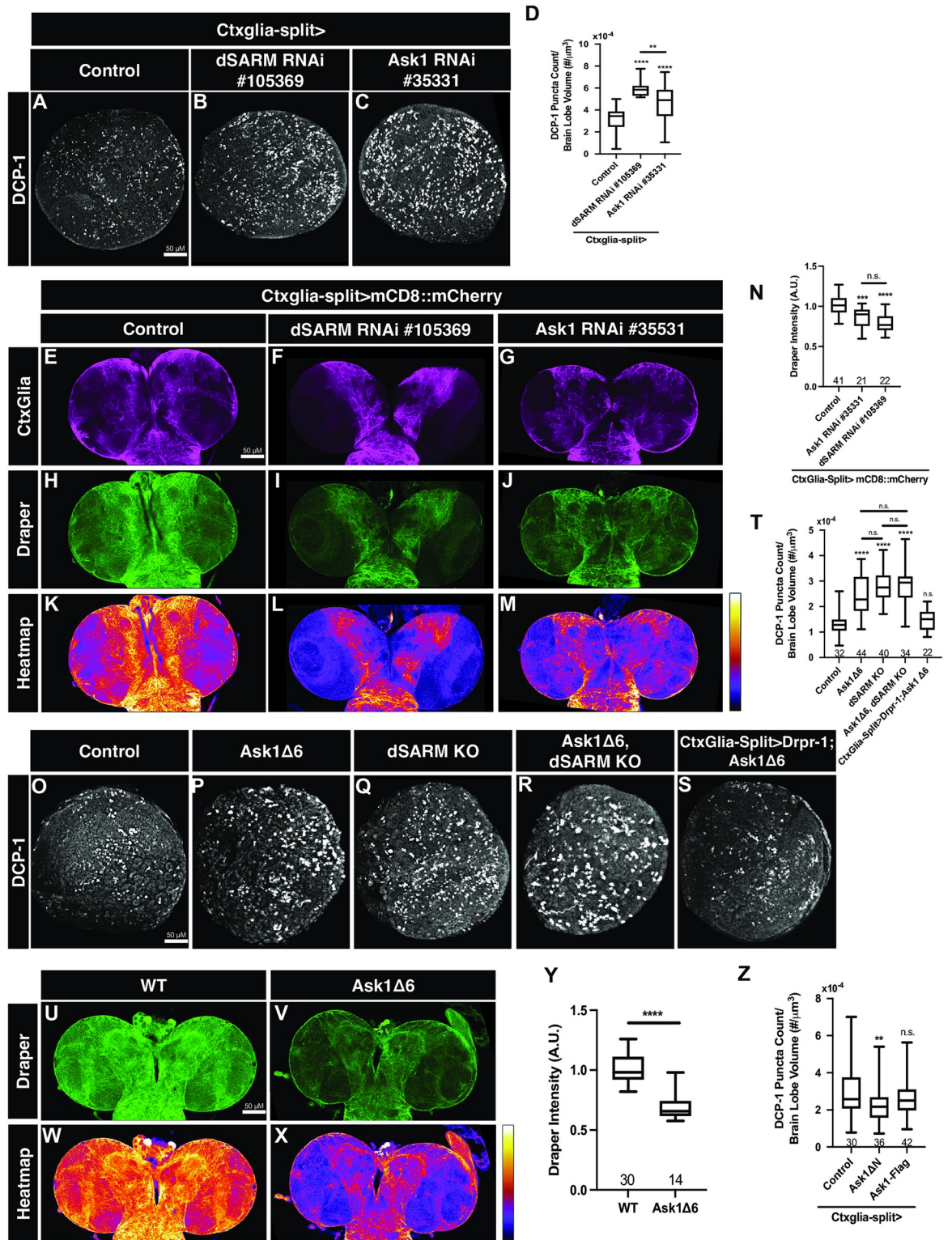


Fig 7. dSARM and Ask1 are in a linear genetic pathway in cortex glia. (A-C) Representative z-projections of brain lobes of the indicated genotypes labeled with anti-Dcp-1. (D) Quantification of the mean number of Dcp-1 puncta per brain lobe normalized to brain lobe volume: Control (Ctxglia-split>OR) (n = 44): 3.05×10^{-4} , Ctxglia-split>dSARM RNAi #105369 (n = 18): 5.98×10^{-4} , and Ctxglia-split>Ask1 RNAi #35331 (n = 42): 4.62×10^{-4} . (E-G) Representative 3 mm z-projections of larval brains of indicated genotypes labeled with anti-mCherry. (H-J) Representative 3 mm z-projections of larval brains of indicated genotypes labeled with anti-Drpr. (K-M)

Representative 3 mm z-projections of larval brains of indicated genotypes labeled with anti-Drpr represented as a heatmap. (N) Quantification of mean Drpr intensity normalized to Control (Ctxglia-split>mCD8::mCherry, LacZ): 1.00, Ctxglia-split>mCD8::mCherry, Ask1 RNAi #35331: 0.86, and Ctxglia-split>mCD8::mCherry, dSARM RNAi #105369: 0.75. (O-S) Representative z-projections of brain lobes of the indicated genotypes labeled with anti-Dcp-1. (T) Quantification of the mean number of Dcp-1 puncta per brain lobe normalized to brain lobe volume: Control (Oregon R): 1.28×10^{-4} , Ask1 $\Delta 6$: 2.42×10^{-4} , dSARM KO: 2.81×10^{-4} , and Ask1 $\Delta 6$, dSARM KO: 2.78×10^{-4} , and Ctxglia-split>Drpr-1; Ask1 $\Delta 6$: 1.45×10^{-4} . (U,V) Representative 3 mm z-projections of larval brains of indicated genotypes labeled with anti-Drpr. (W,X) Representative 3 mm z-projections of larval brains of indicated genotypes labeled with anti-Drpr represented as a heatmap. (Y) Quantification of mean Drpr intensity normalized to control: Control (Oregon R): 1.00 and Ask1 $\Delta 6$: 0.70. (Z) Quantification of the mean number of Dcp-1 puncta per brain lobe normalized to brain lobe volume: Ctxglia-split>Control (Oregon R): 2.99×10^{-4} , Ctxglia-split>Ask1 ΔN : 2.22×10^{-4} , and Ctxglia-split>Ask1-Flag: 2.66×10^{-4} . n values can be found on each graph. n.s., not significant; *, $p < 0.05$; **, $p < 0.01$; ***, $p < 0.001$; ****, $p < 0.0001$.

<https://doi.org/10.1371/journal.pgen.1010257.g007>

Dcp1 puncta (Fig 7A–7D). Glial TLR signaling promotes efficient phagocytosis via upregulation of Drpr [29,41], so we investigated whether cortex glial silencing of Ask1 resulted in reduced Drpr levels comparable to that of other pathway members. We find that RNAi-mediated loss of Ask1 in cortex glia reduces Drpr expression levels in cortex glia comparable to loss of dSARM (Fig 7E–7N). Since an *ask1* null allele did not exist, we employed CRISPR to generate a 6 KB deletion of the *ask1* locus to enable a genetic analysis (*ask1* ^{$\Delta 6$} ; see Materials and methods). We find that loss of Ask1 results in elevated Dcp-1 puncta and mimics loss of dSARM (Fig 7O–7Q and 7T). Loss of Ask1 also results in decreased baseline Drpr levels (Fig 7U–7Y), without changing the gross morphology of cortex glia. The phenotypic similarities between dSARM and *ask1* nulls are consistent with the idea that the genes are in the same genetic pathway. Indeed, *ask1* ^{$\Delta 6$} dSARM^{KO} double mutants display similar levels of Dcp-1 debris to either of the individual single mutants (Fig 7P–7R and 7T), providing genetic evidence that the genes function in a linear pathway. We previously demonstrated that Drpr overexpression in cortex glia is sufficient to suppress the phagocytosis phenotypes observed in dSARM mutants [29]. If Ask1 is required in this signaling pathway, Drpr overexpression should also suppress the *ask1* Dcp-1 phenotype. Indeed, cortex glial Drpr overexpression restores normal debris clearance to *ask1* homozygotes (Fig 7O, 7R and 7S), consistent with the identification of Ask1 as a novel component of this TLR pathway.

Ask1 is a conserved MAP3K in innate immune pathways where it is key to defense systems activated in response to harmful stimuli [42,43]. Ask1 orthologs contain an inhibitory N-terminal domain, and Ask1 proteins lacking this domain can be constitutively active (Ask1 ΔN , [42]. We previously found that Toll-6 overexpression in glia is sufficient to decrease neuronal debris, presumably as a result of accelerated debris clearance [29]. Thus, we wondered if overexpression of Ask1 or Ask1 ΔN might speed engulfment. We find that cortex glial overexpression of Ask1 ΔN , but not full-length Ask1, results in a significant reduction in the number of Dcp1 puncta in the brain relative to controls (Fig 7Z). These findings underscore the involvement of Ask1 in glial TLR signaling and argue that the N-terminal domain of Ask1 plays an inhibitory role in regulating Ask1 activation.

After demonstrating a function for Ask1 in TLR signaling in glial phagocytosis, we were curious as to whether Ask1 contributes to axon degeneration. Thus, we asked whether either loss or overexpression of Ask1 protected ORN axons following axotomy. Here, we quantified total axonal debris to establish any possible delay in axon fragmentation. In the absence of Ask1, we do not see a change in axonal debris indicating there is no delay in degeneration (S2A–S2C Fig). Similarly, when we overexpress wild-type Ask1 or constitutively active Ask1 ΔN , we do not see change in the rate of axonal fragmentation (S2D–S2G Fig). These findings demonstrate that Ask1 does not play a role in axon degeneration. Taken together, these findings indicate that Ask1 plays a role in developmental TLR signal transduction, but not in axon degeneration.

Discussion

Mechanisms of TLR signal transduction are many, but a common feature is that intracellular TIR domains of TLR receptors engage TIR domain-containing adaptors [44]. In TLR pathways, TIR domains have been considered solely as protein-protein interaction domains. We recently defined a glial function for the TIR adaptor dSARM downstream of a TLR that promotes engulfment of neuronal corpses during development [29]. We wondered to what extent dSARM's contribution to TLR signaling is related to its function in pathological axon degeneration [11,13,14]. To address this question, we generated a series of dSARM domain and point mutants via CRISPR/Cas9-mediated genome engineering. We compared the behavior of these new *dSARM* alleles in development and degeneration and find that while dSARM's enzymatic activity is essential in both contexts, SAM domain-mediated multimerization is critical for axon degeneration but dispensable for glial TLR signaling. Conversely, the MAP3K Ask1 is required for glial TLR signaling, but not axon degeneration. These findings align well with the independent companion manuscript from the DiAntonio lab [34]. Together, these studies expand the repertoire of TLR signal transduction mechanisms to include deployment of the dSARM NADase for Ask1 activation. Here we discuss the dichotomous functions of dSARM in developmental and degenerative settings.

An absolute requirement for the NADase activity of dSARM in axon degeneration *in vivo*

We found no difference in the protection afforded to either ORN or wing axons by deletion of *dSARM* or mutation of a key glutamic acid residue in dSARM's active site (E1170A; [14,34]). Thus, the NAD⁺ hydrolase activity is strictly required for axon degeneration in these two *in vivo* paradigms. These results differ from a recently published study [27] that independently generated a *dSARM*^{E1170A} knock-in allele. These authors found that *dSARM*^{E1170A} mutant clones exhibit a weaker phenotype than *dSARM* nulls. In a wing axotomy assay, these *dSARM*^{E1170A} mutant clones provided only 50% protection of severed axons at 7 DPI relative to full protection in *dSARM* nulls [27,37]. This discrepancy may stem from distinct CRISPR strategies or, alternatively, differences in genetic background. To validate our approach, we both sequenced the entire *dSARM* locus in this background and demonstrated that recombination of the wild-type sequence into the founder chromosome fully rescues viability and fertility. The finding of an essential requirement for dSARM's NAD⁺ hydrolase activity in axon degeneration in *Drosophila* is also in excellent agreement with data from mammalian models [14,45].

Unexpectedly, the behavior of the *dSARM*^{TIR} allele differed between ORN and wing sensory axon paradigms. In uninjured ORN axons, *dSARM*^{TIR} mutant clones exhibit spontaneous degeneration over the course of days arguing that SAM-mediated multimerization is not essential for NAD⁺ hydrolysis in the absence of the ARM domain. We propose that free TIR monomers have low-level constitutive activity leading to NAD⁺ loss, metabolic failure, and cellular demise. Consistent with unregulated activity of isolated TIR domains, the lethal phase of homozygous *dSARM*^{TIR} animals is significantly earlier than that of *dSARM*^{KO} homozygotes: early L1 for *dSARM*^{TIR}, wandering L3 for *dSARM*^{KO}. Surprisingly, *dSARM*^{TIR} mutant ORN clones not only exhibited slow, injury-independent degeneration, but were also capable of timely injury-induced degeneration. We suggest that *dSARM*^{TIR} clones are primed to degenerate given ongoing TIR domain activity, and that in this case, TIR monomers can support rapid axon destruction following axotomy. In contrast, *dSARM*^{TIR} behaved equivalently to the null allele in wing sensory axons. We did not see evidence of spontaneous axon degeneration in these neurons and mutant clones were fully protected for at least 7 days following axotomy.

It is possible that this difference reveals an underlying differential genetic sensitivity to NADase activity in these two neuronal populations. However, we hypothesize that the differential behavior of this allele may reflect a difference in timing of clone induction.

The generation of MARCM clones relies on enhancer-driven Flippase (FLP) activity that recombines Flippase Recombination Targets (FRTs) on a chromosomal arm [46]. ORN clones are induced by *ey-FLP* in the eye-antennal imaginal disc: *ey* activity starts in the eye-disc primordium (stage 15 embryo) and is maintained until the late third instar larvae [47]. In contrast, wing sensory neuron clones are induced by *ase-FLP* activity in the wing imaginal disc [37]. The activity of *ase* initiates in sensory organ precursors, which develop in third instar larvae and the first 10 h after puparium formation [48]. Thus, a likely explanation for the differential *dSARM^{TIR}* observation is that ORN clones are generated significantly earlier relative to wing sensory neuron clones, which might result in relatively higher levels of *dSARM^{TIR}* in adult neuron clones.

The NADase activity of dSARM promotes TLR signal transduction

We uncovered a differential requirement for dSARM's SAM domain in injury-induced degeneration and glial TLR signaling. dSARM/SARM1 assembles into an octamer via SAM-SAM mediated interactions [17–19], which is required for axon degeneration [12,18,20]. We generated a *dSARM* allele lacking only the SAM domains and found that it behaves as a null in axon degeneration. Thus, SAM domain-mediated dSARM multimerization is essential for axon degeneration *in vivo*. In contrast, *dSARM^{ARM-TIR}* homozygotes display normal glial TLR signaling, demonstrating that the SAM domains are not required in this context. We propose that in TLR signal transduction, dSARM's TIR domains heterodimerize with TIR domains on TLR receptors. In this model, TIR-TIR interactions between TLRs and dSARM support the NADase activity of dSARM, which is consistent with the finding that catalytically inactive dSARM variants retain the TIR-TIR interactions leading to NADase activation (this work; [49]). These findings raise the possibility that dSARM exists in at least two distinct signaling complexes: a dSARM homomultimer that drives pathological axon degeneration and a dSARM-TLR heteromultimer that promotes signal transduction. It is alternatively possible that TLR activation drives dSARM homodimerization and NADase activity. It will be interesting to determine whether there are distinct pools of dSARM dedicated for each signaling state. While dSARM's SAM domains are dispensable for glial TLR signaling, they must be required for other developmental functions of dSARM since *dSARM^{ARM-TIR}* homozygotes die at the L3/pupal transition. The SAM domains of TIR-1/SARM1 are proposed to regulate its synaptic localization in *C. elegans* [16], suggesting that dSARM's SAM domains may likewise promote synaptic functions in motoneurons [30].

Evidence from multiple groups now argues for a dSARM/SARM1-Ask1 signaling cassette (this work; [16,27,34]). We do not yet know how dSARM activates Ask1, but we demonstrate that dSARM's NADase activity is required for activation of Ask1 in glia. Ask1 orthologs are widely implicated in ROS-mediated signaling [50,51]. Specifically, they are ROS-activated by Thioredoxin (Trx), the first identified Ask1-binding protein and its major cellular inhibitor [42,52]. ROS signaling activates Ask1 because local oxidation relieves Trx-mediated repression and drives Ask1 activation [42,53]. Ask1 proteins lacking the Trx-binding domains (Ask1ΔN) can be constitutively active [42]. Indeed, we found that glial expression of Ask1ΔN activates TLR signaling, arguing that Trx may contribute to Ask1 activation in this context. It is conceivable that NAD⁺ hydrolysis mediated by dSARM could interfere with the maintenance of a reduced Trx pool, thus promoting activation of Ask1. Taken together with the companion study [34], these findings indicate that activation of the dSARM NAD⁺ hydrolase does not

necessarily drive irreversible axon destruction, but rather that NAD⁺ hydrolysis is deployed for signaling in both neurons and glia.

Methods

Drosophila stocks

Drosophila melanogaster stocks were raised on standard molasses formulation. Both male and female flies were included in all analyses. Sex was not considered since phenotypes were generally evenly distributed, suggesting no detectable sex contribution. The following stocks were used: OregonR (OR; wild type), *vasa*>*cas9* (BDSC, #55821), MKRS, *hs-FLP* / *TM6B*, *Cre*, *Tb* (BDSC, #1501), *ey-flp*, *UAS-mCD8::GFP* [11], *OR22a-Gal4*, *UAS-mCD8::GFP* [11], *dSARM*⁸⁹⁶ [11], *FRT2A*, *82B* (BDSC, #8218), *Wrapper932i-Gal4DBD*, *Nrv2-VP16AD* (*Ctxglia-split*; [39]), *Wrapper932i-Gal4DBD*, *Nrv2-VP16AD*, *UAS-mCD8::mCherry* (*Ctxglia-split*>*UAS-mCD8::mCherry*; [39]), *dSARM RNAi* #105369 (VDRC, #105369), *Ask1 RNAi* #35331 (BDSC, #35331), *UAS-LacZ*, *UAS-Ask1-Flag* (Kyoto DGRC, #109845), and *UAS-Ask1ΔN* (Kyoto DGRC, #109846).

CRISPR/Cas9 generation of *dSARM attP KO*

The *dSARM attP KO* was designed following published methods [31,54]. Nucleotides 3L:8064263..8064447 of the endogenous *dSARM* gene were replaced with an *attP* and *loxP* site through homology-directed repair using a donor template. The *attP* site facilitates the knock-in of *dSARM* domain alleles. The *pHD-DsRed-w+* (Addgene, #80898) was used to generate the donor template for homology-directed repair. Briefly, ~1 kb targeting homology arms flanking the domain-encoding exons of the *dSARM* gene, the *pHD-DsRed-w+* backbone, and *attP-loxP-DsRed-loxP* insert were generated by PCR. These four products were then assembled using NEB HiFi DNA assembly (NEB, # E5520S). A *dSARM* targeting chimeric RNA (*chiRNA*) was cloned into the *pU6-BbsI-chiRNA* (DGRC, #1362) vector using site-directed mutagenesis for the following target sequence: 5'- AAGGTTGTAAGGGTCCCCAGGGG -3' (NEB, # E0554S). Both the *chiRNA* and the *pHD-DsRed-w+* plasmids were injected (BestGene) into *vasa*>*Cas9* embryos (BDSC, #55821) to produce *dSARM* deletions. Successful events were screened for by the presence of *DsRed* positive eyes. The allele was named *dSARM attP KO*. Genomic PCR bands corresponding to primers flanking the targeted exons confirmed the deletion of the domain encoding exons of *dSARM attP KO*. The *DsRed* selection marker was removed by crossing to flies expressing *Cre* recombinase (MKRS, *hs-FLP/TM6B*, *Cre*, *Tb*) (BDSC, #1501).

phiC31-mediated recombination of *dSARM* rescue and mutants

As a control, an integration plasmid (*pGE-attB-GMR*) [33] containing wild-type *dSARM* nucleotides 3L:8064263–8064447 were injected (Rainbow Transgenic Flies) into *dSARM attP KO* embryos and integrated at the *dSARM* locus through *phiC31*-mediated recombination. Successful events were screened for by the presence of red eyes, and the red (*w+*) containing cassette was removed by *Cre* recombinase. The resulting *dSARM rescue* flies are homozygous-viable, fertile, and display no apparent phenotypes. To generate *dSARM E1170A*, we mutagenized the *dSARM rescue* plasmid, converting the *NADase* catalytic glutamic acid residue (GAA) to an alanine (GCC) (nucleotides 3L:8105127–8105129). To generate *dSARM ARM--SAM*, we mutagenized the *dSARM rescue* plasmid to remove the nucleotides 3L:8104756–8105455 corresponding to the TIR domain. To generate *dSARM TIR*, we mutagenized the *dSARM rescue* plasmid to remove the nucleotides 3L:8103445–8104722 corresponding to the

ARM and SAM domains. To generate dSARM ARM-TIR, we mutagenized the dSARM rescue plasmid to remove the nucleotides 3L:8104303–8104722 corresponding to the SAM domains. To generate dSARM SAM, we mutagenized the dSARM ARM-SAM plasmid to remove the nucleotides 3L:8103445–8104299 corresponding to the ARM domain.

CRISPR/Cas9 generation of Ask1Δ6

The Ask1Δ6 mutant was designed following published methods [31,54]. The endogenous Ask1 gene (nucleotides 3R:19879704–19886056) was replaced with an attP site through homology-directed repair. The pHD-DsRed-w+ (Addgene, #80898) was used to generate the donor template for homology-directed repair. Briefly, ~1 kb targeting homology arms flanking the 5' and 3' UTRs of the Ask1 gene, the pHD-DsRed-w+ backbone, and attP-loxP-DsRed-loxP insert were generated by PCR. These four products were assembled using NEB HiFi DNA assembly (NEB, # E5520S). An Ask1 targeting chimeric RNA (chiRNA) was cloned into the pU6-BbsI-chiRNA (DGRC, #1362) vector using site-directed mutagenesis for the following CRISPR target sequence: 5'-GTATTTCTTGTTAACTGGAAAGG-3' (NEB, # E0554S). The chiRNA and the pHD-DsRed-w+ plasmids were injected into vasa>Cas9 embryos (BDSC, #55821). Successful events were screened for by the presence of DsRed-positive eyes. The allele was named Ask1Δ6 for the 6350 bp deletion. Genomic PCR bands corresponding to primers flanking the Ask1 gene confirmed the absence of Ask1Δ6. This approach resulted in the deletion of the entire Ask1 gene (upstream flanking sequence: 5'-GTATATTGCTGG-TAGCTGTG-3', downstream flanking sequence: 5'-GAAAGGATTTATAGCTTCTG-3'). The dsRed selection marker was removed by crossing to flies expressing Cre recombinase (MKRS, hs-FLP / TM6B, Cre, Tb).

Antennal injury protocol

We induced antennal injury using a modification of a previously described protocol [11,55]. Animals were aged 1, 7, or 30 days at 25°C. Only the right antennal segment was surgically ablated using forceps. Injured flies were aged at 25°C for the indicated time (12 hours, 1, 2, 7, or 30 days). Number of axons was scored as previously described [8].

Wing injury protocol

We performed wing injuries using a modification of a previously described protocol [38]. One wing per anesthetized fly was cut approximately in the middle. The distal, cut-off part of the wing was mounted in Halocarbon Oil 27 on a microscopy slide, covered with a coverslip, and immediately used to count the amount of cut-off cell bodies (as readout for the number of injured axons) under an epifluorescence microscope. Flies were returned to individual vials. At 7 DPI, wings were mounted onto a slide, and imaged with a spinning disk microscope to assess for intact or degenerated injured axons, as well as the remaining uninjured intact neurons.

Adult immunohistochemistry

Adult heads were fixed with 4% formaldehyde (Thermo Scientific, #28906) in 1x PBS and 0.1% Triton X-100 (PTX) for 30 min and washed 5 times, 2 minutes each with PTX before dissection. Brains were dissected in PTX. Dissected brains were subsequently fixed in 4% formaldehyde in PTX for 10 min and washed 5 times, 2 minutes each with PTX. Primary antibody anti-chicken GFP (Aves Labs, #GFP-1020) was used at 1:500 in PTX and rocked overnight at 4°C. Brains were washed 3 times, 10 minutes each with PTX. Alexa Fluor 488 goat anti-chicken

(Invitrogen, #A11039) was used at 1:100 in PTX and rocked overnight at 4°C. Following antibody incubation brains were washed 3 times, 10 minutes each with PTX. Brains were mounted in ProLong Gold with DAPI (Invitrogen, #P36935).

Confocal microscopy

Fluorescent 16-bit images were acquired on an upright Zeiss LSM 800 (Carl Zeiss) using Zen software (Carl Zeiss). The following objectives were used: 20x Plan-Apochromat (0.8 NA) air objective (larval experiments) or 40x Fluar (1.3 NA) oil immersion objective (adult experiments).

Axonal intensity and axonal debris measurements

Maximum intensity Z-projections were analyzed in Image J/Fiji. Axons were isolated from the image (the glomeruli were not analyzed) one side at a time. A threshold using the default settings was applied to highlight the axons. This threshold was then used to create a selection. From this selection, the average intensity was measured. For axonal debris, we started with a maximum intensity Z-projection in Image J/Fiji. We generated a region of interest on the injured side by applying a threshold to detect the fluorescent signal and generated a selection. From this selection, we used the analyze particles function to get total fluorescent area.

qRT-PCR

Fifty first or second instar larvae of each genotype were collected in an 0.6mL Eppendorf tube in nuclease-free water on ice. The larvae were homogenized in the 0.6 mL tube with a pestle. RNA was isolated using the RNeasy plus kit (Qiagen). cDNA was synthesized from 1 mg total RNA using the iScript kit (BioRad) and the cDNA was diluted 1:5. qRT-PCR was performed using Taqman probes from the Life Technologies database: Rp1140 (Dm02134594_g1) and dSARM (Dm01840803_m1). These were utilized in a StepOnePlus Real-Time PCR system (Applied Scientific/ Thermo Scientific). Rp1140 was used as the reference gene for the DDC_T comparison protocol to quantify relative changes in gene expression, all in technical triplicate. No-reverse transcriptase controls were conducted to confirm the purity of each cDNA sample, and lack of gDNA contamination in the qRT-PCR. We performed 4 biological replicates per mRNA and 3 technical replicates per biological replicate.

Larval immunohistochemistry

Rapid dissections were performed in PBS to expose 3rd instar larval (L3) CNS. Extracted brains were fixed in 4% paraformaldehyde (PFA) in PBS for 20 minutes. Fixed brains were washed 3x 5min in PBS and blocked in PTN (1X PBS, 0.1% Triton X-100, 1% NGS) for 30 minutes and incubated in primary antibody for two overnights at 4°C. Following incubation in primary antibody, brain samples were washed 3x 5min in PTN and incubated in secondary antibody for 2 hours at room temperature. After incubation in secondary antibody, samples were washed 3x 5min in PBS and mounted in Prolong Gold antifade reagent with DAPI (Thermo Fisher). Mounted samples were solidified at room temperature overnight before image acquisition. The following primary and secondary antibodies were used: rabbit anti-cleaved Drosophila Dcp-1 (Asp216) (Cell Signaling Technology; at 1:100), goat anti-rabbit IgG (Alexa-conjugated fluor 568) (Thermo Fisher; at 1:300), and mouse anti-Draper (5D14; DSHB; at 1:300).

Larval Dcp-1 counting

Acquired confocal images of 3rd instar larval (L3) CNS were analyzed using Imaris Microscopy Image Analysis Software (Oxford Instruments). To reduce background noise, a background subtraction filter (2.5 μm in width) under Image Processing function was first applied to the image. After image processing, contour of both brain lobes was traced across top to bottom slices using the surface function to define a region of interest. Each region of interest recapitulates the entirety of an individual brain lobe and measures its volume. Within each region of interest, Spots Detection function (at 2.0 XY diameter and 2.0 Z-axis diameter, with Quality filter) was deployed to automatically label individual Dcp-1 puncta based on a local contrast screening of relative intensity and to generate a total count in each brain lobe. Total Dcp-1 puncta count is then divided by individual brain lobe volume to yield normalized Dcp-1 puncta count ($\#/\mu\text{m}^3$).

Draper quantification

Larval brains were imaged and processed as previously described [29]. Briefly, control and mutant genotypes were imaged using identical acquisition settings. Z-stacks were acquired with optimized confocal settings to ensure that oversaturation did not occur. Average intensity was quantified from 3 μm thick z-projections using Fiji (National Institutes of Health). For cortex glia knockdown experiments, an ROI was defined by mCherry labeling cortex glia expressing UAS-mCD8::mCherry. For analysis of Ask1 $\Delta 6$, we quantified Draper intensity around the neuropil corresponding to cortex glial processes.

Quantification and statistical analysis

All statistical analyses were performed and graphs generated using Prism 9 (GraphPad Software). In all box and whisker plots, the whiskers represent minimum and maximum data points, and the line within the box depicts median values. In all bar graphs, error bars are mean \pm SEM. All pairwise sample comparisons were performed using a Mann-Whitney test. For data in a group of three or more, a Kruskal-Wallis test was used to compare each sample with other samples, and a Dunn's multiple comparison test was subsequently performed. A two-way ANOVA followed by a Dunnett's multiple comparisons test was performed on adult ORN axon degeneration data (Figs 2I, 2Q and 4J). In all figures, p-values for statistical tests are as follow: n.s., not significant; *, $P < 0.05$; **, $P < 0.01$; ***, $P < 0.001$; ****, $P < 0.0001$. n values are found on each graph and/or figure legends.

Supporting information

S1 Fig. *dSARM*^{TIR} homozygous mutant OR22a axons exhibit timely degeneration following injury. (A,B) Representative z-projections of OR22a ORNs of the indicated genotypes labeled with anti-GFP at 12 Hours post injury (HPI). (C) Normalized mean axon intensity at 12 HPI: *dSARM* rescue: 0.80 (n = 24), *dSARM*^{TIR}: 0.56 (n = 22). (PDF)

S2 Fig. Ask1 is not required for injury-induced axon degeneration. (A,B) Representative z-projections of OR22a ORNs of the indicated genotypes labeled with anti-GFP at 7 DPE, 1 DPI. (C) Normalized mean axon intensity at 1 DPI: wild type (FRT2A): 0.91, Ask1 $\Delta 6$: 0.86, (D-F) Representative z-projections of OR22a ORNs of the indicated genotypes labeled with anti-GFP at 7 DPE, 1 DPI. (G) Normalized mean axon intensity at 1 DPI: wild type (FRT2A): 0.85 (n = 35); OR22a-Gal4, UAS-Ask1-Flag: 0.76 (n = 24); OR22a-Gal4, UAS-Ask1 ΔN : 0.61

(n = 26). n.s., not significant.
(PDF)

S3 Fig. dSARM alleles do not have dominant effects on Dcp-1 levels in the L3 brain. (A-G) Representative z-projections of brain lobes of the indicated genotypes labeled with anti-Dcp-1. (H) Quantification of the number of Dcp-1 puncta normalized to brain lobe volume. Mean number of Dcp-1 puncta/brain lobe volume: dSARM^{Rescue}: 1.56×10^{-4} , dSARM^{KO}: 1.45×10^{-4} , dSARM^{ARM-SAM}: 1.53×10^{-4} , dSARM^{ARM-TIR}: 1.36×10^{-4} , dSARM^{E1170A}: 1.72×10^{-4} , dSARM^{SAM}: 1.60×10^{-4} , and dSARM^{TIR}: 1.89×10^{-4} . n values can be found on the graph. n.s., not significant.
(PDF)

S1 Data. Underlying numerical data.
(PDF)

Acknowledgments

We thank E.J. Brace and Aaron DiAntonio for communicating results prior to publication. We are grateful to Scott Gratz and Kate O'Connor-Giles for providing guidance on CRISPR-Cas9 genome engineering. We thank Dan Jindal for his assistance with Imaris analysis. We thank Pam Vanderzalm and members of the Broihier lab for their comments on the project and on the manuscript. We thank the Developmental Studies Hybridoma Bank for antibodies and the Bloomington Drosophila Stock Center for fly stocks.

Author Contributions

Conceptualization: Kelsey A. Herrmann, Yizhou Liu, Arnau Llobet-Rosell, Colleen N. McLaughlin, Heather T. Broihier.

Data curation: Arnau Llobet-Rosell.

Formal analysis: Kelsey A. Herrmann, Yizhou Liu, Arnau Llobet-Rosell, Colleen N. McLaughlin, Lukas J. Neukomm, Jaeda C. Coutinho-Budd.

Funding acquisition: Lukas J. Neukomm, Jaeda C. Coutinho-Budd, Heather T. Broihier.

Investigation: Kelsey A. Herrmann, Yizhou Liu, Arnau Llobet-Rosell, Colleen N. McLaughlin, Lukas J. Neukomm, Jaeda C. Coutinho-Budd.

Methodology: Kelsey A. Herrmann, Yizhou Liu, Arnau Llobet-Rosell, Colleen N. McLaughlin, Lukas J. Neukomm, Jaeda C. Coutinho-Budd.

Project administration: Lukas J. Neukomm, Heather T. Broihier.

Supervision: Lukas J. Neukomm, Jaeda C. Coutinho-Budd.

Validation: Kelsey A. Herrmann, Yizhou Liu, Colleen N. McLaughlin, Lukas J. Neukomm, Jaeda C. Coutinho-Budd, Heather T. Broihier.

Visualization: Kelsey A. Herrmann, Yizhou Liu, Arnau Llobet-Rosell, Colleen N. McLaughlin, Jaeda C. Coutinho-Budd, Heather T. Broihier.

Writing – original draft: Kelsey A. Herrmann, Yizhou Liu, Arnau Llobet-Rosell, Lukas J. Neukomm, Heather T. Broihier.

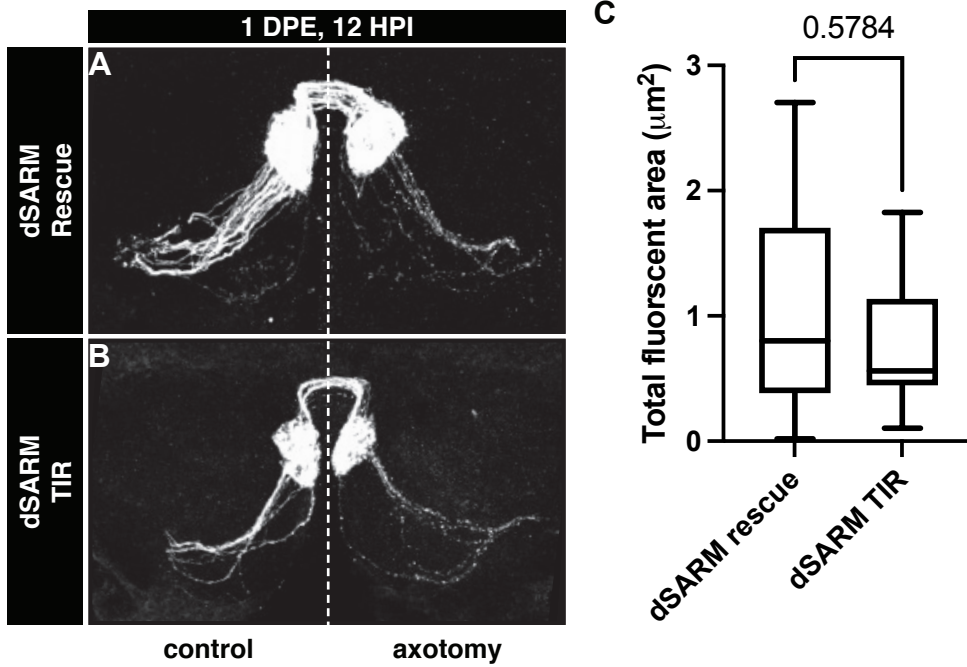
Writing – review & editing: Heather T. Broihier.

References

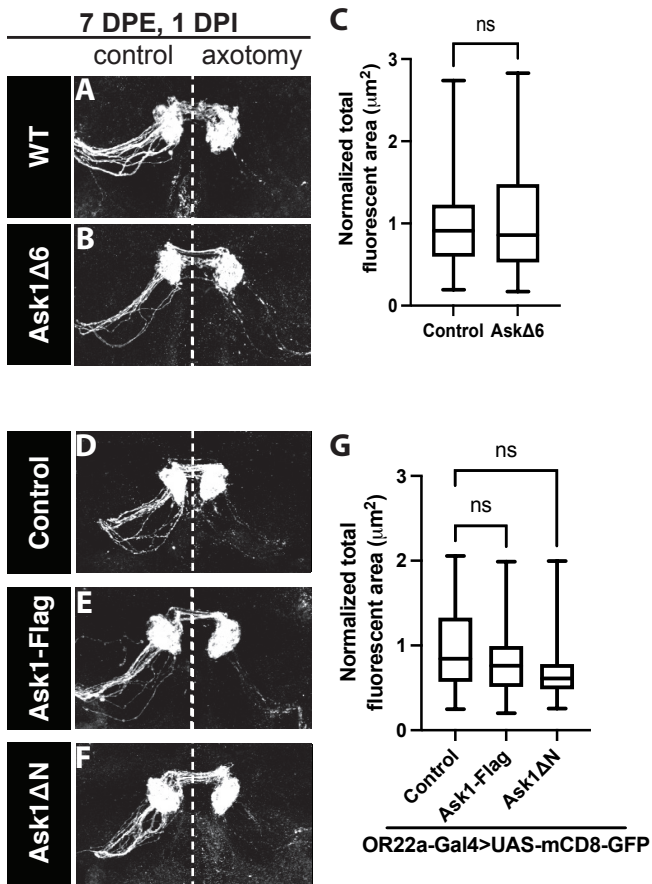
1. Waller AV. XX. Experiments on the section of the glossopharyngeal and hypoglossal nerves of the frog, and observations of the alterations produced thereby in the structure of their primitive fibres. *Philosophical Transactions Royal Soc Lond.* 1850; 140: 423–429. <https://doi.org/10.1098/rstl.1850.0021>
2. Lunn ER, Perry VH, Brown MC, Rosen H, Gordon S. Absence of Wallerian Degeneration does not Hinder Regeneration in Peripheral Nerve. *Eur J Neurosci.* 1989; 1: 27–33. <https://doi.org/10.1111/j.1460-9568.1989.tb00771.x> PMID: 12106171
3. Perry VH, Brown MC, Lunn ER. Very Slow Retrograde and Wallerian Degeneration in the CNS of C57BL/Ola Mice. *Eur J Neurosci.* 1991; 3: 102–105. <https://doi.org/10.1111/j.1460-9568.1991.tb00815.x> PMID: 12106273
4. Mack TGA, Reiner M, Beirowski B, Mi W, Emanuelli M, Wagner D, et al. Wallerian degeneration of injured axons and synapses is delayed by a Ube4b/Nmnat chimeric gene. *Nat Neurosci.* 2001; 4: 1199–1206. <https://doi.org/10.1038/nn770> PMID: 11770485
5. Wang J, Zhai Q, Chen Y, Lin E, Gu W, McBurney MW, et al. A local mechanism mediates NAD-dependent protection of axon degeneration. *J Cell Biology.* 2005; 170: 349–355. <https://doi.org/10.1083/jcb.200504028> PMID: 16043516
6. Jia H, Yan T, Feng Y, Zeng C, Shi X, Zhai Q. Identification of a critical site in Wlds: Essential for Nmnat enzyme activity and axon-protective function. *Neurosci Lett.* 2007; 413: 46–51. <https://doi.org/10.1016/j.neulet.2006.11.067> PMID: 17207927
7. Conforti L, Wilbrey A, Morreale G, Janeckova L, Beirowski B, Adalbert R, et al. WldS protein requires Nmnat activity and a short N-terminal sequence to protect axons in mice. *J Cell Biol.* 2009; 184: 491–500. <https://doi.org/10.1083/jcb.200807175> PMID: 19237596
8. Avery MA, Sheehan AE, Kerr KS, Wang J, Freeman MR. WldS requires Nmnat1 enzymatic activity and N16–VCP interactions to suppress Wallerian degeneration. *J Cell Biol.* 2009; 184: 501–513. <https://doi.org/10.1083/jcb.200808042> PMID: 19237597
9. Araki T, Sasaki Y, Milbrandt J. Increased nuclear NAD biosynthesis and SIRT1 activation prevent axonal degeneration. *Sci New York N Y.* 2004; 305: 1010–3. <https://doi.org/10.1126/science.1098014> PMID: 15310905
10. Rosell AL, Neukomm LJ. Axon death signalling in Wallerian degeneration among species and in disease. *Open Biol.* 2019; 9: 190118. <https://doi.org/10.1098/rsob.190118> PMID: 31455157
11. Osterloh JM, Yang J, Rooney TM, Fox AN, Adalbert R, Powell EH, et al. dSarm/Sarm1 Is Required for Activation of an Injury-Induced Axon Death Pathway. *Science.* 2012; 337: 481–484. <https://doi.org/10.1126/science.1223899> PMID: 22678360
12. Gerdts J, Summers DW, Sasaki Y, DiAntonio A, Milbrandt J. Sarm1-Mediated Axon Degeneration Requires Both SAM and TIR Interactions. *J Neurosci.* 2013; 33: 13569–13580. <https://doi.org/10.1523/JNEUROSCI.1197-13.2013> PMID: 23946415
13. Gerdts J, Brace EJ, Sasaki Y, DiAntonio A, Milbrandt J. SARM1 activation triggers axon degeneration locally via NAD⁺ destruction. *Science.* 2015; 348: 453–457. <https://doi.org/10.1126/science.1258366> PMID: 25908823
14. Essuman K, Summers DW, Sasaki Y, Mao X, DiAntonio A, Milbrandt J. The SARM1 Toll/Interleukin-1 Receptor Domain Possesses Intrinsic NAD⁺ Cleavage Activity that Promotes Pathological Axonal Degeneration. *Neuron.* 2017; 93: 1334–1343.e5. <https://doi.org/10.1016/j.neuron.2017.02.022> PMID: 28334607
15. Summers DW, Gibson DA, DiAntonio A, Milbrandt J. SARM1-specific motifs in the TIR domain enable NAD⁺ loss and regulate injury-induced SARM1 activation. *Proc National Acad Sci.* 2016; 113: E6271–E6280. <https://doi.org/10.1073/pnas.1601506113> PMID: 27671644
16. Chuang C-F, Bargmann CI. A Toll-interleukin 1 repeat protein at the synapse specifies asymmetric odorant receptor expression via ASK1 MAPKKK signaling. *Gene Dev.* 2005; 19: 270–281. <https://doi.org/10.1101/gad.1276505> PMID: 15625192
17. Sporny M, Guez-Haddad J, Lebendiker M, Ulisse V, Volf A, Mim C, et al. Structural Evidence for an Octameric Ring Arrangement of SARM1. *J Mol Biol.* 2019; 431: 3591–3605. <https://doi.org/10.1016/j.jmb.2019.06.030> PMID: 31278906
18. Horsefield S, Burdett H, Zhang X, Manik MK, Shi Y, Chen J, et al. NAD⁺ cleavage activity by animal and plant TIR domains in cell death pathways. *Science.* 2019; 365: 793–799. <https://doi.org/10.1126/science.aax1911> PMID: 31439792
19. Bratkowski M, Xie T, Thayer DA, Lad S, Mathur P, Yang Y-S, et al. Structural and Mechanistic Regulation of the Pro-degenerative NAD Hydrolase SARM1. *Cell Reports.* 2020; 32: 107999. <https://doi.org/10.1016/j.celrep.2020.107999> PMID: 32755591

20. Sporny M, Guez-Haddad J, Khazma T, Yaron A, Dessau M, Shkolnisky Y, et al. The structural basis for SARM1 inhibition and activation under energetic stress. *Elife*. 2020; 9: e62021. <https://doi.org/10.7554/eLife.62021> PMID: 33185189
21. Shen C, Vohra M, Zhang P, Mao X, Figley MD, Zhu J, et al. Multiple domain interfaces mediate SARM1 autoinhibition. *P Natl Acad Sci Usa*. 2021; 118: e2023151118. <https://doi.org/10.1073/pnas.2023151118> PMID: 33468661
22. Jiang Y, Liu T, Lee C-H, Chang Q, Yang J, Zhang Z. The NAD⁺-mediated self-inhibition mechanism of pro-neurodegenerative SARM1. *Nature*. 2020; 588: 658–663. <https://doi.org/10.1038/s41586-020-2862-z> PMID: 33053563
23. Figley MD, Gu W, Nanson JD, Shi Y, Sasaki Y, Cunnea K, et al. SARM1 is a metabolic sensor activated by an increased NMN/NAD⁺ ratio to trigger axon degeneration. *Neuron*. 2021; 109: 1118–1136.e11. <https://doi.org/10.1016/j.neuron.2021.02.009> PMID: 33657413
24. Mink M, Fogelgren B, Olszewski K, Maroy P, Csiszar K. A Novel Human Gene (SARM) at Chromosome 17q11 Encodes a Protein with a SAM Motif and Structural Similarity to Armadillo/ β -Catenin That Is Conserved in Mouse, *Drosophila*, and *Caenorhabditis elegans*. *Genomics*. 2001; 74: 234–244. <https://doi.org/10.1006/geno.2001.6548> PMID: 11386760
25. Carty M, Goodbody R, Schröder M, Stack J, Moynagh PN, Bowie AG. The human adaptor SARM negatively regulates adaptor protein TRIF-dependent Toll-like receptor signaling. *Nat Immunol*. 2006; 7: 1074–81. <https://doi.org/10.1038/ni1382> PMID: 16964262
26. Chen C-Y, Lin C-W, Chang C-Y, Jiang S-T, Hsueh Y-P. Sarm1, a negative regulator of innate immunity, interacts with syndecan-2 and regulates neuronal morphology. *J Cell Biol*. 2011; 193: 769–784. <https://doi.org/10.1083/jcb.201008050> PMID: 21555464
27. Hsu J-M, Kang Y, Corty MM, Mathieson D, Peters OM, Freeman MR. Injury-Induced Inhibition of Bystander Neurons Requires dSarm and Signaling from Glia. *Neuron*. 2021; 109: 473–487.e5. <https://doi.org/10.1016/j.neuron.2020.11.012> PMID: 33296670
28. Izadifar A, Courchet J, Virga DM, Verreet T, Hamilton S, Ayaz D, et al. Axon morphogenesis and maintenance require an evolutionary conserved safeguard function of Wnk kinases antagonizing Sarm and Axed. *Neuron*. 2021; 109: 2864–2883.e8. <https://doi.org/10.1016/j.neuron.2021.07.006> PMID: 34384519
29. McLaughlin CN, Perry-Richardson JJ, Coutinho-Budd JC, Broihier HT. Dying Neurons Utilize Innate Immune Signaling to Prime Glia for Phagocytosis during Development. *Dev Cell*. 2019; 48: 506–522.e6. <https://doi.org/10.1016/j.devcel.2018.12.019> PMID: 30745142
30. McLaughlin CN, Nechipurenko IV, Liu N, Broihier HT. A Toll receptor–FoxO pathway represses Pavarotti/MKLP1 to promote microtubule dynamics in motoneurons. *J Cell Biology*. 2016; 214: 459–474. <https://doi.org/10.1083/jcb.201601014> PMID: 27502486
31. Gratz SJ, Ukken FP, Rubinstein CD, Thiede G, Donohue LK, Cummings AM, et al. Highly specific and efficient CRISPR/Cas9-catalyzed homology-directed repair in *Drosophila*. *Genetics*. 2014; 196: 961–71. <https://doi.org/10.1534/genetics.113.160713> PMID: 24478335
32. Gratz SJ, Harrison MM, Wildonger J, O'Connor-Giles KM. Precise Genome Editing of *Drosophila* with CRISPR RNA-Guided Cas9. *Methods Mol Biology Clifton N J*. 2015; 1311: 335–48. https://doi.org/10.1007/978-1-4939-2687-9_22 PMID: 25981484
33. Huang J, Zhou W, Dong W, Watson AM, Hong Y. Directed, efficient, and versatile modifications of the *Drosophila* genome by genomic engineering. *Proc National Acad Sci*. 2009; 106: 8284–8289. <https://doi.org/10.1073/pnas.0900641106> PMID: 19429710
34. Brace EJ, Essuman K, Mao Xi, Palucki J, Milbrandt J, DiAntonio A. Distinct developmental and degenerative functions of SARM1 require NAD⁺ hydrolase activity. *PLOS Genetics*. 2022. <https://doi.org/10.1371/journal.pgen.1010246>
35. Essuman K, Summers DW, Sasaki Y, Mao X, Yim AKY, DiAntonio A, et al. TIR Domain Proteins Are an Ancient Family of NAD⁺-Consuming Enzymes. *Curr Biol*. 2018; 28: 421–430.e4. <https://doi.org/10.1016/j.cub.2017.12.024> PMID: 29395922
36. Wan L, Essuman K, Anderson RG, Sasaki Y, Monteiro F, Chung E-H, et al. TIR domains of plant immune receptors are NAD⁺-cleaving enzymes that promote cell death. *Science*. 2019; 365: 799–803. <https://doi.org/10.1126/science.aax1771> PMID: 31439793
37. Neukomm LJ, Burdett TC, Gonzalez MA, Züchner S, Freeman MR. Rapid in vivo forward genetic approach for identifying axon death genes in *Drosophila*. *Proc National Acad Sci*. 2014; 111: 9965–9970. <https://doi.org/10.1073/pnas.1406230111> PMID: 24958874
38. Paglione M, Rosell AL, Chatton J-Y, Neukomm LJ. Morphological and Functional Evaluation of Axons and their Synapses during Axon Death in *Drosophila melanogaster*. *J Vis Exp Jove*. 2020. <https://doi.org/10.3791/60865> PMID: 32225164

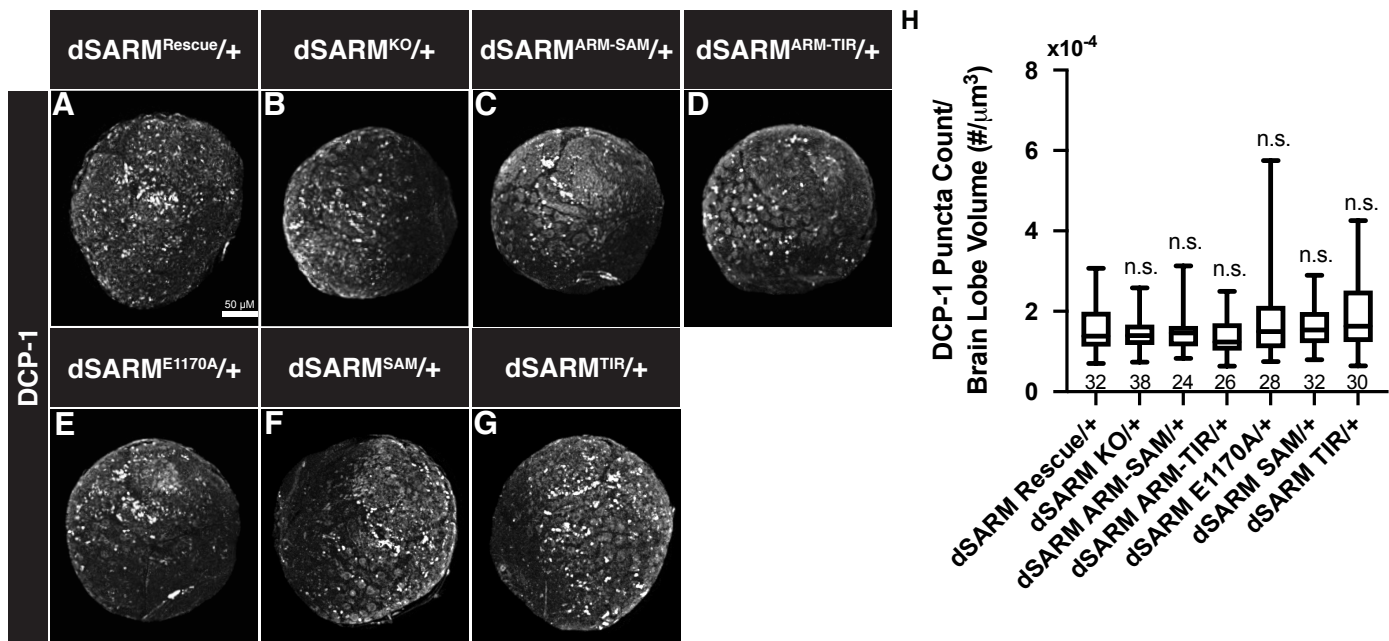
39. Coutinho-Budd JC, Sheehan AE, Freeman MR. The secreted neurotrophin Spätzle 3 promotes glial morphogenesis and supports neuronal survival and function. *Gene Dev.* 2017; 31: 2023–2038. <https://doi.org/10.1101/gad.305888.117> PMID: 29138279
40. Hawley RS, Gilliland WD. Sometimes the Result Is Not the Answer: The Truths and the Lies That Come From Using the Complementation Test. *Genetics.* 2006; 174: 5–15. <https://doi.org/10.1534/genetics.106.064550> PMID: 16988106
41. Freeman MR, Delrow J, Kim J, Johnson E, Doe CQ. Unwrapping Glial Biology. *Neuron.* 2003; 38: 567–580. [https://doi.org/10.1016/s0896-6273\(03\)00289-7](https://doi.org/10.1016/s0896-6273(03)00289-7) PMID: 12765609
42. Takeda K, Noguchi T, Naguro I, Ichijo H. Apoptosis Signal-Regulating Kinase 1 in Stress and Immune Response. *Annu Rev Pharmacol.* 2008; 48: 199–225. <https://doi.org/10.1146/annurev.pharmtox.48.113006.094606> PMID: 17883330
43. Kim DH, Feinbaum R, Alloing G, Emerson FE, Garsin DA, Inoue H, et al. A conserved p38 MAP kinase pathway in *Caenorhabditis elegans* innate immunity. *Sci New York N Y.* 2002; 297: 623–6. <https://doi.org/10.1126/science.1073759> PMID: 12142542
44. O'Neill LAJ, Bowie AG. The family of five: TIR-domain-containing adaptors in Toll-like receptor signaling. *Nat Rev Immunol.* 2007; 7: 353–364. <https://doi.org/10.1038/nri2079> PMID: 17457343
45. Ko KW, Devault L, Sasaki Y, Milbrandt J, DiAntonio A. Live imaging reveals the cellular events downstream of SARM1 activation. *Elife.* 2021; 10: e71148. <https://doi.org/10.7554/eLife.71148> PMID: 34779400
46. Golic KG, Lindquist S. The FLP recombinase of yeast catalyzes site-specific recombination in the *Drosophila* genome. *Cell.* 1989; 59: 499–509. [https://doi.org/10.1016/0092-8674\(89\)90033-0](https://doi.org/10.1016/0092-8674(89)90033-0) PMID: 2509077
47. Newsome TP, Asling B, Dickson BJ. Analysis of *Drosophila* photoreceptor axon guidance in eye-specific mosaics. *Development.* 2000; 127: 851–860. <https://doi.org/10.1242/dev.127.4.851> PMID: 10648243
48. Huang F, Dambly-Chaudière C, Ghysen A. The emergence of sense organs in the wing disc of *Drosophila*. *Dev Camb Engl.* 1991; 111: 1087–95. <https://doi.org/10.1242/dev.111.4.1087> PMID: 1879352
49. Geisler S, Huang SX, Strickland A, Doan RA, Summers DW, Mao X, et al. Gene therapy targeting SARM1 blocks pathological axon degeneration in mice. *J Exp Medicine.* 2019; 216: 294–303. <https://doi.org/10.1084/jem.20181040> PMID: 30642945
50. Toshniwal AG, Gupta S, Mandal L, Mandal S. ROS Inhibits Cell Growth by Regulating 4EBP and S6K, Independent of TOR, during Development. *Dev Cell.* 2019; 49: 473–489.e9. <https://doi.org/10.1016/j.devcel.2019.04.008> PMID: 31063760
51. Matsuzawa A, Saegusa K, Noguchi T, Sadamitsu C, Nishitoh H, Nagai S, et al. ROS-dependent activation of the TRAF6-ASK1-p38 pathway is selectively required for TLR4-mediated innate immunity. *Nat Immunol.* 2005; 6: 587–592. <https://doi.org/10.1038/ni1200> PMID: 15864310
52. Saitoh M, Nishitoh H, Fujii M, Takeda K, Tobiume K, Sawada Y, et al. Mammalian thioredoxin is a direct inhibitor of apoptosis signal-regulating kinase (ASK) 1. *Embo J.* 1998; 17: 2596–2606. <https://doi.org/10.1093/emboj/17.9.2596> PMID: 9564042
53. Guo X, Namekata K, Kimura A, Harada C, Harada T. ASK1 in neurodegeneration. *Adv Biological Regul.* 2017; 66: 63–71. <https://doi.org/10.1016/j.jbior.2017.08.003> PMID: 28882588
54. Gratz SJ, Rubinstein CD, Harrison MM, Wildonger J, O'Connor-Giles KM. CRISPR-Cas9 Genome Editing in *Drosophila*. *Curr Protoc Mol Biology.* 2015; 111: 31.2.1–31.2.20. <https://doi.org/10.1002/0471142727.mb3102s111> PMID: 26131852
55. MacDonald JM, Beach MG, Porpiglia E, Sheehan AE, Watts RJ, Freeman MR. The *Drosophila* Cell Corpse Engulfment Receptor Draper Mediates Glial Clearance of Severed Axons. *Neuron.* 2006; 50: 869–881. <https://doi.org/10.1016/j.neuron.2006.04.028> PMID: 16772169



S1 Fig. dSARM^{TIR} homozygous mutant OR22a axons exhibit timely degeneration following injury. (A,B) Representative z-projections of OR22a ORNs of the indicated genotypes labeled with anti-GFP at 12 Hours post injury (HPI). (C) Normalized mean axon intensity at 12 HPI: dSARM rescue: 0.80 ($n = 24$), dSARM^{TIR}: 0.56 ($n = 22$).



S2 Fig. Ask1 is not required for injury-induced axon degeneration. (A,B) Representative z-projections of OR22a ORNs of the indicated genotypes labeled with anti-GFP at 7 DPE, 1 DPI. (C) Normalized mean axon intensity at 1 DPI: wild type (FRT2A): 0.91, Ask1Δ6: 0.86, (D-F) Representative z-projections of OR22a ORNs of the indicated genotypes labeled with anti-GFP at 7 DPE, 1 DPI. (G) Normalized mean axon intensity at 1 DPI: wild type (FRT2A): 0.85 ($n = 35$); OR22a-Gal4, UAS-Ask1-Flag: 0.76 ($n = 24$); OR22a-Gal4, UAS-Ask1ΔN: 0.61 ($n = 26$). *n.s.*, not significant.

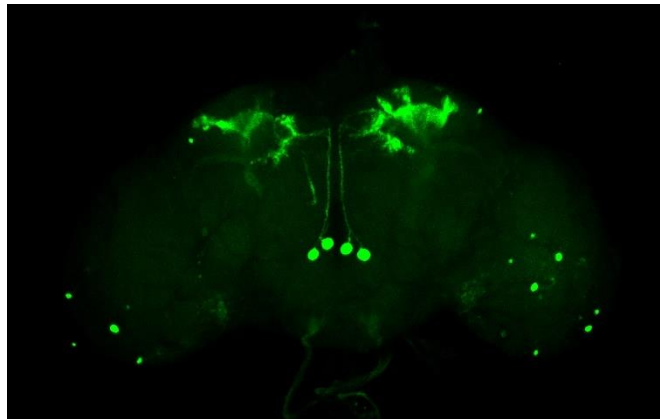


S3 Fig. dSARM alleles do not have dominant effects on Dcp-1 levels in the L3 brain.

(A-G) Representative z-projections of brain lobes of the indicated genotypes labeled with anti-Dcp-1. (H) Quantification of the number of Dcp-1 puncta normalized to brain lobe volume. Mean number of Dcp-1 puncta/brain lobe volume: dSARM^{Rescue}: 1.56×10^{-4} , dSARM^{KO}: 1.45×10^{-4} , dSARM^{ARM-SAM}: 1.53×10^{-4} , dSARM^{ARM-TIR}: 1.36×10^{-4} , dSARM^{E1170A}: 1.72×10^{-4} , dSARM^{SAM}: 1.60×10^{-4} , and dSARM^{TIR}: 1.89×10^{-4} . *n* values can be found on the graph. *n.s.*, not significant.

CHAPTER 6

Adaptive optics in single objective inclined light sheet microscopy enables three-dimensional localization microscopy in whole adult *Drosophila* brains



Mushroom body output neurons $\gamma 2\alpha'1$ expressing GFP in a *Drosophila* brain.

5.1 Summary of the results

In this study, Hung and colleagues combine sensorless adaptive optics (AO) with in-situ 3D-point spread function (PSF) calibration and single-objective lens-inclined light (SOLEIL) sheet microscope to mitigate deep tissue-induced deteriorations. It enables the use of three-dimensional localisation microscopy in whole adult *Drosophila* brains (C. Smith et al., 2022).

5.2 Personal contribution

In this study, I dissected, stained, and mounted *Drosophila* brains for three-dimensional localisation microscopy in deep tissue (C. Smith et al., 2022).



OPEN ACCESS

EDITED BY

Raphaël Turcotte,
Albert Einstein College of Medicine,
United States

REVIEWED BY

Jeongmin Kim,
Seoul National University, South Korea
Alexandra Fragola,
Sorbonne Universités, France

*CORRESPONDENCE

Carlas Smith
c.s.smith@tudelft.nl

SPECIALTY SECTION

This article was submitted to
Brain Imaging Methods,
a section of the journal
Frontiers in Neuroscience

RECEIVED 27 May 2022

ACCEPTED 01 September 2022

PUBLISHED 06 October 2022

CITATION

Hung S-T, Llobet Rosell A, Jurriens D,
Siemons M, Soloviev O, Kapitein LC,
Grußmayer K, Neukomm LJ,
Verhaegen M and Smith C (2022)
Adaptive optics in single objective
inclined light sheet microscopy
enables three-dimensional localization
microscopy in adult *Drosophila* brains.
Front. Neurosci. 16:954949.
doi: 10.3389/fnins.2022.954949

COPYRIGHT

© 2022 Hung, Llobet Rosell, Jurriens,
Siemons, Soloviev, Kapitein,
Grußmayer, Neukomm, Verhaegen
and Smith. This is an open-access
article distributed under the terms of
the [Creative Commons Attribution
License \(CC BY\)](https://creativecommons.org/licenses/by/4.0/). The use, distribution
or reproduction in other forums is
permitted, provided the original
author(s) and the copyright owner(s)
are credited and that the original
publication in this journal is cited, in
accordance with accepted academic
practice. No use, distribution or
reproduction is permitted which does
not comply with these terms.

Adaptive optics in single objective inclined light sheet microscopy enables three-dimensional localization microscopy in adult *Drosophila* brains

Shih-Te Hung¹, Arnau Llobet Rosell², Daphne Jurriens³,
Marijn Siemons³, Oleg Soloviev¹, Lukas C. Kapitein³,
Kristin Grußmayer⁴, Lukas J. Neukomm², Michel Verhaegen¹
and Carlas Smith^{1,5*}

¹Delft Center for Systems and Control, Delft University of Technology, Delft, Netherlands,

²Department of Fundamental Neurosciences, University of Lausanne, Lausanne, Switzerland, ³Cell Biology, Neurobiology and Biophysics, Department of Biology, Faculty of Science, Utrecht University, Utrecht, Netherlands, ⁴Department of Bionanoscience, Kavli Institute of Nanoscience Delft, Delft University of Technology, Delft, Netherlands, ⁵Department of Imaging Physics, Delft University of Technology, Delft, Netherlands

Single-molecule localization microscopy (SMLM) enables the high-resolution visualization of organelle structures and the precise localization of individual proteins. However, the expected resolution is not achieved in tissue as the imaging conditions deteriorate. Sample-induced aberrations distort the point spread function (PSF), and high background fluorescence decreases the localization precision. Here, we synergistically combine sensorless adaptive optics (AO), *in-situ* 3D-PSF calibration, and a single-objective lens inclined light sheet microscope (SOLEIL), termed (AO-SOLEIL), to mitigate deep tissue-induced deteriorations. We apply AO-SOLEIL on several dSTORM samples including brains of adult *Drosophila*. We observed a 2x improvement in the estimated axial localization precision with respect to widefield without aberration correction while we used synergistic solution. AO-SOLEIL enhances the overall imaging resolution and further facilitates the visualization of sub-cellular structures in tissue.

KEYWORDS

Super-resolution Microscopy, localization microscopy, adaptive optics, *Drosophila*, brain

1. Introduction

Single-molecule localization microscopy (SMLM) routinely surpasses the diffraction limit in thin samples (Lidke et al., 2005; Betzig et al., 2006; Hess et al., 2006; Egnér et al., 2007; Manley et al., 2008). This is achieved by estimating the position of the isolated fluorescence molecules with higher precision than the diffraction limit (Smith and Joseph, 2010). For example, SMLM revealed the periodic structure of actin

filaments in axons (Xu et al., 2012), and the distribution of β II spectrin in dendrites (Zhong et al., 2014) in cultured neurons. While these approaches uncover substantial cell-intrinsic details, the effects of extracellular components, such as the extracellular matrix (ECM), cannot be studied *in-vitro* (Kapałczyńska et al., 2016). The absence of the ECM can affect cellular morphology and gene/protein expression (Sanyal, 2017), revealing the limitations of imaging cultured cells. However, the application of SMLM inside *ex-vivo* tissue is also limited due to sample-induced aberrations and high fluorescent background. The refractive index mismatch between the immersion media and tissue induces (high-order) spherical aberrations (Booth and Wilson, 2001). This is particularly problematic for SMLM due to the use of a high NA oil immersion objective lens to optimize the emission fluorescence efficiency. Sample-induced aberrations distort the point spread function (PSF), which can result in artifact-containing reconstructions. Furthermore, imaging in tissue often increases background fluorescence, which results in a decrease in the localization precision (Smith and Joseph, 2010), and thus a decrease in the theoretical maximum spot detection efficiency (Smith et al., 2015). A decrease in the localization precision and the localization density ultimately results in a lower reconstruction resolution (Nieuwenhuizen et al., 2013). Thus, increased background fluorescence leads to a lower reconstruction resolution.

To decrease the background fluorescence, several optical sectioning methods were established, including highly inclined and laminated optical sheet (HILO) microscopy (Tokunaga et al., 2008), and variable-angle epi-fluorescence (VAEM) microscopy (Konopka and Bednarek, 2008) that adopt an inclined widefield illumination profile to achieve optical sectioning at a sub- $10\mu\text{m}$ level. However, the size of the field of view (FOV) is around tens of μm in HILO microscopy, which limits the application of HILO microscopy. Alternatively, selective plane illumination microscopy (SPIM) is widely used to achieve optical sectioning. SPIM relies on two orthogonal objectives, where one illuminates the sample while the other one collects the fluorescence (Ahrens et al., 2013; Lu et al., 2019). Tilted light-sheet microscopy (TILT3D) successfully utilizes a high detection NA objective by illuminating the sample with a tilted light sheet (Gustavsson et al., 2018) in combination with PSF engineering. However, the sample mounting is challenging with dual objective lens configurations because of the need for customized sample holders. Oblique plane microscopy (OPM) alleviates this drawback by the use of the objective for illumination and detection. Optical sectioning is achieved by illuminating the sample with an inclined light sheet. However, OPM requires multiple objective lenses downstream in the emission path to rotate the focal plane matching the inclined light-sheet illumination (Dunsby, 2008; Kumar and Kozorovitskiy, 2019, 2020; Yang et al., 2019; An et al., 2020; Sapoznik et al., 2020). Single objective lens inclined light sheet (SOLEIL) microscopy is based on an oblique light-sheet with

optimal optical sectioning (Hung et al., 2022). The focal plane is not re-positioned by additional objectives; a deformable mirror (DM) is used for PSF engineering instead. SOLEIL is therefore also compatible with 3D SMLM.

To avoid artifacts in SMLM reconstructions an accurate point spread function model (PSF) is needed (Babcock and Zhuang, 2017; Aristov et al., 2018; Li et al., 2018). To mitigate the effects from sample-induced aberrations both numerical (McGorty et al., 2014) and pre-calibration (Tafteh et al., 2015; Cabriel et al., 2018; Li et al., 2019) approaches have been used for modeling depth-dependent PSFs. Both approaches neglect sample-induced aberrations originating from biological variability. To accommodate for this higher order sample-induced aberrations, the PSF should be retrieved from *in-situ* data. The state-of-the-art for *in-situ* PSF calibration is INSPR (Xu et al., 2020).

Sample-induced aberrations deteriorate the localization precision (Młodzianoski et al., 2018). Therefore, in 3D SMLM, *in-situ* PSF calibration should be combined with active aberration correction. To accomplish sample-induced aberration correction, two distinct approaches have been adopted: the first is based on a wave-front sensor to measure sample-induced aberrations and a DM to compensate for the measured aberration (Park et al., 2021); the second on a sensorless approach (Burke et al., 2015; Tehrani et al., 2015; Młodzianoski et al., 2018; Siemons et al., 2021), where the aberrations are minimized by maximizing a metric for the image quality. Both algorithm and metric function should be tailored to an application to avoid non-convergent aberration corrections (Siemons et al., 2021) due to the non-convex dependency of the aberrations (Debarre et al., 2007; Soloviev, 2020).

To alleviate the difficulties of 3D SMLM in tissue we propose AO-SOLEIL, which combines adaptive optics, *in-situ* PSF calibration, and three-dimensional SOLEIL microscopy (Figure 1). We experimentally show the need for AO-SOLEIL as sample-induced aberrations deteriorate the axial localization precision and thereby prevent three-dimensional localization microscopy. To correct for sample-induced aberrations and enable 3D SMLM in tissue, we implemented sensorless adaptive optics combined with *in-situ* PSF calibration. We demonstrate the feasibility of AO-SOLEIL with several samples, including mitochondria in Caco2-BBE cells, and single neurons in the adult *Drosophila* brain. The results show that AO-SOLEIL facilitates the visualization of sub-cellular structures in tissue.

2. AO-SOLEIL

2.1. Principle of AO-SOLEIL

We proposed a synergistical approach (AO-SOLEIL) to optimize for three-dimensional SMLM in tissue. The AO-SOLEIL consists of two modules, SOLEIL illumination

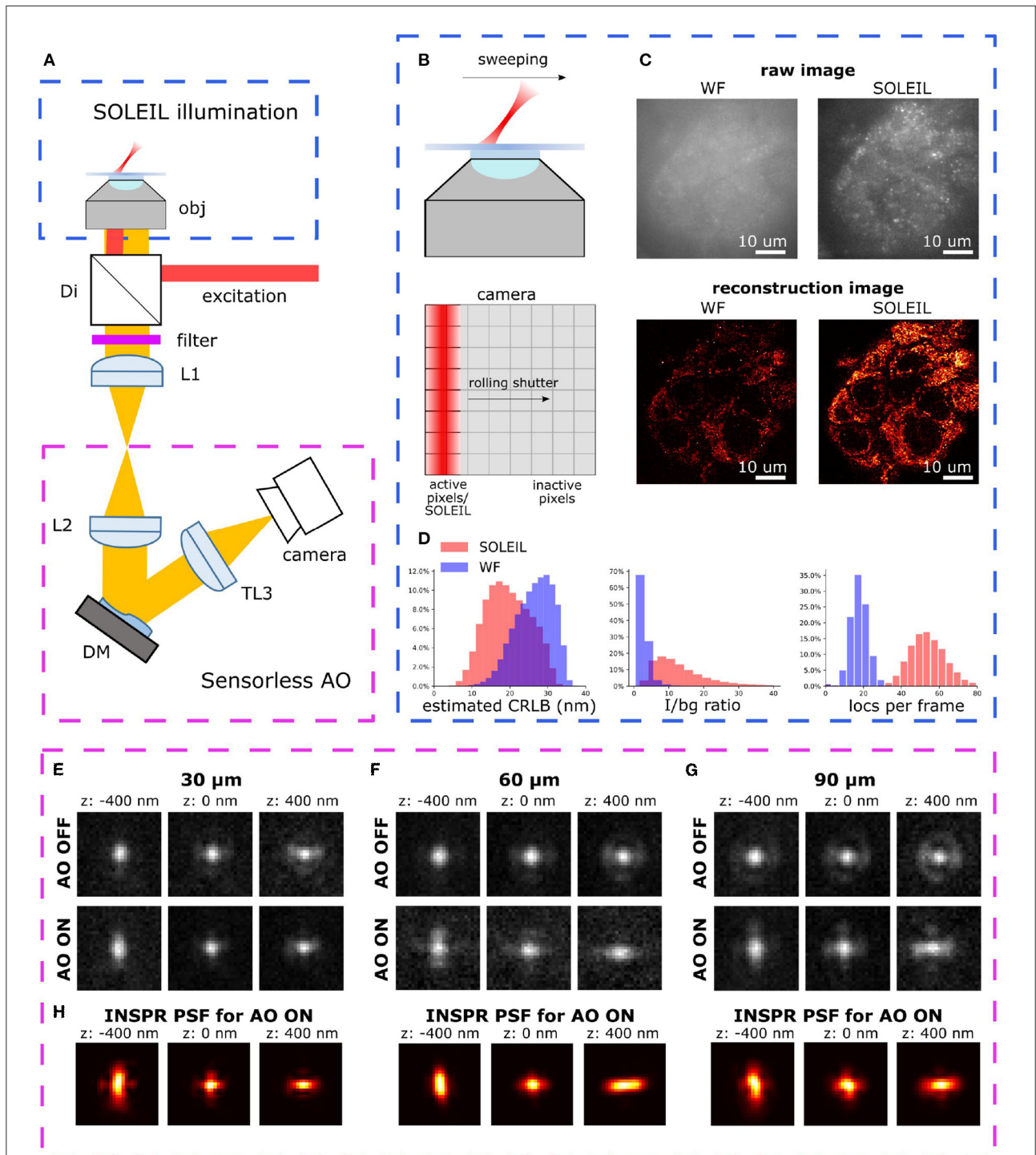


FIGURE 1

(A) Optical setup of AO-SOLEIL microscopy. obj: objective lens, Di: dichroic mirror, filter: emission filter, L1 to L3: achromatic doublet lens, DM: deformable mirror, camera: sCMOS camera. For the details of system, see [Supplementary Section 1](#). (B) Working principle of SOLEIL and camera readout. The camera readout is synchronized with the SOLEIL illumination area (red). The SOLEIL illumination is controlled by a galvo mirror. (C) Demonstration of SOLEIL background reduction (dSTORM) on spheroid Caco2-BBE cells (mitochondria). upper row: raw camera image by widefield and SOLEIL microscopy (equal contrast). lower row: SMLM reconstructions. (D) Comparison between WF and SOLEIL of estimated lateral CRLB, I/bg ratio, and number of localization per frame (loc per frame). (E–G) The astigmatism PSF before (AO OFF) and after (AO ON) AO correction at different imaging depth (30, 60, and 90 μ m). The PSFs were acquired by imaging 23 nm fluorescence beads (Thermo Fisher Scientific, Tetraspeck) embedded in 1% agarose gel. The emission wavelength is 680 nm. (H) The estimated *in-situ* PSF models using the INSPR algorithm.

and sensorless AO (Figure 1A). AO-SOLEIL adopts single objective lightsheet illumination (SOLEIL) for background rejection Hung et al. (2022). Here we synchronized the camera readout pixel and the SOLEIL illumination to expose the whole FOV on a same image frame (Figure 1B). The ability of background rejection is demonstrated by imaging spheroid Caco2-BBE sample, which is a 10 μm thick cell sample (Figures 1C,D). From the raw images, we observed that SOLEIL delivers a higher signal to background ratio (Figure 1C). Furthermore, the reconstruction image from SOLEIL microscopy shows more details than the reconstruction image from widefield microscopy (Figure 1C). We observed that the background rejection delivers a higher detection efficiency and an improved CRLB (Figure 1D). To restore the 3D PSF and improve the CRLB, the 7 Zernike modes ($Z_2^{\pm 2}$, $Z_3^{\pm 1}$, $Z_3^{\pm 3}$, Z_4^0) are corrected using the DM (Figures 1E–G). To enable unbiased estimation the 3D PSF model is estimated directly from the raw SMLM data (Figure 1H). For this *in-situ* PSF calibration we estimated up to the fifth radial order of Zernike modes using the INSPR algorithm (Xu et al., 2020).

We observed that we could restore the astigmatism PSF up to 90 μm depth (Figure 1H).

2.2. Sensorless AO algorithm

In this manuscript, we use a model-based wavefront sensorless approach for aberration correction. Namely, the aberration in the pupil is represented as a linear combination of the first 7 Zernike modes ($Z_2^{\pm 2}$, $Z_3^{\pm 1}$, $Z_3^{\pm 3}$, Z_4^0), and the indirect wavefront sensing is based on the widely accepted (e.g., Debarre et al., 2007; Žurauskas et al., 2019) Fourier annulus image quality metric.

The metric, defined by two radii r_1 and r_2 , is given by relative total energy of the image spatial frequencies \mathbf{m} in the annulus with inner and outer radii given by r_1 and r_2 . In practice, for a digital image $I[x, y]$ and its 2D discrete Fourier Transform $\hat{I}[m, n]$,

$$\hat{I}[m, n] = \mathcal{F}_2 I[x, y], \tag{1}$$

the metric $M(\hat{I}[m, n]) = M(\hat{I}[m, n]; r_1, r_2)$ is defined as

$$M(\hat{I}[m, n]) = \frac{\sum_{m,n} |\hat{I}[m, n]| \cdot w[m, n]}{\sum_{m,n} |\hat{I}[m, n]| \cdot u[m, n]}, \tag{2}$$

with binary masks w, u defined as

$$\begin{aligned} w[m, n] &= \begin{cases} 1, & r_1 < |\mathbf{m}| < r_2 \\ 0, & \text{else} \end{cases}, \\ u[m, n] &= \begin{cases} 1, & |\mathbf{m}| < R \\ 0, & \text{else} \end{cases}, \end{aligned} \tag{3}$$

where $|\mathbf{m}| = \sqrt{m^2 + n^2}$, and R is the radius corresponding to the diffraction-limited maximum spatial frequency. (For a camera with pixel size Δx and resolution $L \times L$, $R = \frac{NA}{\lambda} L \Delta x$.)

The idea is to discard the low spatial frequencies (background variations) and the high spatial frequencies (usually attributed to noise). Radii r_1, r_2 are often expressed in multiples of R (Mlodzianoski et al., 2018; Siemons et al., 2021).

In our work, to achieve sensorless AO correction of spherical aberration, we have used the previous published metric function with $r_1 = 0, r_2 = R/2$ (Mlodzianoski et al., 2018).

As the image I depends on the aberration, represented by its Zernike coefficients vector $\vec{\alpha}$, the metric $M(\hat{I}[m, n])$ is also a function of α , $M = M(\vec{\alpha})$. As the higher values of the metric correspond to a sharper image (Žurauskas et al., 2019), the aberration correction is equivalent to the optimisation problem

$$\hat{\alpha} = \arg \max_{\vec{\alpha}} M(\vec{\alpha}). \tag{4}$$

The optimisation is performed independently for each of the Zernike modes used to control the DM. To this end, for each of the modes we acquired 11 images with the mode amplitude values varying uniformly in the range $[-\lambda/2, \lambda/2]$ and computing the image metric for each of the images. Previously it has been shown that a minimum of $2N + 1$ of measurements are needed for correcting N Zernike modes with sensorless AO correction (Debarre et al., 2007; Žurauskas et al., 2019). With more advanced algorithm, $N+1$ measurements are also possible to achieve AO correction (Antonello et al., 2012; Booth, 2006). In our experiments a minimum of 11 measurement steps are needed to mitigate a high fluorescence background and sparse images (Figure 9).

The correction point for each mode was determined by fitting the metric value points with a Gaussian function $G(M)$ and taking its central point. Namely, with $G(M)$ defined as

$$G(M) = ae^{-\frac{(M-c)^2}{\sigma^2}} + bg, \tag{5}$$

where M is the metric value, a is the amplitude of Gaussian function, σ is the width of Gaussian function, c is the center of Gaussian function, which is the value for aberration correction, and bg is the background of the metric value curve. The optimal value $\hat{\alpha}_i$ for the current mode is c .

We used bounded non-linear least squares to fit the amplitude term a , center c , width σ , and background bg . Based on the design of the metric function, we know the best aberration correction happens at the peak of the metric value curve, so the amplitude term must be positive. The boundary condition of amplitude term is $0 < a < \infty$. The fitting procedure is done by using the *curve fit* function in the Scipy library (version 3.8). We corrected the spherical aberration first and then we corrected the other first order aberrations. In our samples we mainly observed spherical aberration because of refractive index mismatch. Therefore, first two iterations were performed to correct for the spherical aberration (Z_4^0). Subsequently, to

correct for the other aberrations ($Z_2^{\pm 2}, Z_3^{\pm 1}, Z_3^{\pm 3}$) one iteration were done for each mode. In total, the aberration correction uses 88 frames, which is a small fraction in typical dSTORM imaging (10,000 ~ 30,000 frames).

2.3. Defocus compensation for spherical aberration correction

Zernike polynomials, although orthogonal in the phase of the pupil plane, do not guarantee the absence of cross-talk in the optimisation procedure described in the previous subsection. That means that by maximising $M(\vec{\alpha})$ moving along one of the modes, we might move out of the maximum value for the other modes. Different techniques are known to deal with this effect, finding their principles in Gram-Schmidt orthogonalization (Debarre et al., 2007; Soloviev, 2020). In this work, we propose the following simple procedure to establish and to compensate for the major cross-talk effect in our setup, that is between the defocus and spherical aberration terms (Figure 2).

To compensate for the axial defocus that is caused by a DM when correcting for spherical aberrations a calibration is made (Młodzianoski et al., 2018). To create this calibration the defocus offset was measured by imaging fluorescent beads (23 nm; embedded in 1% agarose) on a 2D surface, which means the fluorescence beads only appear at a certain axial plane. This was done as follows: a certain amount of spherical aberration is introduced on the DM. This shifted the focal plane and we then applied a defocus aberration to re-focus the bead images. To determine the amount of defocus for the re-focusing we used the same metric function as for sensorless AO. This procedure was repeated for a different amounts of spherical aberration. Finally, a linear function was fitted by minimizing the mean square error (Figure 2B), which was used as the calibration:

$$\Delta Z_2^0 = \beta \cdot Z_4^0, \quad (6)$$

where Z_2^0, Z_4^0 are defocus and spherical Zernike mode, respectively, ΔZ_2^0 is the defocus aberration, and β is the coupling coefficient, which in our system is 0.00371 $\mu\text{m}/\text{nm}$.

2.4. Impact of AO correction on INSPR PSF model and axial localization precision

To validate the synergy between our sensorless AO algorithm and the INSPR algorithm for improving the axial CRLB, we imaged homogeneously embedded beads (23 nm) in 1% agarose (>100 μm). Firstly, we performed AO correction to minimize the sample-induced aberration. We call this procedure AO ON and without this procedure AO OFF. Then, we introduced an astigmatism aberration with the DM to generate an astigmatism-based PSF for 3D localization. To estimate the *in-situ* PSF, INSPR algorithm needs multiple single-molecules

at different axial positions to build a model (Figures 3A–C) (Xu et al., 2020). To estimate the *in-situ* PSF model with the INSPR algorithm we acquired data by moving the piezo stage in discrete steps (100 nm) along an axial and lateral dimension (2 μm). In Figures 3D–F, we show the theoretical axial CRLB and in Figures 3G–J we show the axial CRLB estimated from the localizations. We found that this synergetic combination of AO correction and INSPR can improve the axial CRLB. However, this effect is not observed in lateral CRLB (Supplementary Figure S2).

2.5. Validation of sensorless AO in combination with *in-situ* PSF calibration

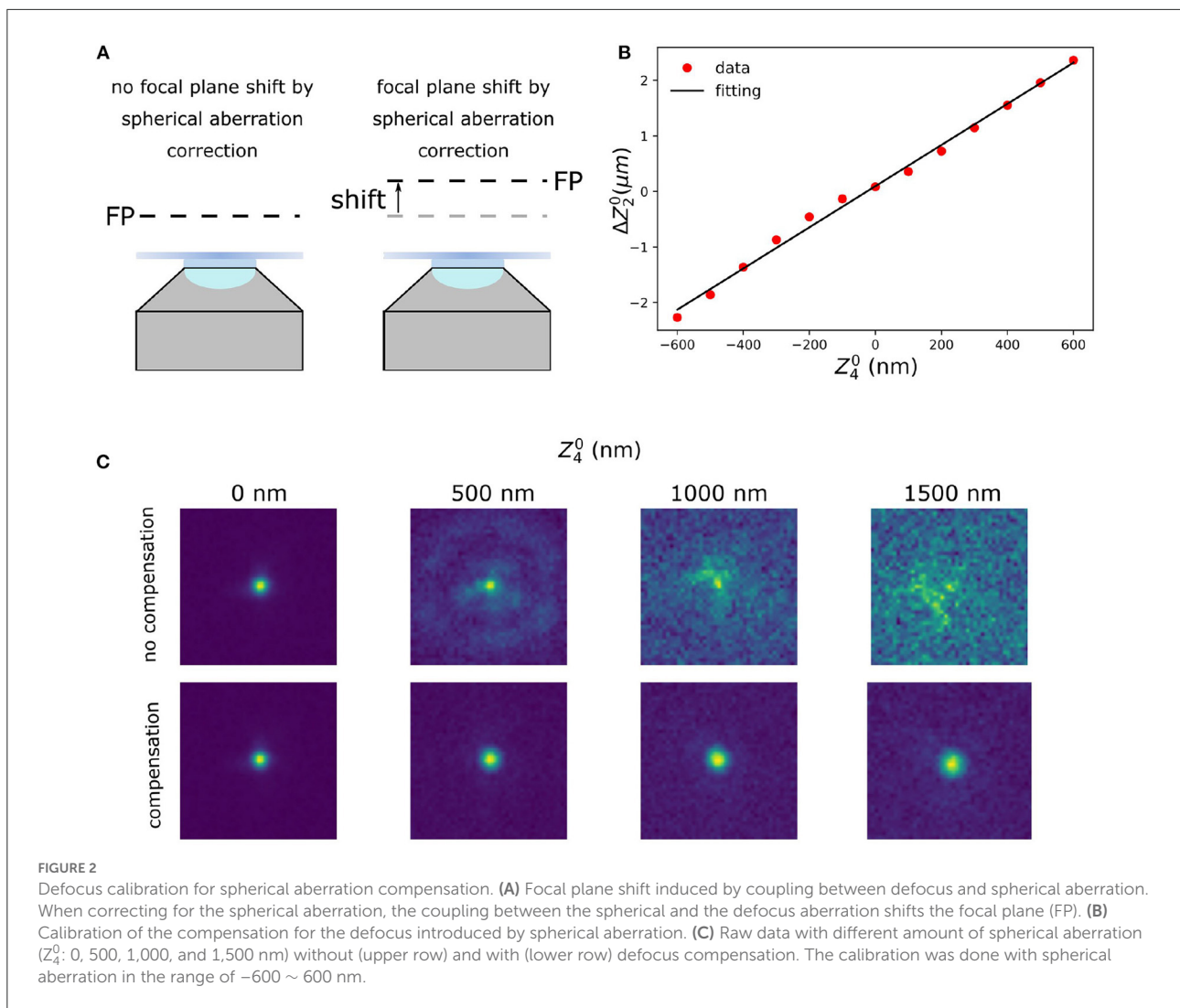
We used active aberration correction to correct the first 7 Zernike modes. Subsequently, *in-situ* PSF calibration (INSPR) was used to calibrate the 3D PSF model (INSPR PSF). To analyze the synergy between aberration correction and *in-situ* PSF calibration, we performed *in-silico* experiments (Figures 4–6). We used the SDS simulator (details of SDS simulator is in Supplementary Section 2) mentioned above to simulate blinking images in the presence of aberrations. To mimic the high aberration situation, we simulated PSFs (see Section 7) by randomly assigning 150 m λ Zernike aberrations uniformly distributed over the first 17 Zernike modes ($Z_2^{\pm 2}, Z_3^{\pm 3, \pm 1}, Z_4^{\pm 4, \pm 2, 0}, Z_5^{\pm 5, \pm 3, \pm 1}$) excluding the piston, tip, tilt, and defocus aberrations. Spherical aberration (220 m λ) was added to mimic the refractive index mismatch between oil immersion and tissue. We term this set of Zernike aberrations as the initial i.e. AO OFF aberration. Then, combining with the SDS, we used the proposed sensorless AO algorithm to correct the 7 Zernike modes ($Z_2^{\pm 2}, Z_3^{\pm 1}, Z_3^{\pm 3}, Z_4^0$). In this step, we input the Zernike aberrations into the SDS and generated images with aberrated blinking single-molecules. Based on this, we can investigate the performance of the proposed sensorless AO algorithm *in-silico*.

To enable the 3D localization of single-molecules an astigmatic PSF was chosen. This PSF was created by adding 100 m λ astigmatism aberration (Z_2^2). To estimate the *in-situ* PSF, we simulated 1,000 frames of blinking images (intensity: 2,000 photons, background: 30 photons/pixel) with the initial aberration (AO OFF) and the final aberration after correction (AO ON) (Figures 4A,B). The ground truth PSFs were computed based on the true initial (AO OFF) and final aberration (AO ON) (Figure 4C).

The χ^2 value was used to compare and evaluate the accuracy of the PSF models (Siemons et al., 2018).

$$\chi^2 = \sum_{i=1}^K \frac{(n_i - u_i(\hat{\theta}))^2}{u_i} \quad (7)$$

$$u_i(\hat{\theta}) = \hat{\theta}_I \cdot \text{PSF}_i(\hat{\theta}_x, \hat{\theta}_y, \hat{\theta}_z) + \hat{\theta}_{bg} \quad (8)$$



where K is the number of pixels of the region of interest, n_i is the photon count of the data at the i^{th} pixel, u_i is the photon count in i^{th} pixel, $PSF_i(\hat{\theta}_x, \hat{\theta}_y, \hat{\theta}_z)$ is the 3D PSF model in i^{th} pixel, $\hat{\theta}$ is the vector with the estimates containing the estimands $\theta_x, \theta_y, \theta_z, \theta_I, \theta_{bg}$. These correspond to the x, y, z position, emitter intensity, and the emitter background, respectively. To calculate $u_i(\hat{\theta})$, the $\hat{\theta}$ is obtained using maximum likelihood estimation (Smith and Joseph, 2010).

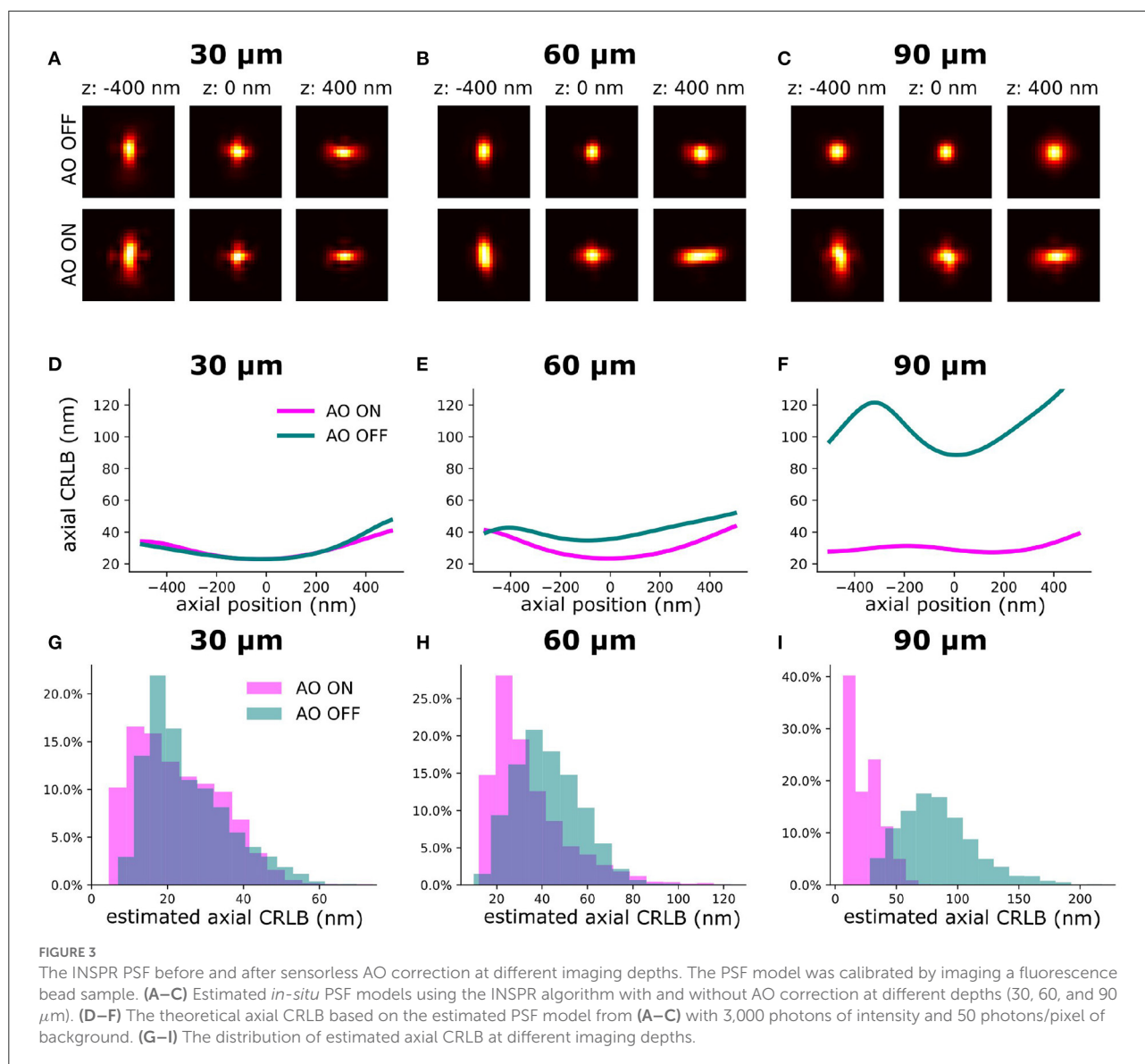
For Poissonian distributed measurement the expected χ^2 value ($E[\chi^2]$) and the variance of χ^2 value ($var[\chi^2]$) can be expressed as following:

$$E[\chi^2] = K \tag{9}$$

$$var[\chi^2] = 2K + \sum_{i=1}^K \frac{1}{u_i} \tag{10}$$

The above equation delivers a statistical way to determine whether the PSF model is accurate and when it's not. The PSF is statistically different (not accurate) from the data when the χ^2 value is larger than the expected χ^2 value plus its standard deviation. The χ^2 was computed based on Equation (8). In Figures 4D,E, the expected χ^2 value of the estimated PSF models vs. intensity are shown. The curve of estimated PSF models are computed by keeping the estimated PSF model constant and generating 51 independent noise realizations (Equation 8). We observed that the χ^2 value increases with increasing intensity (Figures 4D,E). We observed that the INSPR PSF estimated model without AO was statistically different at 1500 photons. The INSPR PSF estimated model with AO was statistically different until 3,000 photons.

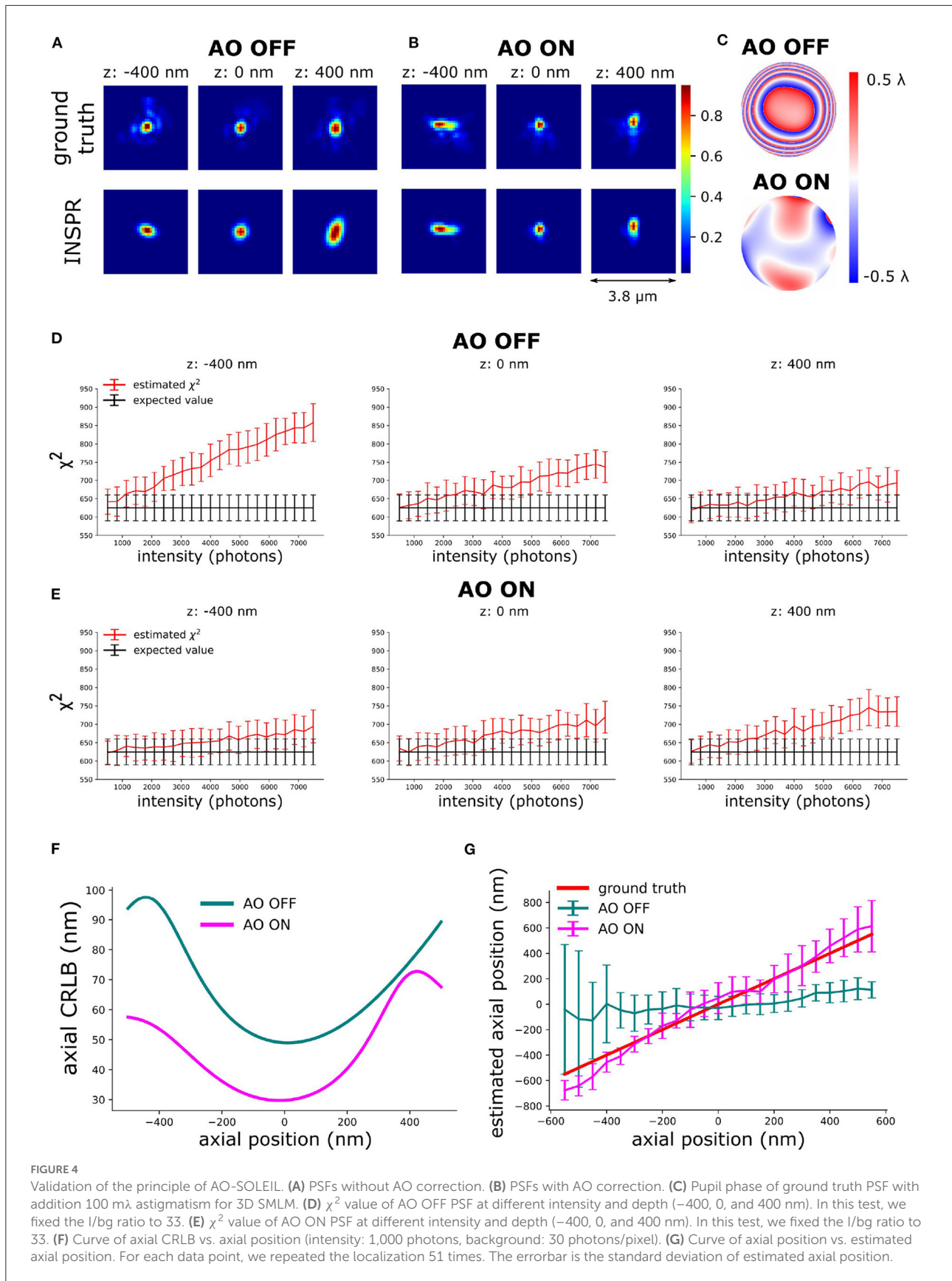
In Figure 4F, we calculated the theoretical axial CRLB over different axial positions and we observed the improvement of theoretical axial CRLB with AO correction over without AO



correction. We observed a 200% improvement of the axial CRLB. Furthermore, the impact of a model mismatch between the estimated and the ground truth PSF was analyzed by calculating the estimation bias in the z direction (Figure 4G). To do this we generated the raw SMLM images with 1,000 photons and background 30 photons/pixel. The reason for choosing 1,000 photons intensity is to make sure the INSPR model is not statistically different from ground truth PSF model and 30 photons/pixel background is to match with the I/bg ratio of 33.33 in χ^2 -test (Figure 4). The INSPR PSF model obtained from INSPR was used for the localization. Figure 4G shows the estimated axial position vs. the ground truth axial position. We observed that the estimated axial position is strongly biased without AO. With AO correction the bias is significantly reduced. The ground z position is within the standard deviation

of estimated axial position up to ± 400 nm. To visualize the impact of the improvement of the CRLB and reduction of the bias raw SMLM data of a 3D ring was simulated. In the 3D ring test, we simulated the 3D PSF blinking spots along the 3D ring structure with the ground truth PSF models and used INSPR PSF model for localization. The reconstructions are shown in Figure 5. We found that in the AO OFF situation the reconstruction has completely failed. This result aligns with the observation in Figure 4G, which is the strong axial position bias occurs in AO OFF model. This result again justifies our motivation to combine AO correction and INSPR method.

To analyze the use of *in-situ* PSF calibration and not use the pre-calibrated cubic spline (cspline) PSF (Babcock and Zhuang, 2017; Li et al., 2018), we performed an *in-silico* experiment (Figure 6). In this experiment, we have the PSFs after AO



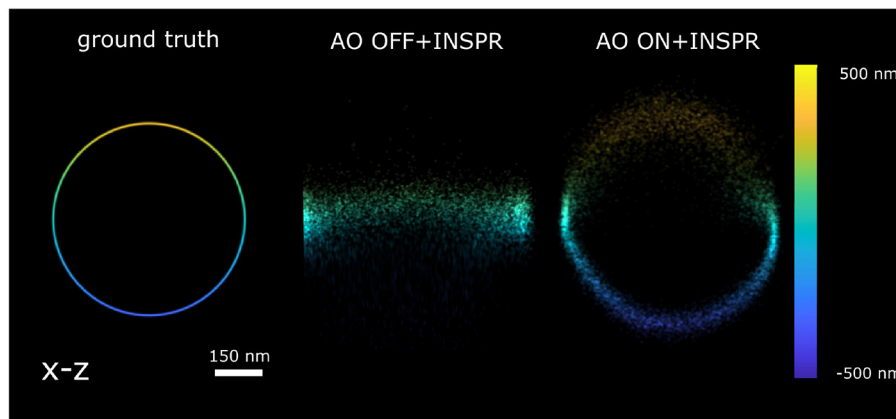


FIGURE 5

Reconstruction x-z cross-section of the 3D ring localized by AO OFF and AO ON INSPR PSF model. ground truth: the x-z view of 3D ring. AO OFF+INSPR: the reconstruction image without AO correction, but *in-situ* PSF estimated using the INSPR algorithm. AO ON+INSPR: the reconstruction image with AO and the *in-situ* PSF estimated using the INSPR algorithm.

correction in Figure 4B and we also have the PSF model calibrated by INSPR. In addition, to mimic a pre-calibrated PSF model from a thin sample with fluorescence beads we simulated astigmatism PSF only with 100 mλ astigmatism aberration (Z_2^2) and without other aberrations and did a cspline calibration with Super-resolution Microscopy Analysis Platform (SMAP, EMBL Heidelberg) (Ries, 2020) (Figure 6A). In Figure 6B, we show the axial localization bias using INSPR PSF model and cspline PSF model. We observed a strong axial bias from the cspline PSF model. In Figure 6C, we show the χ^2 value of cspline and INSPR model, which suggests that a pre-calibrated cspline method is not accurate in tissue SMLM imaging.

3. Methods

3.1. Initial aberration correction of the system

To compensate for the aberrations introduced by the DM and the static aberrations of the microscope we acquired PSFs by imaging single 23 nm beads embedded in 1% agarose. Here, because our input image is small and contains only a single PSF, we don't need to use the extended image quality metric from the previous section, but can just minimize the mean width of the PSF by adopting a second moment metric function:

$$M_{\text{sec}} = \frac{\sum_{i=1}^N \sum_{j=1}^N I(i, j) \cdot [(i - c_x)^2 + (j - c_y)^2]}{\sum_{i=1}^N \sum_{j=1}^N I(i, j)}, \quad (11)$$

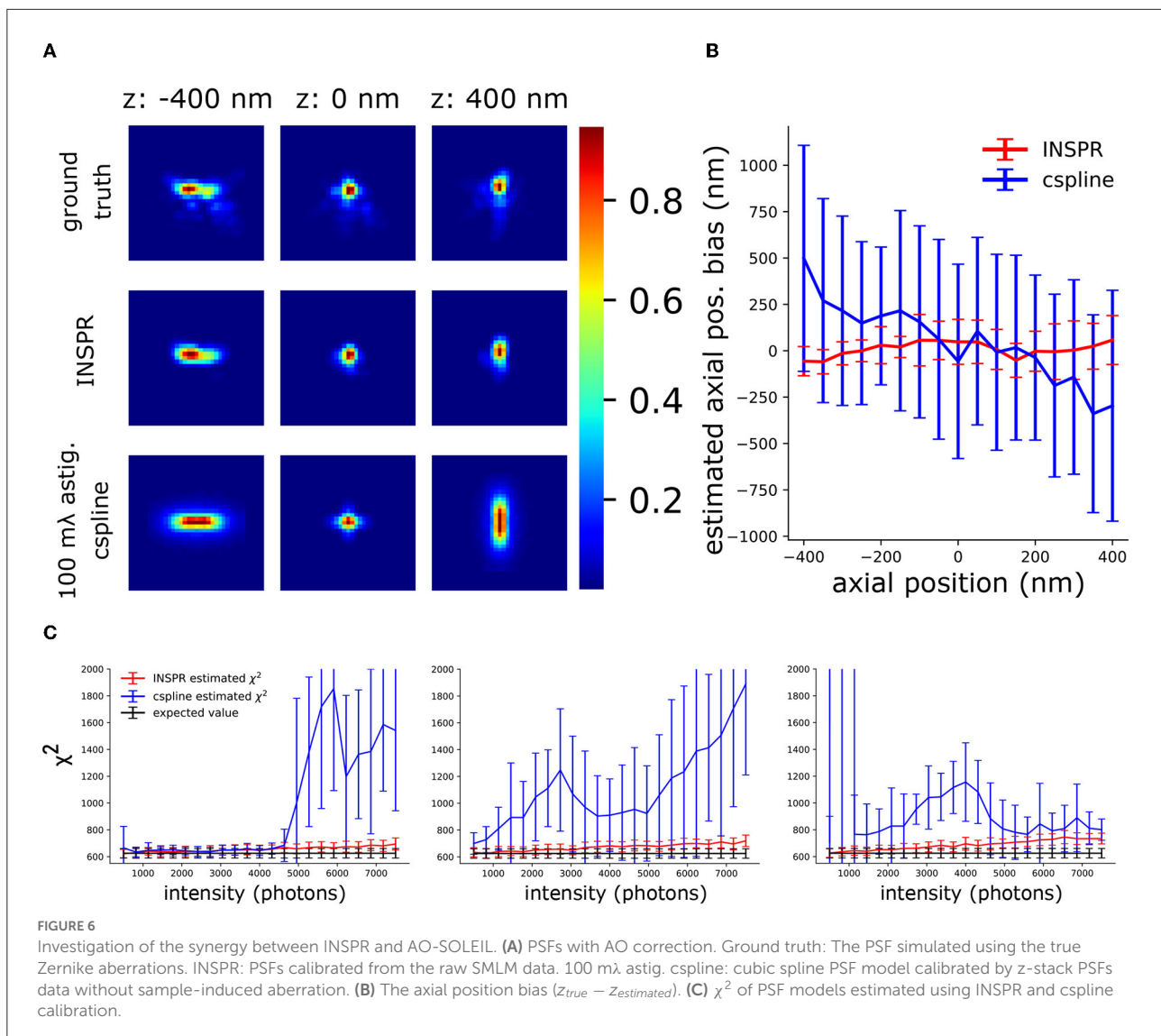
where M_{sec} is the second moment of single PSF, $I(i, j)$ is the pixel value at row i and column j of the acquired image, c_x and c_y are the center of mass of $I(i, j)$, and N is both the width and height of the camera image in pixels. In our experiment, we chose N

as 21 pixels. The metric is minimized by use of the adaptive Nelder-Mead algorithm from the Scipy library (version 1.7.3) for 3,000 iterations with 30 ms of exposure time for each frame. This minimization is not performed in the Zernike basis, but in that of the deformable mirror control voltages, because it leads to more robust performance when strong aberration present in the system (Siemons et al., 2021). In principle, maximum intensity or sharpness metric functions can also be adopted as metric function to minimize the system aberration (Olivier et al., 2009; Linhai and Rao, 2011). However, these metric functions are more susceptible to the photo-bleaching making them unsuited for our application.

3.2. Data acquisition for sensorless AO-SOLEIL microscopy

To reduce the imaging background the sample was pre-bleached for 30–60 s. The pre-bleaching was done while moving the piezo stage (Smartact; x,y an SLC1730; z an SLC1720) through the targeted axial area. Sensorless AO was subsequently performed on this desired 3D FOV while illuminating the sample with widefield illumination (integration time 30 ms).

After AO correction, first the widefield SMLM acquisition was finished and subsequently the SOLEIL benchmark. This order may potentially decrease the quality of SOLEIL imaging including the estimated CRLB and number of localizations per frame because of photo-bleaching. However, in all imaging, we still observe the improvement of SOLEIL microscopy over widefield microscopy. The SOLEIL acquisition deviates from the previous published work (Hung et al., 2022). In this work, the galvo mirror continuously translated the SOLEIL illumination from the top to the bottom of the FOV. To



enable a virtual confocal readout (Baumgart and Kubitschek, 2012; Chakraborty et al., 2020) we used a rolling shutter by activating the Andor SOLIS LightScan PLUS function, see Supplementary Section 9. This allowed us to synchronize the rolling shutter readout of the camera to be synchronized with the light sheet illumination. To synchronize the rolling shutter and SOLEIL illumination, the camera trigger mode was set to external trigger and the camera and galvo mirror were controlled by an Arduino micro-controller.

3.3. Cell culture

3.3.1. Caco2-BBE cells for artificial multilayer sample

Caco2-BBE cells (a gift from S.C.D. van IJzendoorn, University Medical Center Groningen, the Netherlands) were

maintained in DMEM supplemented with 9% FBS (fetal bovine serum), 50 $\mu\text{g}/\mu\text{l}$ penicillin/streptomycin and 2 mM L-glutamine at 37°C and 5% CO₂. Cells were seeded on 18 mm coverslips at a density of $1 \cdot 10^5/\text{cm}^2$ and cultured for 10–12 days to allow for spontaneous polarization and brush border formation. The monolayer of cells was fixed with 4% paraformaldehyde (PFA) in phosphate-buffered saline (PBS) for 10 min, washed with PBS (3×5 min), permeabilized with 0.5% Triton X-100 in miliQ water for 15 min, washed with PBS (3×5 min) and blocked with 3% BSA in PBS for at least 1 h. Cells were incubated overnight at 4°C with a primary antibody against ezrin (mouse, BD Biosciences, 610602, dilution 1:500) from now referred to as ezrin labeled cells. After washing in PBS (3×5 min), the cells were incubated with secondary antibody [goat, anti-Mouse IgG (H+L), Alexa Fluor 647 (Life Technologies, dilution 1:500)] for 1 h at room temperature (RT) and washed with PBS.

3.3.2. Caco2-BBE cells for spheroid sample

To create a more three-dimensional culture a monolayer of Caco2-BBE cells, similar as is mentioned above, was perturbed by forcibly pipetting the culturing medium over the cells. The resulting cell clumps were cultured in suspension for an additional 3 days to allow for the formation of spheroid like structures. Spheroids were fixed with 4% PFA and 4% sucrose in PBS for 15 min, washed with PBS (3×5 min), permeabilized with 0.5% Triton X-100 in miliQ water for 30 min, washed with PBS (3×5 min) and blocked with 3% BSA in PBS for at least 1 h. Cells were incubated overnight at 4°C with a primary antibody against cytochrome C (mouse, BD Biosciences, 556432, dilution 1:500) from now on referred to as mitochondria labeled cells. After washing in PBS (3×5 min), the cells were incubated with secondary antibody [goat, anti-Mouse IgG (H+L), Alexa Fluor 647 (Life Technologies, dilution 1:500)] for 3 h at RT and washed with PBS.

3.3.3. Preparation of *Drosophila* brains

Flies (*Drosophila melanogaster*) were kept on Nutri-Fly Bloomington Formulation with dry yeast at 20°C. Males and females were used as no gender-specific differences were observed. Genotypes used: *10xUAS-IVS-mCD8::GFP / +* ; *MB077c-Gal4 / +* (control) and *10xUAS-IVS-mCD8::GFP / 10xUAS-myr::4xSNAPf; MB077c-Gal4 / +* (experiment). Adult flies were aged at 20°C for 5–7 days before performing brain dissection (Paglione et al., 2020). Brain dissections were performed as described (Paglione et al., 2020). Briefly, decapitated heads were fixed in 4% formaldehyde (47608-250ML-F, Sigma-Aldrich) in PTX (0.1% Triton X-100 (T9284, Sigma-Aldrich) in PBS) for 20 min, and washed 3×10 min with PTX. Brain dissections were performed in PTX, and dissected brains were fixed in 4% formaldehyde in PTX for 10 min, followed by 3×10 min washes with PTX. Brains were incubated with SNAP-Surface Alexa Fluor 647 (Inc. S9136S, New England Biolabs) at a concentration of 0.0625 μ M with rotation for 15 min at RT. Brains were washed 3×10 min with PTX, and subsequently PTX was completely removed and 200 μ L PBS was added.

3.4. Sample preparation and mounting

3.4.1. Preparation of the large fluorescence bead sample

We prepared a glass slide with four strips of double sided tape arranged on the four sides of a rectangle. After that, 1% agarose solution was prepared by adding 100 mg of agarose powder (BP160-100, Thermo Fisher Scientific, Waltham MA, U.S.A.) to 10 mL of PBS buffer followed by 20 min stirring with a magnetic stirrer at 100°C. Then, we prepared a 1:10,000 diluted fluorescence bead stock (Tetraspeck, Thermo Fisher

Scientific) with 1% agarose solution. We quickly mixed the diluted fluorescence bead stock with the agarose solution and added 200 μ L of mixture in the middle of double sided tape. Before the agarose gel became solid, a #1.5 coverslip was mounted on the glass slide attaching the double sided tape. Then, we used nail polish to seal the coverslip. The final thickness of the sample is about 120 μ m.

3.4.2. Spheroid Caco2-BBE cell dSTORM sample

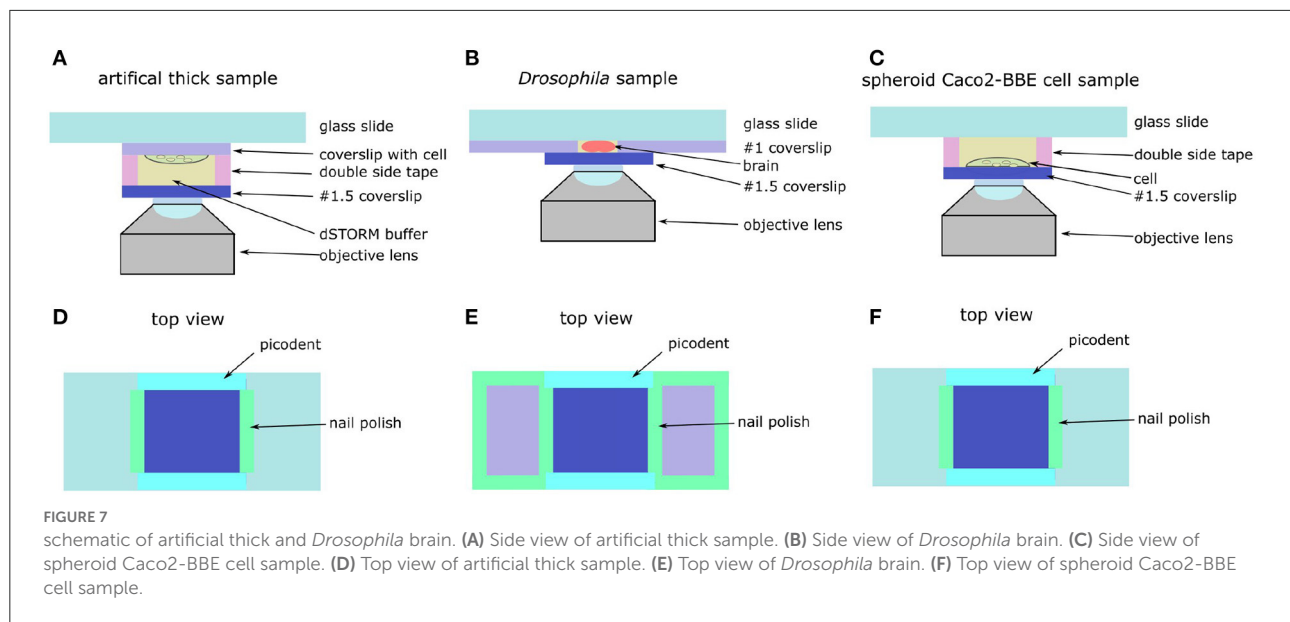
Firstly, we put two strips of double sided tape on a glass slide (MS10UW, Thorlabs) as spacer (Figure 7C). The spheroid Caco2-BBE cell was stored in PBS in Eppendorf tube. We picked up the spheroid Caco2-BBE cell from the Eppendorf tube by pipette and put the cell on a #1.5 coverslip (CG00C2, Thorlabs). Then, 20 μ l of 1% agarose (BP160-100, Thermo Fisher Scientific, Waltham MA, U.S.A.) diluted by PBS was added to stabilize the cell. Before the agarose became solid, the coverslip with the cell was mounted on a glass slide attached with the double sided tape. Then, we used nail polish to seal the edge between the coverslip and the double sided tape. After the nail polish was dry, we added the dSTORM buffer into the chamber and used two-component gel (Picodent, Wipperfurth) to seal the front and backside of the coverslip (Figure 7F).

3.4.3. Artificial Caco2-BBE cell dSTORM sample

A coverslip with Caco2-BBE cell adhered on the microscopy glass slides with double sided tape (Figure 7A). Another coverslip was attached to the cell coverslip with 65 μ m thick double sided tape (details of sample mounting is in Supplementary Figure S3). The thickness of double sided tape was measured by using a homemade setup (Supplementary Figure S4). The left and right sides of the coverslip were sealed by using nail polish and the front and backside of the coverslip were sealed by using the two-component gel. Compared with the original sample, the artificial Caco2-BBE sample had an additional 65 μ m deep buffer layer, which introduced an additional 0.38 λ spherical aberration estimated based on the equation in Booth and Wilson (2001).

3.4.4. Fluorescently labeled single neurons in *Drosophila* brains for dSTORM imaging

Drosophila brains were mounted in glass slides as previously described in Kelly et al. (2017). The dissected brains were stored in PBS buffer at 4°C in 1.5 mL tubes until ready to be mounted. Then, we glued two #0 coverslips (CG00C2, Thorlabs) on a glass slide (MS10UW, Thorlabs) by using nail polish (Figure 7E). The distance between the two coverslips was around 5 mm. A pipette was used to pick up a brain from Eppendorf tube and put the brain on the glass slide between the two #0 coverslips. Then, the



brain was placed in the correct orientation with the help of a 20X magnification (LCAch N 20X, Olympus) stereo microscope (NAME NUMBER). Then, we added 10 μl of 1% agarose diluted in PBS on the brain. Before the agarose became solid, a #1.5 coverslip was mounted on the brain and attached to the #1 coverslips. The left and right sides of the coverslip were sealed with nail polish and the front and backside were sealed by using two-component gel (Figure 7D).

3.4.5. Preparation of dSTORM buffer

In this research, we used oxygen scavenger buffer (Glox-buffer). We prepared a glucose stock solution (300 mM glucose, 50 mM Tris, 10 mM NaCl dissolved in Milli-Q H₂O) and stored it at 4°. The final concentration of each ingredients are 1.25 mg/ml catalase (Sigma, C40-100MG), 1 mg/ml glucose-oxidase (Sigma, G2133-10KU), and 50~150 mM MEA (Sigma, 30070-10G) diluted in glucose stock. We adjusted the blinking density by adjusting the concentration of MEA.

3.5. SMLM data analysis

To perform 2D localization, drift correction, filtering, and visualization, we used Super-resolution Microscopy Analysis Platform (SMAP) (Ries, 2020). We used maximum likelihood estimation (MLE) with a 2D Gaussian PSF model for the estimation. The estimands are the position, intensity, background counts, and the width of the Gaussian PSF model.

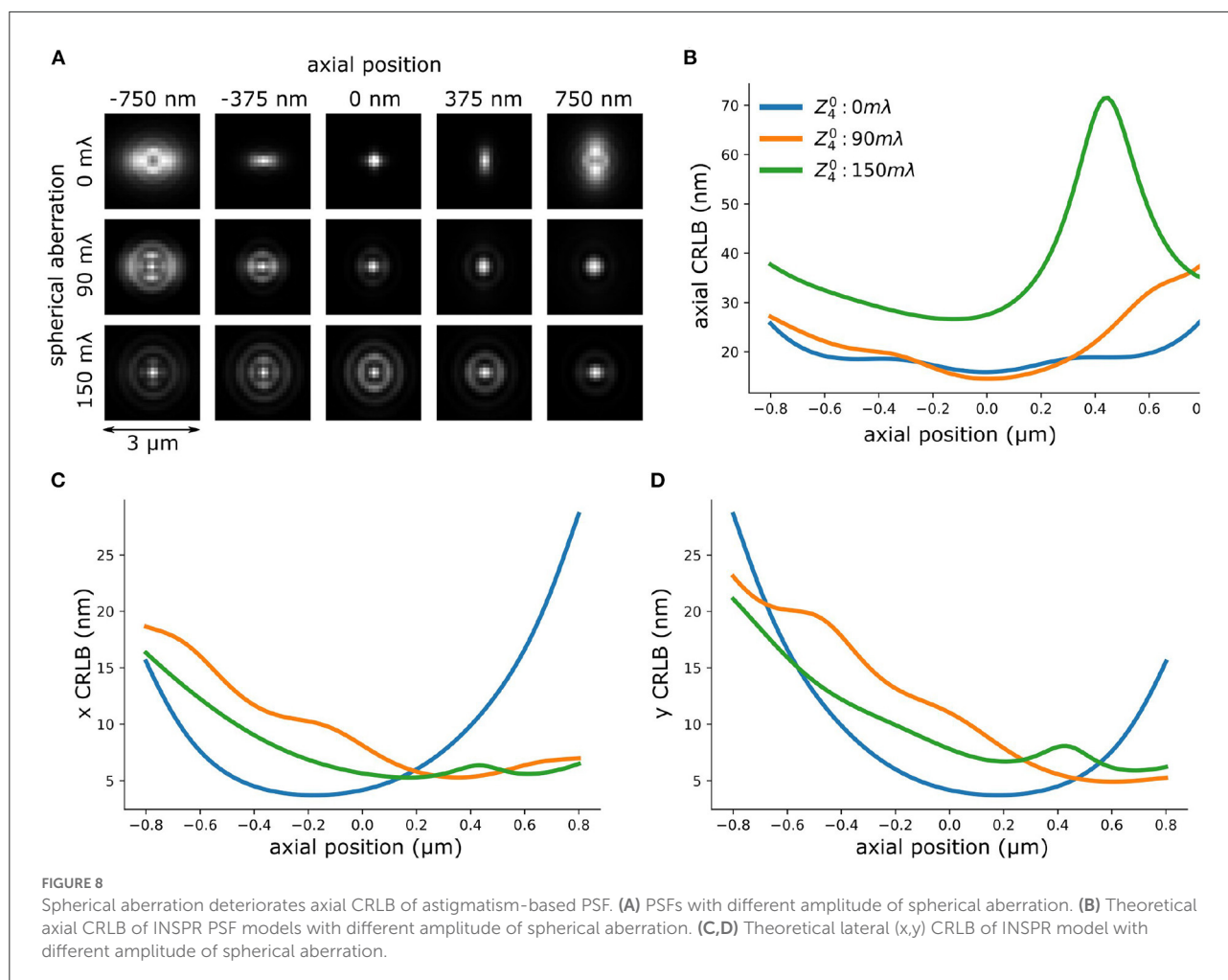
To perform 3D PSF calibration, localization, and drift correction, we used the INSPR algorithm (Xu et al., 2020) to

build the PSF and to localize the single molecules. The region of interest (ROI) of the PSF was 27 pixels which correspond to 2.92 μm . To calibrate the PSF with INSPR only the first 36 Zernike basis functions were considered. The 3D reconstruction was made with SMAP.

4. Results

4.1. Impact of spherical aberration on the three-dimensional localization precision

To investigate the performance of the INSPR algorithm when spherical aberration presents in the PSF model we performed a set of *in-silico* experiments. We simulated vectorial PSFs with varying spherical aberrations (0 ~ 150 m λ) (Figure 8A) (Siemons et al., 2018). The details of the PSF simulation is in Supplementary Section 2. Then, we used the INSPR algorithm to calibrate the PSF model. The *in-situ* calibrated PSF model was used for computing the CRLB. We observed that an increased spherical aberration gradually reduces the ellipticity of astigmatism-based PSF gradually, which reduces the ability to localize in three dimensions. This is inline with previous reported observations (Siemons et al., 2020). We observed in simulation that spherical aberration deteriorates the axial CRLB (Figure 8B), but not the lateral CRLB (Figures 8C,D). This *in-silico* observation aligns with our experimental observation (Figure 8 and Supplementary Figure S2). To investigate if this observation is dependent on the algorithm that was used for PSF calibration, we repeated the same simulation using cubic splines (Supplementary Figure S5) (Babcock and Zhuang, 2017; Li et al.,



2018). We observed a deteriorated axial CRLB when spherical aberration presents in the PSF.

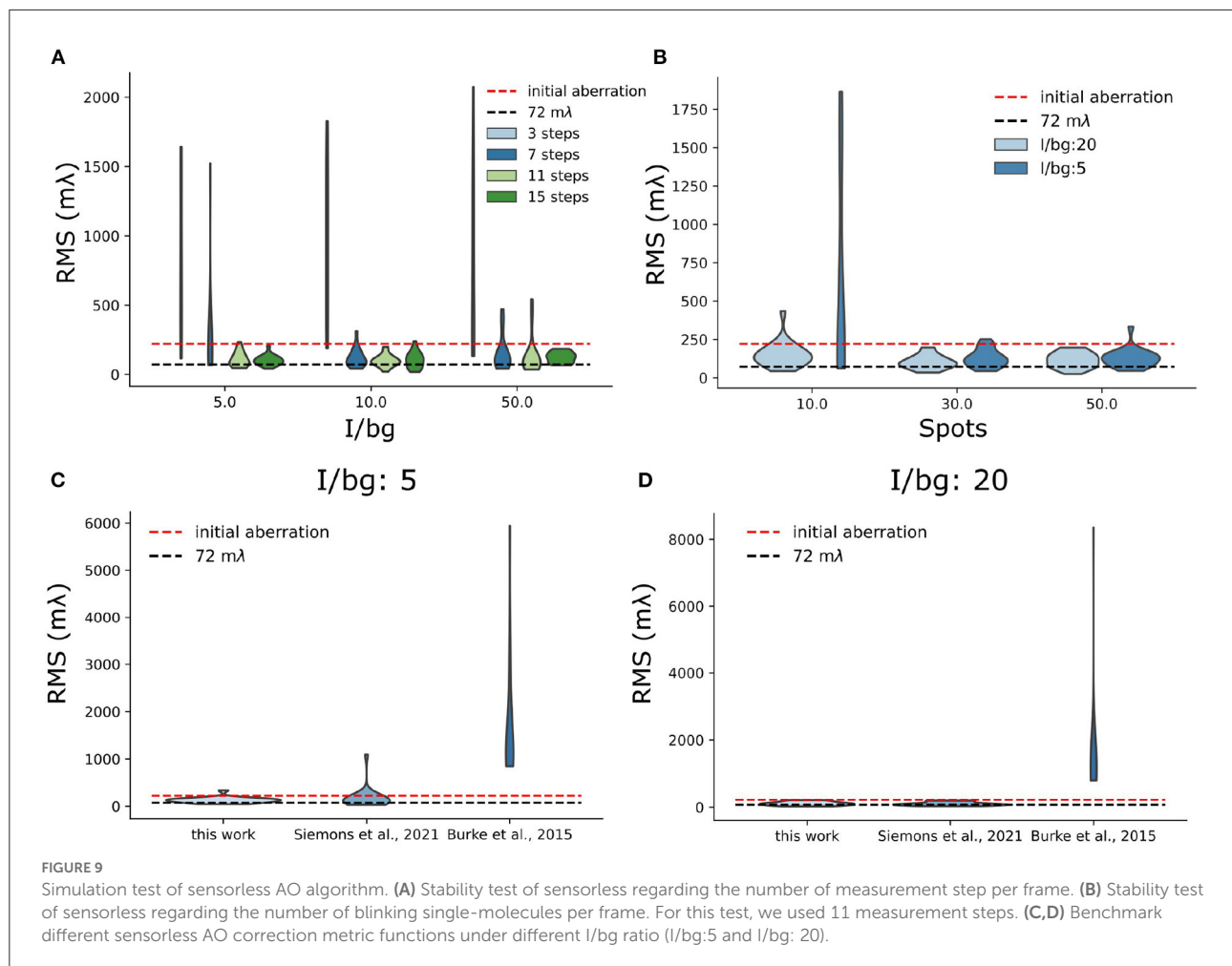
4.2. Sensorless AO performance and benchmark

In this section, we analyze and benchmark the performance of sensorless AO algorithms *in-silico* based on SDS simulator (details of SDS simulator is in [Supplementary Section 2](#)).

In the *in-silico* experiments, we focused on two aspects of sensorless AO algorithm: the number of measurements needed and the sparsity of the acquired images. We found that the number of measurement steps is important for a robust sensorless AO correction. In previous research ([Debarre et al., 2007](#)), it was found that in theory 3 measurement steps for correcting a Zernike mode are sufficient. Less measurements can be expected by using more advanced algorithms ([Booth, 2006](#)). However, in [Figure 9A](#), we found that 7 measurement

steps are the minimal number of measurement steps for stable AO correction in low background situations (I/bg is 10 and 50). We think the reason is that the sparse blinking of localization microscopy images delivers a weak signal in Fourier space, which increases the noise in OTF-based metric functions. For high background situations (I/bg ratio is 5), 11 steps can be more stable than 7 steps. Nevertheless, we didn't observe significant improvement between the result between 11 and 15 measurement steps.

We also observed that the stability of the sensorless AO algorithm depends on the number of blinking single-molecules. In [Figure 9B](#), we investigated the sensorless AO algorithm with different number of blinking spots per frame (10, 30, and 50). The size of each frame is $30 \mu\text{m} \times 30 \mu\text{m}$. The pixel size is 108.33 nm, which is same as our system. In this experiment, we chose the I/bg ratio as 20 and the intensity of each blinking single molecules as 2,000 photons. The initial aberrations were uniformly assigned to the 7 Zernike modes, which is the number of modes that we correct in this research.



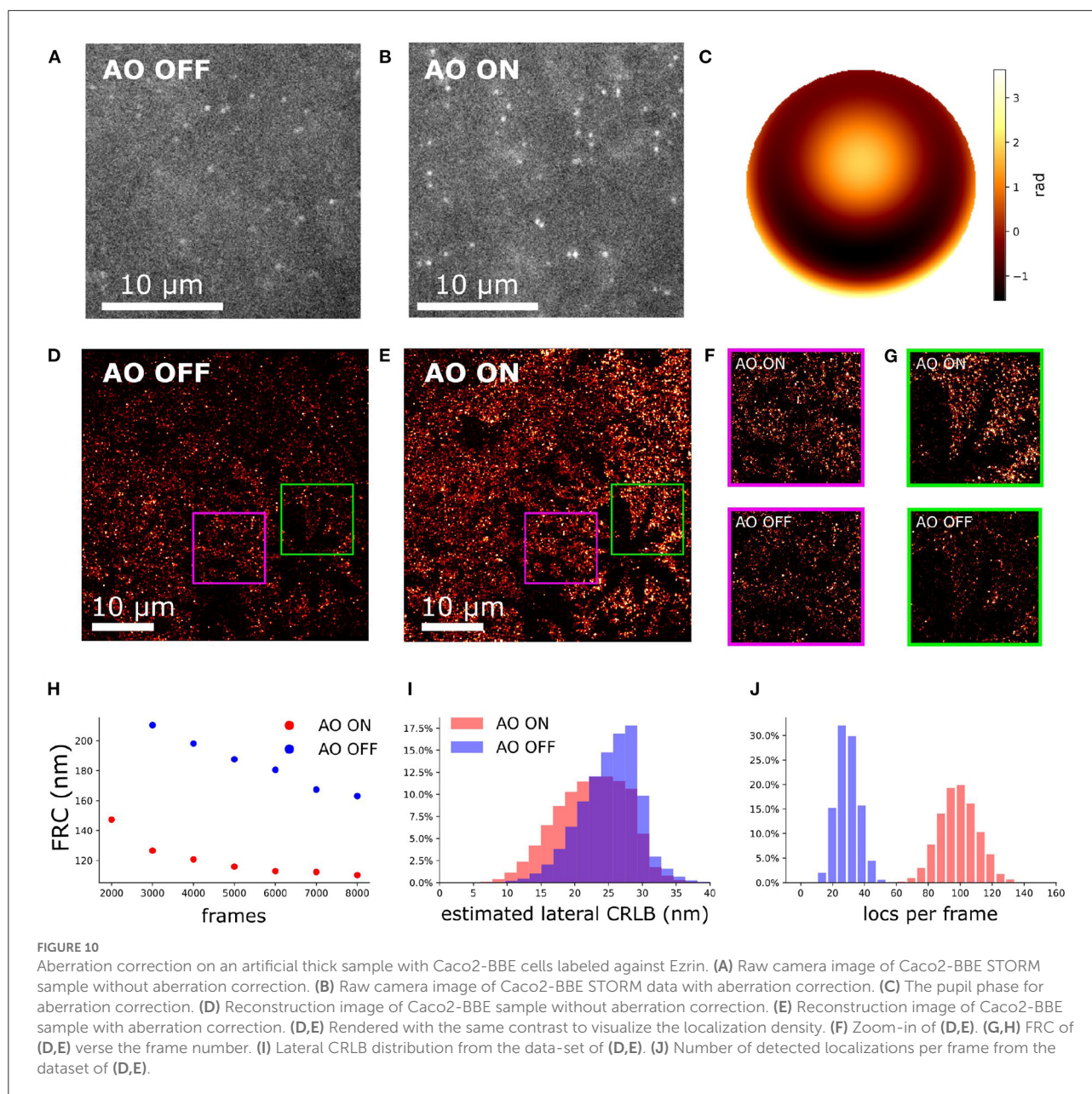
We scaled the initial aberration to be 220 m λ (RMS value). For AO correction we used 11 measurement steps. To investigate the robustness of the approach the experiment was repeated 20 times and we tested low and high background situations corresponding to the I/bg is 20 and 5, respectively. In Figure 9B, we observed that when the number of blinking single-molecules is lower than 30 single-molecules/frame, the sensorless AO correction is likely to become unstable. The high background situation can further deteriorate the result (Figure 9B). We didn't observe significant improvement of the result between 30 single-molecules per frame and 50 single-molecules per frame. In the real experiment, we control the concentration of MEA to adjust the number of blinking. However, it should be noted that in SMLM there is a limit to the number of single-molecules that can be on, because the sparsity of single-molecule is used to achieve the resolution improvement in SMLM.

In addition, we also benchmark our metric with other metric functions used in localization microscopy (Burke et al., 2015; Siemons et al., 2021) (Figures 9C,D). We

found comparing with other metric functions, the proposed metric in this work is more stable in high background situation (I/bg: 5), which suggests it is more stable when performing sensorless AO in tissue imaging (Figure 9C). Nevertheless, in low background situation (I/bg: 20), we didn't observe improvement over REALM (Siemons et al., 2021) (Figure 9D).

4.3. 2D SMLM of Erzin in an artificial thick sample with Caco2-BBE cells

To investigate the performance of our AO in a controlled environment we created an artificial thick sample. To create a predominantly spherical aberration we added a 65 μm thick STORM buffer layer to the Caco2-BBE cell. The Caco2-cells with labeled Erzin to perform dSTORM was at the top of the sandwich (Supplementary Figure S3). This design introduced an additional 380 m λ spherical aberration. The correction enhances the sharpness of PSF (Figures 10A,B) and



improved the estimated localization precision estimation (Figure 10I) and detection efficiency (Figure 10J). The correction phase is shown Figure 10C. This hypothesis was confirmed by simulation (Supplementary Figure S6). The corresponding reconstructions show a better contrast with correction than without correction (Figures 10D–G). A quantitative comparison of the localizations shows a three times higher detection efficiency (Figure 10J), a 12% improvement in CRLB (Figure 10I) and a 45% improvement in Fourier Ring Correlation (FRC) (Figure 10H) (Nieuwenhuizen et al., 2013).

4.4. 2D SMLM of mitochondria in spheroid Caco2-BBE cells

To investigate the performance of the sample-induced aberration correction algorithm we imaged spheroid Caco2-BBE cells at a depth of 17 μm using widefield microscopy (exposure time of 30 ms). The reconstruction images with and without AO correction are shown in Figures 11A,B. For 2D SMLM we observed that the spot detection efficiency was improved by 30% with correction (Figure 11E) and ultimately the FRC resolution (Nieuwenhuizen et al., 2013) was improved by 11%

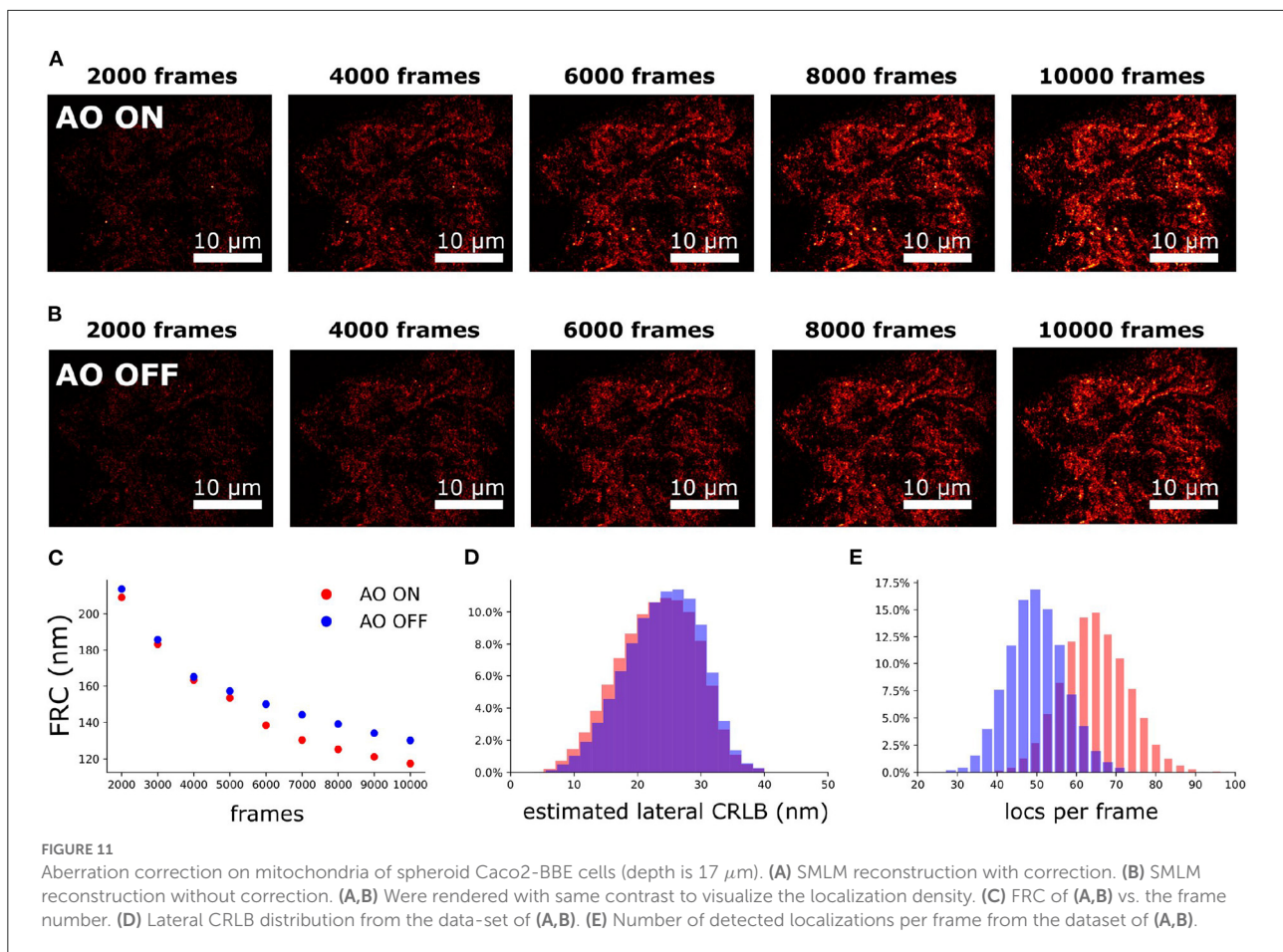


(Figure 11C). The median estimated lateral CRLB is improved by 1 nm with correction (Figure 11D).

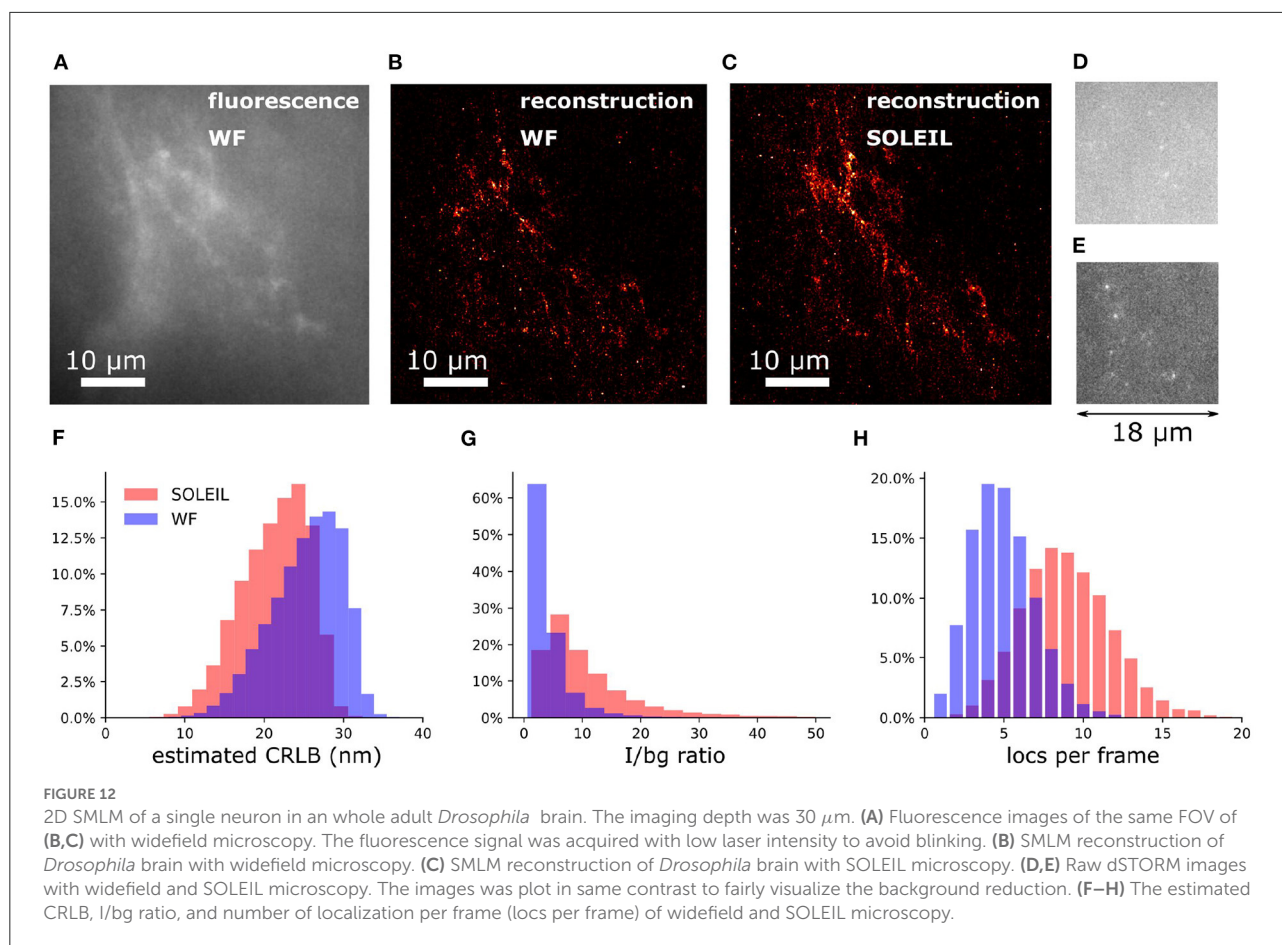
4.5. 2D SMLM of a single neuron in an adult *Drosophila* brain

To demonstrate our methodology in deep tissue, we imaged a single neuron in the brain of adult *Drosophila melanogaster*. We observed that the background in the brain tissue was significantly high, which demonstrates the importance of the optical sectioning delivered by SOLEIL (Figures 12D,E). The fluorescent signal from the expression of membrane-associated protein (myr-SNAP) under control of MB077c-Gal4 were acquired (Figure 12C) and corresponding SMLM reconstructions were made (Figures 12A,B). The quantitative comparison between SOLEIL and widefield microscopy revealed significant statistical improvements (Figures 12F–H). For SOLEIL microscopy, the median value of estimated CRLB was 21.8 nm and for WF microscopy, the median value of estimated CRLB was 25.8 nm. The median

I/bg ratio from WF microscopy was 2.97 and the median I/bg ratio from SOLEIL microscopy was 8.21, which is a 276% improvement. The number of localizations per frame was increased by around 200% when SOLEIL microscopy was used for imaging.

4.6. 3D SMLM of a single neuron in adult *Drosophila* brains

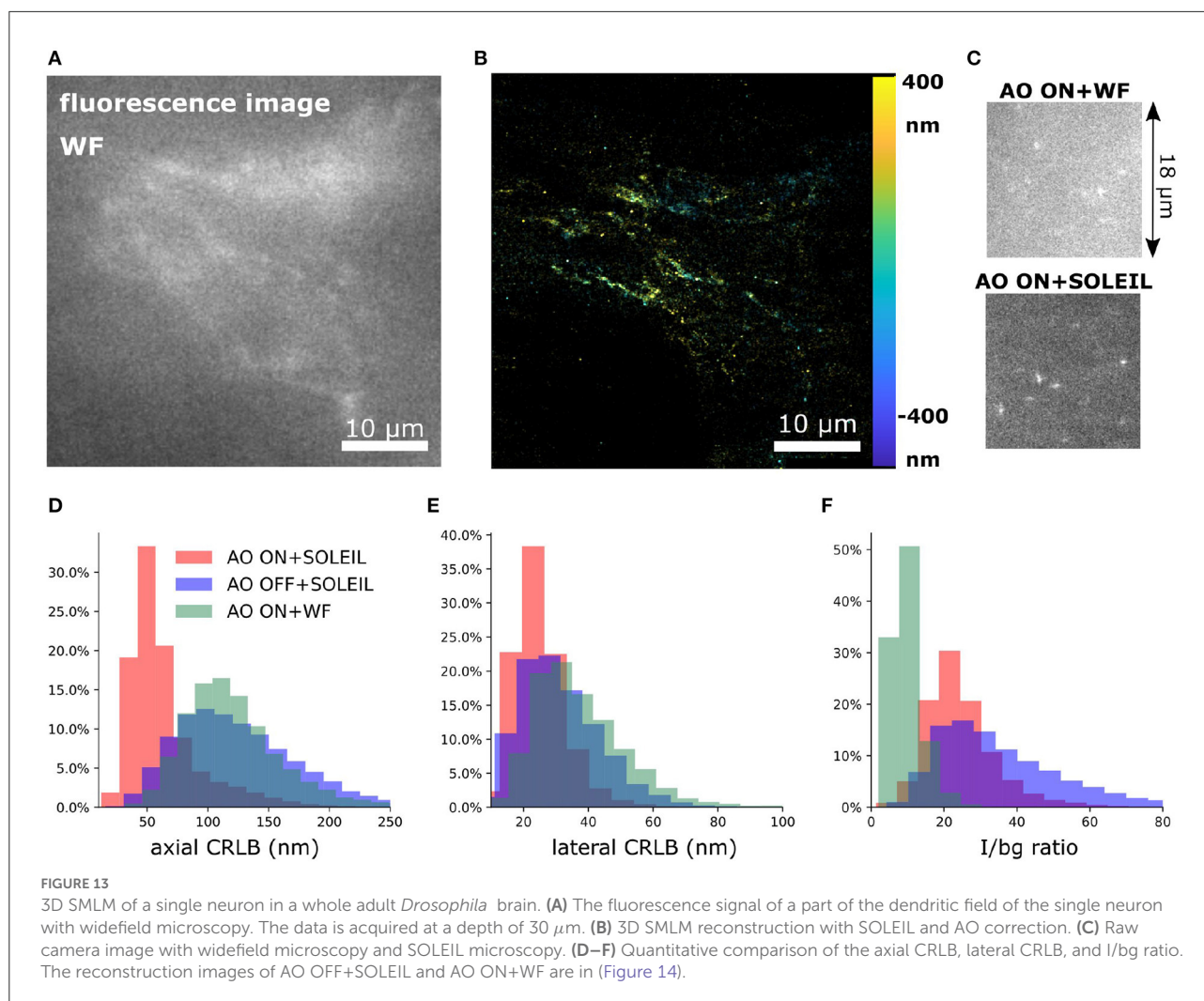
To perform 3D SMLM in adult *Drosophila* brains, we combined SOLEIL illumination, sensorless AO correction, and *in-situ* PSF calibration. SOLEIL microscopy resulted in a significant background reduction (Figures 13A,C). To demonstrate the importance of AO correction and SOLEIL illumination, three different situations were benchmarked: AO correction with SOLEIL microscopy (AO ON+SOLEIL), SOLEIL microscopy alone (AO OFF+SOLEIL), and AO correction with widefield microscopy (AO ON+WF) (Figures 13B, 14). The need for AO correction and the use of SOLEIL microscopy was evident from visual inspection



of the corresponding reconstructions (Figures 13B, 14). The quantitative comparison between the three different situations also demonstrated several statistical improvements. The median axial CRLB value was improved by about 200 % (54.5, 115.7 and 114.1 nm; AO ON+SOLEIL, AO OFF+SOLEIL and AO ON+WF, respectively), suggesting that both AO correction and SOLEIL illumination are necessary for acquiring high-resolution 3D reconstruction image in *Drosophila* brains. The median lateral CRLB value was also slightly decreased (23.8, 29.3, and 34.7 nm; AO ON+SOLEIL, AO OFF+SOLEIL, and AO ON+WF, respectively). Lastly, the median value of the I/bg ratios were 22.95, 34.7, and 8.9 (AO ON+SOLEIL, AO OFF+SOLEIL, and AO ON+WF, respectively). These data suggest that AO-SOLEIL delivers an improvement for in tissue SMLM. In (Figure 14), we show the SMLM reconstruction with AO OFF+SOLEIL and AO OFF+WF. In the axial cross-section with AO ON+SOLEIL, we observed more fine structures while in the axial cross-sections with other two imaging conditions this is not visible.

5. Discussion and conclusion

In this work, to mitigate the sample-induced aberrations and high background effects when imaging thick samples, we synergetically combined sensorless adaptive optics (AO), *in-situ* 3D-PSF calibration, and a single-objective lens inclined light sheet microscope (SOLEIL) into a new methodology (AO-SOLEIL). We have demonstrated that SOLEIL can reject the out-of-focus fluorescence and thereby increase the I/bg ratio, localization precision, and number of detected spots per frame (Figures 1B–D). SOLEIL does not need a customized sample holder and only uses a single objective lens in the whole system thereby it is easier to cooperate adaptive optics element in the emission path. This feature makes the system accessible to non-expert users. We analyzed the benefit of aberration correction for 2D and 3D SMLM. In 2D SMLM, aberration correction can sharpen the PSF, which delivers better FRC resolution and more single-molecules can be detected (Figure 10). In 3D SMLM, we experimentally demonstrated that



aberration correction can improve the axial CRLB (Figures 3, 13). A pitfall of using sensorless AO on three-dimensional structures is that the focal plane shifts during the correction of spherical aberration. This effect is predominant with the cross-talk between defocus and spherical aberration. To compensate for the induced defocus aberration and minimize the shift of the focal plane during the sensorless AO correction this cross-talk is calibrated (Figure 2).

We experimentally verified the improvement of our sensorless AO approach by imaging thick fluorescence bead sample (Figure 3). We demonstrated that sample-induced aberration can deteriorate the axial CRLB when imaging deep region of sample and aberration correction can restore the astigmatism PSF improving the axial CRLB. Furthermore, we demonstrated our approach is compatible with 2D and 3D SMLM dSTORM imaging. For 2D dSTORM, we found that the improvement in the FRC resolution is less significant in a thin sample (Figure 11) than in a thick sample (Figure 10). In the thin sample (17 μm deep; spheroid Caco2-BBE cells),

we observed 11% of improvement in the FRC resolution (Figure 11C) and in the thick samples (65 μm deep; Caco2-BBE cells with artificial layer), we observed 47% improvement in the FRC resolution (Figure 10H). For the 3D SMLM, we combined SOLEIL and sensorless AO method in *Drosophila* brain imaging to achieve the optimal axial CRLB. We performed the imaging with three different conditions (AO ON+SOLEIL, AO OFF+SOLEIL, and AO ON+WF) and benchmarked the estimated axial CRLB. We found that AO ON+SOLEIL achieves around 200% better estimated axial CRLB than in the other two situations, which suggests that both AO correction and SOLEIL illumination improves the SMLM when imaging tissue samples.

We anticipate that our approach can be used to image the whole adult *Drosophila* brain. We foresee that for imaging deeper in tissue the raw data quality can be improved by using photoactivation as an alternative to dSTORM, because photoactivation does not rely on a specialized buffer to penetrate the tissue (Betzig et al., 2006; Hess et al., 2006). Furthermore,

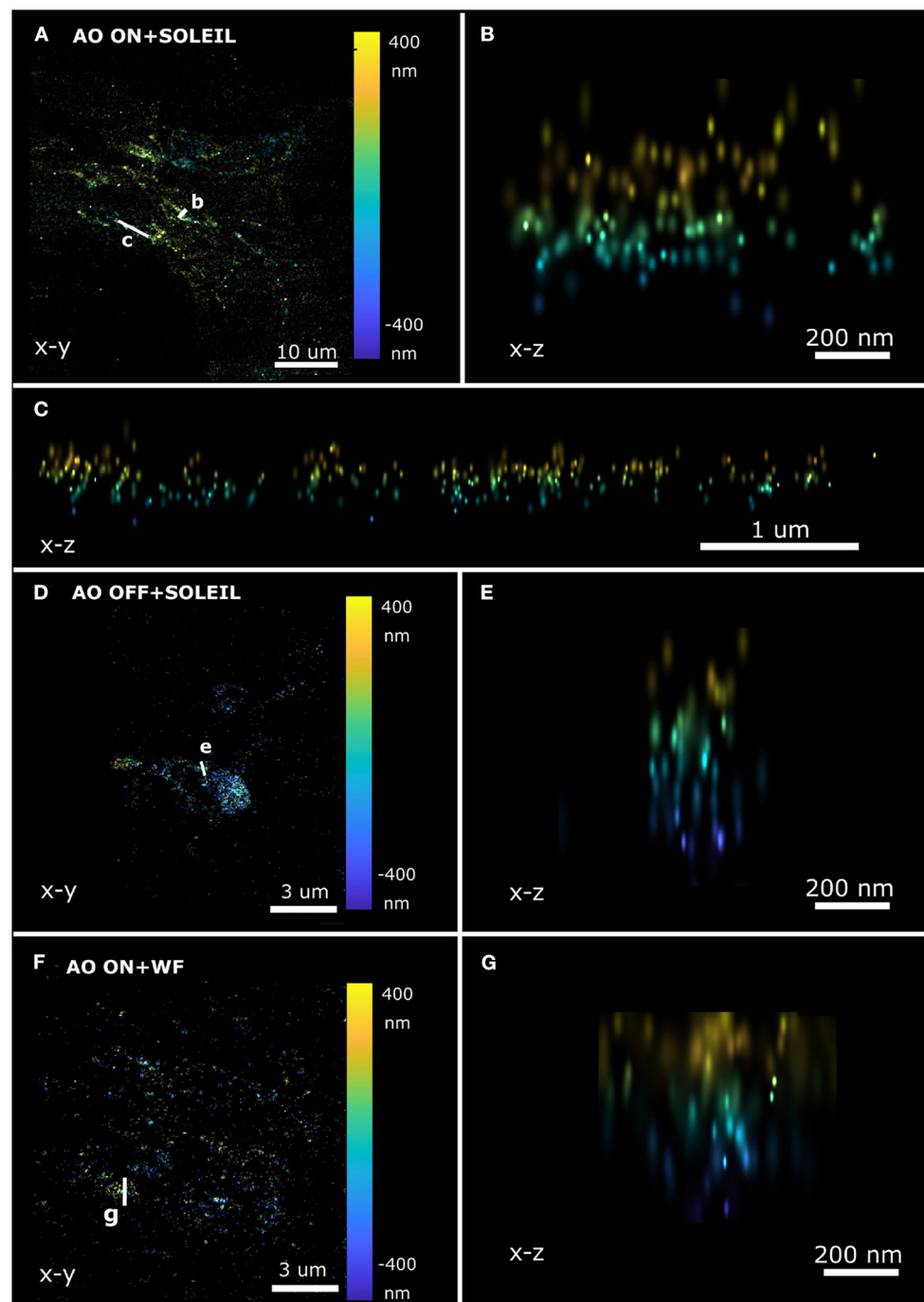


FIGURE 14

Axial SMLM reconstruction cross-section of a single neuron in a whole adult *Drosophila* brain. (A–C) SOLEIL illumination with AO correction. (A) Lateral view and axial cross-section (B,C). (D,E) SOLEIL illumination without AO correction. (D) Lateral view and (E) axial cross-section. (F,G) Widefield illumination with AO correction. (F) Lateral view and (G) axial cross-section.

photoactivation is compatible with clearing tissue methods, which will significantly reduce scattering of the illumination and emission light (Lin et al., 2019).

In our experiments, the imaging time was limited by the stability of the tissue. We hypothesize that the agarose gel gradually heats up during image acquisitions by the

excitation laser, which causes thermal expansion and thus sample drifts. Therefore, the brain could be held in place by alternatives, such as by poly-L-lysine treated coverslips. Nevertheless, our synergistic approach enables super-resolution imaging with single color in sparsely-labeled neurons in adult *Drosophila* brains. To enable relevant 3D SMLM experiments, multi-color imaging would greatly enhance future studies addressing subcellular and molecular localizations of candidates of interest.

Data availability statement

The raw data supporting the conclusions of this article will be made available by the authors, without undue reservation.

Author contributions

All authors listed have made a substantial, direct, and intellectual contribution to the work and approved it for publication.

Funding

S-TH and CS were supported by the Netherlands Organisation for Scientific Research (NWO), under NWO START-UP project no. 740.018.015 and NWO Veni project no. 16761. MS, DJ, and LK were supported by NWO, under FOM Neurophotonics project no. 16NEPH01. AL and LN were supported by the Swiss National Science Foundation SNSF Assistant Professor award (176855 and 211015), the

References

- Ahrens, M., Orger, M., and Robson, D. E. A. (2013). Whole-brain functional imaging at cellular resolution using light-sheet microscopy. *Nat. Methods* 10, 413–420. doi: 10.1038/nmeth.2434
- An, S., Ziegler, K. F., Zhang, P., Wang, Y., Kwok, T., Xu, F., et al. (2020). Axial plane single-molecule super-resolution microscopy of whole cells. *Biomed. Opt. Express* 11, 461–479. doi: 10.1364/BOE.377890
- Antonello, J., Verhaegen, M., Fraanje, R., van Werkhoven, T., Gerritsen, H. C., and Keller, C. U. (2012). Semidefinite programming for model-based sensorless adaptive optics. *J. Opt. Soc. Am. A* 29, 2428–2438. doi: 10.1364/JOSAA.29.002428
- Aristov, A., Lelandais, B., Rensen, E., and Zimmer, C. (2018). Zola-3d allows flexible 3d localization microscopy over an adjustable axial range. *Nat. Commun.* 9, 2409. doi: 10.1038/s41467-018-018-4709-4
- Babcock, H. P., and Zhuang, X. (2017). Analyzing single molecule localization microscopy data using cubic splines. *Scientific Rep.* 7, 552. doi: 10.1038/s41598-017-00622-w
- Baumgart, E., and Kubitschek, U. (2012). Scanned light sheet microscopy with confocal slit detection. *Opt. Express* 20, 21805. doi: 10.1364/OE.20.021805
- Betzig, E., Patterson, G. H., Sougrat, R., Lindwasser, O. W., Olenych, S., Bonifacio, J. S., et al. (2006). Imaging intracellular fluorescent proteins at nanometer resolution. *Science* 313, 1642–1645. doi: 10.1126/science.1127344
- Booth, M. J. (2006). Wave front sensor-less adaptive optics: a model-based approach using sphere packings. *Opt. Express* 14, 1339–1352. doi: 10.1364/OE.14.001339
- Booth, M. J., and Wilson, T. (2001). Refractive-index-mismatch induced aberrations in single-photon and two-photon microscopy and the use of aberration correction. *J. Biomed. Opt.* 6, 266. doi: 10.1117/1.1382808
- Burke, D., Patton, B., Huang, F., Bewersdorf, J., and Booth, M. J. (2015). Adaptive optics correction of specimen-induced aberrations in single-molecule switching microscopy. *Optica* 2, 177–185. doi: 10.1364/OPTICA.2.000174
- Cabriel, C., Bourg, N., Dupuis, G., and Lévêque-Fort, S. (2018). Aberration-accounting calibration for 3d single-molecule localization microscopy. *Opt. Lett.* 43, 174–177. doi: 10.1364/OL.43.000174
- Chakraborty, T., Chen, B., Daetwyler, S., Chang, B.-J., Vanderpoorten, O., Sapoznik, E., et al. (2020). Converting lateral scanning into axial focusing to speed up three-dimensional microscopy. *Light: Sci. Appl.* 9, 165. doi: 10.1038/s41377-020-00401-9

International Foundation for Research in Paraplegia IRP (P180), and SNSF Spark (190919) to LN.

Acknowledgments

The authors would like to thank Y. Deurloo and C.P. Frias for assisting us with the cell culture. The authors would like to thank D. Brinks for using his lab for sample preparation.

Conflict of interest

The authors declare that the research was conducted in the absence of any commercial or financial relationships that could be construed as a potential conflict of interest.

Publisher's note

All claims expressed in this article are solely those of the authors and do not necessarily represent those of their affiliated organizations, or those of the publisher, the editors and the reviewers. Any product that may be evaluated in this article, or claim that may be made by its manufacturer, is not guaranteed or endorsed by the publisher.

Supplementary material

The Supplementary Material for this article can be found online at: <https://www.frontiersin.org/articles/10.3389/fnins.2022.954949/full#supplementary-material>

- Debarre, D., Booth, M. J., and Wilson, T. (2007). Image based adaptive optics through optimisation of low spatial frequencies. *Opt. Express* 15, 8176. doi: 10.1364/OE.15.008176
- Dunsby, C. (2008). Optically sectioned imaging by oblique plane microscopy. *Opt. Express* 16, 20306. doi: 10.1364/OE.16.020306
- Egner, A., Geisler, C., Middendorff, C., v., Bock, H., Wenzel, D., et al. (2007). Fluorescence nanoscopy in whole cells by asynchronous localization of photoswitching emitters. *Biophys. J.* 93, 3285–3290. doi: 10.1529/biophysj.107.112201
- Gustavsson, A., Petrov, P., and Lee, M. E. A. (2018). 3d single-molecule super-resolution microscopy with a tilted light sheet. *Nat. Commun.* 9, 123. doi: 10.1038/s41467-017-02563-4
- Hess, S. T., Girirajan, T. P., and Mason, M. D. (2006). Ultra-high resolution imaging by fluorescence photoactivation localization microscopy. *Biophys. J.* 91, 4258–4272. doi: 10.1529/biophysj.106.091116
- Hung, S.-T., Cnossen, J., Fan, D., Siemons, M., Jurriens, D., Grusmayer, K., et al. (2022). Soleil: single-objective lens inclined light sheet localization microscopy. *Biomed. Opt. Express* 13, 3275–3294. doi: 10.1364/BOE.451634
- Kapałczyńska, M., Kolenda, T., Przybyła, W., Zajączkowska, M., Teresiak, A., Filas, V., et al. (2016). 2d and 3d cell cultures - a comparison of different types of cancer cell cultures. *Arch. Med. Sci.* 14, 63743. doi: 10.5114/aoms.2016.63743
- Kelly, S. M., Elchert, A., and Kahl, M. (2017). Dissection and immunofluorescent staining of mushroom body and photoreceptor neurons in adult *Drosophila melanogaster* brains. *J. Vis. Exp.* 6, 56174. doi: 10.3791/56174
- Konopka, C. A., and Bednarek, S. Y. (2008). Variable-angle epifluorescence microscopy: a new way to look at protein dynamics in the plant cell cortex. *Plant J.* 53, 186–196. doi: 10.1111/j.1365-3113X.2007.03306.x
- Kumar, M., and Kozorovitskiy, Y. (2019). Tilt-invariant scanned oblique plane illumination microscopy for large-scale volumetric imaging. *Opt. Lett.* 4, 1706–1709. doi: 10.1364/OL.44.001706
- Kumar, M., and Kozorovitskiy, Y. (2020). Tilt (in)variant lateral scan in oblique plane microscopy: a geometrical optics approach. *Biomed. Opt. Express* 11, 3346–3359. doi: 10.1364/BOE.389654
- Li, Y., Mund, M., Hoess, P., Deschamps, J., Matti, U., Nijmeijer, B., et al. (2018). Real-time 3d single-molecule localization using experimental point spread functions. *Nat. Methods* 15, 367–369. doi: 10.1038/nmeth.4661
- Li, Y., Wu, Y.-L., Hoess, P., Mund, M., and Ries, J. (2019). Depth-dependent psf calibration and aberration correction for 3d single-molecule localization. *Biomed. Opt. Express* 10, 2708–2718. doi: 10.1364/BOE.10.002708
- Lidke, K. A., Rieger, B., Jovin, T. M., and Heintzmann, R. (2005). Superresolution by localization of quantum dots using blinking statistics. *Opt. Express* 13, 7052–7062. doi: 10.1364/OPEX.13.007052
- Lin, H.-Y., Chu, L.-A., Yang, H., Hsu, K.-J., Lin, Y.-Y., Lin, K.-H., et al. (2019). Imaging through the whole brain of *Drosophila* at $\lambda/20$ super-resolution. *iScience* 14, 164–170. doi: 10.1016/j.isci.2019.03.025
- Lin Hai, H., and Rao, C. (2011). Wavefront sensorless adaptive optics: a general model-based approach. *Opt. Express* 19, 371–379. doi: 10.1364/OE.19.000371
- Lu, C., Tang, W., and Liu, Y., e. a. (2019). Lightsheet localization microscopy enables fast, large-scale, and three-dimensional super-resolution imaging. *Commun. Biol.* 2, 177. doi: 10.1038/s42003-019-0403-9
- Manley, S., Gillette, J., and Patterson, G. (2008). High-density mapping of single-molecule trajectories with photoactivated localization microscopy. *Nat. Methods* 5, 155–157. doi: 10.1038/nmeth.1176
- McGorty, R., Schnitzbauer, J., Zhang, W., and Huang, B. (2014). Correction of depth-dependent aberrations in 3d single-molecule localization and super-resolution microscopy. *Opt. Lett.* 39, 275–278. doi: 10.1364/OL.39.000275
- Mlodzianoski, M. J., Cheng-Hathaway, P. J., Bemiller, S. M., McCray, T. J., Liu, S., Miller, D. A., et al. (2018). Active psf shaping and adaptive optics enable volumetric localization microscopy through brain sections. *Nat. Methods* 15, 583–586. doi: 10.1038/s41592-018-0053-8
- Nieuwenhuizen, R. P. J., Lidke, K. A., Bates, M., Puig, D. L., Grünwald, D., Stallinga, S., et al. (2013). Measuring image resolution in optical nanoscopy. *Nat. Methods* 10, 557–562. doi: 10.1038/nmeth.2448
- Olivier, N., Débarre, D., and Beaufrepaire, E. (2009). Dynamic aberration correction for multiharmonic microscopy. *Opt. Lett.* 34, 3145–3147. doi: 10.1364/OL.34.003145
- Paglione, M., Rosell, A. L., Chatton, J.-Y., and Neukomm, L. J. (2020). Morphological and functional evaluation of axons and their synapses during axon death in *Drosophila melanogaster*. *J. Vis. Exp.* 16, 157. doi: 10.3791/60865
- Park, S., Jo, Y., Kang, M., Hong, J. H., Ko, S., Kim, S., et al. (2021). Restoring single-molecule localizations with wavefront sensing adaptive optics for deep-tissue super-resolution imaging. *bioRxiv*. doi: 10.1101/2021.11.18.469175
- Ries, J. (2020). Smap: a modular super-resolution microscopy analysis platform for smml data. *Nat. Methods* 17, 870–872. doi: 10.1038/s41592-020-0938-1
- Sanyal, S., and Kosovsky, M. (2017). “Materials and assay systems used for three-dimensional cell culture,” in *Technology Platforms for 3D Cell Culture*, ed S. Przyborski (Wiley). doi: 10.1002/9781118851647.ch7
- Sapoznik, E., Chang, B.-J., and Huh, J. (2020). A versatile oblique plane microscope for large-scale and high-resolution imaging of subcellular dynamics. *Elife* 9, e57681. doi: 10.7554/eLife.57681
- Siemons, M., Cloin, B. M. C., Salas, D. M., Nijenhuis, W., Katrukha, E. A., and Kapitein, L. C. (2020). Comparing strategies for deep astigmatism-based single-molecule localization microscopy. *Biomed. Opt. Express* 11, 735–751. doi: 10.1364/BOE.382023
- Siemons, M., Hulleman, C. N., Thorsen, R. O., Smith, C. S., and Stallinga, S. (2018). High precision wavefront control in point spread function engineering for single emitter localization. *Opt. Express* 26, 8397–8416. doi: 10.1364/OE.26.008397
- Siemons, M. E., Hanemaaijer, N. A. K., Kole, M. H. P., and Kapitein, L. C. (2021). Robust adaptive optics for localization microscopy deep in complex tissue. *Nat. Commun.* 12, 3407. doi: 10.1038/s41467-021-23647-2
- Smith, C., and Joseph, N., Rieger, B. (2010). Fast, single-molecule localization that achieves theoretically minimum uncertainty download pdf. *Nat. Methods* 7, 373–375. doi: 10.1038/nmeth.1449
- Smith, C. S., Stallinga, S., Lidke, K. A., Rieger, B., and Grunwald, D. (2015). Probability-based particle detection that enables threshold-free and robust *in vivo* single-molecule tracking. *Mol. Biol. Cell* 26, 4057–4062. doi: 10.1091/mbc.E15-06-0448
- Soloviev, O. (2020). “Alias-free basis for modal sensorless adaptive optics using the second moment of intensity,” in *International Journal of Wavelets, Multiresolution and Information Processing*. doi: 10.1142/S0219691320400081
- Tafteh, R., Scriven, D. R. L., Moore, E. D. W., and Chou, K. C. (2015). Single molecule localization deep within thick cells; a novel super-resolution microscope. *J. Biophotonics* 9, 155–160. doi: 10.1002/jbio.201500140
- Tehrani, K. F., Xu, J., Zhang, Y., Shen, P., and Kner, P. (2015). Adaptive optics stochastic optical reconstruction microscopy (ao-storm) using a genetic algorithm. *Opt. Express* 23, 13677. doi: 10.1364/OE.23.013677
- Tokunaga, M., Imamoto, N., and Sakata-Sogawa, K. (2008). Highly inclined thin illumination enables clear single-molecule imaging in cells. *Nat. Methods* 5, 159–161. doi: 10.1038/nmeth1171
- Xu, F., Ma, D., MacPherson, K. P., Liu, S., Bu, Y., Wang, Y., et al. (2020). Three-dimensional nanoscopy of whole cells and tissues with in situ point spread function retrieval. *Nat. Methods* 17, 531–540. doi: 10.1038/s41592-020-0816-x
- Xu, K., Zhong, G., and Zhuang, X. (2012). Actin, spectrin, and associated proteins form a periodic cytoskeletal structure in axons. *Science* 339, 452–456. doi: 10.1126/science.1232251
- Yang, B., Chen, X., and Wang, Y. E. A. (2019). Epi-illumination spim for volumetric imaging with high spatial-temporal resolution. *Nat. Methods* 16, 501–504. doi: 10.1038/s41592-019-0401-3
- Zhong, G., He, J., Zhou, R., Lorenzo, D., Babcock, H. P., Bennett, V., et al. (2014). Developmental mechanism of the periodic membrane skeleton in axons. *Elife* 3, e04581. doi: 10.7554/eLife.04581
- Žurauskas, M., Dobbie, I. M., Parton, R. M., Phillips, M. A., Göhler, A., Davis, I., et al. (2019). Isosense: frequency enhanced sensorless adaptive optics through structured illumination. *Optica* 6, 370–379. doi: 10.1364/OPTICA.6.000370

Supplementary Material

1 OPTICAL SYSTEM

The design of SOLEIL microscope is shown in (Hung et al., 2022). We used a stick-slip piezo stage as a sample stage (Smartact; x,y an SLC1730; z an SLC1720). The lightsheet was generated by an achromatic doublet cylindrical lens (Thorlabs, ACY254-250-B). Then, an achromatic doublet lens (Thorlabs, AC254-300-A-ML) formed a 4f-telescope with the cylindrical lens. To translate the lightsheet illumination, we placed a galvo mirror (Scanlab, dynAXIS 20 mm) at the pupil plane of the scan lens (TTL200MP, Thorlabs) to work as a scanning module. An achromatic doublet lens (Thorlabs, AC254-200-A-ML) and a reflective mirror (Thorlabs, BB1-E02) were placed on a translation stage (Thorlabs, XR25P/M), which allow us to adjust the angle of inclined lightsheet. A dichroic mirror (Semrock, Di03-R405/488/561/635-t1-25x36) separated the excitation and emission path. A 180 mm focal length tube lens (Olympus, SWTLU-C) was used to form a 60 times imaging system with objective lens (Olympus, UPlanSAPO 60x Oil NA 1.35). In the emission path, an achromatic lens with 200 mm focal length (AC254-200-A-ML) was assembled as a 4f-telescope with the tube lens, which conjugated the back focal plane of the objective lens to the plane of the deformable mirror (Alpao DM69-15). The deformable mirror allowed us to control the pupil phase in the emission path, which enables PSF engineering for 3D SMLM and sensorless AO correction. The deformable mirror was rotated by approximately 15° to reflect the emission light so that the emission light wouldn't reflect back to the original path. An emission filter (AHF, FF01-446/510/581/703-25) was used to filter out the back-reflected excitation laser. An achromatic doublet lens (AC254-200-A-ML) imaged the pupil plane at the plane of deformable mirror to the sCMOS camera (Andor Zyla 4.2). The sCMOS camera and galvo mirror were synchronized by using an Arduino micro-controller.

2 IN-SILICO SMLM DATA GENERATION

To test the stability and the performance of the sensorless AO algorithm, we built a SMLM data simulator (SDS) to simulate the blinking images in the presence of (Zernike) aberrations (Fig. S1). The pipeline of SDS consists of several steps. Firstly, we set up a 3D structure of the sample in the SDS (Fig. S1 (a)). In general, the structure can be any shape and in this experiment we set up the structure of the sample as tubulin-like. In the SDS simulator, the algorithm randomly chooses certain number of spots turning them to be the on-state and the others staying in the off-state. Then, SDS simulates the vector PSFs based on the input Zernike aberration, intensity and I/bg ratio (Fig. S1 (b)). The PSF simulation was done with ROI of $25 \text{ pixels} \times 25 \text{ pixels}$, which is $2.5 \mu\text{m} \times 2.5 \mu\text{m}$.

The high NA aberrated PSF was computed based on the pupil function (Siemons et al., 2018). The pupil function (Eq. S1) consists a phase aberration ($W(\vec{\rho})$) and an applanatic amplitude factor ($A(\vec{\rho})$) (Stallinga, 2015). The pupil function is described by a $91 \text{ pixels} \times 91 \text{ pixels}$ array. The electric field (Eq. S2) is described as the Fourier transform of the pupil function ($v_{l,j}(\vec{\rho})$) (Siemons et al., 2018). For numerical reasons we used the chirp z transform (Siemons et al., 2018; Bakx, 2002). We considered a free-rotating dipole and hence all polarization terms contribute to the PSF equally Eq. S3. Monochromatic light was used for simulating and the wavelength is 680 nm. The NA of objective lens we used is 1.35. The refractive index of immersion media is 1.52 and the refractive index of sample medium is 1.33. The pixel size of the simulated images is 108.33 nm. We neglect supercritical angle fluorescence (SAF) effects because they are neglectable away from the coverslip.

$$P(\vec{\rho}) = A(\vec{\rho}) \exp\left(i \frac{2\pi W(\vec{\rho})}{\lambda}\right) \quad (\text{S1})$$

,where $\vec{\rho}$ is the normalized pupil function radius, $P(\vec{\rho})$ is the pupil function, $A(\vec{\rho})$ is the applanatic amplitude factor, $W(\vec{\rho})$ is the phase aberration, λ is the wavelength.

$$E_{l,j}(\vec{r}) = \int_{|\vec{\rho}| < 1} d^2\rho P(\vec{\rho}) v_{l,j}(\vec{\rho}) \exp(-i\vec{k} \cdot \vec{r}) \quad (\text{S2})$$

,where $E_{l,j}(\vec{r})$ is the electric field with l, j as the direction of polarization (j emitter polarization projects to l polarization on pupil plane), $v_{l,j}(\vec{\rho})$ is the vectorial factor (Stallinga, 2015), \vec{k} is the wavevector.

$$PSF(\vec{r}) = \frac{1}{3} \sum_{l=x,y} \sum_{j=x,y,z} |E_{l,j}(\vec{r})|^2 \quad (\text{S3})$$

, where $PSF(\vec{r})$ is the point spread function function.

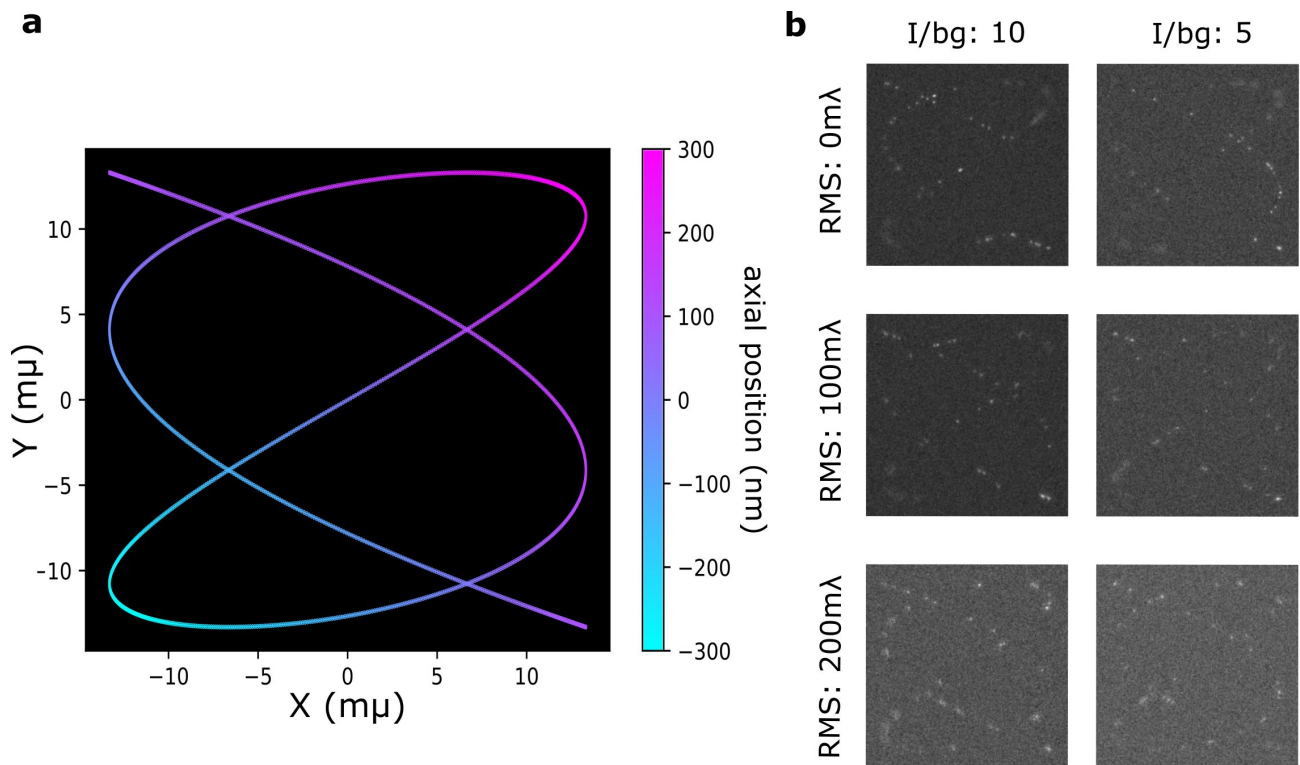


Figure S1. Blinking image simulator. (a) Tubulin structure for blinking image simulation. (b) Aberrated blinking image under different RMS value and I/bg ratio.

3 IMPACT OF AO CORRECTION ON THE LATERAL LOCALIZATION PRECISION FOR IN-SITU PSF ESTIMATION USING THE INSPR ALGORITHM

In this section the impact on the lateral CRLB is investigated. In Fig. 3, we show that AO correction can improve the axial CRLB. In Fig. S2 we found AO correction doesn't improve the lateral CRLB. In Fig. 8, it is also observed that AO correction has no significant improvement in lateral CRLB. Note that in Fig. 3,8 AO correction did improve the axial CRLB.

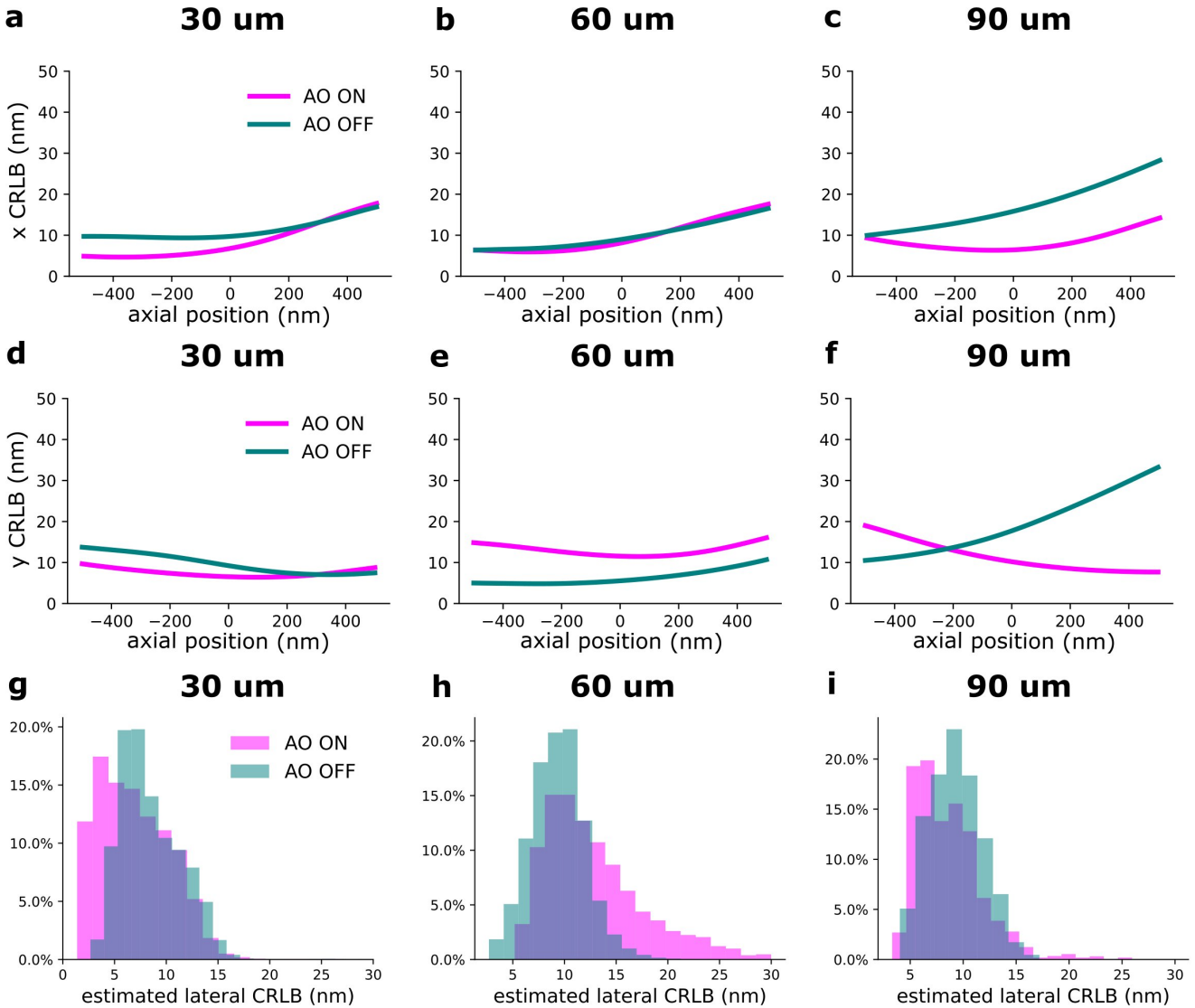


Figure S2. Lateral CRLB of the INSPR model before and after AO correction at different imaging depth. (a-f) The theoretical x,y CRLB based on the INSPR PSF model from Fig. 3 (a-c) with 3000 photon of intensity and 50 photons/pixel of background. (g-i) The distribution of estimated lateral CRLB at different imaging depths.

4 PREPARATION OF THE ARTIFICIALLY THICK CACO2-BBE SAMPLE

In this section, we show the flowchart on making artificial thick Caco2-BBE sample. In Fig. S3 (a), we show the schematic figure of the artificial thick sample from three views (top view and side view1,2). Fig. S3 (b) shows the material we used to make the artificially thick sample. Fig. S3 (c) shows detailed steps to create the artificial sample and how to add dSTORM buffer into the sample.

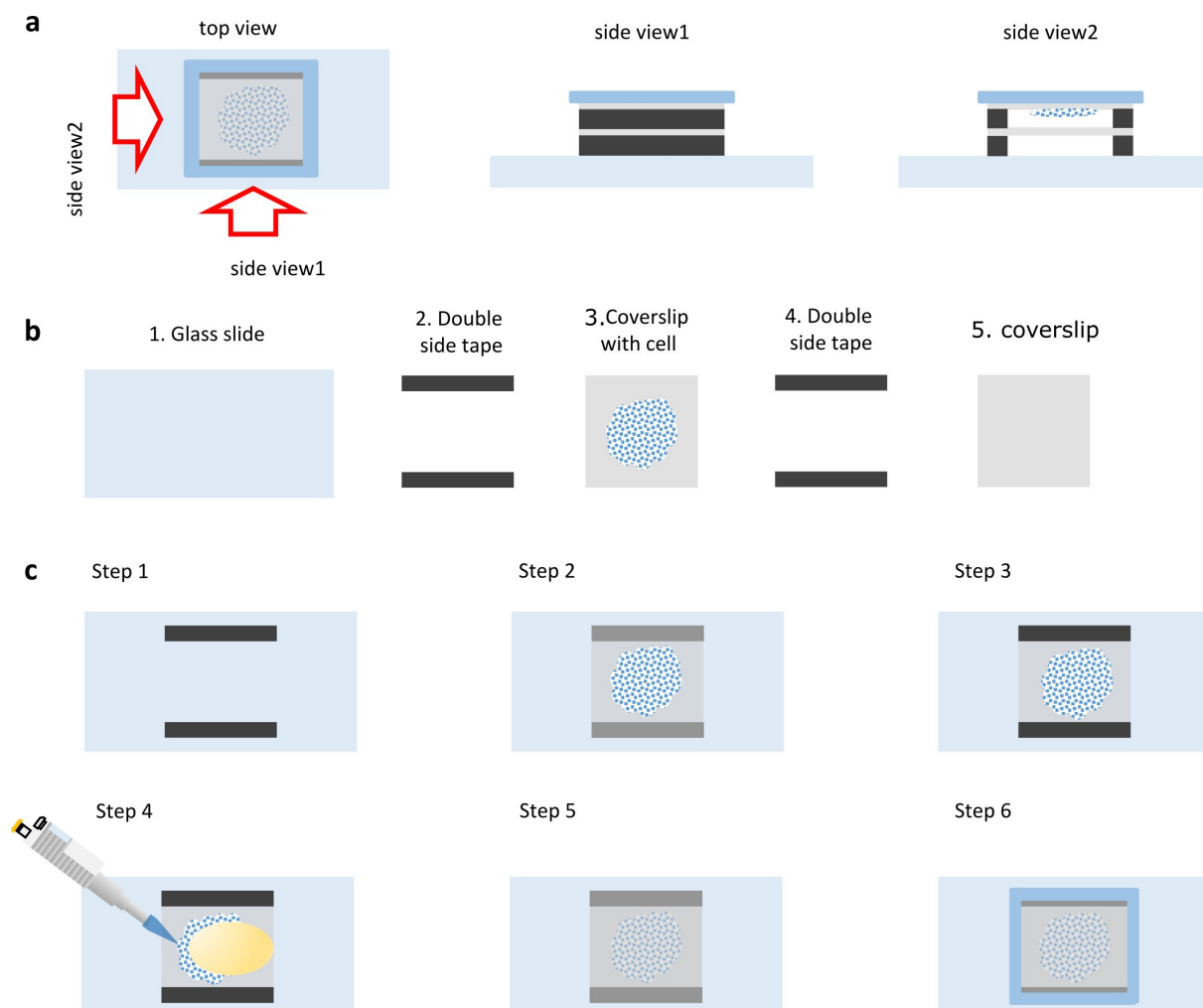


Figure S3. (a) The figure of thick STORM buffer layer Caco2-BBE sample and the sideview. (b) Material to make thick STORM buffer layer Caco2-BBE sample in (a,c). (c) Protocol to make thick STORM buffer layer Caco2-BBE sample. Step 1: put double side tape on glass slides, Step 2: attach a coverslip on the double side tape, Step 3: attach double side tape on the coverslip in Step 2, Step 4: add STORM buffer (yellow ellipse) in the middle of double side tape with pipette, Step 5: cover the cell with another coverslip, Step 6: seal the edge of coverslip by Twinsil (Picodent, Wipperfurth).

5 MEASURE THE THICKNESS OF DSTORM BUFFER LAYER

In the artificially thick Caco2-BBE sample, we added double sided tape as spacer between the cells and the coverslip to increase the thickness of the sample (Fig. S3), which can introduce additional spherical aberration. The thickness of the spacer was measured by the optical setup in Fig. S4 (a). A single mode coherent laser (640 nm) was launched from a reflected collimator and went through the 50:50 beam splitter focusing on the sample by an objective lens. The reflected light from the sample was acquired by the objective lens and went through the 50:50 beam splitter to the camera. When the incident light was focused on the interface between material, such as air-coverslip interface, the peak intensity of reflected light was much higher than the other situation. With this principle, we can identify the stage position from (b). The first interface the light can be focused on is the layer between air and the front side of the first coverslip, which is the P1 point in (b). The second interface can be focused is the back side of second coverslip, which is P2 point in (b). The third interface can be focused is the front side of second coverslip, which is the P3 point. The fourth interface can be focused is the back side of second coverslip. The distance between P2 and P3 is the distance of spacer we add in the sample, which is $64\ \mu\text{m}$.

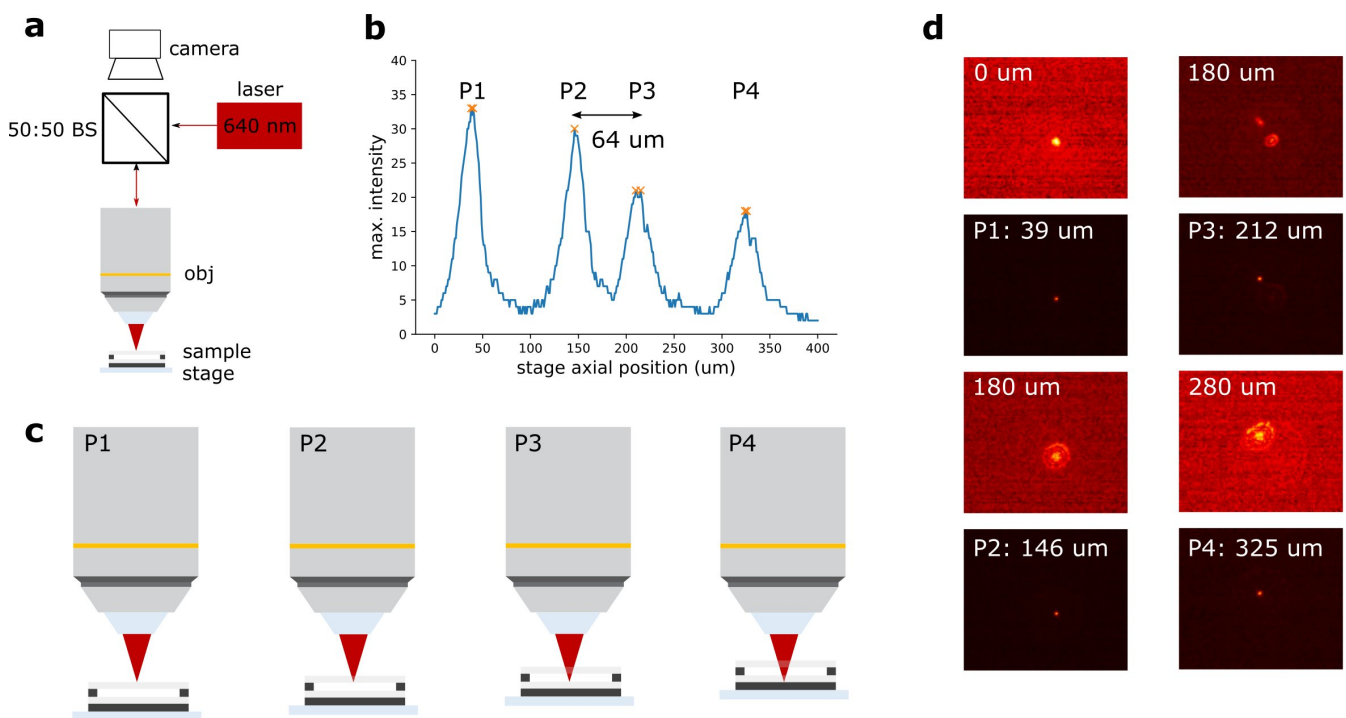


Figure S4. Measurement of the thickness of artificial Caco2-BBE sample. (a) optical setup for sample thickness measurement. 50:50 BS: 50:50 beam splitter (BS013, Thorlabs); camera: CMOS camera (IDS UI3070CP-M-GL); obj: 10X objective lens (UMPlanFL N 10X NA:0.3, Olympus); sample: measured sample; stage: piezo stage (Smactact, x,y an SLC1730; z an SLC1720); laser: 640 nm single mode laser (HLS635, Thorlabs). (b) the maximum image value at different stage position. (c) Schematic of stage position corresponding to the peak of (b). P1: the first peak in (b), where is light is focused at the interface of the front side of first coverslip and air. P2: the second peak in (b), where the light is focused at the interface of the back side of first coverslip. P3: the third peak in (b), where the light is focused at the front side of second coverslip. P4: the fourth peak in (b), where the light is focused at the back side of second coverslip. (d) the raw camera image at different stage position.

6 INFLUENCE OF SPHERICAL ABERRATION ON AXIAL CRLB

The spherical aberration can smooth the PSF along the axial dimension and this has an impact on the axial CRLB. To investigate the influence of spherical aberration on the axial CRLB, we simulated the the astigmatism and tetrapod PSF with additional spherical aberrations (Fig.S5 (a,c)) (Details of PSF simulation is in section 7). In the Fig.S5 (b,d), we computed the CRLB with a intensity of 1000 photons and a background of 50 photons/pixel and found that the spherical aberration can significantly decrease the CRLB of engineered PSF.

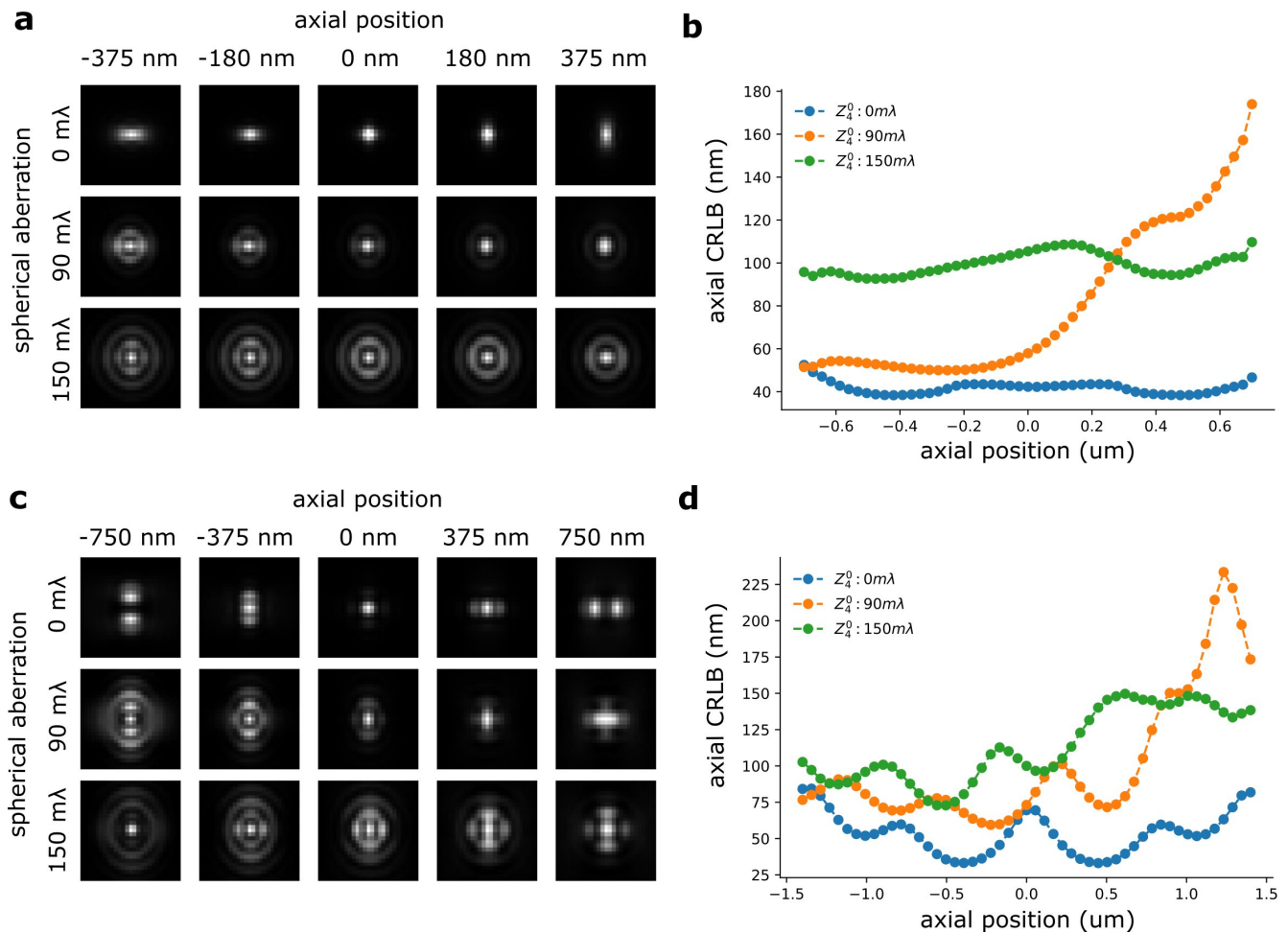


Figure S5. Influence of spherical aberration on axial CRLB. (a) Simulated astigmatism PSF ($100\text{ m}\lambda Z_2^2$) with the addition of different level of spherical aberration. (b) The axial theoretical CRLB of the astigmatism PSF with addition of different level of spherical aberration. The intensity used for simulation is 1000 photons and the background is 50 photons/pixel. (c) Simulated tetrapod PSF ($100\text{ m}\lambda Z_4^4$) with the addition of different level of spherical aberration. (b) The axial theoretical CRLB of the tetrapod PSF with addition of different level of spherical aberration. The intensity used for simulation is 1000 photons and the background is 50 photons/pixel.

7 INFLUENCE OF SPHERICAL ABERRATION ON THE 2D LOCALIZATION PRECISION

To understand the influence of spherical aberration on the 2D localization of single-molecules, we simulated PSFs with different amounts of spherical aberration (details is in section 7) and performed the localization by using Gaussian PSF model. We observed that the spherical aberration deteriorates the achievable localization (Fig. S6 (a)). The reported localization precision is the standard deviation of estimated position from 100 times of localization and we repeated this for 10 time for the errorbar in Fig. S6 (a). The spherical aberration can distort the PSF and the shape of the aberrated PSF doesn't match with a Gaussian function. The PSFs were simulated with the same intensity and background. However, the estimated intensity and background are biased in the presence of spherical aberration (Fig. S6 (c,d)). In the meanwhile, the I/bg decreases (Fig. S6 (e)). The reported CRLB and the estimation precision deteriorate by 40% as the spherical aberration (Z_4^0) increases to $120\text{ m}\lambda$.

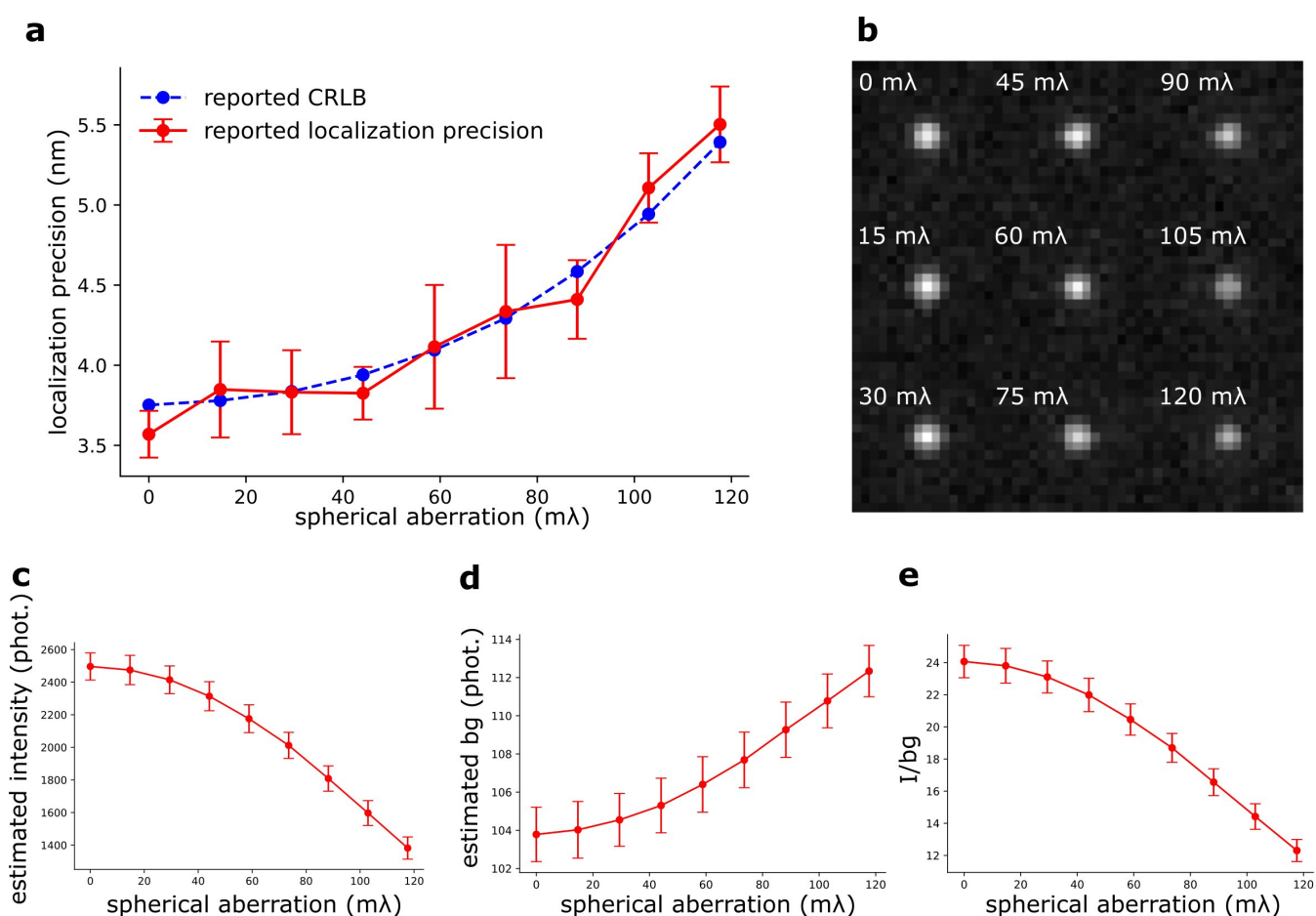


Figure S6. Influence of spherical aberration on the 2D localization precision. (a) the CRLB, reported localization precision versus amplitude of spherical aberration. (b) the simulated PSF with different amplitude of spherical aberration. (c-e) the influence of spherical on estimated intensity (c), background (d), and SBR (e).

8 CAMERA SETTING

In this research, we used Andor Zyla 4.2 sCMOS camera for imaging. For the dSTORM imaging, we used 501 pixels \times 501 pixels, which corresponds to 54 $\mu\text{m}\times$ 54 μm FOV. The camera trigger was set to external trigger, which allows for external signal control from Arduino Micro-controller. In SOLEIL microscopy, the virtual confocal slit readout was achieved with a rolling shutter by activating the Andor SOLIS LightScan PLUS function in down sequential mode. The readout image is 16 bit format.

For initial aberration correction, the camera trigger mode was set to internal trigger and the camera was synchronized with DM through the customized Python script. The FOV was cropped to single PSF spot. The camera exposure time was 30 ms, which is 25 frames/second. The image readout was set to 16 bit mode.

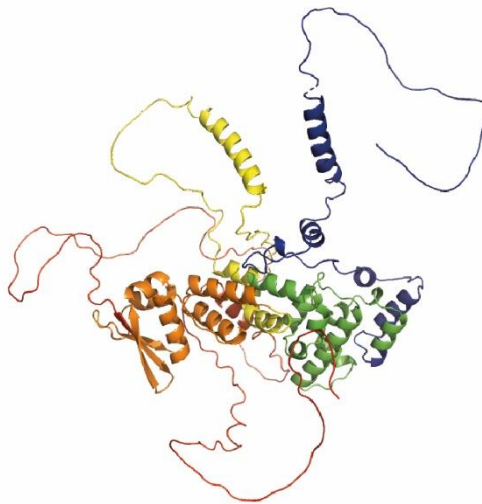
For sensorless AO correction, the camera trigger mode was set to internal trigger and used customized Python script for controlling camera and DM. The camera readout is 16 bit. The FOV was cropped depend on the size of sample. In general, we ensured the FOV is larger than 30 $\mu\text{m}\times$ 30 μm .

REFERENCES

- Bakx, J. L. (2002). Efficient computation of optical disk readout by use of the chirp z transform. *Appl. Opt.* 41, 4897–4903. doi:10.1364/AO.41.004897
- Hung, S.-T., Cnossen, J., Fan, D., Siemons, M., Jurriens, D., Großmayer, K., et al. (2022). Soleil: single-objective lens inclined light sheet localization microscopy. *Biomedical Optics Express* 13, 3275–3294. doi:10.1364/BOE.451634
- Siemons, M., Hulleman, C. N., Thorsen, R. O., Smith, C. S., and Stallinga, S. (2018). High precision wavefront control in point spread function engineering for single emitter localization. *Optics Express* 26, 8397–8416. doi:10.1364/OE.26.008397
- Stallinga, S. (2015). Effect of rotational diffusion in an orientational potential well on the point spread function of electric dipole emitters. *J. Opt. Soc. Am. A* 32, 213–223. doi:10.1364/JOSAA.32.000213

CHAPTER 7

Identification of Axed-interacting proteins



Predicted 3D structure of Axed using AlphaFold.
(N-terminus, red; Back, green; BTB, orange; linker, yellow; C-terminus, blue).

6.1 Summary of the results

In this chapter, I will summarize the experiments that I have performed to better understand the function of *axed* in injury-induced axon degeneration. I will show how we can immunoprecipitate (IP) Axed from *Drosophila* fly heads to subsequently analyse the samples by mass spectrometry to identify possible candidate interactors of Axed. These candidates have been examined by the Database for Annotation, Visualization and Integrated Discovery (DAVID). Finally, I will show the predicted 3D structure of Axed with AlphaFold, and a Distance Matrix Alignment (DALI) analysis that compares protein structures in 3D to find biologically interesting similarities with other proteins.

6.2 Personal contribution

Dominik Kurian, manager at the Proteomics and Metabolomics Facility at Roslin Institute, analysed the mass spectrometry data; Helen McGuinness, a PhD student in the Kobe lab, University of Queensland, performed the AlphaFold prediction and the DALI analysis; Maria Paglione shared the R script to create the graphs of the DAVID analysis. I performed the rest of the experiments.

6.3 Results

Despite being the most downstream component of the axon death signalling cascade, the precise function of Axed remains currently unknown. To identify and characterize its function, I sought to identify Axed-interacting proteins, specifically during activated axon death signalling *in vivo* through IP. Transgenic flies harbouring an *eGFP::3xFLAG* tag specifically engineered into the *axed* genomic locus with an artificial exon (*axed*^{*eGFP::3xFLAG*}) serve as an ideal tool for co-IP, because Axed^{*eGFP::3xFLAG*} is enriched in axons and synapses, and fully able to execute axon death signalling (Neukomm et al., 2017). I was able to confirm that both Axed isoforms (short and long, respectively) are readily detected in Western blots (WB) with anti-FLAG and anti-GFP antibodies (ABs) (Figure 9A). As a proof-of-principle, I used these ABs coupled to magnetic beads to perform an Axed tandem co-IP: starting with a crude extract from 150 fly heads, Axed^{*eGFP::3xFLAG*} was first purified with anti-FLAG ABs. Subsequently, 3xFLAG peptides were used for a competitive elution, whereby Axed^{*eGFP::3xFLAG*} proteins are released from the beads. To get rid of unspecific proteins bound to anti-FLAG Abs or magnetic beads, a second IP was performed with anti-GFP ABs (Figure 9B). WB revealed that this protocol enables a strong enrichment for Axed. In conclusion, tandem co-IP is an excellent approach to purify endogenous Axed from fly heads while presumably getting rid of a considerable amount of background compared to single IPs.

The specific enrichment of Axed by tandem IP should also enrich Axed-interacting proteins, which were co-immunoprecipitated (tandem co-IP). Therefore, the magnetic beads and the proteins bound to them were treated with trypsin, and the resulting peptides were analysed by liquid chromatography-tandem mass spectrometry (LC-MS/MS) in collaboration with Dominic Kurian in the Wishart lab (Roslin Institute, Edinburgh) (Figure 9C). Among the 17 identified proteins, 12 were specifically and 5 non-specifically enriched (red and black circles, respectively) with relatively low overall protein scores (Figure 9C, left). To increase the number of identified

proteins and their scores, I performed a single co-IP using anti-GFP ABs only, with the risk of more unspecific bound proteins (Figure 9C, right). By co-IP, among the 348 detected proteins, 52 were specifically and 180 non-specifically enriched (red and black circles, respectively), with significantly higher overall protein scores. Interestingly, not all proteins identified in the tandem co-IP were also detected in the single co-IP. Taken together, tandem or single co-IP is a robust tool to identify Axed-interacting proteins by LC-MS/MS.

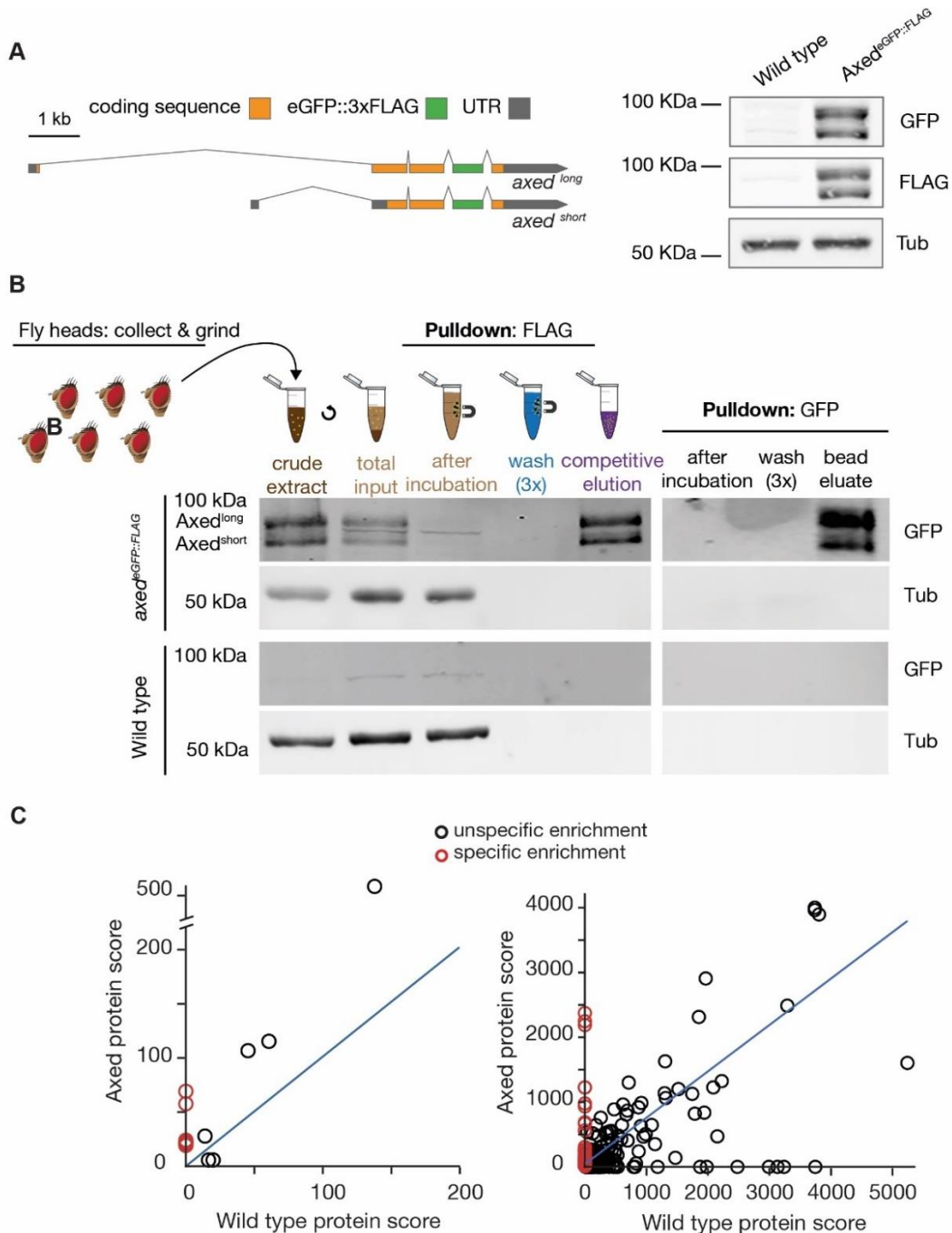


Figure 9. Identification of Axed interacting proteins. **A** Left, genomic locus of *axed* with an endogenously engineered *eGFP::FLAG* tag in an artificial exon (green). Right, detection of short and long Axed isoforms in Western blots. **B** Tandem immunoprecipitation (IP) of Axed. *Axed^{eGFP::3xFLAG}* is sequentially immunoprecipitated using anti-FLAG and anti-GFP antibodies (ABs). 3xFLAG peptides were used for competitive elution. **C** Tandem mass spectrometry (MS/MS) of Axed co-IP proteins. Left, tandem co-IP (FLAG and GFP), 5 and 12 proteins non-specifically and specifically enriched, respectively. Right, co-IP (GFP), 180 and 52 proteins non-specifically and specifically enriched, respectively. Blue, the mean line between the two axes.

Next, I sought to group the list of proteins specifically enriched in Axed (e.g., the red dots in Figure 9) depending on their known function. I ran the list of 52 proteins detected in the Axed co-IP (GFP ABs), through DAVID analysis to gain further insights into their biological processes. The DAVID analysis allows grouping genes from different pathways, creating lists of interacting proteins, and identifying enriched biological themes, among others. I decided to analyse the candidate proteins with Gene Ontology (GO) terms for biological processes, cellular compartments, and molecular functions (Figure 10). For simplicity, the data is shown for the 10 most relevant GO terms for each level, and the number of genes linked to every GO term. In the cellular compartment analysis, most genes function in the cytoplasm. In contrast, no nuclear gene was found, supporting the function of Axed outside the nucleus. In the molecular function analysis, several genes with ATP-related functions were enriched, suggesting Axed could influence ATP energetics. Finally, by analysing biological processes, most of the candidates relate to protein folding, vesicle-mediated transport, and mitochondrial regulation (Figure 10).

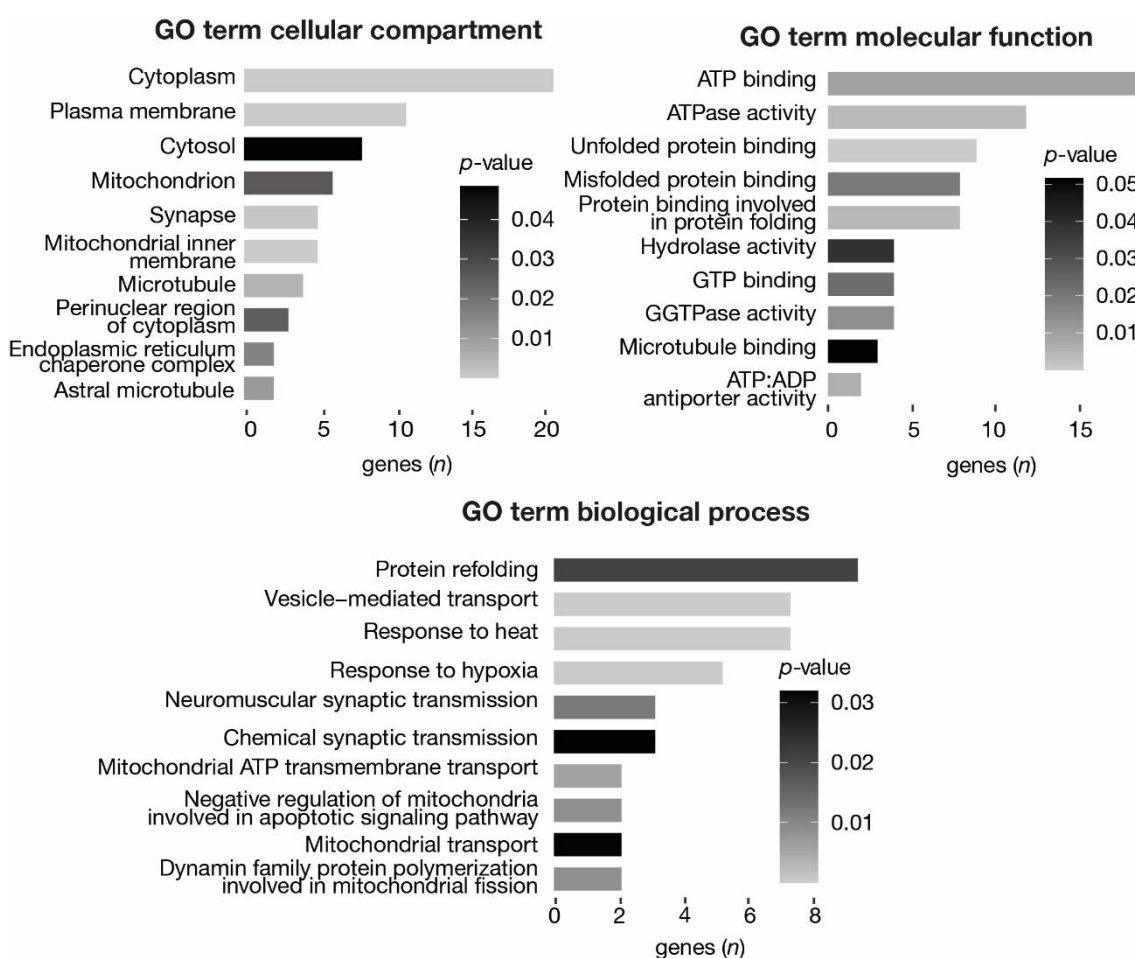


Figure 10. DAVID analysis for candidate Axed-interacting proteins. GO terms are classified as cellular compartments, molecular functions, or biological processes. The 10 most relevant GO terms for each classification are shown. The X-axis indicates the number of genes detected for each GO term, and the grayscale gradient suggests the confidence of a group linked to one GO term: lower p -value = greater confidence.

In collaboration with Helen McGuinness, we used AlphaFold to predict the 3D structure of Axed^{long} (Jumper et al., 2021; Varadi et al., 2022), as well as DALI to perform a structural homology search against the whole protein data bank (PDB) (Figure 11) (Holm, 2022). We aimed

to identify biologically interesting similarities based on the 3D structure between Axed^{long} and other proteins with an already described function.

The 3D structure of Axed^{long} is displayed with the N-terminus (red), the BACK domain (green), the BTB domain (orange), the linker between the two domains (yellow), and the C-terminus (blue) (Figure 11, left). The confidence of the predicted structure is also shown, where red is higher and blue is lower (100% and 0%, respectively) (Figure 10, right).

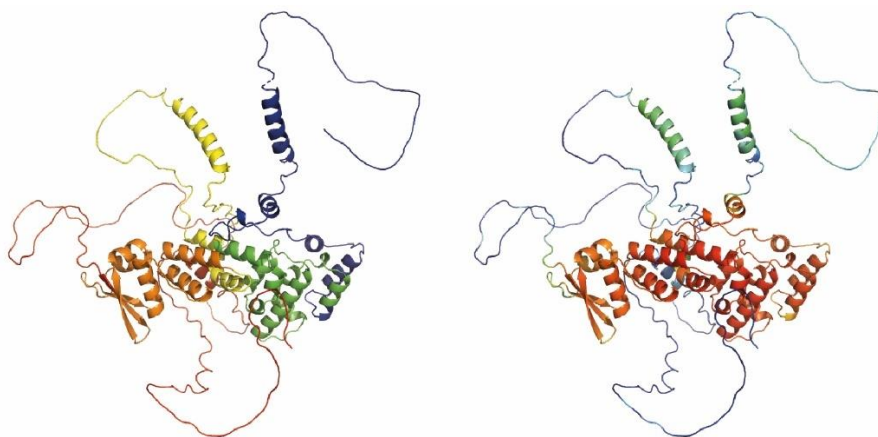


Figure 11. AlphaFold prediction of Axed^{long}. Left: each domain is shown in a different colour (N-terminus, red; BACK, green; BTB, orange; linker, yellow; C-terminus, blue). Right: confidence of the predicted structure (blue = 0%, red = 100%), higher confidence is better.

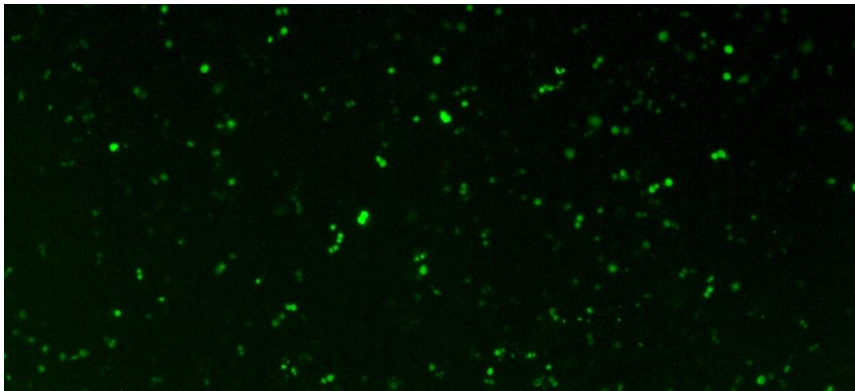
As expected, the DALI homology search revealed many BTB/BACK domain-containing proteins, as it works by superimposing the predicted structure onto other structures in PDB (Annex 2)². Several cytoskeleton-related proteins also appeared in the search, implying that Axed could have a cytoskeleton-related function. Interestingly, the GO terms also indicated that some proteins had a microtubule-binding function (Figure 10). The Axed structure shares similarities with Gigaxonin, a protein—when mutated—linked to giant axonal neuropathy (Mahammad et al., 2013), and with several potassium voltage-gated channels. Potassium currents influence WD (Mishra et al., 2013b).

Together, these results allowed us to purify, detect and classify the possible Axed interactors. The DAVID analysis and the DALI search helped us narrow down our hypotheses and point towards a direction to start investigating the function of Axed.

² "As a rule of thumb, a Z-score above 20 means the two structures are definitely homologous, between 8 and 20 means the two are probably homologous, between 2 and 8 is a gray area, and a Z-Score below 2 is not significant. Small structures will tend to have small Z-scores, whereas a medium Z-score for very large structures need not imply a biologically interesting relationship" (Holm, 2022).

CHAPTER 8

Discussion and perspectives



S2 cultured cells transfected with GFP (20x).

In this section, I will further develop some aspects discussed in the published articles, and the unpublished results.

***Drosophila* as a tool to study axon degeneration**

In the last twenty years, *Drosophila* has emerged as an extremely useful system in which to explore fundamental aspects of neurobiology after neural injury. While the three experimental approaches explained in chapter 1 are the ones that we routinely use the most in our lab, many other experimental designs can be used in *Drosophila* adults such as laser ablation (Soares et al., 2014), ventral nerve cord (VNC) injury (Purice et al., 2017), motor neuron degeneration in flies' legs (Sreedharan et al., 2015) or kicking response stimulated by the mechanical stimulation of the wing (Hsu et al., 2021) among others. In addition, *Drosophila* larvae can also be used to study axon degeneration through larval nerve crush or chemotoxicity-induced degeneration (Rooney & Freeman, 2014).

The speed and simplicity of some experimental approaches, the single axonal resolution, the powerful molecular-genetic tools available and the fact that all the work can be performed *in vivo* to study axon death signalling is unmatched in other model organisms. Some of the genes that promote axon degeneration were first described in flies and then confirmed in mammals (e.g., dSarm (Osterloh et al., 2012), Hiw (Babetto et al., 2013; Xiong et al., 2012), Axed (Neukomm et al., 2017; Schmidt, 2020)).

In addition, several *Drosophila* models of neurodegenerative diseases such as TBI, AD, PD or ALS have been described in the last years (B. Lu & Vogel, 2009). While it is not the scope of this thesis to use or review any of these models, it serves as a clear example of how *Drosophila* is an excellent system for *in vivo* experimentation on this topic.

To date, the signalling pathway of axon death appears to be functionally conserved between flies and mammals, which makes flies a great tool to explore the mechanisms underlying axon degeneration.

The expression of NMN-Deamidase

While the expression of NMN-D in mammals has a clear protective effect on injured axons *in vivo* (di Stefano et al., 2017), its role in *Drosophila* was yet unclear. We showed for the first time in flies that the expression of NMN-D is sufficient to significantly lower NMN levels through metabolite analyses of fly heads. Not only the levels of NMN are lower, but the entire NAD⁺ metabolic flux is altered. Although the metabolite measurements were performed in the absence of injury (e.g., in healthy flies), we expect that these metabolites have similar levels after axonal injury. It would be interesting to measure the metabolites' levels after injury but there is no described method in *Drosophila in vivo*. We can affirm that fly heads are a valuable tool to perform metabolites analyses as a readout for levels of metabolites in neurons (Cox et al., 2017).

Lower NMN levels preserved the morphology of the injured axons for the life span of the fly and its synapses remained circuit integrated for weeks. Lowering NMN levels has a comparable or even better protective effect to loss-of-function mutations in *hiw*, *dsarm* and *axed*, as well as

dnmnat overexpression (Y. Fang et al., 2012; Neukomm et al., 2014, 2017; Osterloh et al., 2012; Xiong et al., 2012). Our result outlasts the protection of 3–5 days accomplished by the expression of NMNd (Hsu et al., 2021). The most plausible explanation is that the N-terminal GFP tag of NMN-D compared to the untagged NMNd provides higher protein stability (Rücker et al., 2001), crucial to continue consuming NMN after injury. Unpublished data from our lab shows that the expression of NMNd depletes NMN levels similar to NMN-D in healthy flies, suggesting that both NMNd and NMN-D have similar kinetics in healthy flies, but NMN-D prevails for longer times after injury.

The modification of the NAD^+ metabolic flux by NMN-D was quite striking. In addition, previous efforts to modulate the flux through overexpression of *dNaam* resulted in an increased median and maximal life span (Balan et al., 2008). Nevertheless, we were surprised to find out that the expression of NMN-D did not influence the life span of flies. A plausible explanation is that flies have homeostasis mechanisms sufficient to compensate for the lower NMN levels or the higher NaMN levels. In line with this, NAD^+ levels are not altered which is crucial not only to prevent neuronal degeneration but for the correct functioning of many other metabolic processes (Sasaki, 2018; Xie et al., 2020).

NAD^+ can be synthesised directly from NMN (e.g., *de novo* pathway) or “indirectly” through NaMN and NaAD (*Preiss-Handler* pathway). Both pathways are *dNmnat* dependent, but the *Preiss-Handler* also depends on Nads. The metabolic analyses suggest that the main production of NAD^+ in wild-type flies is through the *de novo* pathway as NMN is more abundant than NaMN and NaAD. In contrast, when NMN-D is expressed, NaMN and NaAD are more elevated than NMN suggesting that NAD^+ is now produced through the *Preiss-Handler* pathway. That is supported by the disruption of the protection afforded by NMN-D when Nads is knocked down.

In conclusion, the newly developed NMN-D will be useful in many neurodegenerative aspects beyond injury such as in axon morphogenesis and maintenance (Izadifar et al., 2021) and dendrite pruning (Ji et al., 2022).

NMN levels after injury

In this thesis, I provided substantial evidence to confirm that NMN is an instructive signal to activate axon death and trigger axon degeneration after injury. While NMN can be synthesised from NR through NRK1/2 and from NAM through mNAMPT in mammals, *Drosophila* lacks mNAMPT, making *dNrK* the sole enzyme capable of synthesising NMN in flies. We showed for the first time in any model organism that mNAMPT expression in flies results in faster axon degeneration after injury. We know that mNAMPT persists for over 24 h after injury *in vitro* (di Stefano et al., 2014), which is much longer than *dNmnat*'s stability, suggesting that after NAD^+ synthesis is halted, mNAMPT is still able to produce NMN, rising its levels even more than in wild type. Similar experiments in mammals showed opposite effects, as injured axons were protected for up to 48 h. Interestingly, the inhibition of mNAMPT by FK866 attenuated the axon death signalling as well (di Stefano et al., 2014; Sasaki et al., 2016). This difference between species may be explained by the fact that wild-type flies only have one source of NMN (from *dNrK*). Adding a second source of NMN (from mNAMPT) implies increasing the ability to synthesise NMN, and hypothetically *dNmnat* is not capable of consuming all the extra NMN into NAD^+ ,

resulting in elevated NMN levels. Instead, mammals may have a greater capacity to buffer NMN into NAD⁺. For example, overexpression of mNAMPT results in protection because healthy neurons can produce more NAD⁺ while FK866 inhibition prevents NMN from rising after injury.

It would be of special interest to test the inhibition of mNAMPT by FK866 in *Drosophila*, to see whether it reverted the phenotype or if it even provided any protection, or the feeding of NAM with or without the expression of mNAMPT to see whether we could trigger even faster degeneration.

As mentioned above, dNrK is the sole NMN-producing enzyme in flies. Thus, inhibition or loss-of-function mutants of dNrK should impair the NMN synthesis, resulting in axonal protection after injury. Unpublished data from our lab does not support this assumption, as dNrK deficient flies showed wild-type grade axon degeneration. A key question arises from this result: how are axons degenerating considering that there is no NMN synthesis? The wing injury assay is performed using neuronal clones. Only those clones are homozygous for our gene of interest (in this particular case, dNrK deficiency), while the rest of the surrounding tissue is heterozygous or wild type. Injured axons could be receiving NMN from surrounding neurons or glia. Nevertheless, NMN is cell impermeable. NMN would first have to be converted into NR in the extracellular space, transported into the injured axons and then reconverted again into NMN, which makes it a very slow process and thus an improbable explanation. Interestingly, an NMN transporter has been recently characterised *in vitro* in mice (Grozio et al., 2019; Wu & Sinclair, 2019). It remains unknown if the *CG12773* homologue of flies has the same function, but it would speed up the transport of NMN through cells and tissues. In that case, it would be of interest to test what happens in dNrK deficient flies together with the inhibition of the NMN transporter.

The overexpression of dNrK could also result in faster axon degeneration, as observed with mNAMPT. While this hypothesis remains to be tested, the ubiquitous overexpression of dNrK with *Actin-Gal4* and 50 mM supplementation of NR results in lethality (unpublished), suggesting that too high NMN levels could be toxic/prodegenerative, and thus lethal for the flies. It is therefore reasonable to assume that the overexpression of mNAMPT with NAM supplementation is also resulting in lethality. In both cases, it will be interesting to see whether NMN-consuming enzymes such as NMN-D or dNmnat overexpression could revert the lethality.

NMN to NAD⁺ ratio

Until now, we've focused our attention on levels of NMN, but we know that NAD⁺ levels and the ratio between them are crucial as well.

We showed how *nmnat* mutants triggered spontaneous neurodegeneration in 1 to 5-day-old flies. All the NAD⁺ synthesis is dNmnat dependent, thus the lack of dNmnat impairs the NAD⁺ synthesis and neurons subsequently die (Chapter 3). The lack of dNmnat implies that NMN accumulates. Much to our surprise, when we expressed NMN-D in flies lacking dNmnat, neurodegeneration was delayed for several days, suggesting that neurons with low NAD⁺ levels can still survive if NMN is also low.

Until recently, NAD⁺ levels were thought to be the sole contributor to axon degeneration and neurodegenerative diseases (Gilley et al., 2013, 2015, 2018; Gilley & Coleman, 2010). How can neurons survive for longer periods if NAD⁺ is low? The NMN/NAD⁺ ratio has the answer. Below I will try to argue the NMN/NAD⁺ ratios of some of our experiments to explain which ones trigger axon degeneration and which are protective.

- 1) Basal NMN and NAD⁺ (NMN < NAD⁺): this ratio is observed in healthy axons. After injury, NMN can rise (and outcompete NAD⁺) and thus activate axon death signalling.
- 2) Lower NMN and basal NAD⁺ (NMN << NAD⁺): NMN is lowered by NMN-D, whereas NAD⁺ remains unchanged. After injury, NMN fails to rise, thus severed axons are long term preserved.
- 3) Lower NMN and lower NAD⁺ (NAD⁺ < NAD⁺): NMN is lowered by NMN-D, while NAD⁺ is lowered by *Nads^{RNAi}*. After injury, NMN fails to rise, however, NAD⁺ is not high enough to prevent the activation of axon death signalling. Severed axons partially degenerate.
- 4) Higher NMN and basal NAD⁺ (NMN > NAD⁺): NMN is raised by mNAMPT expression, while NAD⁺ remains unchanged. After injury, axons degenerate faster.

Looking at these results, a motif comes up. The ratio needs to be in favour of NAD⁺ to have a protective effect after injury. NMN and NAD⁺ have opposing functions; while NMN works as an instructive signal to trigger axon degeneration, NAD⁺ maintains the axon death signalling pathway inactive. Point 3 shows low NMN and low NAD⁺ but in one case we observe a protective effect and in the other a pro-degenerative effect. This must be due to differences in the ratio between experiments. It shows us that the tipping point of the ratio from protective to pro-degenerative must be somewhere between these two experiments. It also poses the question of whether neurons can obtain NAD⁺ from alternative sources such as NADP/NADPH or surrounding glia (Estrella et al., 2019; Ying, 2008). NAD⁺ is necessary for many metabolic processes, and the lack of it is still detrimental for the cells even if the ratio favours the inhibition of axon death (Sasaki, 2018).

Our results are consistent with previous studies where robust axonal protection was observed in mammalian neurons in three conditions: 1) low levels of NMN and NAD⁺, 2) normal levels of NMN and NAD⁺ and 3) high levels of NMN and NAD⁺ (Sasaki et al., 2016). Figley et al., 2021 also described how an increased NMN to NAD⁺ ratio is pro-degenerative *in vitro*.

SARM1/dSarm as a central executioner of axon degeneration

If the NMN to NAD⁺ ratio is the instructive signal, who is the sensor?

We've shown that dSarm is activated by NMN both *in vitro* and *in vivo* and that NMN binds directly to the auto-inhibitory ARM domain of dSarm as a point mutation that prevents the binding of NMN resulting in a non-inducible dSarm. Other studies have recently published the crystal structure of SARM1, showing that NMN and NAD⁺ compete to bind to the same allosteric site (Figley et al., 2021; Shi et al., 2022). While NAD⁺-bound SARM1 remains inhibited, the substitution of NAD⁺ by NMN triggers reorientation of the ARM domains, and the TIR domains

self-associate to start NAD⁺ hydrolysis that ultimately leads to axon degeneration (Shi et al., 2022; Sporny et al., 2020). This mechanism ensures that in the presence of NMNAT2/dNmnat (e.g., in healthy neurons), SARM1 is always inhibited. SARM1 might be temporarily activated in situations where NMN is momentarily increased, for example by dietary precursor supplementation. But the NMN/NAD⁺ ratio should return quickly to baseline. It is a consensus agreement that keeping SARM1/dSarm inhibited after injury is crucial, and that this can only be accomplished by keeping the NMN/NAD⁺ ratio favourable to NAD⁺ (Figley et al., 2021; Sambashivan & Freeman, 2021).

The understanding of SARM1/dSarm is now much more complete thanks to the precise characterization of the 3D structure and the mechanistic regulation of SARM1. Hopefully, this will provide potential investigations to develop new therapeutic strategies for SARM1 inhibition, such as inhibitors of the allosteric binding site of NMN, the NADase activity or the self-association of the SAM domains (Bratkowski et al., 2020; Figley et al., 2021; Shi et al., 2022; Sporny et al., 2019).

The recently acquainted knowledge of SARM1/dSarm invites the field to try to make a switch to focus on characterizing the cellular and molecular events downstream of SARM1 activation. Are there any effectors downstream of SARM1 that could also be inhibited to block axon degeneration? We already described that Axed acts downstream of dSarm, but it remains unknown whether Axed has a similar function in mammals.

CRISPR/Cas9 mediated KO

The use of traditional genetic mutations enables the manipulation of the genome to study every gene function. Nevertheless, working with traditional mutations has some limitations; for example, it is very difficult to study genes that are homozygous lethal. The discovery CRISPR system enabled the tissue-specific knockout of any gene of interest, converting it into a very powerful technology for tissue-specific mutagenesis (Bassett & Liu, 2014; Jinek et al., 2012).

We generated *sgRNAs* for our genes of interest and tested their efficiency in *Drosophila in vivo*. We show how *dnmnat^{sgRNA}* had a comparable effect to a traditional mutant (*dnmnat¹*) while the rest of the *sgRNAs* tested (*dsarm^{sgRNA}*, *hiw^{sgRNA}* and *axed^{sgRNA}*) were less efficient as we observed axon degeneration at 7 dpa, which is never the case with traditional mutants. Interestingly, we observed how different Cas9-driven expressions lead to different results: *Actin-Cas9* had a better performance with *dsarm^{sgRNA}*, *hiw^{sgRNA}* and *axed^{sgRNA}* while it was lethal combined with *dnmnat^{sgRNA}*, where we used a *UAS-Cas9* version instead. This suggests that every *sgRNA* should be tested beforehand to select the better-suited Cas9. Different Cas9-expressing transgenes with different patterns of endonuclease activities are now available to the community, as well as different tools to optimise the generation of *sgRNAs* (Koreman et al., 2021; Port et al., 2014, 2020).

Until the discovery of CRISPR, the most used tool to silence genes was RNAi. RNAi interferes with mRNA to generate knockdowns while CRISPR has the potential to generate Knockouts at the DNA level with limited off-target effects (Boettcher & McManus, 2015). Nevertheless, CRISPR resembles a knockdown rather than a knockout in our hands.

In conclusion, CRISPR can be a very powerful technique to knock down/knockout genes of interest, but it still needs some improvements to be made. Efforts from the community to generate new and optimised tools, libraries of *sgRNA* to perform screenings and novel applications of CRISPR (such as overexpression of genes) are the best examples that CRISPR will soon show its full potential (Bassett & Liu, 2014; Gratz et al., 2015; Huynh et al., 2018; Koreman et al., 2021; Meltzer et al., 2019; Port et al., 2014, 2020).

The function of Axed

Axed is the most downstream gene required for injury-induced axon degeneration in *Drosophila*, so far. Nevertheless, its mechanistic function remains currently unknown.

Here, I have shown that *Axed* *in vivo* purifications can be readily and robustly performed from whole *Drosophila* heads, which mainly consist of brain tissue. Using this procedure, potential *Axed*-interacting proteins should also be co-immunoprecipitated. The subsequent use of tandem mass spectrometry greatly facilitates the identification of individual *Axed*-interactome proteins that can be grouped and analysed into GO terms of biological processes, cellular compartments, and molecular functions. Finally, the 3D structure prediction of *Axed* using AlphaFold can help discover similarly folded proteins that may (or may not) share the same biological function. These approaches should help us decipher the precise mechanistic function of *Axed*, or at least identify novel essential proteins of the axon death signalling cascade.

Based on our results, *Axed* could be involved in 1) protein folding. *Axed* could be changing the conformation of other proteins to activate or inhibit them; 2) ATP energetics. ATP consumption is essential for cell survival. The impairment of ATP synthesis or ATP consumption results in energetic failure and ultimately axon degeneration (Chamberlain & Sheng, 2019); 3) mitochondrial regulation. ATP is mostly synthesised in mitochondria. Mitochondria are also responsible for calcium homeostasis or signal transmission. Several reports have described the crucial role of mitochondria in axon degeneration (Avery et al., 2012; Campbell & Mahad, 2018; Y. Fang et al., 2012; B. Wang et al., 2021); and 4) cytoskeleton dynamics. The disassembly of the cytoskeleton is a hallmark of axon degeneration. The regulation of the cytoskeleton can influence the outcome of injury-induced axon degeneration (Griffin et al., 1995).

A limitation of the co-IPs performed to date is that we used healthy flies (e.g., when the axon death signalling pathway is inactive). Some *Axed*-interacting proteins may only interact with *Axed* when axon death is activated. It would be of great interest to compare the results of a co-IP where axon death is activated (e.g., *dsarm*^{ARM}), or attenuated (expression of *dnmnat*, or NMN-D).

Finally, it remains unknown whether orthologs of *Axed* in mammals may have the same function. The only hint up to date is an experiment where the knockdown of two of the four orthologues (BTB3 and BTB6) delayed cell death triggered by a constitutively active SARM1 protein (Schmidt, 2020). It suggests that *Axed* function would be preserved between flies and mammals, as is the case for the rest of the axon death pathway.

FINAL REMARKS

At my mid-term evaluation, I wrote:

“The major two questions I would like to address within the next two years are the following ones:

- 1) *What is the precise function of Axed in the axon death signalling pathway?
(...)*
- 2) *How do metabolites modulate axon death signalling?”*

Unfortunately, the precise function of Axed remains unknown. Some advancements have been made and we are one step closer to understanding Axed than we were three years ago. Nevertheless, there is still a long way to go.

On the other hand, we’ve been able to extensively comprehend the NAD⁺ metabolic flux in healthy flies and an activated axon death context. I’ve been able to modulate the metabolic levels of flies and we’ve come to the understanding that NMN/NAD⁺ ratio dictates the fate of injured axons. Additionally, I’ve also described that dSarm is the metabolic sensor of the NMN/NAD⁺ ratio that activates when the ratio tips towards NMN.

Overall, the characterization of the metabolites and genes in axon death signalling has shed light on a process that was long thought to be a passive wasting away of the severed axons (Waller, 1850). Today, we know that this pathway is not only activated upon injury but also in other neurological conditions where axonopathies occur in the absence of injury. I hope that my research has expanded the knowledge of the axon death pathway in axon and neurodegeneration.

REFERENCES

- Adalbert, R., Gillingwater, T. H., Haley, J. E., Bridge, K., Beirowski, B., Berek, L., Wagner, D., Grumme, D., Thomson, D., Celik, A., Addicks, K., Ribchester, R. R., & Coleman, M. P. (2005). A rat model of slow Wallerian degeneration (WldS) with improved preservation of neuromuscular synapses. *European Journal of Neuroscience*, *21*(1), 271–277. <https://doi.org/10.1111/j.1460-9568.2004.03833.x>
- Adalbert, R., Morreale, G., Paizs, M., Conforti, L., Walker, S. A., Roderick, H. L., Bootman, M. D., Siklós, L., & Coleman, M. P. (2012). Intra-axonal calcium changes after axotomy in wild-type and slow Wallerian degeneration axons. *Neuroscience*, *225*, 44–54. <https://doi.org/10.1016/j.neuroscience.2012.08.056>
- Ali, Y. O., Bradley, G., & Lu, H.-C. (2017). Screening with an NMNAT2-MSD platform identifies small molecules that modulate NMNAT2 levels in cortical neurons. *Scientific Reports*, *7*(1), 43846. <https://doi.org/10.1038/srep43846>
- Araki, T. (2004). Increased Nuclear NAD Biosynthesis and SIRT1 Activation Prevent Axonal Degeneration. *Science*, *305*(5686), 1010–1013. <https://doi.org/10.1126/science.1098014>
- Avery, M. A., Rooney, T. M., Pandya, J. D., Wishart, T. M., Gillingwater, T. H., Geddes, J. W., Sullivan, P. G., & Freeman, M. R. (2012). WldS Prevents Axon Degeneration through Increased Mitochondrial Flux and Enhanced Mitochondrial Ca²⁺ Buffering. *Current Biology*, *22*(7), 596–600. <https://doi.org/10.1016/J.CUB.2012.02.043>
- Avery, M. A., Sheehan, A. E., Kerr, K. S., Wang, J., & Freeman, M. R. (2009). Wld^s requires Nmnatl enzymatic activity and N16- VCP interactions to suppress Wallerian degeneration. *Journal of Cell Biology*, *184*(4), 501–513. <https://doi.org/10.1083/jcb.200808042>
- Babetto, E., Beirowski, B., Janeckova, L., Brown, R., Gilley, J., Thomson, D., Ribchester, R. R., & Coleman, M. P. (2010). Targeting NMNAT1 to Axons and Synapses Transforms Its Neuroprotective Potency In Vivo. *Journal of Neuroscience*, *30*(40), 13291–13304. <https://doi.org/10.1523/JNEUROSCI.1189-10.2010>
- Babetto, E., Beirowski, B., Russler, E., Milbrandt, J., & DiAntonio, A. (2013). The Phr1 Ubiquitin Ligase Promotes Injury-Induced Axon Self-Destruction. *Cell Reports*, *3*(5), 1422–1429. <https://doi.org/10.1016/j.celrep.2013.04.013>
- Balan, V., Miller, G. S., Kaplun, L., Balan, K., Chong, Z. Z., Li, F., Kaplun, A., VanBerkum, M. F. A., Arking, R., Freeman, D. C., Maiese, K., & Tzivion, G. (2008). Life span extension and neuronal cell protection by *Drosophila* nicotinamidase. *Journal of Biological Chemistry*, *283*(41), 27810–27819. <https://doi.org/10.1074/jbc.M804681200>
- Barrientos, S. A., Martinez, N. W., Yoo, S., Jara, J. S., Zamorano, S., Hetz, C., Twiss, J. L., Alvarez, J., & Court, F. A. (2011). Axonal Degeneration Is Mediated by the Mitochondrial Permeability Transition Pore. *Journal of Neuroscience*, *31*(3), 966–978. <https://doi.org/10.1523/JNEUROSCI.4065-10.2011>
- Bassett, A. R., & Liu, J. L. (2014). CRISPR/Cas9 and Genome Editing in *Drosophila*. *Journal of Genetics and Genomics*, *41*(1), 7–19. <https://doi.org/10.1016/J.JGG.2013.12.004>
- Beirowski, B., Adalbert, R., Wagner, D., Grumme, D. S., Addicks, K., Ribchester, R. R., & Coleman, M. P. (2005). The progressive nature of Wallerian degeneration in wild-type and slow Wallerian degeneration (WldS) nerves. *BMC Neuroscience*, *6*(1), 1–27. <https://doi.org/10.1186/1471-2202-6-6/FIGURES/14>

- Beirowski, B., Babetto, E., Gilley, J., Mazzola, F., Conforti, L., Janeckova, L., Magni, G., Ribchester, R. R., & Coleman, M. P. (2009). Non-Nuclear WldS Determines Its Neuroprotective Efficacy for Axons and Synapses In Vivo. *Journal of Neuroscience*, *29*(3), 653–668. <https://doi.org/10.1523/JNEUROSCI.3814-08.2009>
- Berger, F., Lau, C., Dahlmann, M., & Ziegler, M. (2005). Subcellular compartmentation and differential catalytic properties of the three human nicotinamide mononucleotide adenylyltransferase isoforms. *The Journal of Biological Chemistry*, *280*(43), 36334–36341. <https://doi.org/10.1074/jbc.M508660200>
- Bernardi, P., Krauskopf, A., Basso, E., Petronilli, V., Blalchy-Dyson, E., di Lisa, F., & Forte, M. A. (2006). The mitochondrial permeability transition from in vitro artifact to disease target. *FEBS Journal*, *273*(10), 2077–2099. <https://doi.org/10.1111/j.1742-4658.2006.05213.x>
- Bloom, A. J., Mao, X., Strickland, A., Sasaki, Y., Milbrandt, J., & DiAntonio, A. (2022). Constitutively active SARM1 variants that induce neuropathy are enriched in ALS patients. *Molecular Neurodegeneration*, *17*(1), 1–15. <https://doi.org/10.1186/s13024-021-00511-x/FIGURES/5>
- Boettcher, M., & McManus, M. T. (2015). Choosing the Right Tool for the Job: RNAi, TALEN or CRISPR. *Molecular Cell*, *58*(4), 575. <https://doi.org/10.1016/j.molcel.2015.04.028>
- Bratkowski, M., Xie, T., Thayer, D. A., Brown, S. P., Bai, X., Correspondence, S. S., Lad, S., Mathur, P., Yang, Y.-S., Danko, G., Burdett, T. C., Danao, J., Cantor, A., Kozak, J. A., & Sambashivan, S. (2020). *Structural and Mechanistic Regulation of the Pro-degenerative NAD Hydrolase SARM1*. <https://doi.org/10.1016/j.celrep.2020.107999>
- Bridge, P. M., Ball, D. J., Mackinnon, S. E., Nakao, Y., Brandt, K., Hunter, D. A., & Hertl, C. (1994). Nerve Crush Injuries—A Model for Axonotmesis. *Experimental Neurology*, *127*(2), 284–290. <https://doi.org/10.1006/EXNR.1994.1104>
- Büki, A., Siman, R., Trojanowski, J. Q., & Povlishock, J. T. (1999). The role of calpain-mediated spectrin proteolysis in traumatically induced axonal injury. *Journal of Neuropathology and Experimental Neurology*, *58*(4), 365–375. <http://www.ncbi.nlm.nih.gov/pubmed/10218632>
- Burgess, R. W., & Crish, S. D. (2018). Editorial: Axonopathy in Neurodegenerative Disease. *Frontiers in Neuroscience*, *12*, 769. <https://doi.org/10.3389/fnins.2018.00769>
- Burke, R. E., & O'Malley, K. (2013). Axon degeneration in Parkinson's disease. *Experimental Neurology*, *246*, 72–83. <https://doi.org/10.1016/j.expneurol.2012.01.011>
- Campbell, G., & Mahad, D. J. (2018). Mitochondrial dysfunction and axon degeneration in progressive multiple sclerosis. *FEBS Letters*, *592*(7), 1113–1121. <https://doi.org/10.1002/1873-3468.13013>
- Chamberlain, K. A., & Sheng, Z. H. (2019). Mechanisms for the maintenance and regulation of axonal energy supply. *Journal of Neuroscience Research*, *97*(8), 897. <https://doi.org/10.1002/jnr.24411>
- Chuang, C.-F., & Bargmann, C. I. (2005). A Toll-interleukin 1 repeat protein at the synapse specifies asymmetric odorant receptor expression via ASK1 MAPKKK signaling. *Genes & Development*, *19*(2), 270–281. <https://doi.org/10.1101/gad.1276505>
- Coleman, M. P., & Perry, V. H. (2002). Axon pathology in neurological disease: a neglected therapeutic target. *Trends in Neurosciences*, *25*(10), 532–537. [https://doi.org/10.1016/S0166-2236\(02\)02255-5](https://doi.org/10.1016/S0166-2236(02)02255-5)

- Conforti, L., Gilley, J., & Coleman, M. P. (2014). Wallerian degeneration: an emerging axon death pathway linking injury and disease. *Nature Reviews Neuroscience*, *15*(6), 394–409. <https://doi.org/10.1038/nrn3680>
- Conforti, L., Tarlton, A., Mack, T. G., Mi, W., Buckmaster, E. A., Wagner, D., Perry, V. H., & Coleman, M. P. (2000). A Ufd2/D4Cole1e chimeric protein and overexpression of Rbp7 in the slow Wallerian degeneration (WldS) mouse. *Proceedings of the National Academy of Sciences of the United States of America*, *97*(21), 11377–11382. <https://doi.org/10.1073/pnas.97.21.11377>
- Cox, J. E., Thummel, C. S., & Tennessen, J. M. (2017). Metabolomic Studies in Drosophila. *Genetics*, *206*(3), 1169. <https://doi.org/10.1534/GENETICS.117.200014>
- Desbois, M., Crawley, O., Evans, P. R., Baker, S. T., Masuho, I., Yasuda, R., & Grill, B. (2018). PAM forms an atypical SCF ubiquitin ligase complex that ubiquitinates and degrades NMNAT2. *Journal of Biological Chemistry*, *293*(36), 13897–13909. <https://doi.org/10.1074/jbc.RA118.002176>
- di Stefano, M., Loreto, A., Orsomando, G., Mori, V., Zamporlini, F., Hulse, R. P., Webster, J., Donaldson, L. F., Gering, M., Raffaelli, N., Coleman, M. P., Gilley, J., & Conforti, L. (2017). NMN Deamidase Delays Wallerian Degeneration and Rescues Axonal Defects Caused by NMNAT2 Deficiency In Vivo. *Current Biology : CB*, *27*(6), 784–794. <https://doi.org/10.1016/j.CUB.2017.01.070>
- di Stefano, M., Nascimento-Ferreira, I., Orsomando, G., Mori, V., Gilley, J., Brown, R., Janeckova, L., Vargas, M. E., Worrell, L. A., Loreto, A., Tickle, J., Patrick, J., Webster, J. R. M., Marangoni, M., Carpi, F. M., Pucciarelli, S., Rossi, F., Meng, W., Sagasti, A., ... Conforti, L. (2014). A rise in NAD precursor nicotinamide mononucleotide (NMN) after injury promotes axon degeneration. *Cell Death & Differentiation* *2015* *22*:5, 22(5), 731–742. <https://doi.org/10.1038/cdd.2014.164>
- di Stefano, M., Nascimento-Ferreira, I., Orsomando, G., Mori, V., Gilley, J., Brown, R., Janeckova, L., Vargas, M. E., Worrell, L. A., Loreto, A., Tickle, J., Patrick, J., Webster, J. R. M., Marangoni, M., Carpi, F. M., Pucciarelli, S., Rossi, F., Meng, W., Sagasti, A., ... Conforti, L. (2015). A rise in NAD precursor nicotinamide mononucleotide (NMN) after injury promotes axon degeneration. *Cell Death and Differentiation*, *22*(5), 731–742. <https://doi.org/10.1038/cdd.2014.164>
- Eddleman, C. S., Ballinger, M. L., Smyers, M. E., Fishman, H. M., & Bittner, G. D. (1998). Endocytotic formation of vesicles and other membranous structures induced by Ca²⁺ and axolemmal injury. *Journal of Neuroscience*, *18*(11), 4029–4041. <https://doi.org/10.1523/jneurosci.18-11-04029.1998>
- Essuman, K., Summers, D. W., Sasaki, Y., Mao, X., DiAntonio, A., & Milbrandt, J. (2017). The SARM1 Toll/Interleukin-1 Receptor Domain Possesses Intrinsic NAD⁺Cleavage Activity that Promotes Pathological Axonal Degeneration. *Neuron*, *93*(6), 1334-1343.e5. <https://doi.org/10.1016/j.neuron.2017.02.022>
- Estrella, M. A., Du, J., Chen, L., Rath, S., Prangley, E., Chitrakar, A., Aoki, T., Schedl, P., Rabinowitz, J., & Korennykh, A. (2019). The metabolites NADP⁺ and NADPH are the targets of the circadian protein Nocturnin (Curled). *Nature Communications* *2019* *10*:1, *10*(1), 1–10. <https://doi.org/10.1038/s41467-019-10125-z>
- Fang, E. F., Lautrup, S., Hou, Y., Demarest, T. G., Croteau, D. L., Mattson, M. P., & Bohr, V. A. (2017). NAD⁺ in Aging: Molecular Mechanisms and Translational Implications. *Trends in Molecular Medicine*, *23*(10), 899–916. <https://doi.org/10.1016/J.MOLMED.2017.08.001>

- Fang, Y., Soares, L., Teng, X., Geary, M., & Bonini, N. M. (2012). A novel drosophila model of nerve injury reveals an essential role of Nmnat in maintaining axonal integrity. *Current Biology*, *22*(7), 590–595. <https://doi.org/10.1016/j.cub.2012.01.065>
- Feng, Y., Yan, T., Zheng, J., Ge, X., Mu, Y., Zhang, Y., Wu, D., Du, J. lin, & Zhai, Q. (2010). Overexpression of WldSor Nmnat2 in mauthner cells by single-cell electroporation delays axon degeneration in live zebrafish. *Journal of Neuroscience Research*, *88*(15), 3319–3327. <https://doi.org/10.1002/jnr.22498>
- Ferri, A., Sanes, J. R., Coleman, M. P., Cunningham, J. M., & Kato, A. C. (2003). Inhibiting Axon Degeneration and Synapse Loss Attenuates Apoptosis and Disease Progression in a Mouse Model of Motoneuron Disease. *Current Biology*, *13*(8), 669–673. [https://doi.org/10.1016/S0960-9822\(03\)00206-9](https://doi.org/10.1016/S0960-9822(03)00206-9)
- Figley, M. D., Gu, W., Nanson, J. D., Shi, Y., Sasaki, Y., Cunnea, K., Malde, A. K., Jia, X., Luo, Z., Saikot, F. K., Mosaib, T., Masic, V., Holt, S., Hartley-Tassell, L., McGuinness, H. Y., Manik, M. K., Bosanac, T., Landsberg, M. J., Kerry, P. S., ... Ve, T. (2021). SARM1 is a metabolic sensor activated by an increased NMN/NAD⁺ ratio to trigger axon degeneration. *Neuron*, *109*(7), 1118–1136.e11. <https://doi.org/10.1016/J.NEURON.2021.02.009>
- Finn, J. T., Weil, M., Archer, F., Siman, R., Srinivasan, A., & Raff, M. C. (2000). Evidence That Wallerian Degeneration and Localized Axon Degeneration Induced by Local Neurotrophin Deprivation Do Not Involve Caspases. *Journal of Neuroscience*, *20*(4), 1333–1341. <https://doi.org/10.1523/JNEUROSCI.20-04-01333.2000>
- Flatters, S. J. L., Dougherty, P. M., & Colvin, L. A. (2017). Clinical and preclinical perspectives on Chemotherapy-Induced Peripheral Neuropathy (CIPN): a narrative review. *British Journal of Anaesthesia*, *119*(4), 737–749. <https://doi.org/10.1093/bja/aex229>
- Fournier, A. J., Hogan, J. D., Rajbhandari, L., Shrestha, S., Venkatesan, A., & Ramesh, K. T. (2015). Changes in Neurofilament and Microtubule Distribution following Focal Axon Compression. *PLOS ONE*, *10*(6), e0131617. <https://doi.org/10.1371/journal.pone.0131617>
- Geisler, S., Doan, R. A., Strickland, A., Huang, X., Milbrandt, J., & DiAntonio, A. (2016). Prevention of vincristine-induced peripheral neuropathy by genetic deletion of SARM1 in mice. *Brain*, *139*(12), 3092–3108. <https://doi.org/10.1093/brain/aww251>
- Geisler, S., Huang, S. X., Strickland, A., Doan, R. A., Summers, D. W., Mao, X., Park, J., DiAntonio, A., & Milbrandt, J. (2019). Gene therapy targeting SARM1 blocks pathological axon degeneration in mice. *The Journal of Experimental Medicine*, *216*(2), 294–303. <https://doi.org/10.1084/JEM.20181040>
- George, B., Glass, D., & Griffin, W. (1995). Axotomy-Induced Axonal Degeneration Influx Through Ion-Specific Channels. *The Journal of Neuroscience*, *15*(10), 6445–6452.
- George, R., & Griffin, J. W. (1994). Delayed macrophage responses and myelin clearance during Wallerian degeneration in the central nervous system: the dorsal radiclotomy model. *Experimental Neurology*, *129*(2), 225–236. <https://doi.org/10.1006/EXNR.1994.1164>
- Gerds, J., Brace, E. J., Sasaki, Y., DiAntonio, A., & Milbrandt, J. (2015). SARM1 activation triggers axon degeneration locally via NAD⁺ destruction. *Science (New York, N.Y.)*, *348*(6233), 453–457. <https://doi.org/10.1126/science.1258366>

- Gerdtts, J., Summers, D. W., Milbrandt, J., & DiAntonio, A. (2016). Axon Self-Destruction: New Links among SARM1, MAPKs, and NAD⁺ Metabolism. *Neuron*, *89*(3), 449–460. <https://doi.org/10.1016/J.NEURON.2015.12.023>
- Gerdtts, J., Summers, D. W., Sasaki, Y., DiAntonio, A., & Milbrandt, J. (2013). Sarm1-Mediated Axon Degeneration Requires Both SAM and TIR Interactions. *Journal of Neuroscience*, *33*(33), 13569–13580. <https://doi.org/10.1523/JNEUROSCI.1197-13.2013>
- Gilley, J., Adalbert, R., Yu, G., & Coleman, M. P. (2013). Rescue of Peripheral and CNS Axon Defects in Mice Lacking NMNAT2. *Journal of Neuroscience*, *33*(33), 13410–13424. <https://doi.org/10.1523/JNEUROSCI.1534-13.2013>
- Gilley, J., & Coleman, M. P. (2010). Endogenous Nmnat2 Is an Essential Survival Factor for Maintenance of Healthy Axons. *PLoS Biology*, *8*(1). <https://doi.org/10.1371/journal.pbio.1000300>
- Gilley, J., Mayer, P. R., Yu, G., & Coleman, M. P. (2018). Low levels of NMNAT2 compromise axon development and survival. *Human Molecular Genetics*. <https://doi.org/10.1093/hmg/ddy356>
- Gilley, J., Orsomando, G., Nascimento-Ferreira, I., & Coleman, M. P. (2015). Absence of SARM1 rescues development and survival of NMNAT2-Deficient axons. *Cell Reports*, *10*(12), 1975–1982. <https://doi.org/10.1016/j.celrep.2015.02.060>
- Gilley, J., Ribchester, R. R., & Coleman, M. P. (2017). Sarm1 Deletion, but Not WldS, Confers Lifelong Rescue in a Mouse Model of Severe Axonopathy. *Cell Reports*, *21*(1), 10–16. <https://doi.org/10.1016/j.celrep.2017.09.027>
- Glass, J. D., Schryer, B. L., & Griffin, J. W. (1994). Calcium-Mediated Degeneration of the Axonal Cytoskeleton in the Ola Mouse. *Journal of Neurochemistry*, *62*(6), 2472–2475. <https://doi.org/10.1046/J.1471-4159.1994.62062472.X>
- Gossmann, T. I., Ziegler, M., Puntervoll, P., de Figueiredo, L. F., Schuster, S., & Heiland, I. (2012). NAD⁺ biosynthesis and salvage – a phylogenetic perspective. *The FEBS Journal*, *279*(18), 3355–3363. <https://doi.org/10.1111/J.1742-4658.2012.08559.X>
- Gratz, S. J., Rubinstein, C. D., Harrison, M. M., Wildonger, J., & O'Connor-Giles, K. M. (2015). CRISPR-Cas9 genome editing in Drosophila. *Current Protocols in Molecular Biology / Edited by Frederick M. Ausubel ... [et Al.]*, *111*, 31.2.1. <https://doi.org/10.1002/0471142727.MB3102S111>
- Griffin, J. W., George, E. B., Hsieh, S. T., & Glass, J. D. (1995). Axonal degeneration and disorders of the axonal cytoskeleton. *The Axon: Structure, Function and Pathophysiology*. <https://doi.org/10.1093/ACPROF:OSO/9780195082937.003.0020>
- Grisold, W., Cavaletti, G., & Windebank, A. J. (2012). Peripheral neuropathies from chemotherapeutics and targeted agents: diagnosis, treatment, and prevention. *Neuro-Oncology*, *14*(suppl 4), iv45–iv54. <https://doi.org/10.1093/neuonc/nos203>
- Grozio, A., Mills, K. F., Yoshino, J., Bruzzone, S., Sociali, G., Tokizane, K., Lei, H. C., Cunningham, R., Sasaki, Y., Migaud, M. E., & Imai, S. ichiro. (2019). Slc12a8 is a nicotinamide mononucleotide transporter. *Nature Metabolism*, *1*(1), 47. <https://doi.org/10.1038/S42255-018-0009-4>

- Hammarlund, M., Jorgensen, E. M., & Bastiani, M. J. (2007). Axons break in animals lacking beta-spectrin. *The Journal of Cell Biology*, *176*(3), 269–275. <https://doi.org/10.1083/jcb.200611117>
- Hampel, S., Franconville, R., Simpson, J. H., & Seeds, A. M. (2015). A neural command circuit for grooming movement control. *ELife*, *4*(September). <https://doi.org/10.7554/eLife.08758>
- Henninger, N., Bouley, J., Sikoglu, E. M., An, J., Moore, C. M., King, J. A., Bowser, R., Freeman, M. R., & Brown, R. H. (2016). Attenuated traumatic axonal injury and improved functional outcome after traumatic brain injury in mice lacking Sarm1. *Brain*, *139*(4), 1094–1105. <https://doi.org/10.1093/brain/aww001>
- Herrmann, K. A., Liu, Y., Llobet-Rosell, A., McLaughlin, C. N., Neukomm, L. J., Coutinho-Budd, J. C., & Broihier, H. T. (2022). Divergent signaling requirements of dSARM in injury-induced degeneration and developmental glial phagocytosis. *PLOS Genetics*, *18*(6), e1010257. <https://doi.org/10.1371/JOURNAL.PGEN.1010257>
- Hicks, A. N., Lorenzetti, D., Gilley, J., Lu, B., Andersson, K. E., Miligan, C., Overbeek, P. A., Oppenheim, R., & Bishop, C. E. (2012). Nicotinamide mononucleotide adenylyltransferase 2 (Nmnat2) regulates axon integrity in the mouse embryo. *PLoS One*, *7*(10). <https://doi.org/10.1371/JOURNAL.PONE.0047869>
- Hill, C. S., Coleman, M. P., & Menon, D. K. (2016). Traumatic Axonal Injury: Mechanisms and Translational Opportunities. *Trends in Neurosciences*, *39*(5), 311–324. <https://doi.org/10.1016/j.tins.2016.03.002>
- Holm, L. (2022). Dali server: structural unification of protein families. *Nucleic Acids Research*, *50*(W1), W210–W215. <https://doi.org/10.1093/NAR/GKAC387>
- Hoopfer, E. D., McLaughlin, T., Watts, R. J., Schuldiner, O., O’Leary, D. D. M., & Luo, L. (2006). Wlds Protection Distinguishes Axon Degeneration following Injury from Naturally Occurring Developmental Pruning. *Neuron*, *50*(6), 883–895. <https://doi.org/10.1016/j.neuron.2006.05.013>
- Hou, Y., Dan, X., Babbar, M., Wei, Y., Hasselbalch, S. G., Croteau, D. L., & Bohr, V. A. (2019a). Ageing as a risk factor for neurodegenerative disease. *Nature Reviews Neurology*. <https://doi.org/10.1038/s41582-019-0244-7>
- Hou, Y., Dan, X., Babbar, M., Wei, Y., Hasselbalch, S. G., Croteau, D. L., & Bohr, V. A. (2019b). Ageing as a risk factor for neurodegenerative disease. *Nature Reviews. Neurology*. <https://doi.org/10.1038/s41582-019-0244-7>
- Hsu, J. M., Kang, Y., Corty, M. M., Mathieson, D., Peters, O. M., & Freeman, M. R. (2021). Injury-Induced Inhibition of Bystander Neurons Requires dSarm and Signaling from Glia. *Neuron*, *109*(3), 473-487.e5. <https://doi.org/10.1016/J.NEURON.2020.11.012>
- Huppke, P., Wegener, E., Gilley, J., Angeletti, C., Kurth, I., Drenth, J. P. H., Stadelmann, C., Barrantes-Freer, A., Brück, W., Thiele, H., Nürnberg, P., Gärtner, J., Orsomando, G., & Coleman, M. P. (2019). Homozygous NMNAT2 mutation in sisters with polyneuropathy and erythromelalgia. *Experimental Neurology*, *320*, 112958. <https://doi.org/10.1016/J.EXPNEUROL.2019.112958>
- Huynh, N., Zeng, J., Liu, W., & King-Jones, K. (2018). A Drosophila CRISPR/Cas9 Toolkit for Conditionally Manipulating Gene Expression in the Prothoracic Gland as a Test Case for Polytene Tissues. *G3: Genes/Genomes/Genetics*, *8*(11), 3593. <https://doi.org/10.1534/G3.118.200539>

- Ichiyama, A., Nakamura, S., & Nishizuka, Y. (1967). Studies on the biosynthesis of nicotinamide adenine dinucleotide (NAD) in mammals and its regulatory mechanism. II. *Arzneimittel-Forschung/Drug Research*, *17*(12), 1525–1530.
- Imai, S. ichiro, & Guarente, L. (2014). NAD⁺ and sirtuins in aging and disease. *Trends in Cell Biology*, *24*(8), 464–471. <https://doi.org/10.1016/J.TCB.2014.04.002>
- Izadifar, A., Courchet, J., Virga, D. M., Verreet, T., Hamilton, S., Ayaz, D., Misbaer, A., Vandenbergaeerde, S., Monteiro, L., Petrovic, M., Sachse, S., Yan, B., Erfurth, M. L., Dascenco, D., Kise, Y., Yan, J., Edwards-Faret, G., Lewis, T., Polleux, F., & Schmucker, D. (2021). Axon morphogenesis and maintenance require an evolutionary conserved safeguard function of Wnk kinases antagonizing Sarm and Axed. *Neuron*, *109*(18), 2864-2883.e8. <https://doi.org/10.1016/J.NEURON.2021.07.006>
- Ji, H., Sapar, M. L., Sarkar, A., Wang, B., & Han, C. (2022). Phagocytosis and self-destruction break down dendrites of Drosophila sensory neurons at distinct steps of Wallerian degeneration. *Proceedings of the National Academy of Sciences*, *119*(4), e2111818119. <https://doi.org/10.1073/PNAS.2111818119>
- Jiang, Y., Liu, T., Lee, C. H., Chang, Q., Yang, J., & Zhang, Z. (2020). The NAD⁺-mediated self-inhibition mechanism of pro-neurodegenerative SARM1. *Nature* *2020* *588*:7839, *588*(7839), 658–663. <https://doi.org/10.1038/s41586-020-2862-z>
- Jinek, M., Chylinski, K., Fonfara, I., Hauer, M., Doudna, J. A., & Charpentier, E. (2012). A programmable dual-RNA-guided DNA endonuclease in adaptive bacterial immunity. *Science (New York, N.Y.)*, *337*(6096), 816–821. <https://doi.org/10.1126/SCIENCE.1225829>
- Jumper, J., Evans, R., Pritzel, A., Green, T., Figurnov, M., Ronneberger, O., Tunyasuvunakool, K., Bates, R., Žídek, A., Potapenko, A., Bridgland, A., Meyer, C., Kohl, S. A. A., Ballard, A. J., Cowie, A., Romera-Paredes, B., Nikolov, S., Jain, R., Adler, J., ... Hassabis, D. (2021). Highly accurate protein structure prediction with AlphaFold. *Nature* *2021* *596*:7873, *596*(7873), 583–589. <https://doi.org/10.1038/s41586-021-03819-2>
- Juster-Switlyk, K., & Smith, A. G. (2016). Updates in diabetic peripheral neuropathy. *F1000Research*, *5*. <https://doi.org/10.12688/f1000research.7898.1>
- Kaneko, S. (2006). Protecting Axonal Degeneration by Increasing Nicotinamide Adenine Dinucleotide Levels in Experimental Autoimmune Encephalomyelitis Models. *Journal of Neuroscience*, *26*(38), 9794–9804. <https://doi.org/10.1523/JNEUROSCI.2116-06.2006>
- Kerschensteiner, M., Schwab, M. E., Lichtman, J. W., & Misgeld, T. (2005). In vivo imaging of axonal degeneration and regeneration in the injured spinal cord. *Nature Medicine*, *11*(5), 572–577. <https://doi.org/10.1038/nm1229>
- Knöferle, J., Koch, J. C., Ostendorf, T., Michel, U., Planchamp, V., Vutova, P., Tönges, L., Stadelmann, C., Brück, W., Bähr, M., & Lingor, P. (2010). Mechanisms of acute axonal degeneration in the optic nerve in vivo. *Proceedings of the National Academy of Sciences of the United States of America*, *107*(13), 6064–6069. <https://doi.org/10.1073/pnas.0909794107>
- Koreman, G. T., Xu, Y., Hu, Q., Zhang, Z., Allen, S. E., Wolfner, M. F., Wang, B., & Han, C. (2021). Upgraded CRISPR/Cas9 tools for tissue-specific mutagenesis in Drosophila. *Proceedings of the National Academy of Sciences of the United States of America*, *118*(14), e2014255118. https://doi.org/10.1073/PNAS.2014255118/SUPPL_FILE/PNAS.2014255118.SAPP.PDF

- Krieg, M., Stühmer, J., Cueva, J. G., Fetter, R., Spilker, K., Cremers, D., Shen, K., Dunn, A. R., & Goodman, M. B. (2017). Genetic defects in β -spectrin and tau sensitize *C. elegans* axons to movement-induced damage via torque-tension coupling. *ELife*, 6. <https://doi.org/10.7554/eLife.20172>
- Llobet Rosell, A., & Neukomm, L. J. (2019). Axon death signalling in Wallerian degeneration among species and in disease. *Open Biology*, 9(8), 190118. <https://doi.org/10.1098/rsob.190118>
- Loreto, A., di Stefano, M., Gering, M., & Conforti, L. (2015). Wallerian Degeneration Is Executed by an NMN-SARM1-Dependent Late Ca²⁺ Influx but Only Modestly Influenced by Mitochondria. *Cell Reports*, 13(11), 2539–2552. <https://doi.org/10.1016/j.celrep.2015.11.032>
- Lu, B., & Vogel, H. (2009). Drosophila Models of Neurodegenerative Diseases. *Annual Review of Pathology*, 4, 315. <https://doi.org/10.1146/ANNUREV.PATHOL.3.121806.151529>
- Lu, T.-Y., MacDonald, J. M., Neukomm, L. J., Sheehan, A. E., Bradshaw, R., Logan, M. A., & Freeman, M. R. (2017). Axon degeneration induces glial responses through Draper-TRAF4-JNK signalling. *Nature Communications*, 8, 14355. <https://doi.org/10.1038/ncomms14355>
- Lukacs, M., Gilley, J., Zhu, Y., Orsomando, G., Angeletti, C., Liu, J., Yang, X., Park, J., Hopkin, R. J., Coleman, M. P., Zhai, R. G., & Stottmann, R. W. (2019). Severe biallelic loss-of-function mutations in nicotinamide mononucleotide adenylyltransferase 2 (NMNAT2) in two fetuses with fetal akinesia deformation sequence. *Experimental Neurology*, 320, 112961. <https://doi.org/10.1016/j.expneurol.2019.112961>
- Lunn, E. R., Perry, V. H., Brown, M. C., Rosen, H., & Gordon, S. (1989). Absence of Wallerian Degeneration does not Hinder Regeneration in Peripheral Nerve. *The European Journal of Neuroscience*, 1(1), 27–33. <http://www.ncbi.nlm.nih.gov/pubmed/12106171>
- Ma, M., Ferguson, T. A., Schoch, K. M., Li, J., Qian, Y., Shofer, F. S., Saatman, K. E., & Neumar, R. W. (2013). Calpains mediate axonal cytoskeleton disintegration during Wallerian degeneration. *Neurobiology of Disease*, 56, 34–46. <https://doi.org/10.1016/j.nbd.2013.03.009>
- MacDonald, J. M., Beach, M. G., Porpiglia, E., Sheehan, A. E., Watts, R. J., & Freeman, M. R. (2006). The Drosophila Cell Corpse Engulfment Receptor Draper Mediates Glial Clearance of Severed Axons. *Neuron*, 50(6), 869–881. <https://doi.org/10.1016/j.neuron.2006.04.028>
- Mack, T. G. A., Reiner, M., Beirowski, B., Mi, W., Emanuelli, M., Wagner, D., Thomson, D., Gillingwater, T., Court, F., Conforti, L., Fernando, F. S., Tarlton, A., Andressen, C., Addicks, K., Magni, G., Ribchester, R. R., Perry, V. H., & Coleman, M. P. (2001). Wallerian degeneration of injured axons and synapses is delayed by a Ube4b/Nmnat chimeric gene. *Nature Neuroscience*, 4(12), 1199–1206. <https://doi.org/10.1038/nn770>
- Macqueen, D. J., & Wilcox, A. H. (2014). Characterization of the definitive classical calpain family of vertebrates using phylogenetic, evolutionary and expression analyses. *Open Biology*, 4(4), 130219–130219. <https://doi.org/10.1098/rsob.130219>
- Mahammad, S., Prasanna Murthy, S. N., Didonna, A., Grin, B., Israeli, E., Perrot, R., Bomont, P., Julien, J. P., Kuczmarski, E., Opal, P., & Goldman, R. D. (2013). Giant axonal neuropathy-associated gigaxonin mutations impair intermediate filament protein degradation. *The Journal of Clinical Investigation*, 123(5), 1964–1975. <https://doi.org/10.1172/JCI66387>

- Mariano, V., Domínguez-Iturza, N., Neukomm, L. J., & Bagni, C. (2018). Maintenance mechanisms of circuit-integrated axons. *Current Opinion in Neurobiology*, *53*, 162–173. <https://doi.org/10.1016/J.CONB.2018.08.007>
- Marner, L., Nyengaard, J. R., Tang, Y., & Pakkenberg, B. (2003). Marked loss of myelinated nerve fibers in the human brain with age. *The Journal of Comparative Neurology*, *462*(2), 144–152. <https://doi.org/10.1002/CNE.10714>
- Martin, S. M., O'Brien, G. S., Portera-Cailliau, C., & Sagasti, A. (2010). Wallerian degeneration of zebrafish trigeminal axons in the skin is required for regeneration and developmental pruning. *Development*, *137*(23), 3985–3994. <https://doi.org/10.1242/dev.053611>
- Matsuda, W., Furuta, T., Nakamura, K. C., Hioki, H., Fujiyama, F., Arai, R., & Kaneko, T. (2009). Single Nigrostriatal Dopaminergic Neurons Form Widely Spread and Highly Dense Axonal Arborizations in the Neostriatum. *Journal of Neuroscience*, *29*(2), 444–453. <https://doi.org/10.1523/JNEUROSCI.4029-08.2009>
- Maxwell, W. L., Bartlett, E., & Morgan, H. (2015). Wallerian Degeneration in the Optic Nerve Stretch-Injury Model of Traumatic Brain Injury: A Stereological Analysis. *Journal of Neurotrauma*, *32*(11), 780–790. <https://doi.org/10.1089/neu.2014.3369>
- McLaughlin, C. N., Perry-Richardson, J. J., Coutinho-Budd, J. C., & Broihier, H. T. (2019). Dying Neurons Utilize Innate Immune Signaling to Prime Glia for Phagocytosis during Development. *Developmental Cell*, *48*(4), 506–522.e6. <https://doi.org/10.1016/j.devcel.2018.12.019>
- McReynolds, M. R., Chellappa, K., & Baur, J. A. (2020). Age-related NAD⁺ decline. *Experimental Gerontology*, *134*, 110888. <https://doi.org/10.1016/J.EXGER.2020.110888>
- Meltzer, H., Marom, E., Alyagor, I., Mayseless, O., Berkun, V., Segal-Gilboa, N., Unger, T., Luginbuhl, D., & Schuldiner, O. (2019). Tissue-specific (ts)CRISPR as an efficient strategy for in vivo screening in Drosophila. *Nature Communications* *2019 10:1*, *10*(1), 1–9. <https://doi.org/10.1038/s41467-019-10140-0>
- Meyer zu Horste, G., Miesbach, T. A., Muller, J. I., Fledrich, R., Stassart, R. M., Kieseier, B. C., Coleman, M. P., & Sereda, M. W. (2011). The Wlds transgene reduces axon loss in a Charcot-Marie-Tooth disease 1A rat model and nicotinamide delays post-traumatic axonal degeneration. *Neurobiology of Disease*, *42*(1), 1–8. <https://doi.org/10.1016/j.nbd.2010.12.006>
- Milde, S., Fox, A. N., Freeman, M. R., & Coleman, M. P. (2013). Deletions within its subcellular targeting domain enhance the axon protective capacity of Nmnat2 in vivo. *Scientific Reports*, *3*, 1–9. <https://doi.org/10.1038/srep02567>
- Milde, S., Gilley, J., & Coleman, M. P. (2013). Subcellular Localization Determines the Stability and Axon Protective Capacity of Axon Survival Factor Nmnat2. *PLoS Biology*, *11*(4). <https://doi.org/10.1371/journal.pbio.1001539>
- Miller, B. R., Press, C., Daniels, R. W., Sasaki, Y., Milbrandt, J., & Diantonio, A. (2009). A dual leucine kinase-dependent axon self-destruction program promotes Wallerian degeneration. <https://doi.org/10.1038/nn.2290>
- Mills, K. F., Yoshida, S., Stein, L. R., Grozio, A., Kubota, S., Sasaki, Y., Redpath, P., Migaud, M. E., Apte, R. S., Uchida, K., Yoshino, J., & Imai, S. ichiro. (2016). Long-Term Administration of Nicotinamide Mononucleotide

- Mitigates Age-Associated Physiological Decline in Mice. *Cell Metabolism*, 24(6), 795–806. <https://doi.org/10.1016/J.CMET.2016.09.013>
- Mishra, B., Carson, R., Hume, R. I., & Collins, C. A. (2013a). Sodium and Potassium Currents Influence Wallerian Degeneration of Injured *Drosophila* Axons. *Journal of Neuroscience*, 33(48), 18728–18739. <https://doi.org/10.1523/JNEUROSCI.1007-13.2013>
- Mishra, B., Carson, R., Hume, R. I., & Collins, C. A. (2013b). Sodium and potassium currents influence Wallerian degeneration of injured *Drosophila* axons. *The Journal of Neuroscience : The Official Journal of the Society for Neuroscience*, 33(48), 18728–18739. <https://doi.org/10.1523/JNEUROSCI.1007-13.2013>
- Mitchell, S. J., Bernier, M., Aon, M. A., Cortassa, S., Kim, E. Y., Fang, E. F., Palacios, H. H., Ali, A., Navas-Enamorado, I., di Francesco, A., Kaiser, T. A., Waltz, T. B., Zhang, N., Ellis, J. L., Elliott, P. J., Frederick, D. W., Bohr, V. A., Schmidt, M. S., Brenner, C., ... de Cabo, R. (2018). Nicotinamide Improves Aspects of Healthspan, but Not Lifespan, in Mice. *Cell Metabolism*, 27(3), 667-676.e4. <https://doi.org/10.1016/J.CMET.2018.02.001>
- Moldovan, M., Alvarez, S., & Krarup, C. (2009). Motor axon excitability during Wallerian degeneration. *Brain : A Journal of Neurology*, 132(Pt 2), 511–523. <https://doi.org/10.1093/BRAIN/AWN332>
- Neukomm, L. J., Burdett, T. C., Gonzalez, M. A., Züchner, S., & Freeman, M. R. (2014). Rapid in vivo forward genetic approach for identifying axon death genes in *Drosophila*. *Proceedings of the National Academy of Sciences*, 111(27), 9965–9970. <https://doi.org/10.1073/pnas.1406230111>
- Neukomm, L. J., Burdett, T. C., Seeds, A. M., Hampel, S., Coutinho-Budd, J. C., Farley, J. E., Wong, J., Karadeniz, Y. B., Osterloh, J. M., Sheehan, A. E., & Freeman, M. R. (2017). Axon Death Pathways Converge on Axundead to Promote Functional and Structural Axon Disassembly. *Neuron*, 95(1), 78-91.e5. <https://doi.org/10.1016/j.neuron.2017.06.031>
- Neukomm, L. J., & Freeman, M. R. (2014). Diverse cellular and molecular modes of axon degeneration. *Trends in Cell Biology*, 24(9), 515–523. <https://doi.org/10.1016/j.tcb.2014.04.003>
- Osterloh, J. M., Yang, J., Rooney, T. M., Fox, A. N., Adalbert, R., Powell, E. H., Sheehan, A. E., Avery, M. A., Hackett, R., Logan, M. A., MacDonald, J. M., Ziegenfuss, J. S., Milde, S., Hou, Y. J., Nathan, C., Ding, A., Brown, R. H., Conforti, L., Coleman, M., ... Freeman, M. R. (2012). dSarm/Sarm1 is required for activation of an injury-induced axon death pathway. *Science*, 337(6093), 481–484. <https://doi.org/10.1126/science.1223899>
- Paglione, M., Llobet Rosell, A., Chatton, J. Y., & Neukomm, L. J. (2020). Morphological and Functional Evaluation of Axons and their Synapses during Axon Death in *Drosophila melanogaster*. *J. Vis. Exp*, 157, 60865. <https://doi.org/10.3791/60865>
- Panneerselvam, P., Singh, L. P., Selvarajan, V., Chng, W. J., Ng, S. B., Tan, N. S., Ho, B., Chen, J., & Ding, J. L. (2013). T-cell death following immune activation is mediated by mitochondria-localized SARM. *Cell Death & Differentiation*, 20(3), 478–489. <https://doi.org/10.1038/cdd.2012.144>
- Park, J. Y., Jang, S. Y., Shin, Y. K., Koh, H., Suh, D. J., Shinji, T., Araki, T., & Park, H. T. (2013). Mitochondrial swelling and microtubule depolymerization are associated with energy depletion in axon degeneration. *Neuroscience*, 238, 258–269. <https://doi.org/10.1016/j.neuroscience.2013.02.033>
- Perry, V. H., Brown, M. C., & Gordon, S. (1987). The macrophage response to central and peripheral nerve injury. A possible role for macrophages in regeneration. *The Journal of Experimental Medicine*, 165(4), 1218–1223. <https://doi.org/10.1084/JEM.165.4.1218>

- Perry, V. H., Brown, M. C., & Lunn, E. R. (1991). Very Slow Retrograde and Wallerian Degeneration in the CNS of C57BL/Ola Mice. *The European Journal of Neuroscience*, 3(1), 102–105. <https://doi.org/10.1111/J.1460-9568.1991.TB00815.X>
- Peters, O. M., Lewis, E. A., Osterloh, J. M., Weiss, A., Salameh, J. S., Metterville, J., Brown, R. H., & Freeman, M. R. (2018). Loss of Sarm1 does not suppress motor neuron degeneration in the SOD1G93A mouse model of amyotrophic lateral sclerosis. *Human Molecular Genetics*, 27(21), 3761–3771. <https://doi.org/10.1093/hmg/ddy260>
- Port, F., Chen, H. M., Lee, T., & Bullock, S. L. (2014). Optimized CRISPR/Cas tools for efficient germline and somatic genome engineering in *Drosophila*. *Proceedings of the National Academy of Sciences of the United States of America*, 111(29), E2967–E2976. https://doi.org/10.1073/PNAS.1405500111/SUPPL_FILE/PNAS.201405500SI.PDF
- Port, F., Strein, C., Stricker, M., Rauscher, B., Heigwer, F., Zhou, J., Beyersdörffer, C., Frei, J., Hess, A., Kern, K., Lange, L., Langner, N., Malamud, R., Pavlović, B., Räddecke, K., Schmitt, L., Voos, L., Valentini, E., & Boutros, M. (2020). A large-scale resource for tissue-specific CRISPR mutagenesis in *Drosophila*. *ELife*, 9. <https://doi.org/10.7554/ELIFE.53865>
- Purice, M. D., Ray, A., Münzel, E. J., Pope, B. J., Park, D. J., Speese, S. D., & Logan, M. A. (2017). A novel *Drosophila* injury model reveals severed axons are cleared through a draper/MMP-1 signaling cascade. *ELife*, 6. <https://doi.org/10.7554/ELIFE.23611>
- Purice, M. D., Speese, S. D., & Logan, M. A. (2016). Delayed glial clearance of degenerating axons in aged *Drosophila* is due to reduced PI3K/Draper activity. *Nature Communications*, 7, 12871. <https://doi.org/10.1038/ncomms12871>
- Ratajczak, J., Joffraud, M., Trammell, S. A. J., Ras, R., Canela, N., Boutant, M., Kulkarni, S. S., Rodrigues, M., Redpath, P., Migaud, M. E., Auwerx, J., Yanes, O., Brenner, C., & Cantó, C. (2016). NRK1 controls nicotinamide mononucleotide and nicotinamide riboside metabolism in mammalian cells. *Nature Communications* 2016 7:1, 7(1), 1–12. <https://doi.org/10.1038/ncomms13103>
- Rechsteiner, M., Hillyard, D., & Olivera, B. M. (1976). Magnitude and significance of NAD turnover in human cell line D98/AH2. *Nature* 1976 259:5545, 259(5545), 695–696. <https://doi.org/10.1038/259695a0>
- Revollo, J. R., Grimm, A. A., & Imai, S. I. (2004). The NAD biosynthesis pathway mediated by nicotinamide phosphoribosyltransferase regulates Sir2 activity in mammalian cells. *The Journal of Biological Chemistry*, 279(49), 50754–50763. <https://doi.org/10.1074/JBC.M408388200>
- Rooney, T. M., & Freeman, M. R. (2014). *Drosophila Models of Neuronal Injury*. <https://doi.org/10.1093/ilar/ilt057>
- Ruan, K., Zhu, Y., Li, C., Brazill, J. M., & Zhai, R. G. (2015). Alternative splicing of *Drosophila* Nmnat functions as a switch to enhance neuroprotection under stress. *Nature Communications*, 6(1), 10057. <https://doi.org/10.1038/ncomms10057>
- Rücker, E., Schneider, G., Steinhäuser, K., Löwer, R., Hauber, J., & Stauber, R. H. (2001). Rapid evaluation and optimization of recombinant protein production using GFP tagging. *Protein Expression and Purification*, 21(1), 220–223. <https://doi.org/10.1006/PREP.2000.1373>

- Saatman, K. E., Creed, J., & Raghupathi, R. (2010). Calpain as a therapeutic target in traumatic brain injury. *Neurotherapeutics*, 7(1), 31–42. <https://doi.org/10.1016/j.nurt.2009.11.002>
- Sambashivan, S., & Freeman, M. R. (2021). SARM1 signaling mechanisms in the injured nervous system. *Current Opinion in Neurobiology*, 69, 247–255. <https://doi.org/10.1016/J.CONB.2021.05.004>
- Sasaki, Y. (2018). Metabolic aspects of neuronal degeneration: From a NAD + point of view. *Neuroscience Research*. <https://doi.org/10.1016/j.neures.2018.07.001>
- Sasaki, Y., Araki, T., & Milbrandt, J. (2006). Stimulation of Nicotinamide Adenine Dinucleotide Biosynthetic Pathways Delays Axonal Degeneration after Axotomy. *Journal of Neuroscience*, 26(33), 8484–8491. <https://doi.org/10.1523/JNEUROSCI.2320-06.2006>
- Sasaki, Y., & Milbrandt, J. (2010). Axonal degeneration is blocked by nicotinamide mononucleotide adenyltransferase (Nmnat) protein transduction into transected axons. *Journal of Biological Chemistry*, 285(53), 41211–41215. <https://doi.org/10.1074/jbc.C110.193904>
- Sasaki, Y., Nakagawa, T., Mao, X., DiAntonio, A., & Milbrandt, J. (2016). NMNAT1 inhibits axon degeneration via blockade of SARM1-mediated NAD+depletion. *ELife*, 5(OCTOBER2016), 1–15. <https://doi.org/10.7554/eLife.19749>
- Sasaki, Y., Vohra, B. P. S., Baloh, R. H., & Milbrandt, J. (2009). Transgenic mice expressing the Nmnat1 protein manifest robust delay in axonal degeneration in vivo. *The Journal of Neuroscience : The Official Journal of the Society for Neuroscience*, 29(20), 6526–6534. <https://doi.org/10.1523/JNEUROSCI.1429-09.2009>
- Schlaepfer, W. W. (1974). Calcium-induced degeneration of axoplasm in isolated segments of rat peripheral nerve. *Brain Research*, 69(2), 203–215. [https://doi.org/10.1016/0006-8993\(74\)90002-X](https://doi.org/10.1016/0006-8993(74)90002-X)
- Schmidt, J. (2020). Molecular mechanisms of the axonal degeneration in hereditary neuropathies. *PhD Thesis*.
- Shade, C. (2020a). The Science Behind NMN—A Stable, Reliable NAD+Activator and Anti-Aging Molecule. *Integrative Medicine: A Clinician's Journal*, 19(1), 12. [/pmc/articles/PMC7238909/](https://pubmed.ncbi.nlm.nih.gov/37238909/)
- Shade, C. (2020b). The Science Behind NMN—A Stable, Reliable NAD+Activator and Anti-Aging Molecule. *Integrative Medicine: A Clinician's Journal*, 19(1), 12. [/pmc/articles/PMC7238909/](https://pubmed.ncbi.nlm.nih.gov/37238909/)
- Shen, H., Hyrc, K. L., & Goldberg, M. P. (2013). Maintaining energy homeostasis is an essential component of WldS-mediated axon protection. *Neurobiology of Disease*, 59, 69–79. <https://doi.org/10.1016/j.nbd.2013.07.007>
- Shi, Y., Kerry, P. S., Nanson, J. D., Bosanac, T., Sasaki, Y., Krauss, R., Saikot, F. K., Adams, S. E., Mosaiab, T., Masic, V., Mao, X., Rose, F., Vasquez, E., Furrer, M., Cunnea, K., Brearley, A., Gu, W., Luo, Z., Brillault, L., ... Ve, T. (2022). Structural basis of SARM1 activation, substrate recognition, and inhibition by small molecules. *Molecular Cell*, 82(9), 1643-1659.e10. <https://doi.org/10.1016/J.MOLCEL.2022.03.007>
- Shin, J. E., Miller, B. R., Babetto, E., Cho, Y., Sasaki, Y., Qayum, S., Russler, E. v., Cavalli, V., Milbrandt, J., & DiAntonio, A. (2012). SCG10 is a JNK target in the axonal degeneration pathway. *Proceedings of the National Academy of Sciences*, 109(52), E3696–E3705. <https://doi.org/10.1073/pnas.1216204109>
- Sievers, C., Platt, N., Perry, V. H., Coleman, M. P., & Conforti, L. (2003). Neurites undergoing Wallerian degeneration show an apoptotic-like process with annexin V positive staining and loss of mitochondrial

- membrane potential. *Neuroscience Research*, 46(2), 161–169. [https://doi.org/10.1016/S0168-0102\(03\)00039-7](https://doi.org/10.1016/S0168-0102(03)00039-7)
- Simon, D. J., & Watkins, T. A. (2018). Therapeutic opportunities and pitfalls in the treatment of axon degeneration. *Current Opinion in Neurology*, 31(6), 693–701. <https://doi.org/10.1097/WCO.0000000000000621>
- Smith, C., Hung, S.-T., Llobet Rosell, A., Jurriens, D., Siemons, M., Soloviev, O., Kapitein, L., Grussmayer, K., Neukomm, L., & Verhaegen, M. (2022). Adaptive optics in single objective inclined light sheet microscopy enables three-dimensional localization microscopy in whole adult *Drosophila* brains. *Frontiers in Neuroscience*, 0, 1622. <https://doi.org/10.3389/FNINS.2022.954949>
- Smith, D. H. (2009). Stretch growth of integrated axon tracts: Extremes and exploitations. *Progress in Neurobiology*, 89(3), 231. <https://doi.org/10.1016/J.PNEUROBIO.2009.07.006>
- Smith, D. H., Wolf, J. A., & Meaney, D. F. (2001). A New Strategy to Produce Sustained Growth of Central Nervous System Axons: Continuous Mechanical Tension. *Tissue Engineering*, 7(2), 131–139. <https://doi.org/10.1089/107632701300062714>
- Smith, R. S., & Bisby, M. A. (1993). Persistence of axonal transport in isolated axons of the mouse. *The European Journal of Neuroscience*, 5(9), 1127–1135. <https://doi.org/10.1111/J.1460-9568.1993.TB00967.X>
- Soares, L., Parisi, M., & Bonini, N. M. (2014). Axon Injury and Regeneration in the Adult *Drosophila*. *Scientific Reports 2014 4:1*, 4(1), 1–12. <https://doi.org/10.1038/srep06199>
- Sporny, M., Guez-Haddad, J., Khazma, T., Yaron, A., Dessau, M., Shkolnisky, Y., Mim, C., Isupov, M. N., Zalk, R., Hons, M., & Opatowsky, Y. (2020). Structural basis for sarm1 inhibition and activation under energetic stress. *ELife*, 9, 1–25. <https://doi.org/10.7554/ELIFE.62021>
- Sporny, M., Guez-Haddad, J., Lebediker, M., Ulisse, V., Volf, A., Mim, C., Isupov, M. N., & Opatowsky, Y. (2019). Structural Evidence for an Octameric Ring Arrangement of SARM1. *Journal of Molecular Biology*, 431, 3591–3605. <https://doi.org/10.1016/j.jmb.2019.06.030>
- Sreedharan, J., Neukomm, L. J., Brown, R. H., & Freeman, M. R. (2015). Age-dependent TDP-43-mediated motor neuron degeneration requires GSK3, hat-trick, and xmas-2. *Current Biology*, 25(16), 2130–2136. <https://doi.org/10.1016/j.cub.2015.06.045>
- Stogios, P. J., & Privé, G. G. (2004). The BACK domain in BTB-kelch proteins. *Trends in Biochemical Sciences*, 29(12), 634–637. <https://doi.org/10.1016/J.TIBS.2004.10.003>
- Summers, D. W., Milbrandt, J., & DiAntonio, A. (2018). Palmitoylation enables MAPK-dependent proteostasis of axon survival factors. *Proceedings of the National Academy of Sciences*, 201806933. <https://doi.org/10.1073/pnas.1806933115>
- Tian, W., Asgharsharghi, A., Valera, G., & Czopka, T. (2018). Systemic loss of *Sarm1* is glioprotective after neurotrauma. 1–55.
- Turkiew, E., Falconer, D., Reed, N., & Höke, A. (2017). Deletion of *Sarm1* gene is neuroprotective in two models of peripheral neuropathy. *Journal of the Peripheral Nervous System*, 22(3), 162–171. <https://doi.org/10.1111/jns.12219>

- Vaquíe, A., Sauvain, A., Duman, M., Nocera, G., Egger, B., Meyenhofer, F., Falquet, L., Bartesaghi, L., Chrast, R., Lamy, C. M., Bang, S., Lee, S.-R., Jeon, N. L., Ruff, S., & Jacob, C. (2019). Injured Axons Instruct Schwann Cells to Build Constricting Actin Spheres to Accelerate Axonal Disintegration. *Cell Reports*, *27*(11), 3152–3166.e7. <https://doi.org/10.1016/J.CELREP.2019.05.060>
- Varadi, M., Anyango, S., Deshpande, M., Nair, S., Natassia, C., Yordanova, G., Yuan, D., Stroe, O., Wood, G., Laydon, A., Zidek, A., Green, T., Tunyasuvunakool, K., Petersen, S., Jumper, J., Clancy, E., Green, R., Vora, A., Lutfi, M., ... Velankar, S. (2022). AlphaFold Protein Structure Database: massively expanding the structural coverage of protein-sequence space with high-accuracy models. *Nucleic Acids Research*, *50*(D1), D439–D444. <https://doi.org/10.1093/NAR/GKAB1061>
- Vargas, M. E., Yamagishi, Y., Tessier-Lavigne, M., & Sagasti, A. (2015). Live Imaging of Calcium Dynamics during Axon Degeneration Reveals Two Functionally Distinct Phases of Calcium Influx. *Journal of Neuroscience*, *35*(45), 15026–15038. <https://doi.org/10.1523/JNEUROSCI.2484-15.2015>
- Vickers, J. C., King, A. E., Woodhouse, A., Kirkcaldie, M. T., Staal, J. A., McCormack, G. H., Blizzard, C. A., Musgrove, R. E. J., Mitew, S., Liu, Y., Chuckowree, J. A., Bibari, O., & Dickson, T. C. (2009). Axonopathy and cytoskeletal disruption in degenerative diseases of the central nervous system. *Brain Research Bulletin*, *80*(4–5), 217–223. <https://doi.org/10.1016/J.BRAINRESBULL.2009.08.004>
- Villegas, R., Martin, S. M., O'Donnell, K. C., Carrillo, S. A., Sagasti, A., & Allende, M. L. (2012). Dynamics of degeneration and regeneration in developing zebrafish peripheral axons reveals a requirement for extrinsic cell types. *Neural Development*, *7*(1). <https://doi.org/10.1186/1749-8104-7-19>
- Villegas, R., Martinez, N. W., Lillo, J., Pihan, P., Hernandez, D., Twiss, J. L., & Court, F. A. (2014). Calcium Release from Intra-Axonal Endoplasmic Reticulum Leads to Axon Degeneration through Mitochondrial Dysfunction. *Journal of Neuroscience*, *34*(21), 7179–7189. <https://doi.org/10.1523/JNEUROSCI.4784-13.2014>
- Walker, L. J., Summers, D. W., Sasaki, Y., Brace, E., Milbrandt, J., & DiAntonio, A. (2017). MAPK signaling promotes axonal degeneration by speeding the turnover of the axonal maintenance factor NMNAT2. *ELife*, *6*. <https://doi.org/10.7554/eLife.22540>
- Waller, A. (1850). Experiments on the Section of the Glossopharyngeal and Hypoglossal Nerves of the Frog, and Observations of the Alterations Produced Thereby in the Structure of Their Primitive. In *Source: Philosophical Transactions of the Royal Society of London* (Vol. 140). <https://www.jstor.org/stable/pdf/108444.pdf?refreqid=excelsior%3A43333c1fb491b96c4dd2967aeff26769>
- Wang, B., Huang, M., Shang, D., Yan, X., Zhao, B., & Zhang, X. (2021). Mitochondrial Behavior in Axon Degeneration and Regeneration. *Frontiers in Aging Neuroscience*, *13*, 103. <https://doi.org/10.3389/FNAGI.2021.650038/BIBTEX>
- Wang, J. T., Medress, Z. A., & Barres, B. A. (2012). Axon degeneration: Molecular mechanisms of a self-destruction pathway. *Journal of Cell Biology*, *196*(1), 7–18. <https://doi.org/10.1083/JCB.201108111>
- Wang, J., Zhai, Q., Chen, Y., Lin, E., Gu, W., McBurney, M. W., & He, Z. (2005). A local mechanism mediates NAD-dependent protection of axon degeneration. *Journal of Cell Biology*, *170*(3), 349–355. <https://doi.org/10.1083/jcb.200504028>

- Wedel, M. J. (2012). A monument of inefficiency: The presumed course of the recurrent laryngeal nerve in sauropod dinosaurs. *Acta Palaeontol. Pol*, 57(2), 251–256. <https://doi.org/10.4202/app.2011.0019>
- Wu, L. E., & Sinclair, D. A. (2019). The elusive NMN transporter is found. *Nature Metabolism* 2019 1:1, 1(1), 8–9. <https://doi.org/10.1038/s42255-018-0015-6>
- Xie, N., Zhang, L., Gao, W., Huang, C., Huber, P. E., Zhou, X., Li, C., Shen, G., & Zou, B. (2020). NAD⁺ metabolism: pathophysiologic mechanisms and therapeutic potential. *Signal Transduction and Targeted Therapy* 2020 5:1, 5(1), 1–37. <https://doi.org/10.1038/s41392-020-00311-7>
- Xiong, X., Hao, Y., Sun, K., Li, J., Li, X., Mishra, B., Soppina, P., Wu, C., Hume, R. I., & Collins, C. A. (2012). The Highwire Ubiquitin Ligase Promotes Axonal Degeneration by Tuning Levels of Nmnat Protein. *PLoS Biology*, 10(12), 1–18. <https://doi.org/10.1371/journal.pbio.1001440>
- Xu, K., Zhong, G., & Zhuang, X. (2013). Actin, spectrin, and associated proteins form a periodic cytoskeletal structure in axons. *Science (New York, N.Y.)*, 339(6118), 452–456. <https://doi.org/10.1126/science.1232251>
- Yaku, K., Okabe, K., Hikosaka, K., & Nakagawa, T. (2018). NAD Metabolism in Cancer Therapeutics. *Frontiers in Oncology*, 8, 622. <https://doi.org/10.3389/fonc.2018.00622>
- Yamagishi, Y., & Tessier-Lavigne, M. (2016). An Atypical SCF-like Ubiquitin Ligase Complex Promotes Wallerian Degeneration through Regulation of Axonal Nmnat2. *Cell Reports*, 17(3), 774–782. <https://doi.org/10.1016/j.celrep.2016.09.043>
- Yan, T., Feng, Y., Zheng, J., Ge, X., Zhang, Y., Wu, D., Zhao, J., & Zhai, Q. (2010). Nmnat2 delays axon degeneration in superior cervical ganglia dependent on its NAD synthesis activity. *Neurochemistry International*, 56(1), 101–106. <https://doi.org/10.1016/j.neuint.2009.09.007>
- Yang, J., Weimer, R. M., Kallop, D., Olsen, O., Wu, Z., Renier, N., Uryu, K., & Tessier-Lavigne, M. (2013). Regulation of axon degeneration after injury and in development by the endogenous calpain inhibitor calpastatin. *Neuron*, 80(5), 1175–1189. <https://doi.org/10.1016/j.neuron.2013.08.034>
- Yang, J., Wu, Z., Renier, N., Simon, D. J., Uryu, K., Park, D. S., Greer, P. A., Tournier, C., Davis, R. J., & Tessier-Lavigne, M. (2015). Pathological axonal death through a MAPK cascade that triggers a local energy deficit. *Cell*, 160(1–2), 161–176. <https://doi.org/10.1016/j.cell.2014.11.053>
- Ying, W. (2008). NAD⁺/NADH and NADP⁺/NADPH in cellular functions and cell death: regulation and biological consequences. *Antioxidants & Redox Signaling*, 10(2), 179–206. <https://doi.org/10.1089/ARS.2007.1672>
- Yoshino, J., Baur, J. A., & Imai, S. ichiro. (2018). NAD + Intermediates: The Biology and Therapeutic Potential of NMN and NR. *Cell Metabolism*, 27(3), 513–528. <https://doi.org/10.1016/J.CMET.2017.11.002>
- Zhai, Q., Wang, J., Kim, A., Liu, Q., Watts, R., Hoopfer, E., Mitchison, T., Luo, L., & He, Z. (2003). Involvement of the Ubiquitin-Proteasome System in the Early Stages of Wallerian Degeneration. *Neuron*, 39(2), 217–225. [https://doi.org/10.1016/S0896-6273\(03\)00429-X](https://doi.org/10.1016/S0896-6273(03)00429-X)
- Zhai, R. G., Cao, Y., Hiesinger, P. R., Zhou, Y., Mehta, S. Q., Schulze, K. L., Verstreken, P., & Bellen, H. J. (2006). Drosophila NMNAT maintains neural integrity independent of its NAD synthesis activity. *PLoS Biology*, 4(12), 2336–2348. <https://doi.org/10.1371/journal.pbio.0040416>

- Zhao, Z. Y., Xie, X. J., Li, W. H., Liu, J., Chen, Z., Zhang, B., Li, T., Li, S. L., Lu, J. G., Zhang, L., Zhang, L. he, Xu, Z., Lee, H. C., & Zhao, Y. J. (2019). A Cell-Permeant Mimetic of NMN Activates SARM1 to Produce Cyclic ADP-Ribose and Induce Non-apoptotic Cell Death. *iScience*, *15*, 452. <https://doi.org/10.1016/J.ISCI.2019.05.001>
- Ziogas, N. K., & Koliatsos, V. E. (2018). Primary Traumatic Axonopathy in Mice Subjected to Impact Acceleration: A Reappraisal of Pathology and Mechanisms with High-Resolution Anatomical Methods. *Journal of Neuroscience*, *38*(16), 4031–4047. <https://doi.org/10.1523/JNEUROSCI.2343-17.2018>
- Ziv, N. E., & Spira, M. E. (1993). Spatiotemporal distribution of Ca²⁺ following axotomy and throughout the recovery process of cultured *Aplysia* neurons. *The European Journal of Neuroscience*, *5*(6), 657–668. <https://doi.org/10.1111/J.1460-9568.1993.TB00531.X>

ANNEX 1

Review: Axon death signalling in Wallerian degeneration among species and in disease

Review



Cite this article: Llobet Rosell A, Neukomm LJ. 2019 Axon death signalling in Wallerian degeneration among species and in disease. *Open Biol.* **9**: 190118. <http://dx.doi.org/10.1098/rsob.190118>

Received: 28 May 2019
Accepted: 2 August 2019

Subject Area:
neuroscience/molecular biology/genetics/
cellular biology/biochemistry

Keywords:
Wallerian degeneration, injury-induced axon degeneration, axon death, neurodegeneration

Author for correspondence:
Lukas J. Neukomm
e-mail: lukas.neukomm@unil.ch

Axon death signalling in Wallerian degeneration among species and in disease

Arnau Llobet Rosell and Lukas J. Neukomm

Department of Fundamental Neurosciences, University of Lausanne, Rue du Bugnon 9, 1005 Lausanne, VD, Switzerland

ALR, 0000-0001-7728-2999; LJN, 0000-0002-5007-3959

Axon loss is a shared feature of nervous systems being challenged in neurological disease, by chemotherapy or mechanical force. Axons take up the vast majority of the neuronal volume, thus numerous axonal intrinsic and glial extrinsic support mechanisms have evolved to promote lifelong axonal survival. Impaired support leads to axon degeneration, yet underlying intrinsic signalling cascades actively promoting the disassembly of axons remain poorly understood in any context, making the development to attenuate axon degeneration challenging. Wallerian degeneration serves as a simple model to study how axons undergo injury-induced axon degeneration (axon death). Severed axons actively execute their own destruction through an evolutionarily conserved axon death signalling cascade. This pathway is also activated in the absence of injury in diseased and challenged nervous systems. Gaining insights into mechanisms underlying axon death signalling could therefore help to define targets to block axon loss. Herein, we summarize features of axon death at the molecular and subcellular level. Recently identified and characterized mediators of axon death signalling are comprehensively discussed in detail, and commonalities and differences across species highlighted. We conclude with a summary of engaged axon death signalling in humans and animal models of neurological conditions. Thus, gaining mechanistic insights into axon death signalling broadens our understanding beyond a simple injury model. It harbours the potential to define targets for therapeutic intervention in a broad range of human axonopathies.

1. Introduction

Neurons use their axons to communicate with remote cells. These axons can be extremely long, ranging from millimetres to centimetres to metres depending on the host, the type of neuron and the target cell [1,2]. In other words, axons can take up more than 99.9% of the neuronal volume. Axons also harbour a remarkably elaborate axonal cytoskeleton (axoskeleton) [3], which allows them to withstand stretch, compression, tension and torsion [4–8]. To ensure continued circuit function, the nervous system established soma-independent, local axonal-intrinsic and glial-extrinsic mechanisms to support lifelong axon survival [9]. If these survival mechanisms are impaired, axons will undergo axon degeneration [10,11]. Axonopathies are increasingly recognized as major contributors in neurological conditions, such as Alzheimer’s disease (AD), amyotrophic lateral sclerosis (ALS) and multiple sclerosis (MS) [12], Parkinson’s disease (PD) [13], traumatic brain injury (TBI) [14], and chemotherapy-induced peripheral neuropathy (CIPN) [15]. Axon degeneration occurs prior to neuronal loss in a broad range of injured and diseased nervous systems, thus targeting it by therapeutics serves as a promising opportunity to ameliorate neurological disorders [16,17]. Gaining insights into underlying mechanisms executing axon degeneration will help to

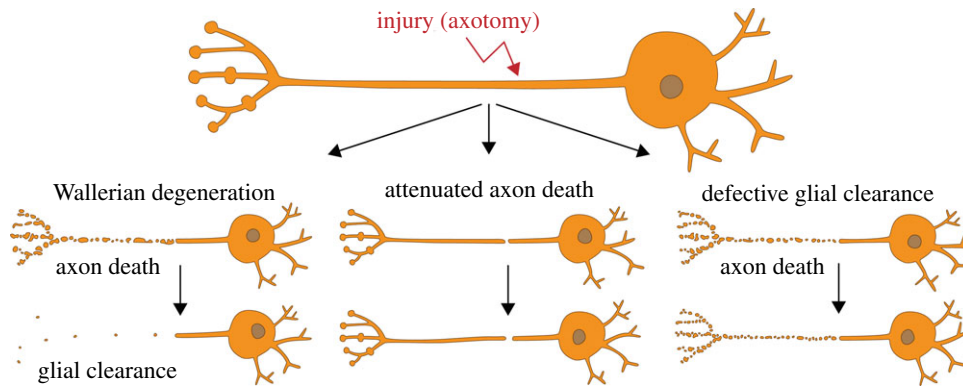


Figure 1. Wallerian degeneration consists of two molecularly distinct programmes. Upon axotomy, the axon separated from the soma actively executes its own fragmentation (axon death), which is mediated by an evolutionarily conserved axon death signalling cascade. The severed axon undergoes axon death within 1 day. Surrounding glial cells will then engage and clear the resulting axonal debris within 3–5 days. Attenuated axon death results in severed axons which remain functionally and morphologically preserved for weeks to months, while defective glial clearance culminates in axonal debris which persists for a similar time *in vivo*.

define targets for the development of efficacious drugs for therapeutic intervention. However, how axon degeneration is mechanistically regulated and executed remains currently largely unknown.

To date, distinct morphological modes of axon degeneration have been observed and underlying molecular mechanisms described [10]. Among them are dying back axon degeneration, retraction, axosome shedding, focal axonal degeneration induced by growth factor withdrawal and pruning, to name a few. Axon degeneration can also be triggered through axonal injury (axotomy), which is probably one of the simplest models to study how axons execute their own destruction. Identified by and named after Augustus Waller, Wallerian degeneration (WD) is an umbrella term under which two distinct mechanisms occur [18] (figure 1): first, severed axons—separated from the soma—actively execute their own disassembly (axon death) within 1 day, through an evolutionary conserved axon death signalling cascade; and second, surrounding glial cells engage and clear the resulting debris within 3–5 days. Axon death and glial clearance are separate processes (figure 1): the attenuation of axon death results in severed axons which remain functionally and morphologically preserved for weeks to months, while defective glial clearance culminates in axonal debris which persists for a similar time *in vivo* [19,20].

Axon death signalling is activated not only when the axon is cut, crushed or stretched [21,22], it also seems to be a major contributor in different animal models of neurological conditions, e.g. where axons degenerate in the absence of injury [23]. Therefore, axon death signalling could provide insights into axon degeneration beyond a simple injury model or, as August Waller wrote [18], 'It is impossible not to anticipate important results from the application of this inquiry to the different nerves of the animal system. But it is particularly with reference to nervous diseases that it will be most desirable to extend these researches'.

Over recent years, significant advancements broadened our understanding of axon death signalling in WD. While these discoveries shed light onto distinct mediators of axon death, they also led to more unanswered questions. First, how complete is our understanding of axon death signalling? Second, what differences or commonalities have been observed across species? And third, how do these findings bring us closer to defining new pharmacological targets

that could prevent axon degeneration in the diseased and injured nervous system?

In this review, we aim to provide answers to the above questions. First, we will comprehensively summarize our current understanding of axon death signalling across species. Second, we will highlight differences observed across model systems and discuss a potential core mechanism shared across species. And third, we will conclude with a brief overview of engaged axon death signalling in the diseased or injured nervous system.

2. Phases of Wallerian degeneration

Immediately after axotomy, the axon that has been separated from the soma goes through a lag phase where its overall morphology remains unchanged for 6–24 h depending on a number of factors, such as *in vitro* or *in vivo* models, and animal systems used (figure 2*a*). During this phase, the earliest feature observed immediately after injury is a rapid, short-term increase of axonal calcium (Ca^{2+}) levels in both the proximal and distal axon stump (figure 2*b*). This is mostly due to extracellular Ca^{2+} influx at the lesion site, and to a lesser extent from axon internal Ca^{2+} stores [24–27]. After the first, rapid short-term Ca^{2+} wave, nicotinamide adenine dinucleotide (NAD^+) and adenosine triphosphate (ATP) are rapidly depleted, thus impairing axonal energy homeostasis [28–30]. Mitochondria lose their membrane potential and begin to swell, thereby increasing the generation of reactive oxygen species (ROS). Ultimately, they release their internal Ca^{2+} stores, which culminates in a second, long-term Ca^{2+} wave [28,31–33]. At this point, the gross axonal morphology remains unchanged, despite the already initiated destabilization of microtubules [28,29].

Suddenly, the execution phase starts (figure 2): the axon begins to disassemble. Catastrophic granular fragmentation is observed at the molecular, ultrastructural and morphological level [28]. Microtubules start to disrupt, alongside the dismantling of the axoskeleton. The axon starts 'beading' or swelling, culminating in catastrophic axonal fragmentation [30,34,35].

During the execution phase, surrounding glial cells and specialized phagocytes not only clear the resulting axonal debris by activating multiple signalling pathways [19,36–39], but also actively enhance axonal fragmentation [40]. To date,

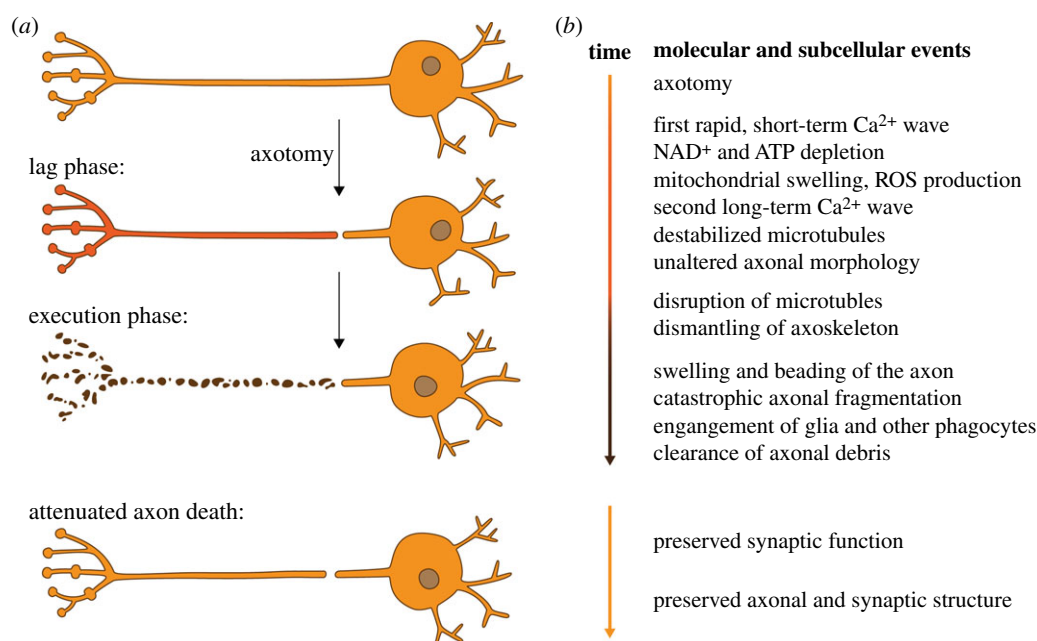


Figure 2. Phases and events during Wallerian degeneration. (a) Morphological phases of Wallerian degeneration. After axotomy, the axon that is separated from the soma goes through a lag phase (red), where its morphology remains grossly intact. During the execution phase (brown), the axon undergoes catastrophic axon fragmentation (axon death). Surrounding glia engage and clear the resulting axonal debris. The attenuation of axon death signalling results in morphologically and functionally preserved axons and synapses. (b) Molecular and subcellular events during Wallerian degeneration. Axotomy, lag and execution phase (orange, red and brown, respectively). The precise onset and duration of each event depends on the model system used. Attenuated axon death signalling preserves the structure and function of axons and their synapses.

several key questions remain unresolved, such as what kind of axonal ‘eat me’ signals are presented to surrounding glia [41], and where within the execution phase glial cells engage to clear axonal debris.

Once the execution phase is over, e.g. when the injured axon is disassembled and the resulting debris cleared by surrounding glia, WD is also over. While WD occurs in both the central and peripheral nervous system (CNS and PNS, respectively), it is of particular importance in the PNS to pave the way for the proximal axon still attached to the neuronal soma, which ultimately activates its regenerative programme, to regrow and thereby to re-establish circuit function [33].

3. The discovery and implications of *Wld^S*

Axon death within WD was long thought to be a simple passive wasting away of severed axons [18]. In 1989, the serendipitous discovery of the ‘Wallerian degeneration slow’ (*Wld^S*) mouse challenged this idea. Severed *Wld^S* axons remained preserved for weeks rather than undergoing axon death within a day (figure 2) [42]. Subsequently, the molecular change in *Wld^S* mice was identified as a tandem triplication of two neighbouring genes: the N-terminal 70 amino acid fragment of the ubiquitination factor E4B (*Ube4b*) fused to full length nicotinamide mononucleotide adenylyltransferase 1 (*Nmnat1*) [43]. This fusion results in a translocation of nuclear *Nmnat1* to the axon, where it exerts axon death attenuation (this will be discussed further below). The *Wld^S* neomorph provided the first evidence that axon death could be an active self-destruction programme to eliminate damaged axons; that is, because this programme is profoundly attenuated by the sole over-expression of *Wld^S*. Following the

identification of *Wld^S*, several important discoveries were made, which are summarized below.

First, *Wld^S* harbours an evolutionary conserved function. While it was first found to delay axon death in mice [42,43], the mouse chimeric protein performs its function equally well in rats [44], fruit flies [19] and zebrafish [33,45]. *Wld^S* is therefore capable of delaying axon death across multiple species.

Second, *Wld^S* acts autonomously in neurons and is dosage dependent. The *Wld^S* mouse harbours a tandem triplication which results in over-expressed *Wld^S* [43]. The higher the levels, the better its capability to preserve severed axons [43].

Third, *Wld^S* acts locally within axons. While abundant in both nuclei and axons, *Wld^S* confers potent attenuation of axon death signalling specifically in axons [46]. Viral transduction of multiple modified versions of *Wld^S* into severed axons up to 4 h after axotomy (e.g. early within the lag phase) is sufficient to attenuate axon death signalling [47].

Fourth, *Wld^S* is specific for axon death. Its expression blocks axon death and seems to have largely no effect on developmental pruning [48], or other types of neuronal death such as apoptosis [49].

And fifth, *Wld^S* is beneficial in many models of neurodegenerative conditions. Since its discovery, the *Wld^S* mouse has been crossed into a vast number of different neurological models to assess its protective ability in the injured and diseased nervous system [23]. These findings support the idea that axon death is shared in injury and disease, and, more importantly, that axon degeneration is a major driver in different neurological conditions.

Wld^S provided the first evidence that, at the molecular level, axon death can be attenuated by over-expression of a single protein. Its discovery and characterization raised two key questions: first, how is *Wld^S* able to attenuate an axonal-intrinsic axon death signalling pathway actively executing the degeneration

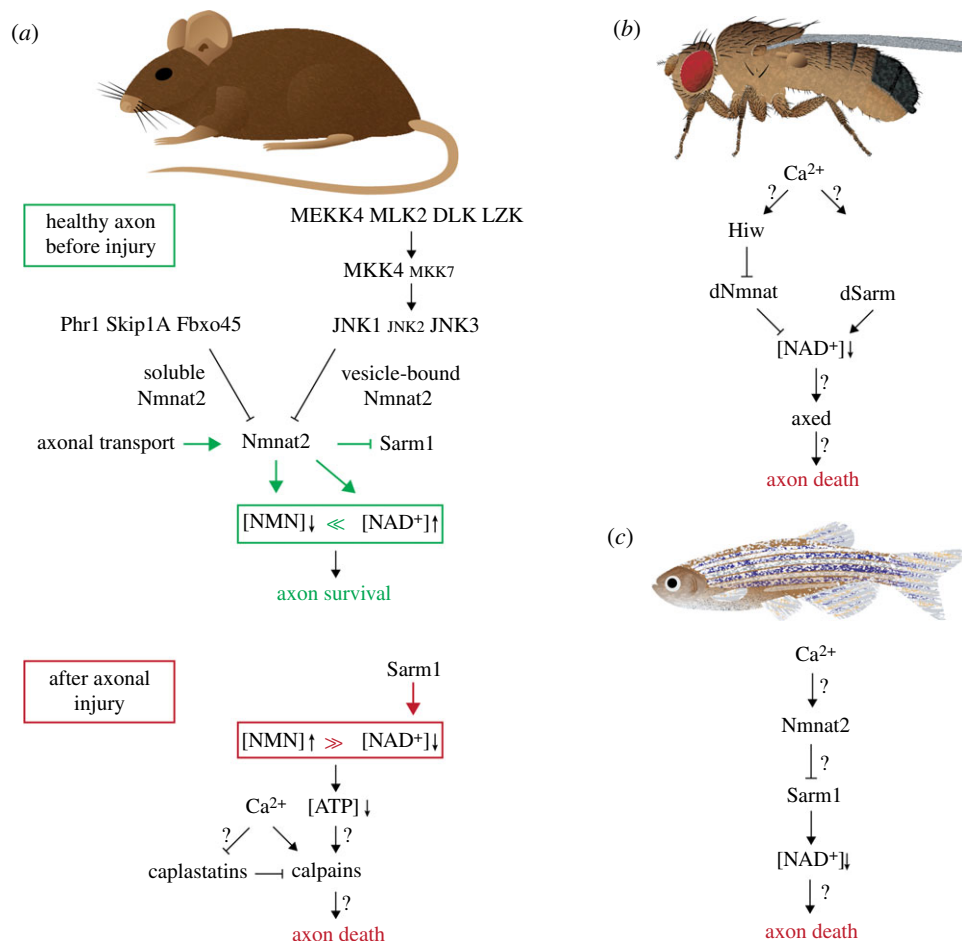


Figure 3. Axon death signalling across species. (a) In mouse axons, axonal survival is ensured by above-threshold levels of Nmnat2. Nmnat2 is constantly replenished by axonal transport, while the atypical ubiquitin ligase complex and the MAPK pathway rapidly degrade soluble and vesicle-bound Nmnat2, respectively. Nmnat2 keeps NMN levels low, and NAD^+ levels constant. Nmnat2 also blocks Sarm1 through an unknown mechanism. Upon axotomy, Nmnat2 drops below threshold levels, which induces axon death. NMN levels rise, and NAD^+ levels are rapidly depleted by the NADase activity of Sarm1. (b) Axon death signalling in flies. See text for details. (c) Axon death signalling in fish. The genetic interactions of Ca^{2+} , Nmnat2 and Sarm1 remain to be determined. See text for details.

of severed axons; and second, what are the mediators of axon death signalling? The next section will summarize our current knowledge related to these two questions.

4. Axon death mediators

To date, axon death in WD is observed in several species such as mice, rats, flies and fish (figure 3). So far, each animal model has contributed to the discovery of important axon death mediators and also offered distinct insights into axon death signalling. Importantly, the modification of each mediator attenuates axon death comparable to the effects of Wld^S , e.g. in the range of days to weeks.

4.1. Ca^{2+}

As mentioned above, a local initial influx of Ca^{2+} right after axotomy from the site of injury is observed in both invertebrate and vertebrate models *in vivo* and *in vitro* [24,27,50,51]. The first, rapid short-term Ca^{2+} wave precedes the lag phase (figure 2). The disassembly of severed axons is initiated by high extra-axonal Ca^{2+} concentrations: if the extracellular environment is devoid of Ca^{2+} (by adding EGTA, or in a medium lacking Ca^{2+}), or when voltage-gated Ca^{2+} channels are inhibited, the fragmentation of severed axons is significantly delayed (figure 3a) [26,50,52–54].

The second, long-term Ca^{2+} wave is present solely in the separated axon. It appears prior to the onset of axonal fragmentation, and is believed to be a key instructive component for the execution phase [51,55]. During the second wave, Ca^{2+} is released from intra-axonal stores (e.g. mainly from mitochondria, and to a lesser extent from the endoplasmic reticulum), and the inhibition thereof can significantly delay the disassembly of the axon [25].

The expression of Wld^S in zebrafish and rodent neuronal cultures largely suppresses the second, but not the first, Ca^{2+} wave, suggesting that the second wave is the one responsible for triggering axon fragmentation [24,51]. In *Drosophila* larvae, Wld^S is also suppressing the first Ca^{2+} wave, reflecting minor differences between the experimental systems [27].

Taken together, the rise in intra-axonal Ca^{2+} , both during the immediate first short-term as well as during the slower and delayed second long-term Ca^{2+} wave, is an important instructive signal to trigger axon death signalling. However, how transient high Ca^{2+} levels are linked to the initiation of axon death signalling remains completely unknown.

4.2. Nmnat2/dNmnat

Wld^S is an over-expressed version of Nmnat1 translocated from the nucleus to the axon [43,56]. Nmnat proteins are essential for ATP-dependent NAD^+ synthesis from either

nicotinamide mononucleotide (NMN) or nicotinic acid mononucleotide (NaMN) [57]. Mammals and zebrafish harbour three different *Nmnat* genes (*Nmnat1–3*) with different subcellular locations and kinetic properties [58]. In contrast, *Drosophila* relies on a single *nmnat* gene (*dnmnat*) [38], which is alternatively spliced to generate variants localized to the nucleus and the cytoplasm [59]. The discovery of *Wld^S*, and subsequently the extensive research on *Nmnat* proteins and their biosynthetic NAD^+ activity, provided the following four major insights: levels and localization of *Nmnat* proteins as well as levels of NAD^+ and its precursor NMN are all crucial for the execution of axon death signalling.

4.2.1. *Nmnat2/dNmnat* levels

Among the three mammalian *Nmnat* isoforms, *Nmnat2* is the gatekeeper of axon death: it is a limiting, labile axon survival factor [60]. Synthesized in the soma and transported into the axon, *Nmnat2* has to be constantly replenished in axons due to its rapid turnover (figure 3*a*): *Nmnat2* is the most labile member of its family with a half-life of less than 4 h, despite being the most highly expressed isoform in the brain [61]. Upon axotomy, *Nmnat2* fails to be transported to the axon; thus, in severed axons, *Nmnat2* levels drop rapidly, and axon death is initiated [60]. Vice versa, depletion of *Nmnat2* in whole neurons is sufficient to induce axon degeneration in the absence of injury: axons undergo Wallerian-like degeneration—because they can be attenuated by *Wld^S*—while the soma remains unaffected [60,62]. Similarly, *Nmnat2*^{-/-} mice harbour perinatal lethality due to limited axon extensions, and their isolated neuronal cultures from both PNS and CNS contain neurite outgrowth consistently stalling at 1–2 mm [63]. Likewise, in *Drosophila*, RNAi-mediated knockdown, or a lack of *dNmnat* in mutants, leads to spontaneous axon degeneration prior to cell body degeneration [64,65]. In zebrafish, over-expression of either *Wld^S* or *Nmnat2* results in a potent attenuation of axon death *in vivo* [33,45]. Whether knock-down of *Nmnat2* also results in Wallerian-like degeneration remains to be determined. Taken together, levels of mammalian, fish and fly *Nmnat2/dNmnat* are crucial for axonal survival (figure 3). It is important to note that any engineered version of stabilized *Nmnat* protein is capable of attenuating axon death in a variety of different models, e.g. *Wld^S* as non-nuclear *Nmnat1*, *Nmnat1* that fails to localize to nuclei (e.g. cytosolic and axonal *Nmnat1*, *cyt-Nmnat1* and *ax-Nmnat1*, respectively), *Nmnat2* able to persist longer in axons, *Drosophila* *dNmnat* over-expressed in cultured mouse dorsal root ganglia (DRG) or mouse *Nmnat1* in *Drosophila* olfactory receptor neurons (ORNs) [45,61,62,66–68]. Therefore, above-threshold levels of *Nmnat2* or modified versions thereof ensure the survival of the axon, while sub-threshold levels trigger axon death.

4.2.2. *Nmnat2/dNmnat* localization

Nmnat2 is predominantly found in cytoplasm and axoplasm, and is associated with membranes of Golgi-derived transport vesicles undergoing fast axonal transport [63]. Both the removal of the vesicle-association domain in *Nmnat2* [62] or the modification of its residues required for palmitoylation [69] lead to increased *Nmnat2* half-lives. Moreover, in mammals or flies, the over-expression of *Nmnat3*, which is predominantly found in mitochondria in mammals, potently attenuates axon death

[67,70]. Therefore, the subcellular localization dictates turnover rates of *Nmnat* proteins. By targeting them to different axonal compartments relative to endogenously localized *Nmnat2*, their turnover is reduced, which results in increased *Nmnat* protein half-lives, and ultimately in attenuated axon death.

4.2.3. *Nmnat* substrate: nicotinamide mononucleotide (NMN)

The attenuation of axon death signalling requires NAD^+ biosynthetic activity of *Nmnat* proteins [33,61,67,71,72]. Metabolic aspects of NAD^+ in neurodegeneration and axon death signalling have recently been comprehensively reviewed in [57]. Importantly, genetic and pharmacological modifications of NAD^+ metabolism result in different levels of attenuation [73]. Here, we will focus on manipulations that result in a robust long-term (days to weeks) or intermediate (2–3 days) attenuation of axon death signalling, respectively. However, we do note that there are manipulations which result in a short-term attenuation, e.g. a delay of axon death signalling in the range of a day. These observations remain subject to further analyses and will not be covered here.

Nmnat proteins use either NMN or NaMN to generate NAD^+ in an ATP-dependent manner. After injury, *Nmnat* protein levels drop, resulting in increased *Nmnat* substrates, e.g. NaMN and/or NMN, and decreased *Nmnat* products, e.g. NAD^+ . But which one is important for axon death signalling?

While levels of NaMN seem to be negligible [73], levels of NMN are crucial: they temporally rise within 6 h in severed axons and seem to be an instructive signal [55,74]. Preventing this NMN rise results in long-term attenuation of axon death: either by the expression of *Wld^S* or modified *Nmnat* proteins that consume NMN to generate NAD^+ or—interestingly—by the expression of a bacterial specific enzyme, NMN deamidase, which consumes NMN but does not generate NAD^+ , both *in vitro* [55,73,74] and *in vivo* in zebrafish and mice [75].

There is an alternative modification to keep NMN levels low: nicotinamide (Nam) is consumed by nicotinamide phosphoribosyltransferase (NAMPT) to generate NMN. The pharmacological inhibition of NAMPT by FK866, either right before or immediately after injury, prevents the rise of NMN, which results in short-term to intermediate attenuation of axon death signalling [73,74].

In summary, distinct pharmacological or genetic manipulations that lead to low levels of NMN also prevent axon death. Thus, the temporal rise of NMN after injury seems to be an instructive signal for axons to execute their own destruction.

4.2.4. *Nmnat* product: nicotinamide adenine dinucleotide (NAD^+)

The involvement of NAD^+ as a product of the biosynthetic activity of *Nmnat* proteins in axon death was observed right after the discovery of *Wld^S*: before or immediately after axonal injury, the exogenous supply of high levels of NAD^+ leads to long-range attenuation of axon death signalling [71,72]. Thus, axon death is triggered by NAD^+ depletion in severed axons. It is important to note that *Wld^S* or engineered *Nmnat* proteins do not generate higher levels of NAD^+ , they solely prevent the depletion thereof by a—yet unknown—mechanism that inhibits an NAD^+ consuming enzyme, which will be discussed further below [73,76].

Wld^S got its foot in the door of axon death signalling and paved the way for several key discoveries related to *Nmnat* proteins. Levels and localization of the axonal survival

factor Nmnat2/dNmnat are crucial for the survival or the degeneration of the axon. Its biosynthetic activity keeps levels of NMN as substrate low, and prevents the depletion of NAD⁺ as product (figure 3a).

Given the essential role of Nmnat proteins in axon death, an important question is how their turnover and half-life is regulated. What are the mechanisms regulating protein levels and therefore biosynthetic activity? Below, we will discuss the mechanisms that are crucial for Nmnat2 protein levels.

4.3. Atypical ubiquitin ligase complex

Following the cloning of Wld^S [43], the ubiquitin proteasome system (UPS) was also found to be involved in the early stages of axon death [29]. The subsequent discovery of Nmnat2 as a labile axon survival factor, which is subjected to rapid turnover in axons [60], led to an attractive hypothesis: could the UPS be responsible for the rapid turnover of Nmnat2 in axons? The first evidence for the UPS system to be involved in axon death was found in *Drosophila*. The E3 ubiquitin ligase Highwire (Hiw) regulates the turnover of dNmnat [20,77]. Likewise, the mammalian homologue PAM/Highwire/RPM-1 (Phr1) also fine-tunes levels of Nmnat2 [78]. Phr1 belongs to an evolutionarily conserved, atypical Skp/Cullin/F-box (SCF)-type E3 ubiquitin ligase complex consisting of S-phase kinase-associated protein 1A (Skip1a), Phr1 and F-box protein 45 (Fbxo45) [78,79]. This atypical SCF complex regulates—through polyubiquitination and the proteasome—levels of Nmnat2, by specifically targeting axoplasmic Nmnat2 for destruction [69,80]. The removal of either component slows down the turnover of Nmnat2, which results in attenuated axon death signalling (figure 3a).

4.4. MAPK signalling

The mitogen-activated protein kinase (MAPK) signalling pathway is also involved in axon death signalling. It is activated within 5 min after axonal injury and culminates in the phosphorylation of c-Jun N-terminal kinases (JNKs): loss-of-function analyses revealed that a partially redundant MAPK cascade is required to execute the degeneration of axons after injury (e.g. MKK4, MLK, DLK, MKK4/7, JNK1/3 and SCG10) [69,81–84]. The MAPK cascade limits levels of Nmnat2 by selectively degrading membrane-associated, palmitoylated Nmnat2 [69,82].

Interestingly, Nmnat2 levels are differentially regulated. Both MAPK signalling and the atypical ubiquitin ligase complex are important for the fine-tuning of Nmnat2 levels. While MAPK signalling targets membrane-associated Nmnat2, the atypical ubiquitin ligase complex selectively degrades axoplasmic Nmnat2 [69,85]. The pharmacological inhibition of both mechanisms results in a strong attenuation of axon death signalling [69]. This suggests that distinct axonal pools of Nmnat2 are differentially regulated (figure 3a).

The above discoveries revealed a central and conserved function for Nmnat2/dNmnat. Levels of the labile axonal survival factor are dictated by three branches (figure 3a): (i) continuous supply of Nmnat proteins by axonal transport, (ii) constant degradation of vesicle-bound Nmnat proteins by the MAPK pathway, and (iii) constant degradation of soluble Nmnat proteins by the atypical ubiquitin ligase complex.

In healthy uninjured axons, Nmnat protein levels are above threshold, ensuring low NMN and high NAD⁺

levels. Vice versa, in injured axons, the supply of Nmnat proteins by axonal transport is cut down, and, therefore, Nmnat protein degradation by the MAPK pathway and the atypical ubiquitin ligase complex takes over. This results in below-threshold levels of Nmnat proteins. Likewise, levels of NMN temporally rise, whereas NAD⁺ levels drop.

So far, the execution of axon death signalling is solely initiated by below-threshold levels of Nmnat proteins. Any modification that sustains levels of Nmnat proteins—e.g. gain of Nmnat stability or loss of Nmnat protein degradation—ultimately attenuates axon death.

At this point, no mediator in axon death signalling had been identified that actively contributes to signalling, e.g. where loss-of-function mutations result in attenuated axon death signalling regardless of Nmnat protein levels. Below, we will discuss such mediators.

4.5. Sarm1/dSarm

The first discovery of a mutation which attenuates axon death irrespective of Nmnat levels was made in *Drosophila*: through an unbiased forward-genetic screen for axon death defective mutants, several loss-of-function alleles of the gene '*Drosophila* sterile alpha and armadillo motif' (*dsarm*) were isolated (figure 3). Mutations in *dsarm* block axon death for the lifespan of the fly [86], *dsarm* is therefore essential for injury-induced axon degeneration. Similarly, mutants or downregulation of the mammalian homologue Sarm1 harbour a potent attenuation of axon death signalling *in vitro* and *in vivo* [76,86–88]. Sarm1/dSarm is a toll-like receptor adaptor family member and mainly expressed in the nervous system [86], yet it also functions in glial cells [89], and in the immune system [90].

Sarm1/dSarm contains three evolutionarily conserved protein domains: an Armadillo/HEAT (ARM) domain, a sterile alpha motif (SAM) (two in mammals and one in flies) and a Toll/interleukin-1 receptor homology (TIR) domain [86,87]. All three domains are essential for Sarm1 function in mice [76,82,87] and dSarm in *Drosophila* [65]. The ARM domain keeps dSarm/Sarm1 inactive, as previously reported in the *C. elegans* homologue TIR-1 [91], and the SAM domain is important for Sarm1 dimerization [76,81]. The TIR domain, rather than harbouring signalling activity, contains an enzymatic activity to consume NAD⁺ (NADase activity) [92]. Sarm1 activation by dimerization is necessary and sufficient locally within axons to execute axon degeneration in the absence of injury. Its activation triggers rapid depletion of NAD⁺ [73,76,92]. Importantly, the TIR domain NADase activity is evolutionarily conserved across flies, zebrafish and mice, where it cleaves NAD⁺ into nicotinamide (Nam) and ADP-ribose (ADPR) or cyclic ADPR (cADPR) with species-specific differences [92]. These findings support a model where, upon injury, Sarm1/dSarm is activated and actively depletes NAD⁺ levels in severed axons. Therefore, Sarm1/dSarm plays a central role in NAD⁺ depletion in severed axons after injury.

4.6. Axundead

Recently, another essential mediator of axon death signalling has been identified in *Drosophila*. Several *axundead* (*axed*) mutants were isolated by another unbiased forward-genetic screen [65]. Similar to *highwire* and *dsarm* mutants, mutations in *axed* attenuate axon death signalling for the lifespan of the

fly (figure 3b) [20,65,86]. The *axed* gene consists of two isoforms (*axed^{long}* and *axed^{short}*), and both isoforms are capable of rescuing *axed* mutants. Axed proteins are predominantly found in axons and synapses, and its levels increase 4–6 h post axotomy and return to baseline 24 h after injury, suggesting either a transient change in localization and/or levels in response to axonal injury. Axed contains two evolutionary conserved domains: a BTB and a BACK domain, which suggests that Axed could dimerize and/or interact with cullin ubiquitin ligases [93]. There are four mammalian paralogues (BTBD1, BTBD2, BTBD3, BTBD6), and it remains to be determined which paralogue(s) could have an active role in axon death in mammals [65]. The precise mechanistic function of Axed remains currently unknown.

4.7. Calpains and Calpastatin

Calpains have recently also been shown to be involved in axon death signalling (figure 3a) [81]. Calpains are Ca^{2+} -dependent non-lysosomal proteases, and they are involved in neuronal degeneration in traumatic brain injury, cerebral ischaemia and AD [94]. Among the 15 mammalian isoforms, Calpain-1 and Calpain-2 are ubiquitously expressed, predominantly in the brain, and are present in both neurons and glia [95]. Within minutes after experimental traumatic axonal injury (TAI), axonal Calpain activity is elevated [96]. Vice versa, mice lacking Calpain-1/2 show a significant delay in axon death compared with wild-type mice [81].

Calpastatin is an endogenous *in vivo* inhibitor of Calpains. After axonal injury, levels of Calpastatin drop within 10 h, which correlates with the morphological degeneration of axons [34]. In contrast, transgenic mice expressing human Calpastatin harbour robust attenuation of axon death in transected optic nerves in the CNS and sciatic nerves in the PNS [97].

Calpastatin-mediated regulation of Calpains is likely the most downstream cascade of axon death signalling. However, the mechanistic link between the above mediators of axon death signalling and Calpains in mammals, and whether Calpains are also involved in other species, remains to be determined.

4.8. Other mediators

So far, axon death mediators were discussed whose modification results in a robust attenuation. Yet also other modifications have been reported that are capable of delaying axon death, such as the mitochondrial permeability transition [31], recycling endosomes [98], autophagy [99,100], sodium and potassium currents [50], the ubiquitin ligase ZNRF-1 [101], microtubule destabilization mediated by CRMP2 [102,103] and the transcription factor Pebbled/RREB1 [104]. The precise interaction of these mediators with the signalling cascade remains to be determined, because of either tissue-specific phenotypes or the involvement of whole organelles.

5. Interspecies commonalities and differences

Wild^S attenuates axon death in a variety of models across evolution [19,33,42–44,48]. Each animal system offers unique insights into axon death signalling, thus also distinct observations have been made between them. How is axon death

studied in different animal models, and what is common, or different, among them? Below, we will briefly discuss each animal model where axon death is extensively studied, followed by highlighting commonalities and differences in axon death signalling across species.

5.1. Animal models

Mice are frequently used for both *in vitro* and *in vivo* axon death assays: *in vitro* cultured neurons from superior cell ganglia (SCGs) and dorsal root ganglia (DRGs) from the PNS, and retinal ganglion cells (RGCs) from the CNS, are subjected to axon death assays. Moreover, pharmacogenetic manipulation of metabolism can also be applied *in vitro*. Broadly used *in vivo* assays are optic nerve injuries (CNS) and sciatic nerve lesions (PNS).

Rats facilitate stereotaxic injections because of their larger brains, and lesions of optic or facial nerves and nerve roots can also be readily performed. Moreover, nerves are longer than those in mice, putting them closer to human axons, although human axons can still be 10-fold longer than their rat counterparts [24,44]. Rats also provide more abundant sources of tissue for biochemical and proteomic studies.

Zebrafish provides a major advantage with its powerful *in vivo* live imaging, as the complete time course of axon death, with the resolution of single axons, can readily be observed. It is important to mention that zebrafish offers the unique ability to visualize temporal Ca^{2+} events *in vivo*.

Flies harbour the unique advantage of unbiased forward-genetic screens. Axon death is observed *in vivo* by antennal or maxillary palp ablation, wing injuries, and during larval development by nerve crush. These techniques were recently reviewed in [105]. Moreover, by the use of optogenetics, the functional preservation of axons and their synapses can readily be assessed by a simple grooming assay.

5.2. Commonalities and differences across species

Genetic analyses in the above animal systems provided important insights over recent years. These findings led to the definition of an axon death signalling pathway. It is tempting to combine all analyses to define a core signalling cascade across multiple species. Yet these analyses also revealed subtle differences that should not be neglected. Below, we will highlight common features as well as species-specific axon death signalling differences among mouse, fly and fish.

5.2.1. Conserved mediators

Ca^{2+} plays a crucial role in all model systems tested so far. Both Ca^{2+} entry into the axon after injury (first, rapid short-term Ca^{2+} wave) and the Ca^{2+} release from intracellular stores at the end of the lag phase (second, long-term Ca^{2+} wave) have been observed across multiple species. It is therefore likely that the first conserved mediator of axon death signalling is external Ca^{2+} influx into severed axons.

Nmnat2/dNmnat in mice, fish and flies harbour an evolutionary conserved feature too. As a labile axon survival factor, levels of Nmnat proteins matter: high or robust levels potentially protect severed axons from undergoing axon death, and low levels induce axon degeneration in all species tested [33,45,60,64]. Alongside Nmnat, its biosynthetic NAD^{+} activity is also conserved across species. It remains to be

determined whether levels of NMN and NAD⁺, or ratios thereof, define when axon death is initiated, not only in mice but also in flies and fish.

Atypical ubiquitin ligase complex members, which regulate Nmnat protein levels, are conserved in mice and flies (Skip1a, Phr1, Fbxo45 in mouse, and Phr1 in fly). Interestingly, while the MAPK pathway plays an important role in mice, it seems to be negligible in flies [65]. Whether the fish homologues of the atypical ubiquitin ligase complex and the MAPK signalling cascade regulate levels of Nmnat2 in a similar way remains elusive.

The function of the dSarm/Sarm1 homologues in flies and mice, and Sarm1 in fish [106], is also evolutionarily conserved. Loss-of-function mutants block axon death signalling, and the TIR domain of these species harbours the ability to pathologically degrade NAD⁺ to generate Nam and ADPR or cADPR [92].

It is equally important to note that species-specific pathway analyses revealed some remarkable differences. This indicates that we are far from fully understanding axon death signalling mechanisms. Below, we will briefly discuss these differences.

5.2.2. Differences across species

Mice lacking *Nmnat2* contain truncated axons during embryogenesis and die perinatally [63]. This lethality is partially rescued by over-expression of *Wld^S* [107], and fully rescued by *Sarm1* mutants [88]. Therefore, Sarm1 executes axon death following below-threshold levels of Nmnat2. Sarm1 likely acts downstream of Nmnat2 (figure 3a). However, it could also act in parallel to it, but certainly not upstream of Nmnat2.

As soon as Nmnat2 levels drop below threshold, Sarm1 unleashes its TIR domain to consume NAD⁺. Nmnat2, rather than maintaining NAD⁺ levels through its NAD⁺ biosynthetic activity, blocks NAD⁺ consumption of Sarm1, which seems central to axon death signalling [73,76]. It remains completely unknown how Nmnat2 inhibits the NADase activity of Sarm1.

As mentioned above, *Nmnat2*^{-/-} mice contain truncated axons during embryogenesis and die perinatally [63]. *Wld^S* mice and *Sarm1* mutants are not the only two candidates able to rescue both: surprisingly, the expression of the bacterial NMN deamidase does the same in a dosage-dependent manner [75]. This finding suggests that, besides the pathological NAD⁺ consumption of Sarm1, the temporal rise of NMN is also crucial for axon death signalling, after Nmnat2 has disappeared in severed axons (figure 3a).

In flies, sensory neurons mutant for the sole *dnmnat* gene undergo rapid neurodegeneration, which, unlike in mammals, is not blocked by *dsarm*, but by *axed* mutants [65]. These findings imply that neurodegeneration induced by below-threshold levels of dNmnat is not executed by dSarm, but by Axed. Similarly, axon and neurodegeneration induced by the expression of a constitutively active NADase version of dSarm lacking the inhibitory ARM domain (dSarm^{ΔARM}), which promotes rapid NAD⁺ depletion, is blocked by *axed* mutants. This suggests that Axed is also downstream of dSarm. Finally, axon and neurodegeneration induced together by *dnmnat* mutants and by dSarm^{ΔARM} expression is also blocked by *axed* mutants, suggesting that axon death signalling converges on Axed to execute the disassembly of the axon (figure 3b) [65].

In fish, axon death is attenuated by the over-expression of *nmnat2* and by *Wld^S* [33,45]. Moreover, loss of *sarm1* also

attenuates axon death, suggesting that its function is conserved in fish [106]. However, it remains to be seen whether below-threshold levels of Nmnat2 are sufficient to trigger axon degeneration. Last but not least, the genetic interaction among Ca²⁺, Nmnat2 and Sarm1 remains to be determined (figure 3c).

Above, we have summarized conserved axon death mediators, and we also highlighted differences observed across species. Despite these subtle differences, it is tempting to extract a core axon death mechanism which could be evolutionarily conserved. This will be discussed below.

5.3. The NMN/NAD⁺ ratio

One speculative possibility is a crucial ratio between NMN and NAD⁺. Under normal, healthy conditions, the ratio between NMN and NAD⁺ is highly in favour of NAD⁺ (NMN ≪ NAD⁺), which is supported by the observation of lower axonal concentrations of NMN and higher concentrations of NAD⁺ [73,74,88] (figure 3a). Injury leads to below-threshold levels of the labile axonal survival factor Nmnat2, which in turn leads to a temporal rise of NMN and lower levels of NAD⁺, thus reducing the ratio (NMN < NAD⁺). This ratio could already be sufficient to activate axon death. Importantly, below-threshold levels of Nmnat2 also discontinue Nmnat2-mediated inhibition of Sarm1, which discharges the NADase activity of Sarm1: the resulting Sarm1-mediated NAD⁺ consumption tips the ratio towards NMN (NMN ≫ NAD⁺). This ratio could therefore dictate whether axons should survive, or degenerate. Axon survival is favoured by NMN ≪ NAD⁺: preventing the rise of NMN, or the consumption of NAD⁺, both potently attenuate axon death. Vice versa, conditions altering this ratio will induce axon death: the forced depletion of NAD⁺ by a constitutively active NADase activity of Sarm1/dSarm is sufficient to trigger axon (and cell body) death. If this were true, high NMN levels—significantly higher than NAD⁺—should also be capable of triggering axon death *in vivo*. This remains to be tested, but also harbours technical difficulties: Nmnat proteins efficiently synthesize NAD⁺ from NMN, thus a rise in NMN automatically results in a rise of NAD⁺ [58,73]. Interestingly, high levels of a cell-permeable analogue of NMN (which cannot be used as substrate for Nmnat-mediated NAD⁺ synthesis) are sufficient to activate Sarm1 in cultured neurons, thereby depleting NAD⁺, which results in non-apoptotic cell death. Whether this is also true in severed axons remains to be determined [108].

We are still far from understanding why and how axons execute their own disassembly. Our knowledge of axon death as an emerging signalling cascade is still in its infancy. Each axon death mediator revealed crucial mechanistic insights over recent years, and helped to define Sarm1 as a first target that can be translated to the clinic. In the section below, we will briefly discuss where targeting of Sarm1 is beneficial in mouse models of neurological conditions.

6. Axon death signalling in disease

Mutations in human Nmnat2 have been linked to fetal akinesia deformation sequence (FADS), and to childhood-onset polyneuropathy and erythromelalgia [109,110]. These discoveries provide the first direct molecular evidence that axon death in WD is involved in a human axonal disorder. They support

the idea that axonopathies are a major contributor to certain human neurodegenerative disorders [12–15].

Wld^S and its capacity to slow down injury-induced axon degeneration offered the first opportunity to attenuate axonopathies which occur in the absence of injury. Over recent years, distinct outcomes were observed in a broad range of disease models, including extended lifespan, age-dependent effects, improved performance, or a lack of amelioration [23]. The promising neuroprotective function of Wld^S also led to efforts developing drugs to stabilize Nmnat proteins [111]. However, while the efficacy of Wld^S or any other form of engineered Nmnat protein seems promising in certain models of neurological conditions, therapeutic potential may be limited due to a gain-of-function protein: its efficacy relies on dosage, which could be challenging during long-term therapeutic treatments [43]. Moreover, Wld^S harbours age-dependent effects [112], and while it is capable of slowing down axon death, it is not able to fully block it [107]. Therefore, alternative or complementary approaches would increase the chance of ameliorating axonopathies.

The manipulation of the NMN/NAD⁺ ratio could offer an attractive alternative. It could be achieved by pharmacological targeting of specific metabolic pathways, or by simple oral supplement of NAD⁺ or its precursors. Preventing either NAD⁺ consumption or a temporal rise of NMN could serve as attractive strategies [113,114]. However, without any specificity towards neuronal tissue, the manipulation of NAD⁺ metabolism also bears great risks [115].

The discovery of Sarm1/dSarm has offered a novel and unique therapeutic opportunity. In order to block axon death signalling, Sarm1 protein or its activity has to be decreased, rather than increased such as with Nmnat2. Like Wld^S, *Sarm1* mutant mice offer a range of outcomes in mouse models of neurological conditions:

When axons are challenged by mechanical forces, *Sarm1*^{-/-} mice harbour reduced neurological deficits and a better functional outcome in a model of TBI [116]. *Sarm1*^{-/-} mice also contain significantly reduced axonal lesions in a model of TAI with impact acceleration of heads [117]. In addition, an *in vivo* gene therapy approach using adeno-associated virus to deliver a dominant-negative version of Sarm1 had similar effects in an injury-induced axon degeneration model to that in *Sarm1*^{-/-} mice [118]. These findings strongly suggest that Sarm1 serves as a promising therapeutic target to ameliorate force-induced axonopathies.

In two models of CIPN (e.g. vincristine or paclitaxel), and in a model of metabolic-induced peripheral neuropathy, mice lacking *Sarm1* prevent the distal degeneration of myelinated axons and electrophysiological abnormalities [119,120]. These findings fuel hope that axonopathies caused by chemotherapy or by diabetes—the most common causes of peripheral neuropathies [121,122]—could also be therapeutically targeted in patients.

However, while Sarm1 harbours the potential to ameliorate certain axonopathies, it is important to note that the lack of *Sarm1* does not suppress motor neuron degeneration in a mouse model of ALS [123]. It remains to be determined whether *Sarm1* is dispensable in other ALS mouse models.

So far, *Sarm1*^{-/-} mutants have beneficial effects in certain models of neurological conditions. This raises hope that Sarm1 and other axon death mediators could serve as drug-gable targets to halt axon loss. Axon death signalling serves therefore as an attractive pathway to develop therapies against, with the ultimate goal to prevent and treat axon loss in a broad range of neurological diseases.

7. Conclusion

The discovery and characterization of axon death signalling, which is activated by injury, not only provided exciting insights into the underlying mechanism mediating axonal self-destruction after injury. It also revealed that the axon death pathway is hijacked in other challenging conditions for the nervous system where axonopathies occur in the absence of injury. Therefore, it is crucial to fill missing mechanistic gaps among already identified axon death mediators, and to identify other key mediators required for axon death signalling. This will help to expand our understanding of a signalling pathway that ultimately leads to the death of the axon. Overall, there is certainly a lot left to do, and axon death research will therefore continue to be a lively field in the future.

Data accessibility. This article has no additional data.

Competing interests. The authors declare that they have no competing interests.

Funding. This work is supported by a Swiss National Science Foundation (SNSF) Assistant Professor Grant (176855), the État de Vaud (University of Lausanne) and the International Foundation for Research in Paraplegia (IRP) (P180) to L.J.N.

Acknowledgements. The authors thank Dr Tilmann Achsel and Maria Paglione for helpful comments.

References

- Matsuda W, Furuta T, Nakamura KC, Hioki H, Fujiyama F, Arai R, Kaneko T. 2009 Single nigrostriatal dopaminergic neurons form widely spread and highly dense axonal arborizations in the neostriatum. *J. Neurosci.* **29**, 444–453. (doi:10.1523/JNEUROSCI.4029-08.2009)
- Wedel MJ. 2012 A monument of inefficiency: the presumed course of the recurrent laryngeal nerve in sauropod dinosaurs. *Acta Palaeontol. Pol.* **57**, 251–256. (doi:10.4202/app.2011.0019)
- Xu K, Zhong G, Zhuang X. 2013 Actin, spectrin, and associated proteins form a periodic cytoskeletal structure in axons. *Science* **339**, 452–456. (doi:10.1126/science.1232251)
- Smith DH, Wolf JA, Meaney DF. 2001 A new strategy to produce sustained growth of central nervous system axons: continuous mechanical tension. *Tissue Eng.* **7**, 131–139. (doi:10.1089/107632701300062714)
- Hammarlund M, Jorgensen EM, Bastiani MJ. 2007 Axons break in animals lacking beta-spectrin. *J. Cell Biol.* **176**, 269–275. (doi:10.1083/jcb.200611117)
- Smith DH. 2009 Stretch growth of integrated axon tracts: extremes and exploitations. *Prog. Neurobiol.* **89**, 231–239. (doi:10.1016/J.PNEUROBIO.2009.07.006)
- Fournier AJ, Hogan JD, Rajbhandari L, Shrestha S, Venkatesan A, Ramesh KT. 2015 Changes in neurofilament and microtubule distribution following focal axon compression. *PLoS ONE* **10**, e0131617. (doi:10.1371/journal.pone.0131617)
- Krieg M, Stühmer J, Cueva JG, Fetter R, Spilker K, Cremers D, Shen K, Dunn AR, Goodman MB. 2017 Genetic defects in β -spectrin and tau sensitize *C. elegans* axons to movement-induced damage via torque-tension coupling. *Elife* **6**, e20172. (doi:10.7554/elife.20172)
- Mariano V, Domínguez-Ilturza N, Neukomm LJ, Bagni C. 2018 Maintenance mechanisms of circuit-

- integrated axons. *Curr. Opin. Neurobiol.* **53**, 162–173. (doi:10.1016/j.conb.2018.08.007)
10. Neukomm LJ, Freeman MR. 2014 Diverse cellular and molecular modes of axon degeneration. *Trends Cell Biol.* **24**, 515–523. (doi:10.1016/j.tcb.2014.04.003)
 11. Burgess RW, Crish SD. 2018 Editorial: Axonopathy in neurodegenerative disease. *Front. Neurosci.* **12**, 769. (doi:10.3389/fnins.2018.00769)
 12. Vickers JC *et al.* 2009 Axonopathy and cytoskeletal disruption in degenerative diseases of the central nervous system. *Brain Res. Bull.* **80**, 217–223. (doi:10.1016/j.brainresbull.2009.08.004)
 13. Burke RE, O'Malley K. 2013 Axon degeneration in Parkinson's disease. *Exp. Neurol.* **246**, 72–83. (doi:10.1016/j.expneurol.2012.01.011)
 14. Hill CS, Coleman MP, Menon DK. 2016 Traumatic axonal injury: mechanisms and translational opportunities. *Trends Neurosci.* **39**, 311–324. (doi:10.1016/j.tins.2016.03.002)
 15. Flatters SJL, Dougherty PM, Colvin LA. 2017 Clinical and preclinical perspectives on Chemotherapy-Induced Peripheral Neuropathy (CIPN): a narrative review. *Br. J. Anaesth.* **119**, 737–749. (doi:10.1093/bja/aez229)
 16. Coleman MP, Perry VH. 2002 Axon pathology in neurological disease: a neglected therapeutic target. *Trends Neurosci.* **25**, 532–537. (doi:10.1016/S0166-2236(02)02255-5)
 17. Simon DJ, Watkins TA. 2018 Therapeutic opportunities and pitfalls in the treatment of axon degeneration. *Curr. Opin. Neurol.* **31**, 693–701. (doi:10.1097/WCO.0000000000000621)
 18. Waller A. 1850 Experiments on the section of the glossopharyngeal and hypoglossal nerves of the frog, and observations of the alterations produced thereby in the structure of their primitive fibres. *Phil. Trans. R. Soc.* **140**, 423–429.
 19. MacDonald JM, Beach MG, Porpiglia E, Sheehan AE, Watts RJ, Freeman MR. 2006 The *Drosophila* cell corpse engulfment receptor Draper mediates glial clearance of severed axons. *Neuron* **50**, 869–881. (doi:10.1016/j.neuron.2006.04.028)
 20. Neukomm LJ, Burdett TC, Gonzalez MA, Züchner S, Freeman MR. 2014 Rapid in vivo forward genetic approach for identifying axon death genes in *Drosophila*. *Proc. Natl Acad. Sci. USA* **111**, 9965–9970. (doi:10.1073/pnas.1406230111)
 21. Bridge PM, Ball DJ, Mackinnon SE, Nakao Y, Brandt K, Hunter DA, Hertl C. 1994 Nerve crush injuries—a model for axonotmesis. *Exp. Neurol.* **127**, 284–290. (doi:10.1006/EXNR.1994.1104)
 22. Maxwell WL, Bartlett E, Morgan H. 2015 Wallerian degeneration in the optic nerve stretch-injury model of traumatic brain injury: a stereological analysis. *J. Neurotrauma* **32**, 780–790. (doi:10.1089/neu.2014.3369)
 23. Conforti L, Gilley J, Coleman MP. 2014 Wallerian degeneration: an emerging axon death pathway linking injury and disease. *Nat. Rev. Neurosci.* **15**, 394–409. (doi:10.1038/nrn3680)
 24. Adalbert R, Morreale G, Paizs M, Conforti L, Walker SA, Roderick HL, Bootman MD, Siklós L, Coleman MP. 2012 Intra-axonal calcium changes after axotomy in wild-type and slow Wallerian degeneration axons. *Neuroscience* **225**, 44–54. (doi:10.1016/j.neuroscience.2012.08.056)
 25. Villegas R, Martinez NW, Lillo J, Pihan P, Hernandez D, Twiss JL, Court FA. 2014 Calcium release from intra-axonal endoplasmic reticulum leads to axon degeneration through mitochondrial dysfunction. *J. Neurosci.* **34**, 7179–7189. (doi:10.1523/JNEUROSCI.4784-13.2014)
 26. George B, Glass D, Griffin W. 1995 Axotomy-induced axonal degeneration influx through ion-specific channels. *J. Neurosci.* **15**, 6445–6452. (doi:10.1523/jneurosci.15-10-06445.1995)
 27. Avery MA, Rooney TM, Pandya JD, Wishart TM, Gillingwater TH, Geddes JW, Sullivan PG, Freeman MR. 2012 WldS prevents axon degeneration through increased mitochondrial flux and enhanced mitochondrial Ca²⁺ buffering. *Curr. Biol.* **22**, 596–600. (doi:10.1016/j.cub.2012.02.043)
 28. Park JY, Jang SY, Shin YK, Koh H, Suh DJ, Shinji T, Araki T, Park HT. 2013 Mitochondrial swelling and microtubule depolymerization are associated with energy depletion in axon degeneration. *Neuroscience* **238**, 258–269. (doi:10.1016/j.neuroscience.2013.02.033)
 29. Zhai Q, Wang J, Kim A, Liu Q, Watts R, Hoopfer E, Mitchison T, Luo L, He Z. 2003 Involvement of the ubiquitin-proteasome system in the early stages of Wallerian degeneration. *Neuron* **39**, 217–225. (doi:10.1016/S0896-6273(03)00429-X)
 30. Shen H, Hyrc KL, Goldberg MP. 2013 Maintaining energy homeostasis is an essential component of WldS-mediated axon protection. *Neurobiol. Dis.* **59**, 69–79. (doi:10.1016/j.nbd.2013.07.007)
 31. Barrientos SA, Martinez NW, Yoo S, Jara JS, Zamorano S, Hetz C, Twiss JL, Alvarez J, Court FA. 2011 Axonal degeneration is mediated by the mitochondrial permeability transition pore. *J. Neurosci.* **31**, 966–978. (doi:10.1523/JNEUROSCI.4065-10.2011)
 32. Bernardi P, Krauskopf A, Basso E, Petronilli V, Blalchy-Dyson E, Di Lisa F, Forte MA. 2006 The mitochondrial permeability transition from *in vitro* artifact to disease target. *FEBS J.* **273**, 2077–2099. (doi:10.1111/j.1742-4658.2006.05213.x)
 33. Martin SM, O'Brien GS, Portera-Cailliau C, Sagasti A. 2010 Wallerian degeneration of zebrafish trigeminal axons in the skin is required for regeneration and developmental pruning. *Development* **137**, 3985–3994. (doi:10.1242/dev.053611)
 34. Yang J, Weimer RM, Kallop D, Olsen O, Wu Z, Renier N, Uryu K, Tessier-Lavigne M. 2013 Regulation of axon degeneration after injury and in development by the endogenous calpain inhibitor calpastatin. *Neuron* **80**, 1175–1189. (doi:10.1016/j.neuron.2013.08.034)
 35. Villegas R, Martin SM, O'Donnell KC, Carrillo SA, Sagasti A, Allende ML. 2012 Dynamics of degeneration and regeneration in developing zebrafish peripheral axons reveals a requirement for extrinsic cell types. *Neural Dev.* **7**, 19. (doi:10.1186/1749-8104-7-19)
 36. Perry VH, Brown MC, Gordon S. 1987 The macrophage response to central and peripheral nerve injury. A possible role for macrophages in regeneration. *J. Exp. Med.* **165**, 1218–1223. (doi:10.1084/JEM.165.4.1218)
 37. Purice MD, Speese SD, Logan MA. 2016 Delayed glial clearance of degenerating axons in aged *Drosophila* is due to reduced PI3 K/Draper activity. *Nat. Commun.* **7**, 12871. (doi:10.1038/ncomms12871)
 38. Zhai RG, Cao Y, Hiesinger PR, Zhou Y, Mehta SQ, Schulze KL, Verstreken P, Bellen HJ. 2006 *Drosophila* NMNAT maintains neural integrity independent of its NAD synthesis activity. *PLoS Biol.* **4**, 2336–2348. (doi:10.1371/journal.pbio.0040416)
 39. Lu T-Y, MacDonald JM, Neukomm LJ, Sheehan AE, Bradshaw R, Logan MA, Freeman MR. 2017 Axon degeneration induces glial responses through Draper-TRAF4-JNK signalling. *Nat. Commun.* **8**, 14355. (doi:10.1038/ncomms14355)
 40. Vaquié A *et al.* 2019 Injured axons instruct Schwann cells to build constricting actin spheres to accelerate axonal disintegration. *Cell Rep.* **27**, 3152–3166.e7. (doi:10.1016/j.celrep.2019.05.060)
 41. Shacham-Silverberg V, Sar Shalom H, Goldner R, Golan-Vaishenker Y, Gurwicz N, Gokhman I, Yaron A. 2018 Phosphatidylserine is a marker for axonal debris engulfment but its exposure can be decoupled from degeneration. *Cell Death Dis.* **9**, 1116. (doi:10.1038/s41419-018-1155-z)
 42. Lunn ER, Perry VH, Brown MC, Rosen H, Gordon S. 1989 Absence of Wallerian degeneration does not hinder regeneration in peripheral nerve. *Eur. J. Neurosci.* **1**, 27–33. (doi:10.1111/j.1460-9568.1989.tb00771.x)
 43. Mack TGA *et al.* 2001 Wallerian degeneration of injured axons and synapses is delayed by a Ube4b/Nmnat chimeric gene. *Nat. Neurosci.* **4**, 1199–1206. (doi:10.1038/nn770)
 44. Adalbert R *et al.* 2005 A rat model of slow Wallerian degeneration (WldS) with improved preservation of neuromuscular synapses. *Eur. J. Neurosci.* **21**, 271–277. (doi:10.1111/j.1460-9568.2004.03833.x)
 45. Feng Y, Yan T, Zheng J, Ge X, Mu Y, Zhang Y, Wu D, Du JL, Zhai Q. 2010 Overexpression of WldSor Nmnat2 in mauthner cells by single-cell electroporation delays axon degeneration in live zebrafish. *J. Neurosci. Res.* **88**, 3319–3327. (doi:10.1002/jnr.22498)
 46. Beirowski B, Babetto E, Gilley J, Mazzola F, Conforti L, Janeckova L, Magni G, Ribchester RR, Coleman MP. 2009 Non-nuclear WldS determines its neuroprotective efficacy for axons and synapses *in vivo*. *J. Neurosci.* **29**, 653–668. (doi:10.1523/JNEUROSCI.3814-08.2009)
 47. Sasaki Y, Milbrandt J. 2010 Axonal degeneration is blocked by nicotinamide mononucleotide adenylyltransferase (Nmnat) protein transduction into transected axons. *J. Biol. Chem.* **285**, 41 211–41 215. (doi:10.1074/jbc.C110.193904)
 48. Hoopfer ED, McLaughlin T, Watts RJ, Schuldiner O, O'Leary DDM, Luo L. 2006 WldS protection distinguishes axon degeneration following injury

- from naturally occurring developmental pruning. *Neuron* **50**, 883–895. (doi:10.1016/j.neuron.2006.05.013)
49. Finn JT, Weil M, Archer F, Siman R, Srinivasan A, Raff MC. 2000 Evidence that Wallerian degeneration and localized axon degeneration induced by local neurotrophin deprivation do not involve caspases. *J. Neurosci.* **20**, 1333–1341. (doi:10.1523/JNEUROSCI.20-04-01333.2000)
50. Mishra B, Carson R, Hume RI, Collins CA. 2013 Sodium and potassium currents influence Wallerian degeneration of injured *Drosophila* axons. *J. Neurosci.* **33**, 18 728–18 739. (doi:10.1523/JNEUROSCI.1007-13.2013)
51. Vargas ME, Yamagishi Y, Tessier-Lavigne M, Sagasti A. 2015 Live imaging of calcium dynamics during axon degeneration reveals two functionally distinct phases of calcium influx. *J. Neurosci.* **35**, 15 026–15 038. (doi:10.1523/JNEUROSCI.2484-15.2015)
52. Schlaepfer WW. 1974 Calcium-induced degeneration of axoplasm in isolated segments of rat peripheral nerve. *Brain Res.* **69**, 203–215. (doi:10.1016/0006-8993(74)90002-X)
53. Kerschensteiner M, Schwab ME, Lichtman JW, Misgeld T. 2005 *In vivo* imaging of axonal degeneration and regeneration in the injured spinal cord. *Nat. Med.* **11**, 572–577. (doi:10.1038/nm1229)
54. Knöferle J *et al.* 2010 Mechanisms of acute axonal degeneration in the optic nerve *in vivo*. *Proc. Natl Acad. Sci. USA* **107**, 6064–6069. (doi:10.1073/pnas.0909794107)
55. Loreto A, Di Stefano M, Gering M, Conforti L. 2015 Wallerian degeneration is executed by an NMN-SARM1-dependent late Ca^{2+} influx but only modestly influenced by mitochondria. *Cell Rep.* **13**, 2539–2552. (doi:10.1016/j.celrep.2015.11.032)
56. Conforti L, Tarlton A, Mack TG, Mi W, Buckmaster EA, Wagner D, Perry VH, Coleman MP. 2000 A *Ufd2/D4Cole1e* chimeric protein and overexpression of *Rbp7* in the slow Wallerian degeneration (*Wld^S*) mouse. *Proc. Natl Acad. Sci. USA* **97**, 11 377–11 382. (doi:10.1073/pnas.97.21.11377)
57. Sasaki Y. 2018 Metabolic aspects of neuronal degeneration: from a NAD^+ point of view. *Neurosci. Res.* **52**, 442–447. (doi:10.1016/j.neures.2018.07.001)
58. Berger F, Lau C, Dahlmann M, Ziegler M. 2005 Subcellular compartmentation and differential catalytic properties of the three human nicotinamide mononucleotide adenyltransferase isoforms. *J. Biol. Chem.* **280**, 36 334–36 341. (doi:10.1074/jbc.M508660200)
59. Ruan K, Zhu Y, Li C, Brazill JM, Zhai RG. 2015 Alternative splicing of *Drosophila Nmnat* functions as a switch to enhance neuroprotection under stress. *Nat. Commun.* **6**, 10057. (doi:10.1038/ncomms10057)
60. Gilley J, Coleman MP. 2010 Endogenous Nmnat2 is an essential survival factor for maintenance of healthy axons. *PLoS Biol.* **8**, e1000300. (doi:10.1371/journal.pbio.1000300)
61. Yan T, Feng Y, Zheng J, Ge X, Zhang Y, Wu D, Zhao J, Zhai Q. 2010 Nmnat2 delays axon degeneration in superior cervical ganglia dependent on its NAD synthesis activity. *Neurochem. Int.* **56**, 101–106. (doi:10.1016/j.neuint.2009.09.007)
62. Milde S, Gilley J, Coleman MP. 2013 Subcellular localization determines the stability and axon protective capacity of axon survival factor Nmnat2. *PLoS Biol.* **11**, e1001539. (doi:10.1371/journal.pbio.1001539)
63. Gilley J, Adalbert R, Yu G, Coleman MP. 2013 Rescue of peripheral and CNS axon defects in mice lacking NMNAT2. *J. Neurosci.* **33**, 13 410–13 424. (doi:10.1523/JNEUROSCI.1534-13.2013)
64. Fang Y, Soares L, Teng X, Geary M, Bonini NM. 2012 A novel *drosophila* model of nerve injury reveals an essential role of Nmnat in maintaining axonal integrity. *Curr. Biol.* **22**, 590–595. (doi:10.1016/j.cub.2012.01.065)
65. Neukomm LJ *et al.* 2017 Axon death pathways converge on Axundead to promote functional and structural axon disassembly. *Neuron* **95**, 78–91.e5. (doi:10.1016/j.neuron.2017.06.031)
66. Sasaki Y, Vohra BPS, Baloh RH, Milbrandt J. 2009 Transgenic mice expressing the Nmnat1 protein manifest robust delay in axonal degeneration *in vivo*. *J. Neurosci.* **29**, 6526–6534. (doi:10.1523/JNEUROSCI.1429-09.2009)
67. Avery MA, Sheehan AE, Kerr KS, Wang J, Freeman MR. 2009 *Wld^S* requires Nmnat1 enzymatic activity and N16–VCP interactions to suppress Wallerian degeneration. *J. Cell Biol.* **184**, 501–513. (doi:10.1083/jcb.200808042)
68. Babetto E, Beirowski B, Janeckova L, Brown R, Gilley J, Thomson D, Ribchester RR, Coleman MP. 2010 Targeting NMNAT1 to axons and synapses transforms its neuroprotective potency *in vivo*. *J. Neurosci.* **30**, 13 291–13 304. (doi:10.1523/JNEUROSCI.1189-10.2010)
69. Summers DW, Milbrandt J, DiAntonio A. 2018 Palmitoylation enables MAPK-dependent proteostasis of axon survival factors. *Proc. Natl Acad. Sci. USA* **115**, E8746–E8754. (doi:10.1073/pnas.1806933115)
70. Sasaki Y, Araki T, Milbrandt J. 2006 Stimulation of nicotinamide adenine dinucleotide biosynthetic pathways delays axonal degeneration after axotomy. *J. Neurosci.* **26**, 8484–8491. (doi:10.1523/JNEUROSCI.2320-06.2006)
71. Araki T, Sasaki Y, Milbrandt J. 2004 Increased nuclear NAD biosynthesis and SIRT1 activation prevent axonal degeneration. *Science* **305**, 1010–1013. (doi:10.1126/science.1098014)
72. Wang J, Zhai Q, Chen Y, Lin E, Gu W, McBurney MW, He Z. 2005 A local mechanism mediates NAD-dependent protection of axon degeneration. *J. Cell Biol.* **170**, 349–355. (doi:10.1083/jcb.200504028)
73. Sasaki Y, Nakagawa T, Mao X, DiAntonio A, Milbrandt J. 2016 NMNAT1 inhibits axon degeneration via blockade of SARM1-mediated NAD^+ depletion. *Elife* **5**, 1–15. (doi:10.7554/eLife.19749)
74. Di Stefano M *et al.* 2015 A rise in NAD precursor nicotinamide mononucleotide (NMN) after injury promotes axon degeneration. *Cell Death Differ.* **22**, 731–742. (doi:10.1038/cdd.2014.164)
75. Di Stefano M *et al.* 2017 NMN deamidase delays Wallerian degeneration and rescues axonal defects caused by NMNAT2 deficiency *in vivo*. *Curr. Biol.* **27**, 784–794. (doi:10.1016/j.cub.2017.01.070)
76. Gerdtts J, Brace EJ, Sasaki Y, DiAntonio A, Milbrandt J. 2015 SARM1 activation triggers axon degeneration locally via NAD^+ destruction. *Science* **348**, 453–457. (doi:10.1126/science.1258366)
77. Xiong X *et al.* 2012 The Highwire ubiquitin ligase promotes axonal degeneration by tuning levels of Nmnat protein. *PLoS Biol.* **10**, 1–18. (doi:10.1371/journal.pbio.1001440)
78. Babetto E, Beirowski B, Russler E, Milbrandt J, DiAntonio A. 2013 The Phr1 ubiquitin ligase promotes injury-induced axon self-destruction. *Cell Rep.* **3**, 1422–1429. (doi:10.1016/j.celrep.2013.04.013)
79. Yamagishi Y, Tessier-Lavigne M. 2016 An atypical SCF-like ubiquitin ligase complex promotes Wallerian degeneration through regulation of axonal Nmnat2. *Cell Rep.* **17**, 774–782. (doi:10.1016/j.celrep.2016.09.043)
80. Desbois M, Crawley O, Evans PR, Baker ST, Masuho I, Yasuda R, Grill B. 2018 PAM forms an atypical SCF ubiquitin ligase complex that ubiquitinates and degrades NMNAT2. *J. Biol. Chem.* **293**, 13 897–13 909. (doi:10.1074/jbc.RA118.002176)
81. Yang J *et al.* 2015 Pathological axonal death through a MAPK cascade that triggers a local energy deficit. *Cell* **160**, 161–176. (doi:10.1016/j.cell.2014.11.053)
82. Walker LJ, Summers DW, Sasaki Y, Brace E, Milbrandt J, DiAntonio A. 2017 MAPK signaling promotes axonal degeneration by speeding the turnover of the axonal maintenance factor NMNAT2. *Elife* **6**, e22540. (doi:10.7554/eLife.22540)
83. Miller BR, Press C, Daniels RW, Sasaki Y, Milbrandt J, DiAntonio A. 2009 A dual leucine kinase-dependent axon self-destruction program promotes Wallerian degeneration. *Nat. Neurosci.* **12**, 387–389. (doi:10.1038/nn.2290)
84. Shin JE *et al.* 2012 SCG10 is a JNK target in the axonal degeneration pathway. *Proc. Natl Acad. Sci. USA* **109**, E3696–E3705. (doi:10.1073/pnas.1216204109)
85. Milde S, Fox AN, Freeman MR, Coleman MP. 2013 Deletions within its subcellular targeting domain enhance the axon protective capacity of Nmnat2 *in vivo*. *Sci. Rep.* **3**, 1–9. (doi:10.1038/srep02567)
86. Osterloh JM *et al.* 2012 dSarm/Sarm1 is required for activation of an injury-induced axon death pathway. *Science* **337**, 481–484. (doi:10.1126/science.1223899)
87. Gerdtts J, Summers DW, Sasaki Y, DiAntonio A, Milbrandt J. 2013 Sarm1-mediated axon degeneration requires both SAM and TIR interactions. *J. Neurosci.* **33**, 13 569–13 580. (doi:10.1523/JNEUROSCI.1197-13.2013)
88. Gilley J, Orsomando G, Nascimento-Ferreira I, Coleman MP. 2015 Absence of SARM1 rescues development and survival of NMNAT2-deficient axons. *Cell Rep.* **10**, 1975–1982. (doi:10.1016/j.celrep.2015.02.060)

89. McLaughlin CN, Perry-Richardson JJ, Coutinho-Budd JC, Broihier HT. 2019 Dying neurons utilize innate immune signaling to prime glia for phagocytosis during development. *Dev. Cell* **48**, 506–522.e6. (doi:10.1016/j.devcel.2018.12.019)
90. Panneerselvam P, Singh LP, Selvarajan V, Chng WJ, Ng SB, Tan NS, Ho B, Chen J, Ding JL. 2013 T-cell death following immune activation is mediated by mitochondria-localized SARM. *Cell Death Differ.* **20**, 478–489. (doi:10.1038/cdd.2012.144)
91. Chuang C-F, Bargmann CI. 2005 A Toll-interleukin 1 repeat protein at the synapse specifies asymmetric odorant receptor expression via ASK1 MAPKKK signaling. *Genes Dev.* **19**, 270–281. (doi:10.1101/gad.1276505)
92. Essuman K, Summers DW, Sasaki Y, Mao X, DiAntonio A, Milbrandt J. 2017 The SARM1 Toll/interleukin-1 receptor domain possesses intrinsic NAD⁺ cleavage activity that promotes pathological axonal degeneration. *Neuron* **93**, 1334–1343.e5. (doi:10.1016/j.neuron.2017.02.022)
93. Stogios PJ, Privé GG. 2004 The BACK domain in BTB-kelch proteins. *Trends Biochem. Sci.* **29**, 634–637. (doi:10.1016/J.TIBS.2004.10.003)
94. Saatman KE, Creed J, Raghupathi R. 2010 Calpain as a therapeutic target in traumatic brain injury. *Neurotherapeutics* **7**, 31–42. (doi:10.1016/j.nurt.2009.11.002)
95. Macqueen DJ, Wilcox AH. 2014 Characterization of the definitive classical calpain family of vertebrates using phylogenetic, evolutionary and expression analyses. *Open Biol.* **4**, 130219. (doi:10.1098/rsob.130219)
96. Büki A, Siman R, Trojanowski JQ, Povlishock JT. 1999 The role of calpain-mediated spectrin proteolysis in traumatically induced axonal injury. *J. Neuropathol. Exp. Neurol.* **58**, 365–375. (doi:10.1097/00005072-199904000-00007)
97. Ma M, Ferguson TA, Schoch KM, Li J, Qian Y, Shofer FS, Saatman KE, Neumar RW. 2013 Calpains mediate axonal cytoskeleton disintegration during Wallerian degeneration. *Neurobiol. Dis.* **56**, 34–46. (doi:10.1016/j.nbd.2013.03.009)
98. Bhattacharya MRC, Geisler S, Pittman SK, Doan RA, Wehl CC, Milbrandt J, DiAntonio A. 2016 TMEM184b promotes axon degeneration and neuromuscular junction maintenance. *J. Neurosci.* **36**, 4681–4689. (doi:10.1523/JNEUROSCI.2893-15.2016)
99. Wang H *et al.* 2019 Rapid depletion of ESCRT protein Vps4 underlies injury-induced autophagic impediment and Wallerian degeneration. *Sci. Adv.* **5**, eaav4971. (doi:10.1126/sciadv.aav4971)
100. Wakatsuki S, Tokunaga S, Shibata M, Araki T. 2017 GSK3B-mediated phosphorylation of MCL1 regulates axonal autophagy to promote Wallerian degeneration. *J. Cell Biol.* **216**, 477–493. (doi:10.1083/jcb.201606020)
101. Araki T, Wakatsuki S. 2018 Regulation of neuronal/axonal degeneration by ZNRF1 ubiquitin ligase. *Neurosci. Res.* **139**, 21–25. (doi:10.1016/j.neures.2018.07.008)
102. Kinoshita Y, Kondo S, Takahashi K, Nagai J, Wakatsuki S, Araki T, Goshima Y, Ohshima T. 2019 Genetic inhibition of CRMP2 phosphorylation delays Wallerian degeneration after optic nerve injury. *Biochem. Biophys. Res. Commun.* **514**, 1037–1039. (doi:10.1016/j.bbrc.2019.05.060)
103. Zhang J-N *et al.* 2016 Calpain-mediated cleavage of collapsin response mediator protein-2 drives acute axonal degeneration. *Sci. Rep.* **6**, 37050. (doi:10.1038/srep37050)
104. Farley JE, Burdett TC, Barria R, Neukomm LJ, Kenna KP, Landers JE, Freeman MR. 2018 Transcription factor Pebbled/RREB1 regulates injury-induced axon degeneration. *Proc. Natl Acad. Sci. USA* **115**, 1358–1363. (doi:10.1073/pnas.1715837115)
105. Rooney TM, Freeman MR. 2014 *Drosophila* models of neuronal injury. *ILAR J.* **54**, 291–295. (doi:10.1093/ilar/ilt057)
106. Tian W, Asgharsharghi A, Valera G, Czopka T, Haehnel-Taguchi M, López-Schier H. 2018 Systemic loss of Sarm1 is glioprotective after neurotrauma. *bioRxiv.* (doi:10.1101/493163)
107. Gilley J, Ribchester RR, Coleman MP. 2017 *Sarm1* deletion, but not *Wld^S*, confers lifelong rescue in a mouse model of severe axonopathy. *Cell Rep.* **21**, 10–16. (doi:10.1016/j.celrep.2017.09.027)
108. Zhao ZY *et al.* 2019 A cell-permeant mimetic of NMN activates SARM1 to produce cyclic ADP-ribose and induce non-apoptotic cell death. *iScience* **15**, 452–466. (doi:10.1016/j.isci.2019.05.001)
109. Lukacs M *et al.* 2019 Severe biallelic loss-of-function mutations in *nicotinamide mononucleotide adenyltransferase 2 (NMNAT2)* in two fetuses with fetal akinesia deformation sequence. *Exp. Neurol.* **320**, 112961. (doi:10.1016/j.expneurol.2019.112961)
110. Huppke P *et al.* 2019 Homozygous *NMNAT2* mutation in sisters with polyneuropathy and erythromelalgia. *Exp. Neurol.* **320**, 112958. (doi:10.1016/J.EXPNEUROL.2019.112958)
111. Ali YO, Bradley G, Lu H-C. 2017 Screening with an NMNAT2-MSD platform identifies small molecules that modulate NMNAT2 levels in cortical neurons. *Sci. Rep.* **7**, 43846. (doi:10.1038/srep43846)
112. Ferri A, Sanes JR, Coleman MP, Cunningham JM, Kato AC. 2003 Inhibiting axon degeneration and synapse loss attenuates apoptosis and disease progression in a mouse model of motoneuron disease. *Curr. Biol.* **13**, 669–673. (doi:10.1016/S0960-9822(03)00206-9)
113. Kaneko S, Wang J, Kaneko M, Yiu G, Hurrell JM, Chitnis T, Khoury SJ, He Z. 2006 Protecting axonal degeneration by increasing nicotinamide adenine dinucleotide levels in experimental autoimmune encephalomyelitis models. *J. Neurosci.* **26**, 9794–9804. (doi:10.1523/JNEUROSCI.2116-06.2006)
114. Meyer zu Horste G, Miesbach TA, Müller JI, Fledrich R, Stassart RM, Kieseier BC, Coleman MP, Sereda MW. 2011 The *Wlds* transgene reduces axon loss in a Charcot-Marie-Tooth disease 1A rat model and nicotinamide delays post-traumatic axonal degeneration. *Neurobiol. Dis.* **42**, 1–8. (doi:10.1016/j.nbd.2010.12.006)
115. Yaku K, Okabe K, Hikosaka K, Nakagawa T. 2018 NAD metabolism in cancer therapeutics. *Front. Oncol.* **8**, 622. (doi:10.3389/fonc.2018.00622)
116. Henninger N, Bouley J, Sikoglu EM, An J, Moore CM, King JA, Bowser R, Freeman MR, Brown RH. 2016 Attenuated traumatic axonal injury and improved functional outcome after traumatic brain injury in mice lacking *Sarm1*. *Brain* **139**, 1094–1105. (doi:10.1093/brain/aww001)
117. Ziogas NK, Koliatsos VE. 2018 Primary traumatic axonopathy in mice subjected to impact acceleration: a reappraisal of pathology and mechanisms with high-resolution anatomical methods. *J. Neurosci.* **38**, 4031–4047. (doi:10.1523/JNEUROSCI.2343-17.2018)
118. Geisler S, Huang SX, Strickland A, Doan RA, Summers DW, Mao X, Park J, DiAntonio A, Milbrandt J. 2019 Gene therapy targeting SARM1 blocks pathological axon degeneration in mice. *J. Exp. Med.* **216**, 294–303. (doi:10.1084/jem.20181040)
119. Geisler S, Doan RA, Strickland A, Huang X, Milbrandt J, DiAntonio A. 2016 Prevention of vincristine-induced peripheral neuropathy by genetic deletion of SARM1 in mice. *Brain* **139**, 3092–3108. (doi:10.1093/brain/aww251)
120. Turkiew E, Falconer D, Reed N, Höke A. 2017 Deletion of *Sarm1* gene is neuroprotective in two models of peripheral neuropathy. *J. Peripher. Nerv. Syst.* **22**, 162–171. (doi:10.1111/jns.12219)
121. Grisold W, Cavaletti G, Windebank AJ. 2012 Peripheral neuropathies from chemotherapeutics and targeted agents: diagnosis, treatment, and prevention. *Neuro. Oncol.* **14**, iv45–iv54. (doi:10.1093/neuonc/nos203)
122. Juster-Switlyk K, Smith AG. 2016 Updates in diabetic peripheral neuropathy. *F1000Res.* **5**, 738. (doi:10.12688/f1000research.7898.1)
123. Peters OM, Lewis EA, Osterloh JM, Weiss A, Salameh JS, Metterville J, Brown RH, Freeman MR. 2018 Loss of *Sarm1* does not suppress motor neuron degeneration in the SOD1G93A mouse model of amyotrophic lateral sclerosis. *Hum. Mol. Genet.* **27**, 3761–3771. (doi:10.1093/hmg/ddy260)

ANNEX 2

DALI search for Axed 3D structure

PDB	Chain	Z	rmsd (Å)	lali	nres	%id	Description
4ap2-	A	15,5	5	226	266	14	KELCH-LIKE PROTEIN 11;
6i2m-	A	13,5	2,3	172	196	13	KELCH REPEAT AND BTB DOMAIN-CONTAINING PROTEIN A5
4j8z-	A	12,7	5,6	157	179	13	SPECKLE-TYPE POZ PROTEIN;
3hve-	A	12	3,3	183	216	14	GIGAXONIN;
6w67-	A	12	4,6	108	129	9	KELCH-LIKE ECH-ASSOCIATED PROTEIN 1;
3ga1-	B	12	4,9	98	122	9	NUCLEUS ACCUMBENS-ASSOCIATED PROTEIN 1;
1cs3-	A	11,3	4,5	98	116	15	ZINC FINGER PROTEIN PLZF;
4hxi-	A	11,2	2,7	167	192	14	KELCH-LIKE PROTEIN 3;
3b84-	A	11,2	4,8	95	113	12	ZINC FINGER AND BTB DOMAIN-CONTAINING PROTEIN 48;
6guw-	A	11	4,7	99	118	8	POZ (BTB) AND AT HOOK-CONTAINING ZINC FINGER 1;
7mk3-	B	10,7	8,9	173	365	14	REGULATORY PROTEIN NPR1;
6w66-	C	10,7	2,6	101	130	10	S-PHASE KINASE-ASSOCIATED PROTEIN 1;
4ues-	C	10,6	2,3	92	97	14	KCTD10;
5fta-	C	10,6	2,3	92	97	14	BTB/POZ DOMAIN-CONTAINING ADAPTER FOR CUL3-MEDIAT
2nn2-	B	10,6	4,8	99	117	14	ZINC FINGER AND BTB DOMAIN-CONTAINING PROTEIN 7A;
6xxs-	F	10,6	18,4	107	129	9	B-CELL LYMPHOMA 6 PROTEIN;
3ohv-	E	10,5	4,6	98	119	10	TRANSCRIPTION REGULATOR PROTEIN BACH2;
6zbu-	J	10,5	21,4	109	132	8	NUCLEAR RECEPTOR COREPRESSOR 1,B-CELL LYMPHOMA 6
6m8r-	B	10,4	2,4	89	96	15	BTB/POZ DOMAIN-CONTAINING PROTEIN KCTD16;
6m91-	B	10,3	2,6	111	132	14	F-BOX/WD REPEAT-CONTAINING PROTEIN 1A;
6er1-	A	10,3	5	100	121	13	CENTROSOME-ASSOCIATED ZINC FINGER PROTEIN CP190;
7bde-	A	10,3	5,1	104	126	10	ISOFORM 2 OF B-CELL LYMPHOMA 6 PROTEIN;
2vkp-	A	10,1	2,7	96	103	16	BTB/POZ DOMAIN-CONTAINING PROTEIN 6;
1buo-	A	10,1	3,9	102	121	15	PROTEIN (PROMYELOCYTIC LEUKEMIA ZINC FINGER PROTE
4zou-	A	10,1	2,8	93	119	13	STRUCTURE-SPECIFIC ENDONUCLEASE SUBUNIT SLX4;
4yy8-	B	10,1	3,7	118	377	10	KELCH PROTEIN;
3m4t-	A	10	4,9	95	115	13	TRANSCRIPTIONAL REGULATOR KAISO;
7shk-	C	10	2	81	98	12	CULLIN_2 DOMAIN-CONTAINING PROTEIN;
1fqv-	J	10	3,3	114	137	11	SKP2;
6n34-	B	10	5,1	101	119	10	INFLUENZA VIRUS NS1A-BINDING PROTEIN;
4u2m-	A	10	2,9	102	228	8	ZINC FINGER AND BTB DOMAIN-CONTAINING PROTEIN 17,
1p22-	B	9,9	2,8	112	131	15	F-BOX/WD-REPEAT PROTEIN 1A;
5a6r-	B	9,9	2,4	93	101	14	BTB/POZ DOMAIN-CONTAINING PROTEIN KCTD17;
2ovq-	A	9,9	2,8	111	134	12	S-PHASE KINASE-ASSOCIATED PROTEIN 1A;
5an3-	D	9,8	2	93	102	15	SGT1;
5ibk-	D	9,8	2,9	113	140	11	S-PHASE KINASE-ASSOCIATED PROTEIN 1,S-PHASE KINAS
2vpk-	A	9,8	2,1	92	115	10	MYONEURIN;
2ihc-	C	9,8	4,7	97	117	10	TRANSCRIPTION REGULATOR PROTEIN BACH1;
3ogk-	C	9,7	3,1	112	145	15	SKP1-LIKE PROTEIN 1A;
6i5j-	C	9,7	2	79	97	13	SUPPRESSOR OF CYTOKINE SIGNALING 2;
7cjb-	C	9,7	2	78	90	13	VON HIPPEL-LINDAU DISEASE TUMOR SUPPRESSOR;
5k35-	B	9,7	2,8	113	146	13	ANKYRIN-REPEAT PROTEIN B;
6wnx-	B	9,7	2,8	111	142	12	F-BOX/WD REPEAT-CONTAINING PROTEIN 11;
-2,00E+31	B	9,7	3	111	133	12	F-BOX ONLY PROTEIN 2;
1fs1-	B	9,6	2,2	100	116	12	CYCLIN A/CDK2-ASSOCIATED P19;
4crh-	A	9,5	1,8	88	94	15	SH3KBP1-BINDING PROTEIN 1;
5nw1-	H	9,5	2	77	89	13	ELONGIN-B;
5t35-	G	9,5	2	76	88	13	BROMODOMAIN-CONTAINING PROTEIN 4;
3drz-	A	9,4	2,7	95	103	16	BTB/POZ DOMAIN-CONTAINING PROTEIN KCTD5;
6v88-	B	9,4	1,9	94	116	15	SCF UBIQUITIN LIGASE COMPLEX PROTEIN SKP1A;
3v7d-	A	9,4	2,9	108	139	14	SUPPRESSOR OF KINETOCHORE PROTEIN 1;
2fnj-	C	9,4	1,8	75	88	13	CG2944-PF, ISOFORM F;
4w9g-	E	9,4	1,9	76	88	13	TRANSCRIPTION ELONGATION FACTOR B POLYPEPTIDE 2;
5bxh-	D	9,3	2,4	93	100	20	BTB/POZ DOMAIN-CONTAINING PROTEIN KCTD9;
4n9f-	B	9,3	1,7	75	87	13	CULLIN-5;
7jto-	K	9,3	1,8	75	87	13	WD REPEAT-CONTAINING PROTEIN 5;
1vcb-	B	9,3	1,9	75	88	13	PROTEIN (ELONGIN B);
6hax-	C	9,3	2	76	88	13	PROBABLE GLOBAL TRANSCRIPTION ACTIVATOR SNF2L2;

6hr2-	C	9,3	2	75	87	13 TRANSCRIPTION ACTIVATOR BRG1;
5jh5-	B	9,3	2,7	110	149	13 LYSINE-SPECIFIC DEMETHYLASE 2B;
3wso-	B	9,3	3	112	139	13 F-BOX ONLY PROTEIN 44;
2izv-	C	9,1	1,9	73	85	14 SUPPRESSOR OF CYTOKINE SIGNALING 4;
1ldk-	D	9,1	2,1	99	118	13 CULLIN HOMOLOG;
1lm8-	C	9,1	2,1	75	88	13 ELONGIN B;
6s4l-	A	9,1	3,1	104	217	13 BTB/POZ DOMAIN-CONTAINING PROTEIN KCTD1;
6r7f-	Q	9,1	6,4	92	112	11 COP9 SIGNALOSOME COMPLEX SUBUNIT 1;
7b5r-	S	9,1	2,9	107	138	9 CULLIN-1;
6brp-	C	9	2,9	112	137	15 F-BOX/LRR-REPEAT MAX2 HOMOLOG;
6p59-	E	9	2,1	78	96	13 CORE-BINDING FACTOR SUBUNIT BETA;
7azw-	B	9	2,5	90	114	12 ZINC FINGER AND BTB DOMAIN-CONTAINING PROTEIN 17
3zkj-	B	8,9	1,9	72	82	14 ANKYRIN REPEAT AND SOCS BOX PROTEIN 9;
1nex-	A	8,9	3	104	129	14 CENTROMERE DNA-BINDING PROTEIN COMPLEX CBF3
6o60-	D	8,8	3,2	118	148	12 PROTEIN PRENYLTRANSFERASE ALPHA SUBUNIT REPEAT-CO
6gyp-	D	8,8	3,5	120	151	12 CENTROMERE DNA-BINDING PROTEIN COMPLEX CBF3 SUBUN
5n4w-	C	8,5	2,3	78	91	13 CULLIN-2;
6p7x-	D	8,5	2,8	99	126	13 NDC10;
6vcd-	C	8,5	3	115	135	11 IRON-RESPONSIVE ELEMENT BINDING PROTEIN 2, ISOFOR
4bgc-	A	8,5	2,8	92	102	9 POTASSIUM VOLTAGE-GATED CHANNEL SUBFAMILY A MEMBE
6v9h-	D	8,4	1,9	71	81	13 CREATINE KINASE B-TYPE;
3m5b-	A	8,4	2,3	84	109	12 ZINC FINGER AND BTB DOMAIN-CONTAINING PROTEIN 32;
1dsx-	D	8,4	2,4	76	87	12 PROTEIN (KV1.2 VOLTAGE-GATED POTASSIUM CHANNEL);
7phk-	H	8,4	6,8	128	393	12 POTASSIUM VOLTAGE-GATED CHANNEL, SHAW-RELATED SUB
5zb2-	B	8,3	2	70	78	16 DNA REPAIR PROTEIN RAD7;
1qdw-	A	8,3	2,4	76	87	12 KV1.2 VOLTAGE-GATED POTASSIUM CHANNEL;
7e8e-	C	8,3	15,7	160	460	12 KV CHANNEL-INTERACTING PROTEIN 1;
6guv-	A	8,3	5,1	103	134	11 BTB DOMAIN;
3kvt-	A	8,3	3	91	103	9 POTASSIUM CHANNEL PROTEIN SHAW;
1exb-	E	8,2	2,6	78	91	12 KV BETA2 PROTEIN;
1a68-	A	8,2	2,5	77	87	10 POTASSIUM CHANNEL KV1.1;
6p7v-	D	8,1	2,8	99	126	13 CTF13;
2i2r-	K	8,1	4,4	103	132	10 POTASSIUM VOLTAGE-GATED CHANNEL SUBFAMILY D MEMBE
2r9r-	B	8,1	11,5	135	386	7 VOLTAGE-GATED POTASSIUM CHANNEL SUBUNIT BETA-2;